

AD-A161 674

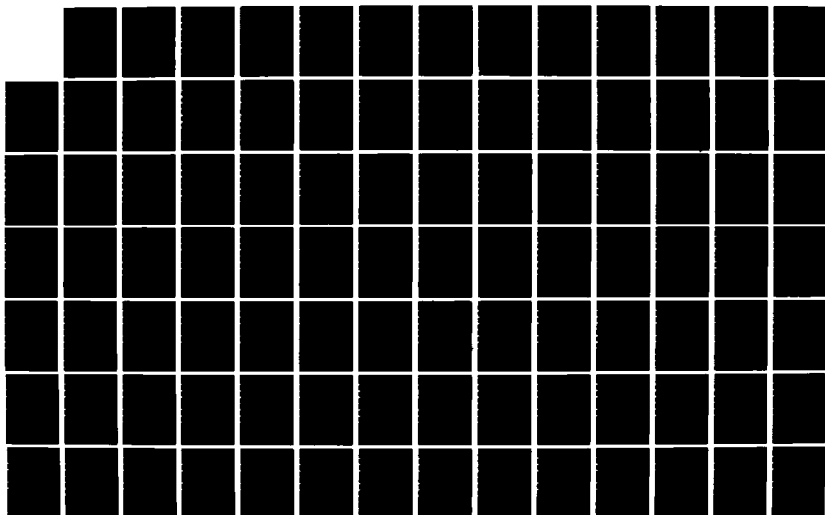
FLUORESCENCE FROM ELECTRON IRRADIATED GASES IN
REFURBISHED LABCEDE(U) PHYSICAL SCIENCES INC ANDOVER MA
B D GREEN ET AL SEP 85 PSI-TR-433 AFGL-TR-84-8218
F19628-80-C-0168

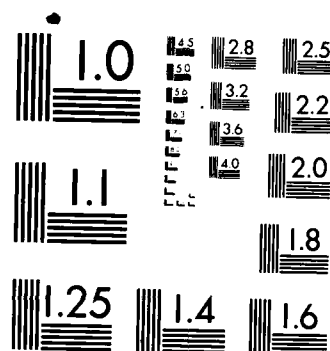
1/4

UNCLASSIFIED

F/G 4/1

NL





MICROCOPY RESOLUTION TEST CHART
NATIONAL BUREAU OF STANDARDS-1963-A

AFGL-TR-84-0218

12

FLUORESCENCE FROM ELECTRON IRRADIATED GASES
IN REFURBISHED LABCEDE

B. D. Green
L. G. Piper
G. E. Caledonia
P.F. Lewis
H.C. Murphy
W.J. Marinelli

Physical Sciences Inc
Dascomb Research Park
P.O. Box 3100
Andover, MA 01810

September 1985

Final Report
25 September 1980 - 29 February 1984

APPROVED FOR PUBLIC RELEASE; DISTRIBUTION UNLIMITED

AIR FORCE GEOPHYSICS LABORATORY
AIR FORCE SYSTEMS COMMAND
UNITED STATES AIR FORCE
HANSOM AIR FORCE BASE, MASSACHUSETTS 01731


DTIC
ELECTE
NOV 25 1985
S B

11 20-85 0611

AD-A161 674


DTIC FILE COPY

"This technical report has been reviewed and is approved for publication"


ALASTAIR R. FAIRBAIRN
Contract Manager


R. O'NEIL
Branch Chief

FOR THE COMMANDER


RANDALL E. MURPHY
Division Director

This report has been reviewed by the ESD Public Affairs Office (PA) and is releasable to the National Technical Information Services (NTIS).

Qualified requesters may obtain additional copies from the Defense Technical Information Center. All others should apply to the National Technical Information Service.

UNCLASSIFIED

SECURITY CLASSIFICATION OF THIS PAGE

AD-A161674

REPORT DOCUMENTATION PAGE

1a. REPORT SECURITY CLASSIFICATION Unclassified			1b. RESTRICTIVE MARKINGS		
2a. SECURITY CLASSIFICATION AUTHORITY			3. DISTRIBUTION/AVAILABILITY OF REPORT Approved for public release; distribution unlimited		
2b. DECLASSIFICATION/DOWNGRADING SCHEDULE					
4. PERFORMING ORGANIZATION REPORT NUMBER(S) PSI TR-433			5. MONITORING ORGANIZATION REPORT NUMBER(S) AFGL-TR-84-0218		
6a. NAME OF PERFORMING ORGANIZATION Physical Sciences Inc.		6b. OFFICE SYMBOL (If applicable)	7a. NAME OF MONITORING ORGANIZATION Air Force Geophysics Laboratory (OPR)		
6c. ADDRESS (City, State and ZIP Code) Dascomb Research Park, P.O. Box 3100 Andover, MA 01810			7b. ADDRESS (City, State and ZIP Code) Hanscom AFB Massachusetts 01731		
8a. NAME OF FUNDING/SPONSORING ORGANIZATION Air Force Geophysics Laboratory		8b. OFFICE SYMBOL (If applicable)	9. PROCUREMENT INSTRUMENT IDENTIFICATION NUMBER F19628-80-C-0168		
8c. ADDRESS (City, State and ZIP Code) Hanscom AFB Massachusetts 01731			10. SOURCE OF FUNDING NOS.		
			PROGRAM ELEMENT NO. 61102F	PROJECT NO. 2310	TASK NO. G4
					WORK UNIT NO. AU
11. TITLE (Include Security Classification) FLUORESCENCE FROM ELECTRON IRRADIATED GASES IN REFURBISHED LABCEDE (U)					
12. PERSONAL AUTHOR(S) B.D. Green, L.G. Piper, G.E. Caledonia, P.F. Lewis, H.C. Murphy, and W.J. Marinelli					
13a. TYPE OF REPORT Final		13b. TIME COVERED FROM 9/25/80 to 2/29/84		14. DATE OF REPORT (Yr., Mo., Day) September 1985	
				15. PAGE COUNT 366	
16. SUPPLEMENTARY NOTATION					
17. COSATI CODES			18. SUBJECT TERMS (Continue on reverse if necessary and identify by block number)		
FIELD	GROUP	SUB. GR.	Electron irradiation, fluorescence, cryogenic, interferometry, circularly variable filters, photometers, electron beam; NO, CO ₂ , beam plasma discharge,		
19. ABSTRACT (Continue on reverse if necessary and identify by block number) This report describes our efforts directed toward the study of electron-irradiated gases of atmospheric interest as part of the LABCEDE project. The cryogenic LABCEDE facility has progressed from the engineering refurbishment stage, through preliminary scoping experiments, to the acquisition of quantitative visible and infrared fluorescence data during this program. The facility has met all its design goals and typical operational ranges are described, along with optical detection networks. Emission spectra of nitrogen and air between 185 and 900 nm were surveyed and compared to observations of auroral radiances. Infrared spectral surveys using a CVF and interferometer provided many intriguing observations which suggest numerous future measurements programs. A series of measurements undertaken on the higher-pressure apparatus identified N(² D) as responsible for NH formation in N ₂ /H ₂ mixtures by altering the neutral and ionic kinetics with trace species. The					
20. DISTRIBUTION/AVAILABILITY OF ABSTRACT UNCLASSIFIED/UNLIMITED <input checked="" type="checkbox"/> SAME AS RPT. <input type="checkbox"/> DTIC USERS <input type="checkbox"/>			21. ABSTRACT SECURITY CLASSIFICATION Unclassified		
22a. NAME OF RESPONSIBLE INDIVIDUAL Alastair R. Fairbairn			22b. TELEPHONE NUMBER (Include Area Code) (617) 861-3661		22c. OFFICE SYMBOL OPR

DD FORM 1473, 83 APR

EDITION OF 1 JAN 73 IS OBSOLETE

UNCLASSIFIED
SECURITY CLASSIFICATION OF THIS PAGE

19. ABSTRACT (continued)

absolute production rates of vibrationally excited NO in irradiated N₂/O₂ mixtures are determined, with N(²D) felt to be the reaction precursor. About two percent of the total energy deposited in the gas by the electron beam appears as NO vibrational energy. A discussion of self-trapping of CO₂(v₃) emission is given to illustrate the modification of the observed fluorescence spectrum due to "hot band" and isotopic emissions. The excitation and quenching of Meinel bands by air and nitrogen are also reported. Large intensity enhancements have been observed in the presence of applied magnetic fields. Preliminary observations and explanations of this beam plasma discharge phenomenon are given. We would like to acknowledge the assistance of F. E. Ruccia, R. H. Krech, E. R. Pugh, and G. Kothandaraman in various aspects of this project.

18. SUBJECT TERMS (continued)

NH, MEINAL, quenching, ozone, production efficiencies, magnetic fields.

CONTENTS

		<u>Page</u>
Paragraph 1	INTRODUCTION	1
2	CRYOGENIC SHROUD MODIFICATIONS	7
2.1	Introduction/overview	7
2.2	Cryogenic shroud thermal performance.	8
2.2.1	Some cryogenic design considerations.	9
2.2.2	Aluminum shroud fabrication	11
2.2.3	Shroud thermal performance.	15
2.3	Gas flow network.	18
2.3.1	Introduction.	18
2.3.2	Pumping system modifications.	20
2.3.3	Gas flow in the shroud.	23
2.3.4	Concentration profiles.	33
2.3.5	Outgassing and pumpdown times	35
2.3.6	Observed vacuum performance	40
2.3.7	Modeling of flow in LABCEDE	42
2.4	Electron transport/primary beam characteristics and secondary electron spatial distribution .	63
2.4.1	Introduction.	63
2.4.2	Magnetic confinement coils.	63
2.4.3	Electron source modifications	67
2.4.4	Electron beam characteristics	70
2.4.5	Secondary electron density distribution	72
2.5	Detection capabilities.	85
2.5.1	Refurbishment	85
2.5.2	Capabilities.	86
2.5.3	Detection networks and geometries	87
2.5.4	Experimental intensity predictions.	89
2.5.5	391.4 nm scanning photometer.	93
2.5.6	Liquid He-cooled CVF.	101
2.5.7	Cryogenic LABCEDE IR optical environment. . . .	104
3	VISIBLE MEASUREMENTS	115
3.1	Introduction.	115
3.2	Experimental.	115
3.3	Spectral surveys and their comparison with field observations.	117
3.3.1	Visible results	117
3.3.2	Ultraviolet results	120
3.4	Variation in intensities of several features as functions of operating parameters	126
3.5	Summary of the visible measurements	137
4	INFRARED OBSERVATIONS.	139
4.1	Operational considerations.	139
4.1.1	Michelson interferometer.	139
4.1.2	The cryogenic CVF	141

CONTENTS

		<u>Page</u>
Paragraph 1	INTRODUCTION	1
2	CRYOGENIC SHROUD MODIFICATIONS	7
2.1	Introduction/overview	7
2.2	Cryogenic shroud thermal performance.	8
2.2.1	Some cryogenic design considerations.	9
2.2.2	Aluminum shroud fabrication	11
2.2.3	Shroud thermal performance.	15
2.3	Gas flow network.	18
2.3.1	Introduction.	18
2.3.2	Pumping system modifications.	20
2.3.3	Gas flow in the shroud.	23
2.3.4	Concentration profiles.	33
2.3.5	Outgassing and pumpdown times	35
2.3.6	Observed vacuum performance	40
2.3.7	Modeling of flow in LABCEDE	42
2.4	Electron transport/primary beam characteristics and secondary electron spatial distribution .	63
2.4.1	Introduction.	63
2.4.2	Magnetic confinement coils.	63
2.4.3	Electron source modifications	67
2.4.4	Electron beam characteristics	70
2.4.5	Secondary electron density distribution	72
2.5	Detection capabilities.	85
2.5.1	Refurbishment	85
2.5.2	Capabilities.	86
2.5.3	Detection networks and geometries	87
2.5.4	Experimental intensity predictions.	89
2.5.5	391.4 nm scanning photometer.	93
2.5.6	Liquid He-cooled CVF.	101
2.5.7	Cryogenic LABCEDE IR optical environment.	104
3	VISIBLE MEASUREMENTS	115
3.1	Introduction.	115
3.2	Experimental.	115
3.3	Spectral surveys and their comparison with field observations.	117
3.3.1	Visible results	117
3.3.2	Ultraviolet results	120
3.4	Variation in intensities of several features as functions of operating parameters	126
3.5	Summary of the visible measurements	137
4	INFRARED OBSERVATIONS.	139
4.1	Operational considerations.	139
4.1.1	Michelson interferometer.	139
4.1.2	The cryogenic CVF	141

CONTENTS (Continued)

		<u>Page</u>
Paragraph 4.1.3	Gas transport and kinetic regimes	
	in LABCEDE	142
4.2	Molecular systems	144
4.2.1	Electronic transitions of N ₂ and O ₂	144
4.2.2	N ₂ O MWIR fluorescence	147
4.2.3	Excitation efficiency of NO and CO.	149
4.2.4	NO(v) relaxation by NO.	151
4.2.5	Ozone fluorescence	160
4.2.6	CO ₂ fluorescence	163
5	OBSERVATIONS OF NH INFRARED CHEMILUMINESCENCE. . .	167
5.1	Introduction.	167
5.2	Experiment description.	167
5.3	Experimental results and interpretation	167
5.4	Summary	172
6	ABSOLUTE PRODUCTION RATES AND EFFICIENCIES OF NO IN	
	ELECTRON-IRRADIATED N ₂ /O ₂ MIXTURES	173
6.1	Introduction.	173
6.2	Experimental and data analysis.	173
6.3	Kinetic analysis.	179
6.4	Summary	188
7	ELECTRON EXCITATION AND COLLISIONAL QUENCHING	
	OF N ₂ ⁺ (A) MOLECULES BY N ₂ AND O ₂	189
7.1	Introduction.	189
7.2	Experimental.	190
7.3	Measurement technique	192
7.4	Experimental results.	195
7.4.1	Quenching rates	195
7.4.2	Relative excitation rates	206
7.5	Discussion	207
7.6	Summary.	211
8	ON SELF-TRAPPING OF CO ₂ (v ₃) FLUORESCENCE.	213
9	PRELIMINARY OBSERVATIONS OF BEAM PLASMA	
	DISCHARGES IN LABCEDE	219
9.1	Introduction	219
9.2	Qualitative description.	220
9.3	A quantitative look at the beam plasma	
	discharge in the LABCEDE device	223
9.4	Experimental results relevant to the beam	
	plasma discharges	231
9.5	Threshold measurements	241
9.6	Future investigations.	249
10.	REFERENCES.	251

CONTENTS (Continued)

	<u>Page</u>
APPENDIX A - REPORT ON THE CONCEPTUAL DESIGN OF THE LABCEDE CRYOSHROUD.	261
APPENDIX B - REPORT ON THE DESIGN OF THE LABCEDE CRYOSHROUD.	275
APPENDIX C - LABCEDE SPECTROMETER ANALYSIS	293
APPENDIX D - N.E.S.R. CALCULATIONS FOR DIFFERENT TYPES OF SPECTRORADIOMETER	341

Accd	
By	
Date	
Time	
Subject	
Remarks	
Dist	
A-1	

FIGURES

	<u>Page</u>
FIGURE 1. Cool down curves of cryogenic LABCEDE facility demonstrating quick cooling, temperature homogeneity, and continuous operation.	16
2. Estimated heating times for shroud assuming full heating input	19
3. Specified and measured flow rate/pressure curves for various stages of LABCEDE pumping system.	22
4. LABCEDE shroud throttle valve schematic	25
5. LABCEDE experimental volume pressure as a function of valve position for conical and flat valve seats, assuming viscous flow, 1300 sccm, and a pressure of 1 mT outside the shroud	27
6. Schematic of the experimental set-up for flow through a porous tube	28
7. Calculated and observed flow rates of nitrogen through a porous tube	29
8. Scaling of observed flow rates through porous tube array. .	31
9. Porous tube array	32
10. Diffusion of dosed gas in cryogenic LABCEDE	36
11. Pump-down for LABCEDE chamber	39
12. Beam excited species concentration gradients as a function of time for several flow velocities	44
13. Geometry for determining concentration, C, of species at a given position at time t' after delta function excitation.	45
14. Field of view along optical (x) axis.	45
15. Cross section of field of view at position x'	45
16. M(T) versus T	47
17. The integrated concentration along the line of sight at 1/4 mtorr pressure as a function of time for several excited state lifetimes, τ	49
18. The integrated concentration along the line of sight at 1 mtorr pressure as in Figure 17	50
19. The integrated concentration along the line of sight at 6 mtorr pressure for several flows and radiative lifetimes	51
20. Line of sight concentration after beam termination for several excited state lifetimes at 1/4 mtorr.	53
21. Line of sight concentration after beam termination for several excited state lifetimes at 1 mtorr.	54
22. Line of sight concentration after beam termination for several excited state lifetimes at 6 mtorr.	55
23. Tank clearing time (90%) as a function of flow.	58

FIGURES (continued)

	<u>Page</u>
FIGURE 24. Larmor radius of 2 and 5 kV electrons as a function of magnetic field strength	65
25. Filament region pressure as a function of restrictive orifice size for several exo-shroud pressures	68
26. Electron beam current as a function of filament current for 3 keV acceleration voltage.	71
27. Secondary electron distribution from 2 keV primary electrons for scattering from N ₂ and O ₂	79
28. Excitation cross sections for several excited molecular states using values from Ref. 18.	80
29. Spatial distribution of molecular ionic excited states as a function of chamber pressure	83
30. Estimated CO ₂ (v ₂) Q-branch intensities for various experimental operating conditions as compared with expected detection system noise equivalent spectral radiances. . .	92
31. Spectral response function for CVF ES-1B.	105
32. DC background signal levels in cryogenic LABCEDE as acquired by CVF	107
33. MWIR segment of data of Figure 32	108
34. LWIR portion of 9 June 1983 data of Figure 32	108
35. Radiances at a number of discrete wavelengths as calculated from data of Figure 32	109
36. Blackbody radiances versus wavelength for several temperatures of interest.	111
37. Contributions from three sources to observed radiances. . .	113
38. Visible spectrum of 2 mtorr of air irradiated by 8 mA of 3 keV electrons for two values of magnetic field . . .	118
39. LABCEDE UV spectrum of 1 mtorr air irradiated by 15 mA of 6 keV electrons, with an applied magnetic field of 26 Gauss.	121
40. LABCEDE UV spectrum of 1 mtorr nitrogen irradiated under the same conditions as Figure 39.	122
41. EXCEDE UV spectrum of the upper atmosphere irradiated by 3 keV electrons	123
42. Higher resolution (0.2 nm) LABCEDE UV spectrum of air for the same conditions as Figure 39.	124
43. Variation in intensity of N ₂ ⁺ (B ² Σ _u ⁺ , v' ₁ =0 → X ² Σ _g ⁺ , v''=0) at 391.4 nm as a function of pressure of air in absence of a magnetic field.	127
44. Variation in intensity of N ₂ ⁺ (B ² Σ _u ⁺ , v' ₁ =0 → X ² Σ _g ⁺ , v''=0) band at 391.4 nm as a function of pressure of air for four different magnetic field strengths for a 3.0 kV, 8 mA beam	130
45. Variation in the intensity of the N ₂ ⁺ (B ² Σ _u ⁺ , v' ₁ =0 → X ² Σ _g ⁺ , v''=0) transition at 391.4 nm as a function of E-beam current for five different magnetic fields at each of three different pressures.	132

FIGURES (continued)

	<u>Page</u>
FIGURE 46. Variation in intensity of $N_2^+(B^2\Sigma_u^+, v'=0 - X^2\Sigma_g^+, v''=0)$ transition at 391.4 as a function of E-beam current for five different values of E-beam energy . . .	133
47. Variation in intensity of $N_2(C^3\Pi_u, v'=0-B^3\Pi_g, v''=2)$ band at 380.4 nm as a function of the pressure of air for several different values of magnetic field	135
48. Variation in intensity of $N_2(C^3\Pi_u, v'=0-B^3\Pi_g, v''=2)$ band at 380.4 nm as a function of E-beam current at four different magnetic fields for each of three different pressures of air	136
49. Variation in the intensity of the $N_2(C^3\Pi_u, v'=0 - B^3\Pi_g, v''=2)$ band at 380.4 nm as a function of magnetic field at six different pressures of air	138
50. NO(1 + 0) fluorescence decay times in Ar/NO mixtures at 77 K using CVF.	143
51. SWIR spectrum of 1.83 mt of N_2 under slow flow conditions.	145
52. MWIR spectrum of 1.8 mt of N_2 under medium flow conditions	146
53. SWIR spectrum of 2.7 mt of O_2 when beam plasma discharge is occurring	146
54. Emission from 24 mt of N_2O as irradiated by 7 mA of 3 kV electrons with an applied field of 85 gauss	148
55. Emission from 0.5 mt N_2O in 43 mt of Ar when irradiated by 6 mA of 3 kV electrons under an applied field of 80 gauss	148
56. Fluorescence from 4% of O_2 in N_2 at a total pressure of 20 mtorr with no applied field.	149
57. Spectrum of 0.5 mt NO, 0.5 mt CO mixture irradiated by 6 mA of 6 kV electrons.	151
58. NO fundamental band fluorescence at beam termination from an Ar/NO (5%) mixture at 6 mt total pressure.	153
59. Synthetic spectrum comprised of emission from NO($v < 16$) which is best fit to the data of Figure 58	154
60. NO vibrational distributions at beam termination and 40 ms later for Ar/NO data at 6 mt pressure.	155
61. Vibrational population histories for representative vibrational levels	156
62. Total relaxation rates for Ar/NO 6 mt data	158
63. Preliminary relaxation rate coefficients for NO(v) by NO at 90K.	159
64. Ozone ν_3 band fluorescence from 6.3 mt of O_2 flowing at 250 sccm as irradiated by 6 mA of 5.5 kV electrons with no applied magnetic field	150
65. Scans of O_2 irradiated by 6 mA of 5.5 keV electrons.	161
66. CO_2 ν_3 and CO fundamental band fluorescence as detected by the CVF.	164

FIGURES (continued)

	<u>Page</u>
FIGURE 67. CO ₂ (ν_1) and partial (ν_2) features under some conditions as shown in Figure 66.	164
68. MWIR fluorescence from N ₂ 200 sccm/CO ₂ mixture at 1.7 mt total pressure when irradiated by 3.8 mA of 5.9 kV electrons.	166
69. NH($\Delta v=1$) emission observed in a mixture of 7.5 torr N ₂ /0.05 torr H ₂	168
70. NO fundamental band fluorescence spectrum at beam pulse termination from a 50 torr N ₂ , 1.5 torr O ₂ mixture . . .	175
71. The temporal behavior of the vibrational populations of NO($v=1-5$) deduced from the spectral fitting of the time resolved fluorescence	178
72. Normalized excitation rates for NO(v) compared with observations of Ref. 65	181
73. The fraction of total integrated intensity in the 780-795 nm region that can be attributed to N ₂ (B ³ Π_g - A ³ Σ_u^+ , 7,6) band	197
74. Variation in the ratio of the 391.4 nm intensity to that for the Meinel 2,0 band as a function of pressure of air	199
75. Stern-Volmer quenching plot for the Meinel bands in air. .	200
76. Current and voltage dependence of quenching constant of Meinel 2,0 band in air.	201
77. Meinel 2,0 quenching by N ₂ /O ₂ mixtures	203
78. Quenching of Meinel 2,0 band in N ₂ /O ₂ mixtures	204
79. Predicted and measured CO ₂ (ν_3) band transmitted intensity normalized to individual peak radiance	215
80. Comparison of three sets of Doppler predictions for CO ₂ (ν_3) band radiation at 0.25 torr CO ₂ with a) all transitions, b) no hot bands, but all isotopic fundamentals, and c) only C ¹² O ₂ ¹⁶ fundamental.	217
81. Relative contributions of individual bands to the total transmitted radiation as a function of CO ₂ pressure. . .	218
82. Energy deposition as a function of radial distance for several pressures for a 3 kV beam of electrons for scattering from a 300K gas	227
83. The total radial luminosity as a function of axial distance	227
84. Effect of slit height on intensity as a function of pressure	229
85. Variation in intensity of N ₂ ⁺ (B ² Σ_u^+ , $v'=0$ + X ² Σ_g^+ , $v''=0$) at 391.4 nm as a function of pressure of air in absence of a magnetic field	230
86. Effect of magnetic field on radial intensity distribution.	232

FIGURES (continued)

	<u>Page</u>
FIGURE 87. Variation in intensity of $N_2^+(B\ 2\Sigma_u^+, v'=0-X^2\Sigma_g^+, v''=0)$ band at 391.4 nm as a function of pressure of air for four different magnetic field strengths for a 3.0 kV, 8 mA beam.	233
88. Variation in intensity of $N_2(C^3\Pi_u\ v'=0-B^3\Pi_g\ v''=2)$ band at 380.4 nm as a function of the pressure of air for several different values of magnetic field	234
89. Bounds on quenching of BPD enhancements from the N_2C state as a function of pressure and magnetic field . . .	236
90. Characteristic beam frequencies in LABCEDE	238
91. Effect of magnetic field on observed intensity for N_2B and N_2C state emissions.	240
92. BPD intensity enhancements as a function of pressure for several currents	242
93. Pressure dependence of BPD thresholds in nitrogen as a function of beam current for 4.5 keV electrons and 44 Gauss applied field	243
94. Discharge ignition thresholds for 4.5 keV electrons into nitrogen over a range of B field.	245
95. Ignition and quenching thresholds in air from 391.4 nm measurements for 4.5 keV electrons	247
96. BPD enhancement of the $O_3(v_3)$ band from pure O_2 irradiated by 6 mA of 5.5 keV electrons.	248

TABLES

		<u>Page</u>
TABLE 1.	Thermocouples on the LABCEDE shourd	13
2.	Recommended outgassing rates for degreased stainless steel.	38
3.	Electron excitation efficiencies in absence of beam plasma discharge and quenching effects.	77
4.	CO ₂ (v ₂) molecules excited per ion pair.	90
5.	Relative gains for EMI9956B PMT	97
6.	Aperture-to-lens distances and magnification ratios for wavelengths other than 391.4 nm.	98
7.	Observations of NH fundamental band peak intensity. . . .	172
8.	Meinel-Band Quenching Rate Coefficients	205
9.	Relative Meinel-band excitation rates	206
10.	Ignition threshold criteria from several groups	246

1. INTRODUCTION

This report describes our experimental and analytical investigations using the LABCEDE Facility at the Air Force Geophysics Laboratory (AFGL) to measure and interpret the infrared fluorescence arising from electron irradiated gas mixtures. Previously, that system's operating capabilities were reviewed,¹ and it was concluded that major design modifications were required before definitive measurements would be possible. As a result, the great majority of our efforts during this contract have been restricted to improving system performance. Prior to system modification, measurements of absolute intensities and excitation efficiencies were not possible due to a lack of calibration and diagnostics. Also spectroscopic and kinetic data were often clouded by impurities and low signal levels. Moreover, system turnaround times were long and there was little flexibility in the operational conditions. The recommendations of the system study were that the electron beam be magnetically confined to increase energy deposition, the gas flow system be improved to allow smooth pressure control and to reduce impurity levels (both due to leaks and recirculation into the beam) and the fluorescence diagnostics be improved and the number observation ports be increased. In order to reduce the unwieldiness of the system and improve detection sensitivity it was recommended that the apparatus length be reduced by one-third. This would increase access to the (shorter) cryogenic liner or shroud.

Our design goals, details of the refurbishment and system performance are presented in Section 2. Because the existing shroud would have to be extensively rebuilt to achieve improved cool down times, background uniformity, gas flow control, and optical access, it was decided that a new shroud be fabricated. The details of the design and construction of the shroud are presented in Subsection 2.2 and Appendices A and B.

Pumping system improvements, design and construction of a gas inlet network to insure flow uniformity across the tank, design of the shroud's throttle valve to allow continuously variable pressures in the observation

volume, and calculations of the spatial distributions of beam-created species and condensible gases and modeling of gas flow are presented in Subsection 2.3. Experimental verifications of system performance are presented.

Improvements to the electron beam network are described in Subsection 2.4. Magnetic coils were designed to be capable of generating a field which would restrict the electrons to the observation volume (even at the highest pressures). This will facilitate the measurement of energy depositions as well as increasing signal intensities. Changes to the electron source were also made. Both magnetic coils and electron gun are operating satisfactorily on the rebuilt system.

The expected sensitivity limits of the rebuilt LABCEDE facility have been calculated previously.¹ These findings are used in the design of the new shroud in Subsection 2.5. An evaluation of the available spectroscopic detection networks is also presented and recommendations for future instruments are made. Continuing efforts to improve the facility are described: the interfacing of the liquid helium temperature circular variable filter (LHe:CVF) to the shroud; and the details of the optical design and construction of a beam energy deposition/spatial distribution diagnostic. Finally, the optical environment inside the LABCEDE facility under cryogenic conditions has been determined using the calibrated CVF. It was found that the background LWIR radiances correspond closely to the measured shroud wall temperatures. The radiance levels between 5 and 11 μm are lower than the 13 to 15 μm radiances but do not scale as an 85K blackbody. They are dominated by blackbody emission having the spectral distribution of a 220K emitter but with an apparent emissivity of a few parts in 10^4 . This component represents leakage or emissivity of the optics and is considered to be at an acceptable level. Finally, in the SWIR digitizer noise dominates the apparent background.

During this program the low pressure cryogenic LABCEDE facility has progressed from the engineering refurbishment stage, through preliminary scoping experiments, to the point where quantitative fluorescence data is being acquired in the visible and in the infrared. The modifications completed previously have permitted the major design goals to be met: improved cool down

times; cryogenic background uniformity; gas flow control; optical assessability; and the flexibility to allow a range of experimental measurements programs to be undertaken.

The first quantitative visible fluorescence measurements in LABCEDE are presented in Section 3. The emission spectra of nitrogen and air between 185 and 900 nm were surveyed and compared to observations of auroral radiances. The variation of several band intensities with pressure, beam current and voltage, and applied magnetic field was also studied. Large intensity enhancements have been observed in the presence of this field as a result of trapping and alteration of the secondary electron distribution. Beam growth modeling in the low pressure device is also applied to the experimental fluorescence observations.

Infrared fluorescence measurements were made using the CVF and Michelson interferometer and are described in Section 4. Observations were generally of a survey nature and are meant to define operating regimes for future detailed measurement programs. Order of magnitude fluorescent intensities are given to illustrate sensitivities. Electronic transitions between near-resonant electronic states (such as the W and B states in N_2) were observed in pure N_2 and pure O_2 . Fluorescence from N_2O was observed under a variety of conditions. NO and CO fundamental bands could be simultaneously observed. Their relative excitation efficiencies could not be accurately measured because of optical thickness, alteration of secondary electron distribution and diffusion effects. Measurement of the excitation and quenching of $NO(v)$ in Ar was undertaken to demonstrate the capability to perform kinetic measurements in the cryogenic apparatus. Preliminary quenching coefficients for $NO(v < 8)$ by NO at 90K are reported. In mixtures containing oxygen, ozone v_3 fluorescence at 9 to 10 μm was nearly always present. The dependence of this emission on flow, pressure, and applied magnetic fields are discussed in Subsection 4.2.5. $CO_2(v_2)$ emission at 15 μm was detected as well as v_3 , $v_1 + v_3$ and $v_1 + v_2$ emission at 4.3, 2.7, and 13.9 μm , respectively.

Although the major portion of our effort has been directed toward the low pressure cryogenic facility, three projects involving the high-pressure, room temperature apparatus were completed. They are reported in Sections 5, 6, and 8.

A series of kinetic measurements were completed to investigate NH fluorescence. It was found that $N(^2D)$ was responsible for $NH(v < 3)$ formation when N_2/H_2 mixtures were irradiated by 40 keV electrons. The fundamental band infrared fluorescence spectrum was observed using a Michelson interferometer. The addition of a trace species such as CO or NO permitted alteration of the kinetics, allowing the formation mechanism to be isolated. The results of these measurements are presented in Section 5.

In Section 6 the study of absolute production rates of vibrationally excited NO in electron irradiated N_2/O_2 mixtures is discussed. This was a difficult measurement because it involved absolute spectral calibrations and proper mapping of the interferometer's quasi-gaussian field of view onto the non-uniform fluorescence source. The deduced NO spectral radiances were compared with synthetic spectra to determine excited vibrational state populations. These, coupled with computer modeling of the electron energy deposition, resulted in an estimate of one vibrationally excited NO being created per ion pair. The distribution observed was nearly independent of vibrational level (i.e., constant for levels 1-7). Metastable $N(^2D)$ is felt to be the reaction precursor. About two percent of the total energy deposited in the gas by the electron beam appears as NO vibrational energy. These results have direct application in the interpretation of the radiances of the disturbed upper atmosphere and in model atmosphere refinement.

Section 8 was written in response to a recent journal publication about self-trapping of $CO_2(v_3)$ emission. Previous experiments on the high pressure LABCEDE apparatus have considered the transmission of electron-induced fluorescence through a resonantly absorbing non-irradiated medium (CO_2 : Ar mixtures). The observed emission spectrum was analyzed to deduce that the transmitted spectrum consisted mainly of "hot band" and isotopic fundamental transitions even at relatively low CO_2 pressures.

Our observations of the kinetics of the $N_2^+ A$ state are presented in Section 7. The Meinel bands in the visible-"red" spectral region were used as our primary diagnostic. This study grew out of our preliminary observations of Section 3 and provided many useful insights into the behavior of gases and electrons inside LABCEDE. We have measured the rate coefficients for quenching of $N_2^+(A \ 2\pi_u)$ by air to be nearly gas kinetic ($7 \times 10^{-10} \text{ cm}^3 \text{ molecule}^{-1} \text{ s}^{-1}$) for vibrational levels 2-4. Quenching of level 2 has been measured to be faster by nitrogen than by O_2 ($7.5:6.2 \times 10^{-10} \text{ cm}^3 \text{ molecule}^{-1} \text{ s}^{-1}$). Our results show that Meinel-band quenching becomes significant at altitudes below 100 km. Measurements of the fluorescent intensities of various Meinel bands at low pressures have permitted us to determine relative excitation rates for $N_2^+ A$, $v=2-7$.

Section 9 presents our preliminary observations of the thresholds for onset of the Beam Plasma Discharge phenomenon. Our results are compared with observations from other facilities and a review of theoretical understanding of this phenomenon is presented.

The authors would like to acknowledge the great assistance of R. H. Krech, E. R. Pugh, and G. Kothandaraman in the completion of various phases of this project.

2. CRYOGENIC SHROUD MODIFICATIONS

2.1 Introduction/Overview

The aim of the refurbishment program was to achieve several key system performance improvements. These included: more rapid cool down time, a uniform, low operating temperature; precooled test gases; reduction of the role of impurities and beam-created species - requiring a directed flow network, and enhanced detection capabilities - by decreasing background leakage levels, using high emissivity paint, and increasing the number of viewports and diagnostics. It was jointly decided by Physical Sciences Inc., (PSI)/AFGL personnel that too many changes of the existing aluminum shroud would be required and that the most efficient course was to fabricate a new shroud

Several possible concepts for the new shroud were devised. They included a sealed dewar, an assembly of sections of expanded stainless steel panels, and a cylindrical sheet with spiral tubing carrying the cryogen. Although all designs appeared capable of fulfilling our needs, it was decided to subcontract the conceptual design to an experienced cryogenic engineer, Frank Ruccia of A. D. Little. His recommended design involved a closed cycle recirculation system with pressurized (4 atm) liquid nitrogen flowing through tubing curved over a copper cylinder. Cooling occurs initially by vaporizing the liquid nitrogen, and during steady-state operation by heating the liquid. The liquid is recooled by flash expansion into a reservoir tank which collects and recycles the liquid. This design insures uniform low temperature operation while maintaining flexibility for later system modification. A report of this conceptual design by Frank Ruccia is included as Appendix A. It accurately delineates system operation constraints as determined by PSI/AFGL personnel and explains the conceptual design. The flow and radiation goals of the refurbishment which determined these constraints are discussed in later sections of this section.

Frank Ruccia was subsequently asked to complete a detailed engineering design of an entire cryogenic system based on his conceptual design. Some

example calculations of system operating parameters are given in the next section of this section. The final report of this engineering design is included as Appendix B. A set of blueprints were also provided by Frank Ruccia. These are presently being stored both at PSI and AFGL.

The copper shroud designed by ADL proved to be much too expensive to fabricate and did not permit elevated temperature operation (to permit bakeout of impurities from the walls). An aluminum shroud was constructed by Shawsheen Fabrications, Inc. The design modification was completed by PSI personnel (with advice from W. Toscano, another cryogenics engineer). The new aluminum design permitted 300°C operation. Some of the design modifications are discussed in Subsection 2.2.2. The shroud arrived at AFGL in July 1981 and was leak checked then fitted with numerous temperature and pressure sensors as described in Subsection 2.2.2. The shroud was then installed inside the vacuum enclosure, pumped down and gas flow measurements performed at room temperature. The liquid nitrogen recirculation system was completed, leak-proofed, insulated and put into operation (as described in Subsection 2.2.2). Cooldown of the shroud occurred in the fall of 1982. Generally, the system's operational parameters met or exceeded our design goals of improved cooldown times, background uniformity, gas flow control and easy optical access. Comparisons of these goals and performance are given throughout this section. This improved performance has permitted us to undertake quantitative measurements programs on this apparatus. The insulation blanket was not constructed at this time because system component failures or cryogenic leaks arising from recycling can be located more easily without the insulation. Additionally, the shroud met design goals without the insulation blanket in place. Operation at temperature below ~85K will require blanket installation.

2.2 Cryogenic Shroud Thermal Performance

The goal of cryogenic LABCEDE's shroud is to reduce background thermal emission sufficiently to permit observation of LWIR emission from low pressure gases (notably CO₂ (ν_2) fluorescence at 15 μ m) with sufficient sensitivity to resolve kinetic mechanisms and assign fluorescent efficiencies. In this

section we first cover our design constraints, then describe shroud fabrication in the next two sections. The shroud's thermal performance as monitored by the numerous thermocouples is described in Subsection 2.2.3. Our ultimate test - the LWIR optical environment is assessed in Subsection 2.2.4.

2.2.1 Some Cryogenic Design Considerations² - In order to calculate the liquid nitrogen requirements of the refurbished system, the expected heat load on the shroud was estimated. The radiative heat load, q_{rad} , of a warm surface 1 (tank) surrounding a colder surface 2 (shroud) is given by Eq. (1) the expression

$$q_{\text{rad}} = \sigma A_2 \frac{\epsilon_1 \epsilon_2}{\epsilon_1 + \frac{A_2}{A_1} (1 - \epsilon_1) \epsilon_2} (T_1^4 - T_2^4) \quad (1)$$

where σ is the Stefan-Boltzmann constant, A is the surface area, ϵ is the emissivity, and T is the temperature (K). The infrared emissivity of the stainless steel vacuum enclosure is 0.2. Aluminum is a good infrared reflector, but depending on its surface condition its emissivity may vary from 0.04 to 0.1. The corresponding heat load on the shroud from Eq. (1) will be 140 to 300W.

The other major heat load will be conduction by the residual gas outside the shroud. The expected operating conditions will have submicron pressures in the vacuum annulus; free molecular flow best describes the gas under those conditions. The transition to continuum flow occurs at only slightly higher pressures. In the molecular regime the heat transfer is simply described by the formula

$$q_{\text{cond}} = 0.016 \text{ apA}_2 \Delta T \quad (2)$$

where a is the accommodation or sticking coefficient (0.8) and P is in torr. The conductive heat load is 315W at 1 μm and approaches 0 at blank off pressures. Independent calculations by Toscano agree to within 15 percent. Additional losses by conduction through solids were minimized by supporting the shroud on Teflon® pads and using thin-walled stainless steel tubing as the supply line-vacuum connections. The power deposited by a 20 mA, 3 kV beam at

50 percent duty cycle is only 30W. The calculations do not include the effects of a Fiber-frax® (felted glass fiber) insulation blanket which would reduce the total radiative and conductive heat load to less than 50 W. In any case, with a total heat load of 400 W, liquid nitrogen consumption during steady-state (post-cooldown) operation would be 9 l/hr (175 l/day).

The new aluminum shroud is expected to weigh less than 180 kg. The heat which must be removed from this mass to cool from 300 to 77K is

$$\int_{77}^{300} m_{\text{shroud}} C_p dT . \quad (3)$$

The heat capacity (C_p) is a function of temperature, but has an integrated value 38.8 cal/gm-K. Assuming that cooling occurs both by the vaporization of liquid nitrogen and some heating of the gaseous boiloff, about 100 l of liquid nitrogen would be required to cool the shroud. The continuous line recirculation system optimizes heat extraction by the vaporized liquid nitrogen.

Detailed calculations of the shroud cool-down time were completed. Only a summary will be presented here. Heat transfer occurs very rapidly through the tubing walls and into the recirculating liquid. Less than a half hour should be required to completely, uniformly ($\Delta T < 3K$) cool the aluminum cylinder walls once liquid nitrogen is in the surrounding tubing lines. The liquid flow in the cooling lines is turbulent (aiding heat transfer). The recirculation pump or external tank pressure is sufficient to provide liquid nitrogen mass flows in excess of 300 g/s. Thus, sufficient liquid to cool the shroud to 80K would flow in only 5 min. Unfortunately, the gas boil-off chokes the flow at a much lower level, lengthening cool down time accordingly.

Once the shroud cylinder walls are cold (or cooling) the radiation baffle (sled) and throttle valve will begin to cool by radiation and conduction. Estimates of their cooling times were made using Eq. (1) and assuming that the surrounding surfaces (in this case the shroud walls) were already at 77K. In

light of the discussion above (where cooling will occur rapidly once liquid nitrogen fills a section of the tubing), this is a reasonable assumption. Additional cooling by conduction through the aluminum, q_k , is given by the formula

$$q_k = -kA \frac{dT}{dx} \quad (4)$$

where k is the thermal conductivity, A is the cross sectional area of the heat transfer path, and dT/dx is the temperature gradient along the conduction path. The sled will be painted black and have a high emissivity. Nevertheless, conduction across the face of the sled through the conduction straps to the cooled valve collar will dominate radiational cooling at all temperatures. The baffle surface should be below 100K in less than 1/2 hr after the adjacent cooling lines are cold.

The throttle valve is mounted on a stainless steel shaft and cooling is provided only through four lengths of flexible braided copper strapping running from the edge of the valve to the valve collar. The initial design permitted 300K emission to leak onto the valve through the cylindrical pumping channel around the rear edge of the shroud. Due to its poor thermal sinking, the valve would never be cooled to less than 140K. Additional braided copper straps would restrict gas flow (increase pumping conductance) and hamper valve travel. As a result, additional chevron radiation baffles were added in the cylindrical pumping channel (in a "water-wheel" configuration). Consequently, the radiation load on the valve was reduced by at least two orders of magnitude and the valve should achieve sub 90K temperatures. At present it was hoped that a one to 1 to 1/2 hr cooldown period (all temperatures less than 100K) can be achieved for the entire shroud (exclusive of the radiatively-cooled valve).

2.2.2 Aluminum Shroud Fabrication - The decision to switch from copper to aluminum for the shroud material was made due to the prohibitive cost of copper and the desire to bake out the shroud after extended runs or exposure

to the laboratory environment. Although copper is more dense, the two have about the same thermal diffusivity ($\frac{k}{\rho C_p}$) and the design did not have to be seriously altered. Welding of the cooling tubing was possible with aluminum. Helicoil inserts had to be used for screw threads in the double-sided ports. All low melting temperature materials were eliminated from the design (such as lead gaskets). Explosion bonded junctions Al-stainless were required for cooling line connection to the recirculation network. Cajon® zero-clearance connectors were substituted for the flexible bellows on the door hinge assembly due to space limitations. Shawsheen Fabrications did an excellent job constructing the shroud and interacting with PSI personnel. Because of concerns about aluminum tubing being porous and susceptible to leaks, a careful leak-checking procedure was followed. The entire shroud was shocked twice (liquid nitrogen was forced through the cooling lines). The sections of the shroud were then pressurized and bubble checked; evacuated overnight and a leak rate determined; and finally checked with a helium leak detector at AFGL. The last method is the most sensitive by many orders of magnitude. A relatively large leak was found in the door section and repaired by removing the top half of the tubing welding the burned through section and resealing the top portion. Two additional very small leaks were located near the beam plane. They were not repaired, but used to determine the sensitivity of the vacuum system to leaks. They were easily detectible with the helium detector through over 100 ft of 3/4 in. I.D. tubing, yet their observed leak rates are less than a few sccm. Future large scale leaks will be easily located.

Once the shroud was at AFGL, resistors for elevating the shroud temperature were attached (see below). Copper constantan (type T) thermocouples were spread over the outer surface and inside of the shroud to verify temperature uniformity and cooldown times. Forty-three thermocouples were potted into position using a heat conductive electrically-insulating blue epoxy (Wakefield Engineering) to avoid ground loop problems. This epoxy was measured to be stable over repeated cyclings between 77 to 530K. The positions of the thermocouples are given in Table 1. The 0.01 in. wires were fed to central terminal strips at the top rear of shroud, and then out of the vacuum through two detachable multipin connectors. The thermoelectric voltages generated

TABLE 1. THERMOCOUPLES OF THE LABCEDE SHROUD

Thermocouple	Display	Position on Shroud
1	LN 1	Entry point LN ₂ line (broken)
2	LN 2	Near LN ₂ line mid cylinder
3	LN 3	Near LN ₂ line exit point
4	LN 4	Top of door
5	LN 5	On center support rings of cylinder
6	LN 6	In beam plane 1:30; far from resistive heater
7	LN 7	In beam plane exit side 10:00
8	LN 8	Rear cover plate valve area
9	LN 9	On beam entrance port 3:00 on top (cf. TC 35)
10		On beam exit port 9:00 on top (cf. TC 36)
11	LN 11	In beam plane 12:00 on side
12	LN 12	On door, center port between lines
13	LN 13	On door, beam side port between LN ₂ lines (cf. TC 33)
14	LN 14	On side port #8: 3:00
15	Omega 1	Near heater on door-bottom
16	Omega 2	Near heater door end of cylinder near TC 4
17	Omega 3	Near heater at TC junction strips
18	Omega 4	On non-condensable gas line inlet
19	Omega 5	On non-condensable gas heat exchanger
20	Omega 6	On condensable gas line inlet
21	Omega 7	On condensable heat exchanger
22	Omega 8	At center of sled
23	Omega 9	Halfway out sled
24	Omega 10	At edge of sled 11:00
25	LN 15	On radiation baffles, top plate 11:00
26	LN 16	On valve collar outside 12:00
27	LN 17	At center of valve
28		At edge of valve
29	LN 19	On front bearing housing of valve
30	LN 20	On porous array-center, on copper line
31	LN 21	On porous array on aluminum standoff 9:00
32	LN 22	On porous tube stainless steel 12:30
33		On door on port near hinge (cf. TC 13)
34	LN 23	In beam plane at exit 7:30
35		At beam entrance 3:00 on bottom (cf. TC 9)
36	LN 10	At beam exit 9:00 on bottom (cf. TC 10)
37		At edge of sled 4:00
38	LN 24	On valve strap holder
39		On rear bearing housing for valve shaft
40		On top rear port (TC port)
41		3/4 down cylinder between LN ₂ lines
42	LN 18	On top of end cap far from LN ₂ lines 12:00
43		On radiation baffle baseplate 9:00

^aTimes refer to circumferential positions viewing from door down cylinder

^bLN = Leeds Northrup display 24 channels

^cOmega = 10 channel multimeter scanner

were corrected by an electric reference junction at 273K and displayed as a voltage on a scanning multimeter. They could also be converted to a temperature and plotted on a Leeds Northrup chart display, where the readings from up to 24 thermocouples could be sequentially displayed. Several of the junctions were immersed in liquid nitrogen (at 1 atm pressure) and found to be accurate to greater than 1K. Consequently they should accurately reflect the local shroud temperature.

The recirculation system (composed of the flash tank reservoir, liquid nitrogen pump and connecting lines) was constructed at AFGL while the shroud was being built. The flash tank was also built by Shawsheen Fabrications. The pump was purchased from Cosmodyne. It is a centrifugal impeller pump which can output up to 32 l/s of liquid nitrogen with a maximum 50 psi head. It required a static head of several feet of liquid at its input to prevent cavitation. As a result, it was positioned one story below the LABCEDE apparatus. The work required to raise the liquid to the experiment will tend to heat the liquid. The temperature rise has been calculated to be ~ 1K by Ruccia, Toscano, and Cosmodyne separately.

The circulation lines were constructed of 1 in. I.D. copper with numerous pressure relief valves as per ADL's specifications. The system was leak checked then insulated with 3 in. of preformed foam and covered with a vapor barrier. Some difficulty was encountered in achieving successful recirculation pump operation. Liquid nitrogen was flowing through the passive pump, the shroud, and collecting in the flash tank, but the pump cavitated when the recirculation mode was attempted. Conversations with Frank Ruccia of A. D. Little helped resolve the situation. The pressure of the liquid nitrogen at the recirculation pump was above atmospheric (or at the pressure in the storage tank). Unless the liquid nitrogen transport lines between the storage tank (or flash tank) and the pump are well insulated, the liquid nitrogen rapidly absorbed heat from the walls of the copper lines and becomes a saturated liquid gas mixture at its boiling point (77 to 90K). The centrifugal pump creates a lower pressure at its inlet, the liquid-gas mixture vaporizes forming a gas pocket and the pump cavitates. Supporting evidence for this

explanation included lack of liquid air ($T_b = 78$ to $81K$) condensing off the pump faceplate, and the asymptotic temperature of the shroud was $\sim 90K$. Extreme care was taken to insulate and have a vapor barrier over every cryogenic surface between the flash tank and the shroud in order to insure low temperature operation of the shroud. Routine operation in the recirculation mode was then achieved. It was also suggested that the outer surface of the shroud should be insulated to decrease its radiative and conductive heat load. The shroud reached an acceptable temperature without the insulating blanket (as described below) and blanket installation was postponed until the results of the LWIR background radiance measurements in LABCEDE demonstrate a clear need for colder walls. It was noted that similar temperatures were achieved using a cool down procedure which slowed the liquid nitrogen flow to a trickle after liquid began to appear in the flash tank. At present, either approach can be used to achieve steady state operation.

2.2.3 Shroud Thermal Performance - A typical time history of the thermocouples during a routine cooldown is plotted in Figure 1. The improved system performance is clearly demonstrated. After 2 hr of cooling, nearly all thermocouples (TC) are reading below $100K$ ($-276^\circ F$) and the system is operating in the recirculation mode. The TC's which drop fastest are near the inlet cooling line on the door of the shroud. Different TC drop at different rates - those on the cooling lines show a rapid temperature drop once that section of the tubing is cooling. TC's far from cooling lines show a more gradual decrease. The general trend is a sequential cooling of the shroud from the door through the beam plane, to the valve (which is the liquid nitrogen flow direction). The more thermally isolated positions are the slowest to cool. These are (in order of decreasing cooling rates): the porous tube array, the valve collar and holders, the chevron baffles, the valve shaft bearing housings, the non-condensable gas heat exchanger, the sled, the valve and the condensable gas heat exchanger. The center of the pressure control valve (LN 17) is seen to asymptotically cool toward the temperature of the rest of the shroud, reaching $110K$ after 6 hr (even though the liquid nitrogen flow had stopped). Although there is a fairly large temperature spread in the TC readings, most of the shroud's surface is felt to be fairly homogeneous at

90 \pm 5K. The TC's were placed at the hardest regions to cool, especially in the valve region. The radiation baffle sled allows little emission from the valve and chevron baffles (and the room temperature outer walls) from entering the shroud. It was found that the shroud and experiment could have a suitable background for cryogenic experiments by 11:00 a.m. each morning. It can be noted from Figure 1 that the addition of gases increases the cooling rate of the slower components (conductive transport from cold shroud walls to the relatively warmer valve and collar. Also, no appreciable beam heating occurs even at locations where the beam is stopped by the walls. The beam has a power of 75W (5 kV, 15 mA) and produces a visible hot spot on the inner shroud wall. Conduction by the aluminum is sufficient that the temperature rise of the shroud wall is not detectable. All these observations bear out our design calculations and result in a very flexible experimental apparatus.

The temperature rise of the passive system overnight was observed to be 10 K/hr with no vacuum pumping occurring. This corresponds to an average heating load of 350W. This is in rough agreement with our calculations of continuum conduction dominated heating. If, as is typical, the system is operated till late, and is to be used the next day, the temperature will have risen to only 200K (with all components in equilibrium). Consequently, cooling to < 100K occurs more quickly on the second day. At present, cooldown has become a routine procedure and the late morning start for experiments has never proven to be an inconvenience.

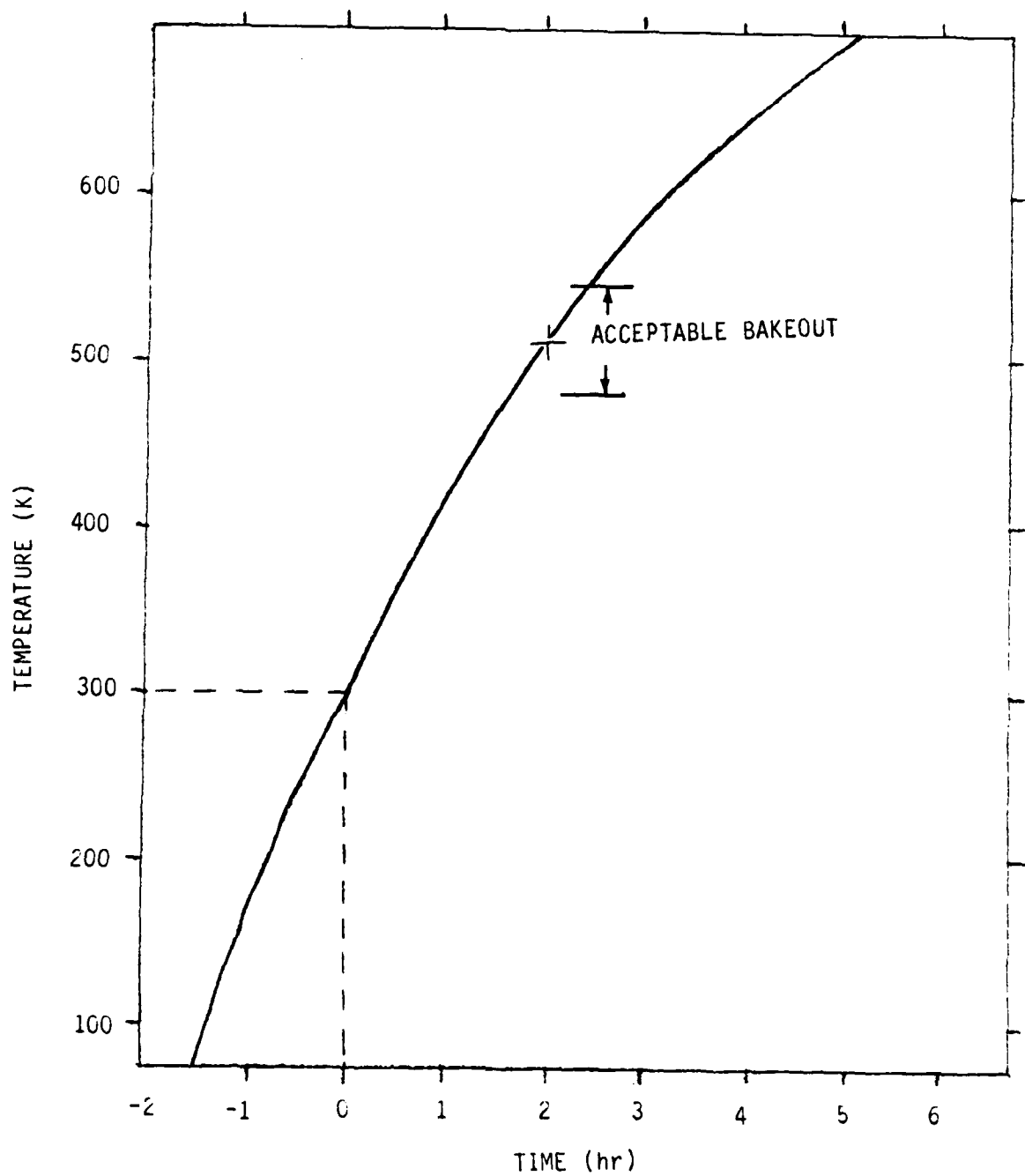
In order to expedite the outgassing of impurities from the walls, the shroud was designed to withstand elevated temperatures so that it could be "baked-out" to vaporize these species. All components of the shroud (wiring, paint, plastic connectors) were independently temperature checked for stability to the temperature extremes. A practical limit of 260°C (500°F, 533K) was found to exist. All components on the shroud are safe up to this temperature. A distributed heating network was used. A total of 250-25W (480 ohm) resistors were uniformly distributed over the surface of the shroud. The bottoms of the resistors were curved to ensure good thermal contact in the vacuum environment. The resistors are connected in parallel in five separate

strands. Each is controlled by a separate 10A, 120V variac. Resistors for different variacs were interspersed so that if one variac became inoperational, uniform heating was still possible. An estimate of the time required to heat the shroud is plotted in Figure 2. The curve includes both radiational and conduction losses from the shroud without an insulating blanket with full power input (6000W). Thus heating the shroud from liquid nitrogen to ambient temperatures would take less than 1-1/2 hr. It should only require ~2 hr to bring the shroud from room temperature up to 250°C where outgassing occurs at a rapid rate.

Resistive heaters were attached to the surface of the shroud to provide bakeout and the capability for rapid warmup from cryogenic temperatures. They were designed to provide something less than 6 kW of heat to the shroud. Because emission from contaminants (H_2O , CO_2) has not been observed, the heaters have been used only infrequently. Nevertheless, a new calibration and graph paper were purchased to permit the Leed Northrup thermocouple display unit to plot temperatures between -200° and +200°C. The shroud was successfully heated (under nearly full power) to 200°C (473K) with no detrimental effects.

2.3 Gas Flow Network

2.3.1 Introduction - One of the major goals of the refurbishment effort is the exclusion of spurious radiators from the observed infrared fluorescence. These emitters could arise from a variety of sources including: leaks; outgasing; electron sputtering from the walls; or recirculation of previously-irradiated, excited molecules or molecular fragments back into the electron beam volume. The procedure adopted to achieve our goal was to create a directed flow of pure inlet gas sweeping smoothly through the beam plane carrying beam created species rapidly (time scale milliseconds) out of the irradiated volume. In order to create this plug flow, the momentum is removed from the inlet gases using a porous tube array. The residence time in the beam is minimized by magnetically confining the beam (see Subsection 2.4) and by maximizing pumping speeds. Outgasing will be diminished by baking the



A-1748

Figure 2. Estimated heating times for shroud assuming full heating input.

shroud at elevated temperatures prior to experimental data acquisition if necessary.

The next section discusses pumping system modifications implemented to achieve maximum pump throughputs. The measured flows in the rebuilt system are compared with calculations. In Subsection 2.3.3 the design of the gas flow system in the shroud is covered. The complex throttle valve was designed to minimize pumping conductance yet allow an accurately variable experimental operating pressure inside the shroud. (The same design also was required to minimize leakage of 300K radiation inside the shroud.) The gas inlet manifold (porous tube array) final design is also discussed in that section. Small-scale experiments were performed and their findings scaled to LABCEDE operating conditions. The porous array was calculated to be capable of easily delivering the required gas flow and the throttle valve conductance were estimated to not seriously restrict the gas flow. These design goals have been achieved as verified by experimental flow measurements on the warm shroud inside LABCEDE. These results are presented in Subsection 2.3.3. Centimeter/millisecond gas flow velocities are achieved, resulting in short (ms) beam residence times.

Additional calculations of the profiles of beam created species as they flow and diffuse out of the beam and of the concentrations of condensibles (e.g., CO_2) which will reach the beam plane during cryogenic operation are presented in Subsection 2.3.4. Estimates of outgasing levels are presented in Subsection 2.3.5. The observed vacuum performance is described in Subsection 2.3.6. Various models of the flow in LABCEDE are presented in Subsection 2.3.7.

2.3.2 Pumping System Modifications - Because of the great size of the old LABCEDE facility, the shroud could not be easily removed for repair or replacement unless the vacuum enclosure was shortened and rotated. Accordingly, the 3×10^3 kg LABCEDE apparatus was rotated 65 deg and the shroud removed. A 1.6m length of the vacuum enclosure (including one of the NRC HS-32-50000 diffusion pump ports) was cut away. The remaining diffusion pump

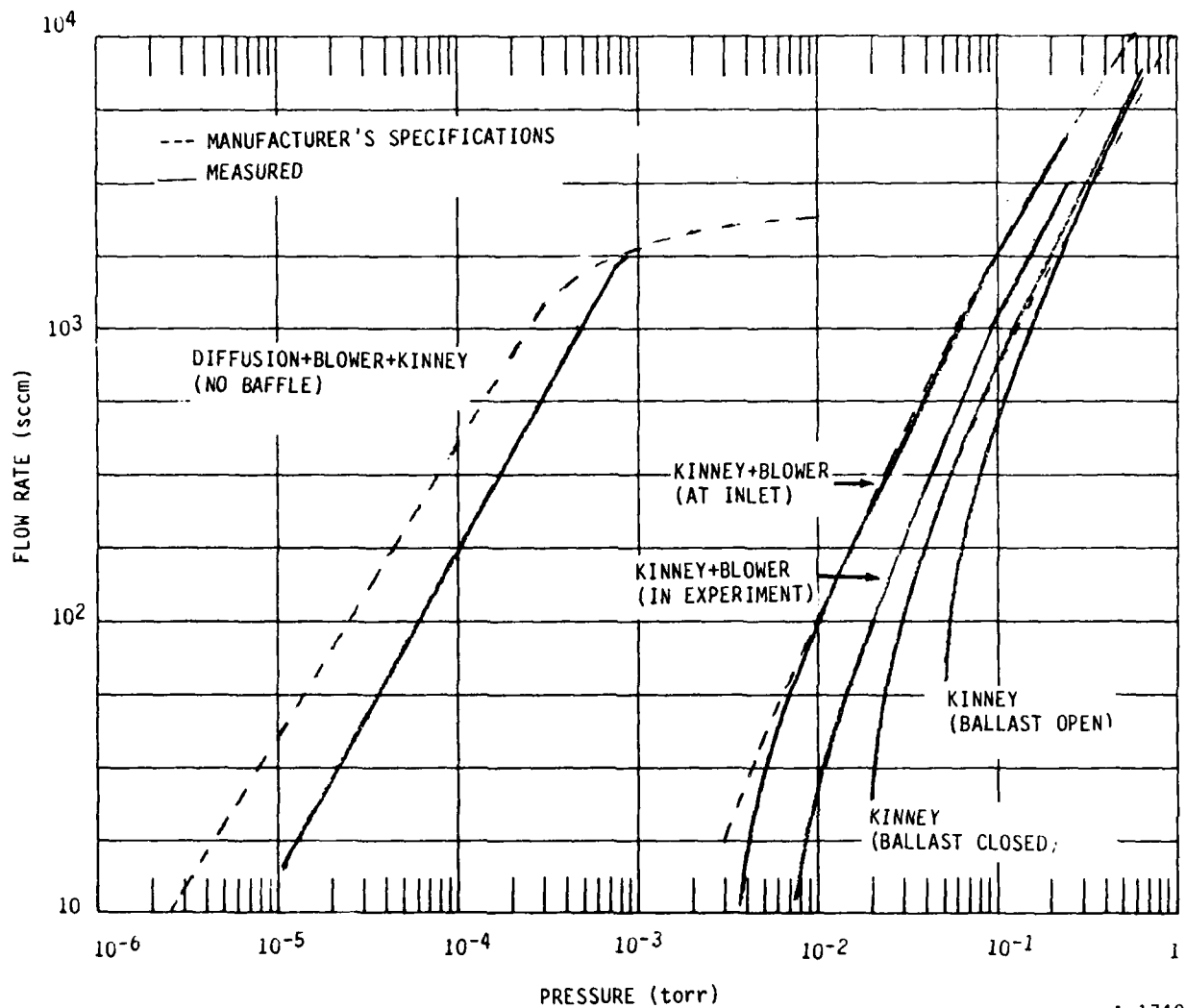
was detached and lowered during this process. A total reconditioning of the pumping network was undertaken with an aim of increasing pumping network throughput especially at high mass loadings.

The rough pump for the system is a Kinney KT500 which pumps 350 to 450 cfm under LABCEDE operating conditions. The flow rate pressure characteristics of this pump at the pump inlet were measured and the pump is operating up to specifications. These values are plotted in Figure 3. At high mass loads the Kinney may have insufficient pumping speed to maintain the diffusion pump forepressure at an acceptable level. Thus, a Root's Blower WA 1000 (650 cfm) was installed between the diffusion and Kinney pumps. The increased throughput of the blower-Kinney combination is also displayed in Figure 3. A new, more conductive pumpline was built with the following features:

- a. Six inch I.D. piping with large radius elbows
- b. A 1/2m extension at the diffusion pump exit to prevent diffusion pump oil blow-over at high mass flows
- c. Two vibration-isolation bellows located near the diffusion pump exit (axis horizontal) and at the inlet to the Kinney (axis vertical)
- d. A remote control (dead man) gate valve at the entrance to the blower
- e. Multiple venting and pressure sensing stations.

With this new pumpline, the measured flow rate-pressure characteristics as measured in the experiment were only reduced by a factor of two from the front face blower values, i.e., the conduction of the inert diffusion pump and pumpline reduced pumping speed only by a factor of two.

The 50,000 l/s diffusion pump was cleaned, repaired, and filled with DC702 oil. This oil rather than DC704 was chosen because its lower boiling



A-1749

Figure 3. Specified and measured flow rate/pressure curves for various stages of LABCEDE pumping system. Losses due to conduction are seen to be factor of two. All curves are taken using laboratory air.

point provides more mass at the inlet jets thus providing more throughput at higher pressures. As a result, the measured flow-pressure behavior of the entire pumping system (diffusion + blower + Kinney) meets specifications exactly at the highest throughputs (Figure 3). At lower flows where conductance is important the network is a factor of 2.5 slower. The maximum gas flow was increased to over 1800 sccm of air by the system improvements. The addition of the liquid nitrogen baffle will reduce the throughput at lower pressures by another factor of two but will not change the maximum throughput appreciably. This throughput (2.1 g/min) exceeds the design goal and will permit rapid transit of the gas through the beam.

Because vibration was felt to be detrimental to infrared detection systems (interferometers, spectrometers), an effort was made to reduce this level during rebuilding. In addition to the perpendicular sets of bellows in the pump line, the Kinney air bag supports were inflated and dense rubber pads (FABCELL) were positioned under the entire LABCEDE apparatus and under the Roots blower. In this manner pump vibrations were less strongly coupled into the pumpline and less reached the experimental area through the diffusion pump. The pads under the experiment reduced vibration transmitted through the building to the laboratory floor. A considerable reduction in the vibration levels has been achieved - no detectible vibrations can be felt on the vacuum enclosure.

2.3.3 Gas Flow in the Shroud - After the vacuum enclosure was shortened, the new shroud was designed to permit introduction of gases at the end away from the pump. The shroud would be relatively vacuum-tight so that the gas flow was directed across the beamplane to an exit point located over the diffusion pump. The momentum of the incoming gases was removed using a porous tube array. The resulting flow down the length of the shroud should be smooth (plugged) and any minor surface irregularities (such as observation port flanges) of the size of the mean free path (2 cm) should not disturb the flow characteristics. At present no flow velocity distribution diagnostics are being implemented. At the low pressures in LABCEDE, a differential pressure measurement (upstream-downstream) would have to detect changes in pressure

about an order of magnitude smaller than detectable using the most sensitive Baratron head. A visible fluorescence or phosphorescence diagnostic could be implemented in the future if a flow diagnostic is required.

The exit port was designed to minimize pumping conductance yet allow reproducible pressure control inside the shroud. A schematic of the throttle valve is shown in Figure 4. This design was chosen to minimize room temperature emission entering the shroud (see Subsection 2.5). The throttling occurs as the valve is inserted inside a 15-deg tapering cone. The decreased cross-sectional area open to the flow gradually decreases as the valve is closed, choking the flow. As a result, pressures of up to 75 mT (100 μ m) can be maintained inside the shroud without sacrificing diffusion pump throughput. As the valve is closed, the gas flow rate can be maintained (at up to 1800 sccm), but as the pressure rises the flow velocity decreases linearly. Thus if the flow velocity in the shroud is 4.50 m/s at 7 mT and 1800 sccm, then at 70 mT and the same flow, the velocity will be 45 cm/s.

The flow conductance for the exit valve of the shroud was calculated using standard formulae in Dushman³ where the individual conductances of the various flow restrictions in the exit path contribute to the net conductance as their reciprocals and the conductance of each restriction is given by

$$F = \frac{1}{4} d^2 \frac{\pi}{2\rho_1}^{1/2} \quad (5)$$

where ρ_1 is the density outside the shroud and d is the effective aperture diameter. The net conductance at 300K is calculated to be 5×10^6 cm³/s. The pressure expected inside the shroud is calculated from

$$Q = F (P_{\text{shroud}} - P_1) \quad (6)$$

where Q is the throughput (sccm), P_1 is the pressure outside the shroud and P_{shroud} is the pressure inside. Pressure values calculated from these

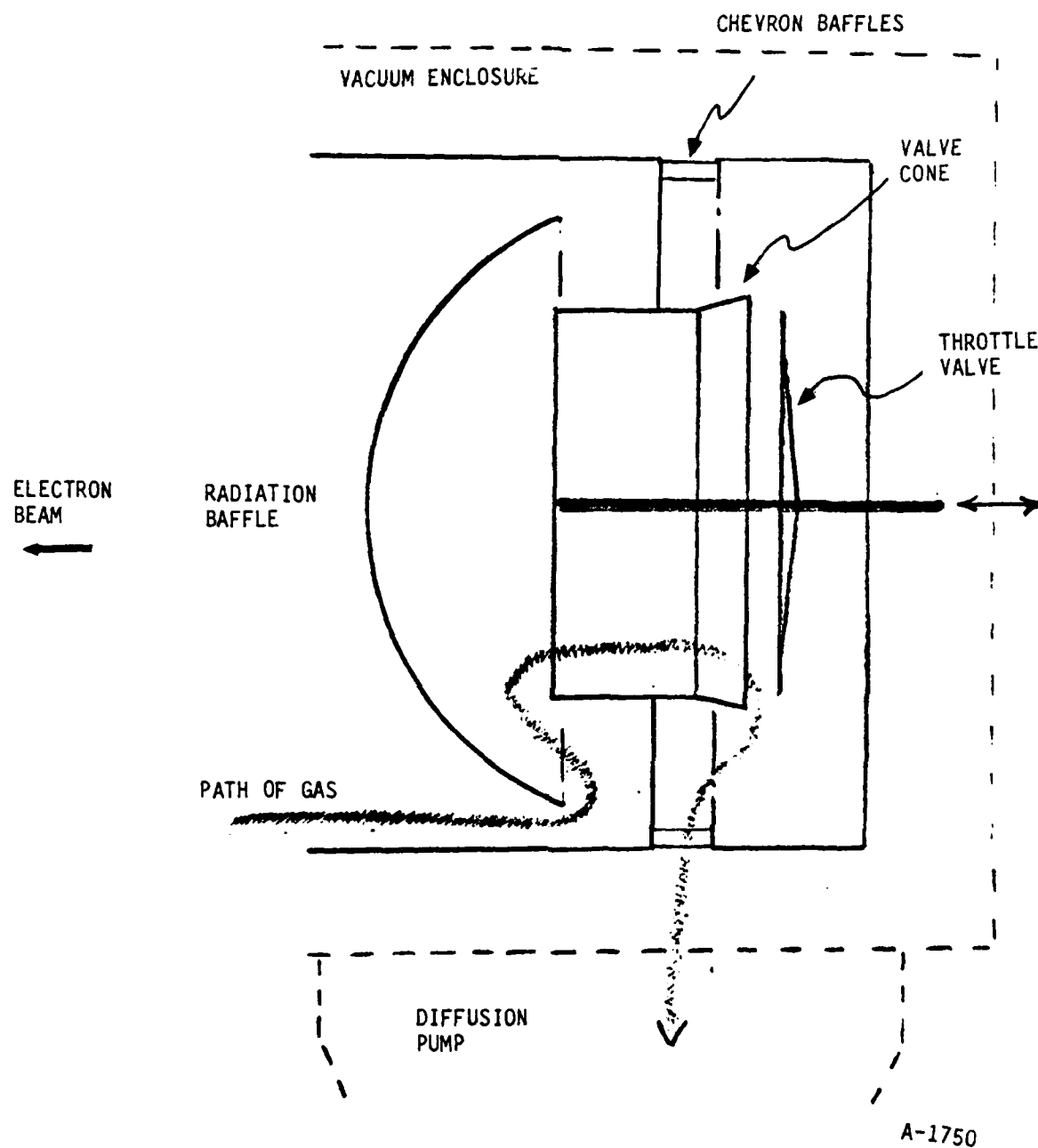
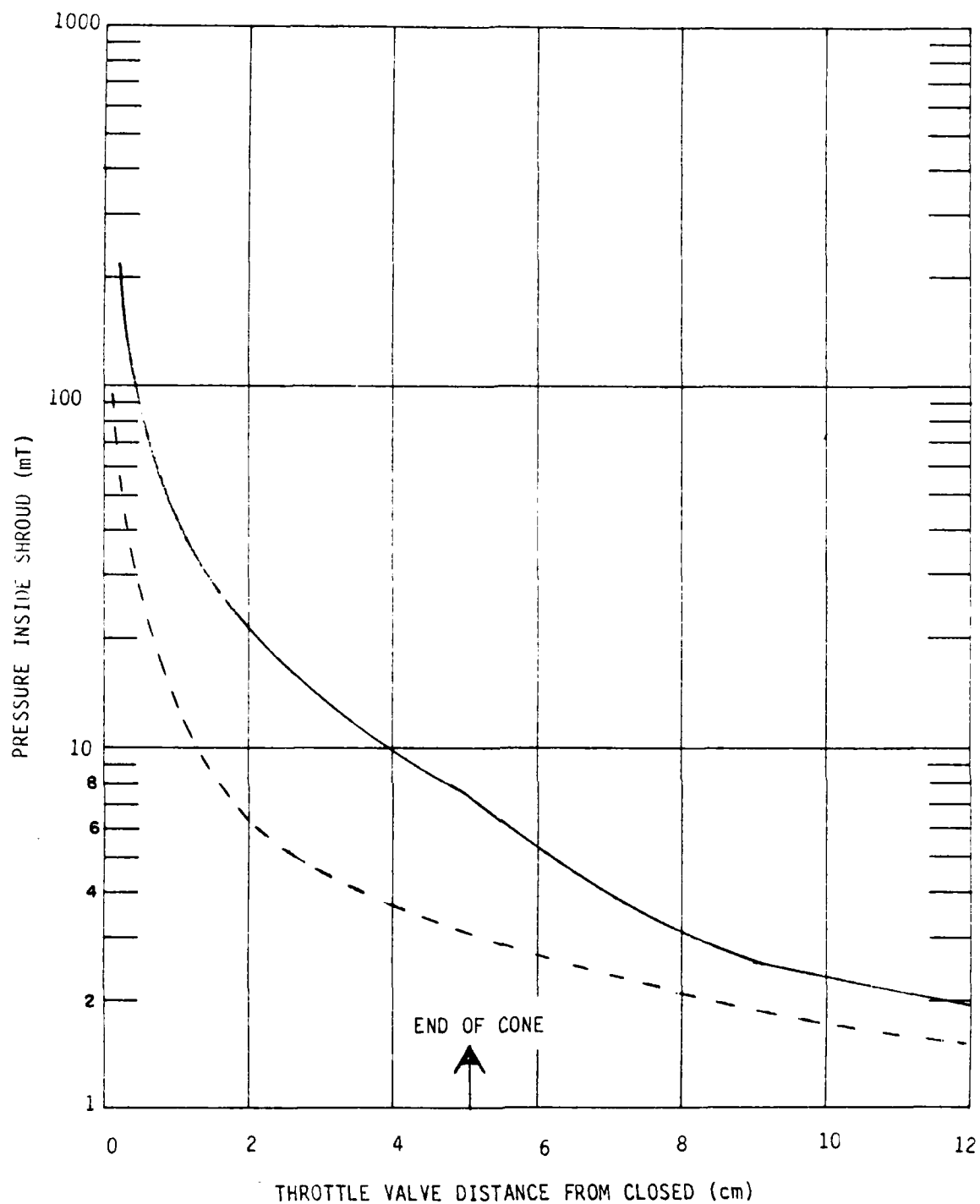


Figure 4. LABCEDE shroud throttle valve schematic. All solid line surfaces will be cooled to cryogenic temperature. Scale 1/8 actual.

formulae are about 20 percent lower than measured at large flows and increasing lower as flow is decreased. At a flow of 1700 sccm, a pressure of 4.7 mT was expected inside the shroud, 5.8 mT was observed.

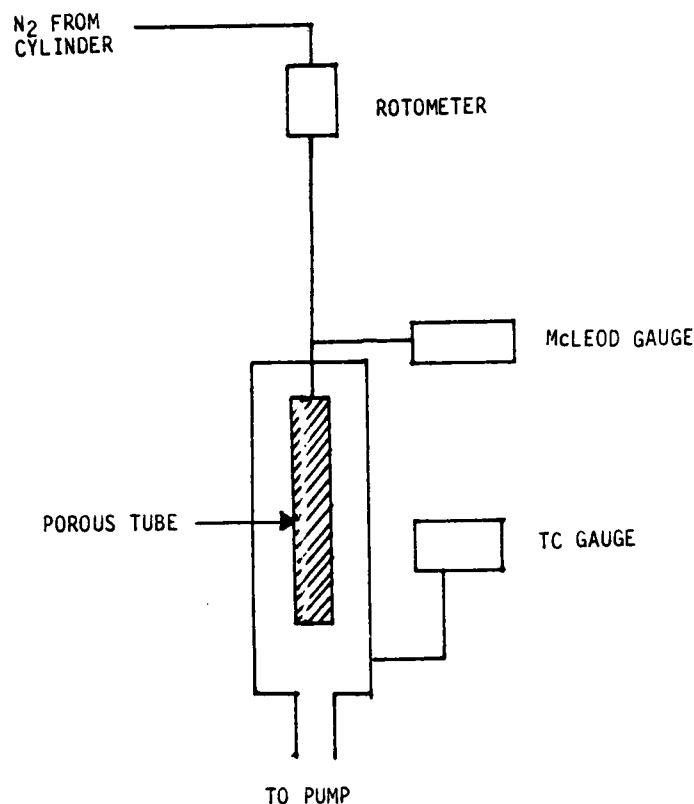
A calculation of the variation of shroud pressure for a given flow rate and exoshroud pressure as a function of throttle valve position is shown in Figure 5. The advantage of a conical valve seat over a flat ring is evident in that figure. This calculation assumes viscous flow through a tube. If the flow is molecular the curve moves upward on the figure. Additionally, as Q and P_0 increase the curve also moves upward. Pressures of up to 83 mT (100 μ m) have been achieved inside the shroud with this design. The lower pressure limit at maximum flow will be conductance limited and is ~6 mT. Lower operating pressures will require lower flow rates. The gas inlet network will be discussed next.

In our LABCEDE studies gases such as O_2 , O_3 and CO_2 in low concentrations are introduced in the primary flow of nitrogen. A mass flow rate of 2.5 to 0.005 g/min, a background pressure of 1 to 100 μ in the tank and a temperature of less than 90K are required. At a 1 μ chamber pressure and a mass flow of 2.5 g/min, the final average velocity of the flow should be 17.5 m/s. It is necessary to ensure a smooth flow of gases through the tank in the axial direction. In a previous report⁴ it was recommended that the best way to ensure plug flow in the tank is to introduce the gas through an array of porous tubes. The flow pattern of the gas issuing from such an array of porous tubes has been investigated by Avidor, Kemp and Knight.⁵ For a tube spacing of 7.5 cm, it was observed that approximately four spacings downstream of the array, a uniform flow is established. In those experiments, the pressure inside the porous tubes was 150 psig, considerably higher than that in LABCEDE. To ensure that the required mass flow can be achieved under LABCEDE conditions (i.e., low pressures) a simple bench-top experiment was performed. The schematic of the experimental setup is shown in Figure 6. Nitrogen gas from a gas cylinder was introduced through a porous tube into a vacuum chamber. The vacuum in the chamber was maintained by continuously pumping by a 5 cfm vacuum pump. The quantity of the gas flowing through the porous tube



A-1751

Figure 5. LABCEDE experimental volume pressure as a function of valve position for conical and flat valve seats, assuming viscous flow, 1300 sccm, and a pressure of 1 mT outside the shroud.

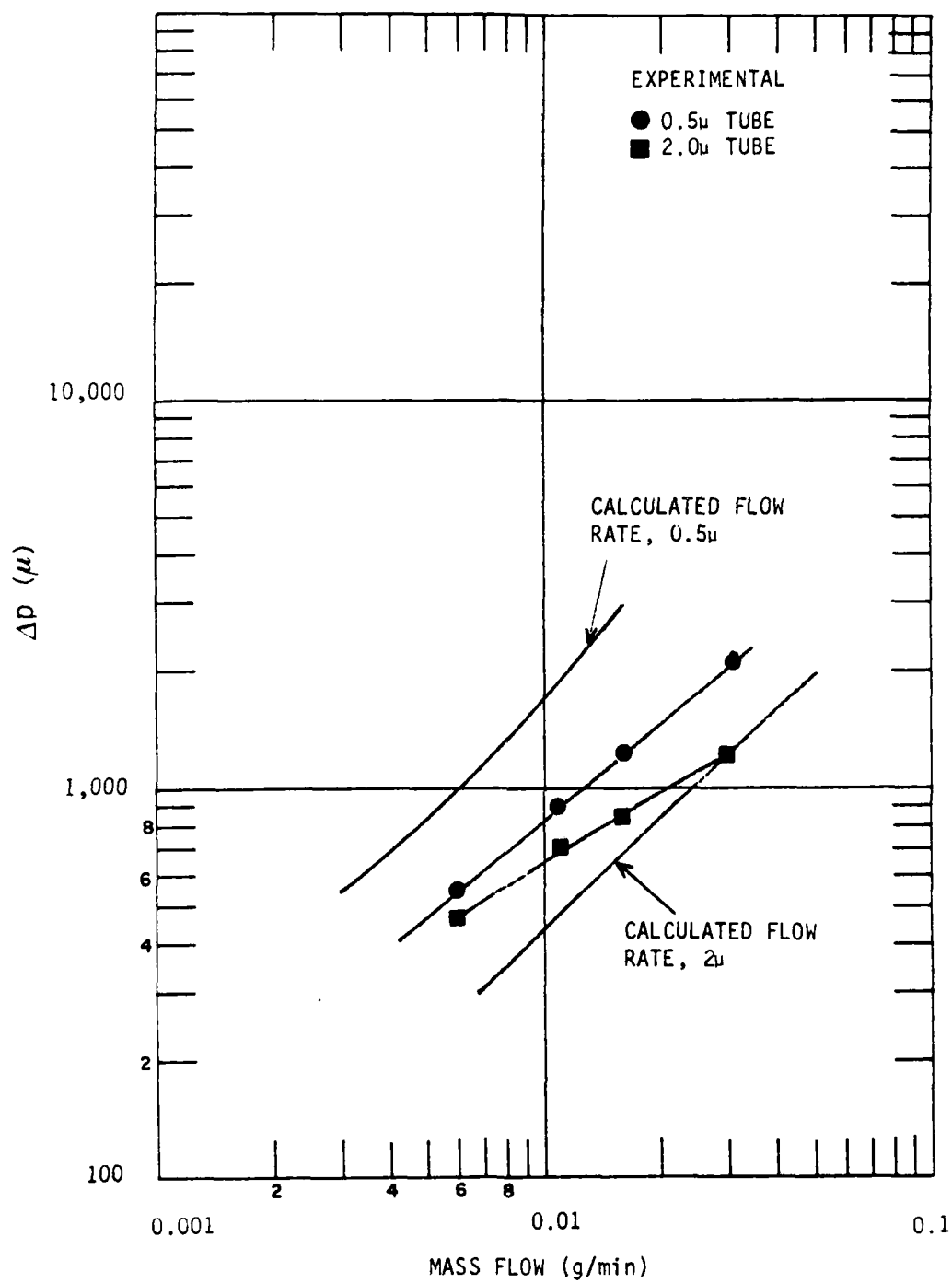


A-1752

Figure 6. Schematic of the experimental setup for flow through a porous tube.

was monitored by a precalibrated Matheson 601 Rotometer. A McLeod gauge and a thermocouple gauge monitored the pressures at the inlet to the porous tube and the vacuum enclosure, respectively. The measured differential pressure across 0.5 and 2 μ porous tubes for the various mass flow rates are shown in Figure 7. The mass flows were calculated using a capillary model. The flow rate Q is given by:⁶

$$Q = \left(\frac{D_{KA}}{D_{AA} + D_{KA}} \right) \left[D_{AA} + \frac{\pi}{4} D_{KA} + \frac{d^2}{32 \mu} P \right] \frac{\Delta p M \epsilon}{RT \ell} \left(\frac{L}{L_e} \right)^2 \quad (7)$$



A-1753

Figure 7. Calculated and observed flow rates of nitrogen through a porous tube.

where

$$D_{KA} = \text{Knudsen diffusion coefficient} = \bar{v} \frac{d}{3}$$

$$D_{AA} = \text{Self diffusion coefficient} = \frac{v\lambda}{3}$$

$$\bar{v} = \left(\frac{8}{\pi} \frac{RT}{M} \right)^{1/2}$$

p = total pressure

Δp = pressure difference

$$\frac{L}{L_e} = \text{ratio of diffusion length to straight pore length} - 1/\sqrt{2}$$

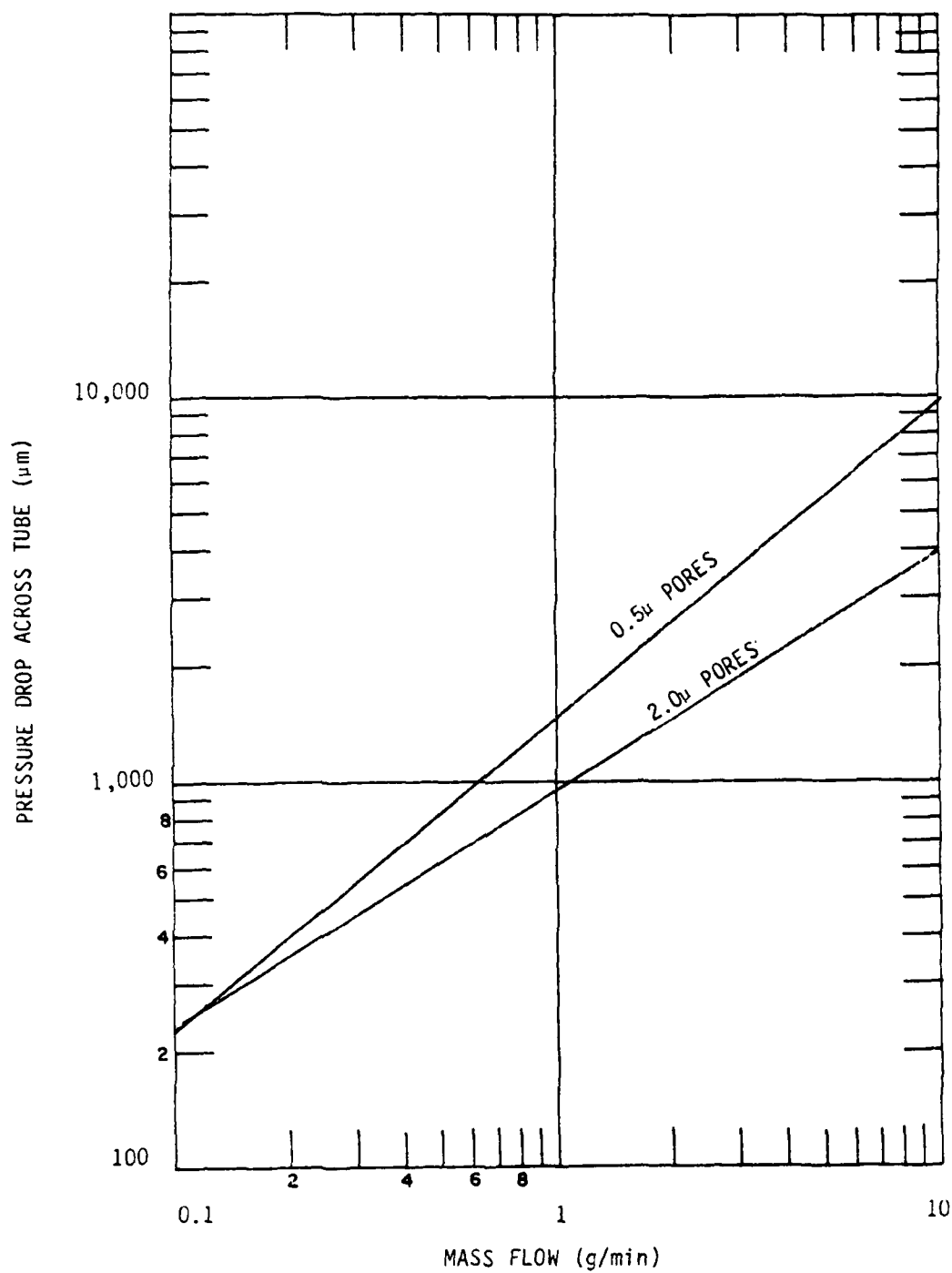
ϵ = porosity

μ = viscosity coefficient

Q = mass flow rate

d = pore diameter

In the above equation there are contributions due to Knudsen diffusion, self-diffusion and viscous effects. In the present experiment the viscous term is negligible compared with Knudsen and self-diffusion terms. The calculated flow rates through 0.5 and 2 μ porous tubes 12 in. long, 0.375 in. O.D. are also shown in Figure 7. While the agreement between experimental and theory is not excellent, the theoretical predictions are within a factor of two. The experimental results were scaled for LABCEDE conditions, i.e., 77K, 24 ft length and are shown in Figure 8. From this figure it is clear that porous tubes of 2.0 or 0.5 μ pores will be sufficient for 2.5 q/min flow rate. Tubes with 0.5 μ pore diameters were chosen since these were readily available.



A-1754

Figure 8. Scaling of observed flow rates through porous tube array.

A schematic of the porous tube array is shown in Figure 9. This configuration is easy to assemble and ensures that the mass flow rate is uniform over the cross-section of the tank. The tube lengths in each section of the array is such that the mass flow per unit area is the same through the chamber. The porous tubes, 3/8 in. O.D., 1/16 in. wall made of stainless steel were purchased from Mott Metallurgical. The connecting tubes are 3/8 in. O.D. wrought copper pipes to ensure thermal conduction. The porous tubes were silver brazed to the copper pipes. Clearances have been provided for the viewing windows. The entire porous tube array is fastened at the end of each length of tubing and at several places along the centerline to the aluminum backing plate with aluminum blocks to ensure good thermal contact with the shroud. As expected no problem was encountered passing this gas flow through the porous tube array. The gas flow network system inside the shroud has met design goals, although the scintered stainless steel tubes cool slowly.

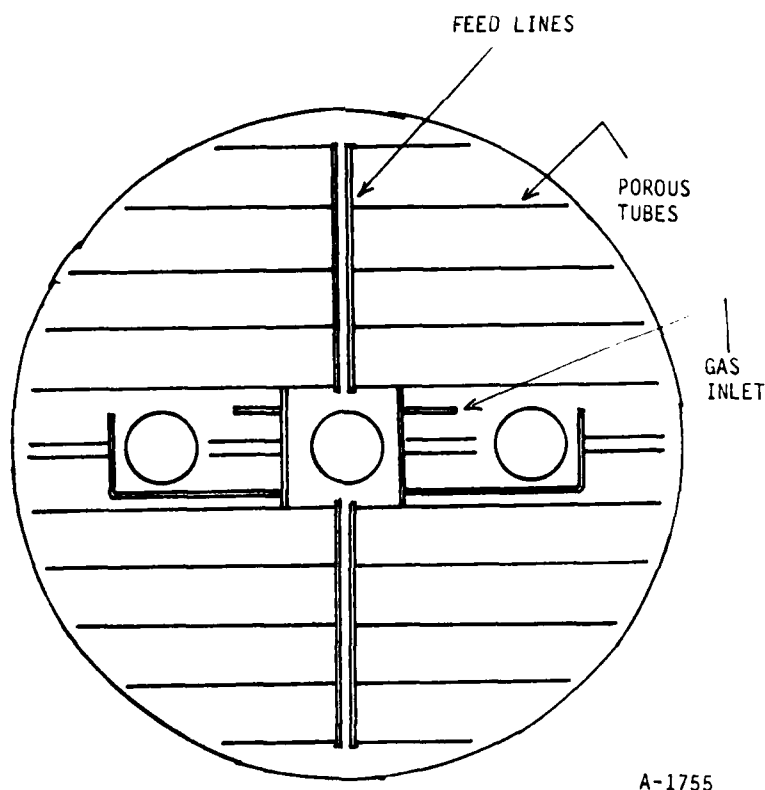


Figure 9. Porous tube array.

2.3.4 Concentration Profiles - For studying reactions of gases such as CO_2 and H_2O which are condensible at 77K, the ambient temperature of the LABCEDE experiment, the gases will be passed through the secondary heat exchanger and not allowed to cool to 77K. They then would be introduced through an orifice as a jet which will expand into the background gas. For the case of jet expansion, the concentration of the gas at the location of the electron beam was estimated. The details of the calculations are given below.

The gas pressure at the inlet to the tank is expected to be about 5 torr and the flow rate between 5×10^{-4} to 0.033 g/s. The pressure in the tank will vary from 0.1 to 0.001 torr. Thus there is a reduction in pressure by a factor of 50 to 5000. There is an expansion of the inlet flow into a relative vacuum. The structure surrounding the free expansion region is depicted by a barrel shock. Caledonia et al.⁷ in their COCHISE report have calculated the density profile in such a barrel shock. In their model, the gas reaches the limiting velocity in which all of the thermal energy of the flow is converted into kinetic energy

$$u_2 = (u_1^2 + 2C_p T_1)^{1/2} \quad (8)$$

where u_1 and T_1 are the velocity and temperature of the gas at the inlet, u_2 the limiting velocity, and T_1 inlet temperature of the gas. If the inlet Mach number is subsonic

$$u_2 = \left(\frac{2}{\gamma - 1} \right)^{1/2} a_1 \quad (9)$$

where a_1 is the speed of sound at the inlet temperature. The gas density in the free expansion is approximately given by:

$$P_2 = \frac{A f(\theta) \dot{M}}{u_2 r_2^2} \quad (10)$$

where \dot{M} is the mass flow rate and r_2 is the spherical radius from the exit plane of the inlet tube.

$$f(\theta) = \left[\cos \left(\frac{\pi \theta}{2 \theta_{\infty}} \right) \right]^{2/\gamma - 1} \quad (11)$$

$$A = \left[2\pi \int_0^{\theta_{\infty}} f(\theta) \sin \theta \, d\theta \right]^{-1}$$

where θ_{∞} is the maximum turning angle for the expansion of an isentropic gas into a vacuum ($\theta_{\infty} = 130.6$ for $\gamma = 1.4$).

If the inlet tube is located along the centerline of the tank 75 cm away from the e-beam the above model predicts the density at the e-beam location to be 1.5×10^{-9} M g/cc. For the mass flow stated, the concentration at the electron beam axis would be $0.02 - 1 \times 10^{12}$ molecules/cm³ ($2 \times 10^{-4} - 10^{-2}$ mT). Knowing the approximate angular expansion of the jet from the nozzle and integrating over all angles, we can estimate that 43 percent of the molecules reach the beam plane without seeing the walls. Additionally, the probability that a molecule will stick to the wall upon collision is not unity and the actual density reaching the beam plane will be greater. The vapor pressure of CO₂ at 85K is $\sim 10^{-3}$ mT. It should be noted, however, that the above model holds only up to one spherical radius of the Mach disc, R given by:

$$R_{MD} = \left(\frac{P^*}{P_{\infty}} \right)^{1/2} r^* \quad (12)$$

For $r^* = 0.32$ cm, $P^* = 5$ torr, $P_{\infty} = 0.1$ torr, $R_{MD} = 2.26$ cm. For $P_{\infty} = 0.001$ torr, $R_{MD} = 22.6$ cm. Since the e-beam is located at 75 cm, the above calculation may only be approximate.

To estimate the relative importance of diffusion, one can calculate the diffusion time to the walls of the tank and compare with the flow velocity. The diffusion time τ_D is given by:

$$\tau_D = \frac{r^2}{\lambda \bar{v}} \quad (13)$$

where λ is the mean free path and \bar{v} the RMS velocity of the molecules. At $T = 77K$, $v_{CO_2} = 1.922 \times 10^4$ cm/s and $\lambda_{1\mu} = 0.831$ cm. For $r = 45$ cm:

$$\begin{aligned}\tau_{D,77K}^{1\mu} &= 0.127s \\ \tau_{D,77K}^{100\mu} &= 12.7s\end{aligned}\tag{14}$$

At 1μ pressure the linear flow velocity is 1400 cm/s and the gas will take 0.054 sec to reach the location of the e-beam. At 100μ pressure, the linear flow velocity is 14 cm/s, the gas will take 5.36 sec to reach the e-beam location. The diffusion times are comparable to the flow velocity. Therefore the problem should be solved by treating the free expansion and diffusion simultaneously. In order to form a lower bound, however, even assuming a unit sticking coefficient 7 percent of the molecules will reach the beam plane. As mentioned above, the vapor pressure of CO_2 at 85K (the design goal of the shroud) is 10^{-3} mT and it is unlikely that the CO_2 concentration will fall below this concentration.

Beam-created species will be simultaneously diffusing and undergoing a directed flow velocity out of the beam volume. Simplistically, species of mass 28 will require a time to reach the shroud walls which is inversely proportional to shroud pressure as shown in Eq. (13). However, the directed flow velocity is also inversely proportional to pressure and as a result, the downstream distribution of dosed gases will be independent of pressure. At maximum flow the dosed gases will contact the shroud walls 16 cm downstream from the beam plane as illustrated in Figure 10. Of course the time required to reach the walls will be inversely proportional to the pressure, about one second at 100 mT, 10 msec at 1 mT.

2.3.5 Outgassing and Pumpdown Times - In the LABCEDE facility the experiments are to be conducted at pressures of 1 to 100μ Hg and temperature $\sim 80K$. The system should achieve these conditions as quickly as feasible in order to minimize the run time. In addition to an efficient pumping system, the materials used in the hardware of the system should have as low a vapor pressure

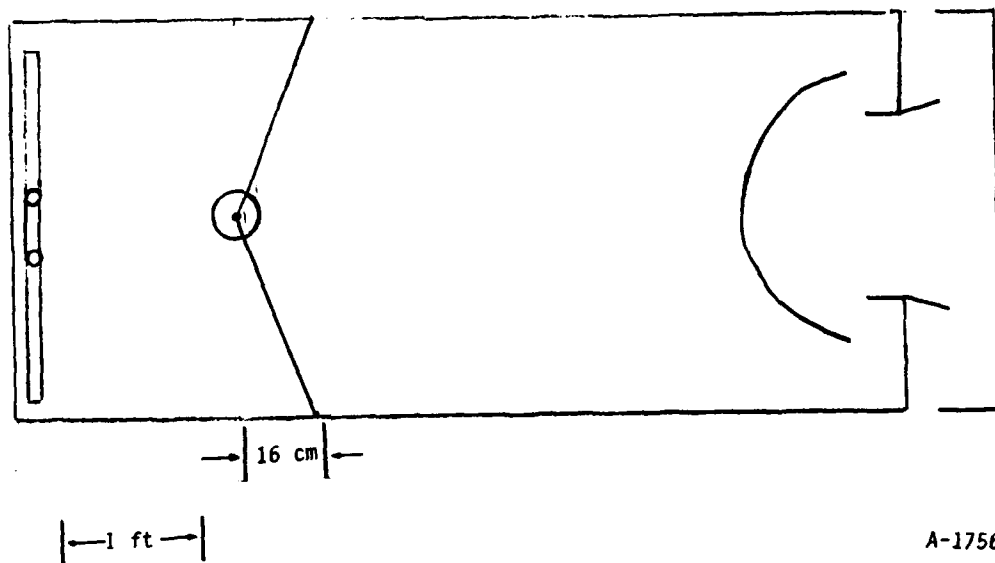


Figure 10. Diffusion of dosed gas in cryogenic LABCEDE. The shape is independent of pressure at constant throughout (1.8 slm), although time scales linearly with pressure.

as possible in order to minimize outgassing rates. Further, since the system is operated at cryogenic temperatures there is an associated problem of condensation of water inside the system in case a leak is developed. It will be beneficial to have the capability of heating the system for speedy removal of condensed water vapor, etc. Some simple calculations were made in order to assess the requirements for an optimal system. These are discussed in this section.

In order to assess some of the requirements, we should understand the process of achieving the vacuum. After a roughing pump removes the bulk gas the system pressure P is determined by the outgassing rate Q of all the inner surfaces divided by the pumping speed S of the pump:

$$P = Q/S \quad (15)$$

Q is the total outgassing from all possible sources, such as the vapor pressure of the base materials and surface impurities, release of adsorbed gases on the surface, and release of gas dissolved in bulk material by diffusion.

Solid-state diffusion, physical and chemical adsorption and desorption rates were calculated to estimate their effects.

Evolution of Dissolved Gas From Metals - The quantity of gas diffusing across a plate of surface area A is given by:

$$q_s = - DA \frac{dc}{dx} \quad (16)$$

where D is the diffusion coefficient of the solid and dc/dx is the concentration gradient. Assuming 1 cc of gas (STP) is dissolved per 100g of metal at 25°C and that it is uniformly distributed within the metal (SS 304) one obtains the concentration within the metal to be 3.5×10^{-6} moles/cc. The diffusion coefficient D is extrapolated from Dushman³ to be 2×10^{-54} cm²/s. Taking the concentration gradient to be C_0/a , where C_0 is the concentration of the dissolved gas in the metal and a the thickness one finds:

$$q_s = DA \frac{C_0}{a} \quad (17)$$

For $A = 3.78 \times 10^5$ cm², surface area of chamber one obtains the outgassing rate to be 5×10^{-47} μ liter/s which is clearly negligible.

Desorption - The gases are either physisorbed or chemisorbed depending on the nature of the gas and the surface. The activation energy for desorption of physisorbed molecules is few kcal/mole while that for chemisorbed species can be several tens of kcal/mole. Glasstone, Laidler, and Eyring⁸ have shown that the rate constant for desorption of diatomic molecules is given by:

$$K_d = \frac{1}{2} \frac{kT}{h} e^{-\frac{\Delta E}{RT}} s^{-1} \quad (18)$$

where

$$k = 1.38 \times 10^{-16} \text{ erg/deg.}$$

$$h = 6.627 \times 10^{-27} \text{ ergs s}$$

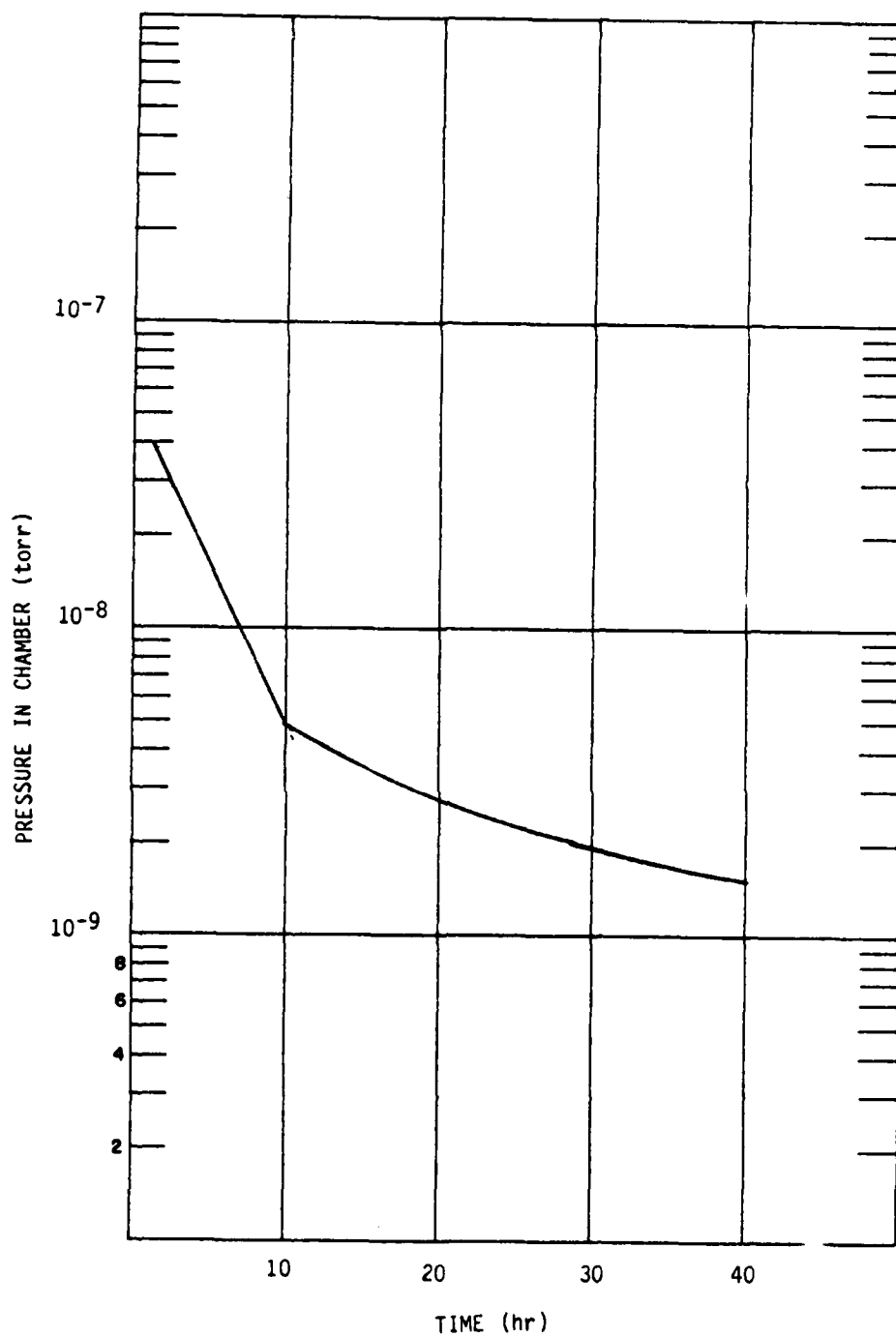
$$R = 1.987 \text{ cal/deg mole.}$$

and ΔE is the activation energy. For the common adsorbants such as H_2O , N_2 , and O_2 , the activation energies for SS304 are 22.4, 16.6, and 17 kcal/mole, respectively. Using an average value of 20 kcal/mole, K_d is calculated to be $8. \times 10^{-3} \text{ s}^{-1}$ ($\tau_d = K_d^{-1} = 120\text{s}$). Thus, the desorption would be nearly complete in 10 min ($5 \tau_d$), which is a very short time. The above calculation assumes the absence of any small pores in the system. Since desorption from porous materials are controlled by diffusion it can be a slow process and use of porous materials should be avoided.

Time to Evacuate the System - Wheeler⁹ has recommended outgassing rates for various metals including stainless steel. The values for stainless steel are reproduced in Table 2. Using these values, the surface area of the LABCEDE Chamber and the pumping speed, one can calculate the pressure P inside the chamber at various times using Eq. (15). For $A = 3.78 \times 10^5 \text{ cm}^2$, $S = 20,000 \text{ l/s}$, one obtains the pressure-time curve shown in Figure 11. A pressure of 10^{-3} torr is achieved in less than 10 hr.

TABLE 2. RECOMMENDED OUTGASSING RATES FOR DEGREASED STAINLESS STEEL

Time (hr)	Outgassing Rate (torr liters/cm ² s)
1	2×10^{-9}
4	1×10^{-9}
10	2.5×10^{-10}
40	8×10^{-11}



A-1757

Figure 11. Pumpdown for LABCEDE chamber.

2.3.6 Observed Vacuum Performance - System ultimate vacuum and overnight leak rate gradually improved after the system had been under vacuum for extended periods of time. This suggests that outgassing from the huge interior surface forms a large component of the observed pressure "leaks." This effective "leak" rate has been reduced to the 2.5 mtorr/hour level into the entire system - a leak of 0.3 sccm into the 5900l volume. Thus, during an experiment, if this leak were homogeneously distributed, it would form a 0.02 percent (200 ppm) contamination of the inlet gas flow. Because the gases are introduced inside the semi-vacuum enclosure shroud and because all leaks arise outside the shroud, the actual contamination in the observation volume will be considerably less. Typical blank off pressures for the system are 3×10^{-7} torr, although levels of 6×10^{-8} torr have been achieved.

As described previously, the porous tube array was capable of passing 1.8 l/m of gas with no adverse effects. The valve/radiation baffle network design did provide some increase in conductance for the pumping network - 6 mT being the pressure inside the shroud at maximum gas flow with the valve fully open. The valve position was controlled using a 5-in. linear translator vacuum feedthrough. The screw thread on the translator is 32/in. - 140 turns required for complete translation. A counting and thumbwheel network was constructed to permit accurate, reproducible positioning of the valve anywhere along its length of travel. It was found that pressure settings could be reproduced to within the stability of the baratron pressure monitor (0.03 mtorr). Pressures of 75 mT have been achieved when flowing 1600 sccm of air when the valve is closed. The ultimate pressure is slightly less than design specifications because a large 20 cm² opening is maintained to permit beam entrance into the shroud. Once the beam geometry is better understood, this opening will be reduced and pressures in excess of 100 mT (densities $> 3 \times 10^{15}$ molecules/cm³) will be possible. Another benefit of reducing the beam entrance aperture will be the reduction of the fraction of the flow pumped out through that opening. At present a large portion of the flow exits there when the valve is closed - distorting the flow field and perhaps enhancing beam created species effects. When the entrance aperture is decreased, the valve will not have to be closed to achieve comparable pressures and flow

will be down the cylinder axis for the most part. Thus, at present, experimental pressures range from 0.1 mtorr (minimum detectible pressure) to ~80 mT (as limited by the shroud). (Note that the valve was designed with a 6-in. maximum path. The translator was capable of only 5 in. An adaptor was constructed which allows two settings of the valve travel: closed to almost fully open, and fully open to almost closed. Because the highest pressures could be achieved only with the highest flows and the valve closed, while a fully open valve would only slightly reduce the lowered pressure at maximum flow, the former setting was chosen. To switch settings, the rear face plate at the valve vacuum feedthrough must be removed to gain access to the adaptor piece.)

In order to calibrate the MKS baratron gauge which is used in most of our experimental measurements, its linearity and the absolute magnitude of its readings had to be checked. A fairly detailed procedure was followed. The baratron head was moved closer to the monitoring port at the top of the tank. This reduced the effects of tubing conductance and minor leaks and fortuitously reduced thermal gradients. Consequently the zero pressure reading stability increased markedly to the 0.03 mt/hr level.

The volume of the LABCEDE facility was first established by expanding a calibrated flask (2.145l) at 1 atm into the evacuated facility. The calculated volume agreed to within 3 percent of the measured value of 6060 ± 20 l. This volume includes the entire system up to the gate valve. Multiple expansions indicated that baratron pressure reading was reproducible and was linear to greater than 0.1 percent (i.e. it was not measurably non-linear). A Hasting gauge was used to verify low pressure linearity and magnitude. The flow meters in the baratron however, give erroneous readings with channel A reading 15 percent too low and channels B&C reading 18 percent too low. (For example, when the baratron indicates a flow of 1000 sccm in Channel C, 1180 sccm of gas is actually entering the tank.) The flows are reproducible and linearly additive.

Operationally we should zero the baratron with no gas flow added, using the Hastings gauge as zero pressure check. The baratron is accurate to 0.6 mt for pressures up to 1.0 torr. The errors at low pressure may be 0.2 mt (which is a large fractional error). The baratron is currently operating with sufficient accuracy to allow quantitative quenching rate constants and absolute radiance measurements to be made.

2.3.7 Modeling of Flow in LABCEDE

A. Delta Function Source

First consider an infinite flow with a delta function cylinder of excitation perpendicular to it making species in concentration C in a gaussian of initial concentration C_0 at the center and width \bar{r}_0 (HWHM). The solution to this problem is a moving cylinder:¹⁰

$$C/C_0 = \frac{\tau_0}{\tau_0 + t} \exp(-r^2/4D(\tau_0 + t))$$

$$\tau_0 = \bar{r}_0^2/4D\ln 2$$

where t is the time after the source, D is the diffusivity, and r is measured from $X = ut$ (see below). The half radius changes with time as

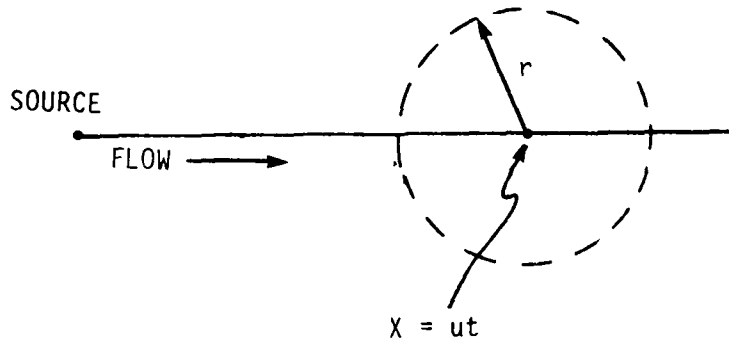
$$\frac{\bar{r}}{\bar{r}_0} = (1 + t/\tau_0)^{1/2}.$$

If \bar{r}_0 is 1 cm and the walls are at $r = 20$ cm, we need $t > 100 \tau_0$ to worry about walls. $\tau_0 \approx 3.6 \times 10^{-5} p(\mu)\bar{r}_0^2(\text{cm})$.

A criterion can be established for the time when convection dominates over diffusion by looking at the decay at the source point with time.

$$C/C_0(x = 0) = \frac{\tau_0}{\tau_0 + t} \exp\left(-\left(\frac{ut}{\bar{r}_0}\right)^2 \frac{\ln 2}{1 + t/\tau_0}\right).$$

This is shown in Figure 12 for various $\alpha = \frac{u\tau_o}{\bar{r}_o}$. We see that for convection to dominate we want $\alpha > 0.4$ or



$$\alpha = \frac{u\tau_o}{\bar{r}_o} = \frac{u\bar{r}_o}{4D\ln 2} = 10^{-5} \bar{r}_o F > 0.4$$

(α is about 0.4 times the Reynolds number based upon radius.) Thus it is desirable to have $\bar{r}_o F > 4 \times 10^4$ where \bar{r}_o is in centimeters and F is the flow rate in standard cubic centimeters per minute.

B. Continuous Source with Optics (Field of View)

The next step is to look at a continuous source with no walls as a function of time and determine what the optics will see. We assume that the source creates states described by the value C which decay with a time constant τ_D . We solve this problem by superposition of delta function solutions. The field of view is given by a full angle θ from X_o looking down the axis from X_{10} to X_m and the source is at X_o .

The value at a point (X, r) from the delta function source at C time t' after the source is found by looking at Figure 13.

$$C_1(X, r, t') = \frac{\tau_o}{\tau_o + t'} \exp \left(- \frac{(r^2 + (ut' - X)^2)}{4D(\tau_o + t')} \right) \exp (- t'/\tau_D) .$$

The integrated value at this point is

$$C_2(X, r, t) = \int_0^t C_1(X, r, t') dt' .$$

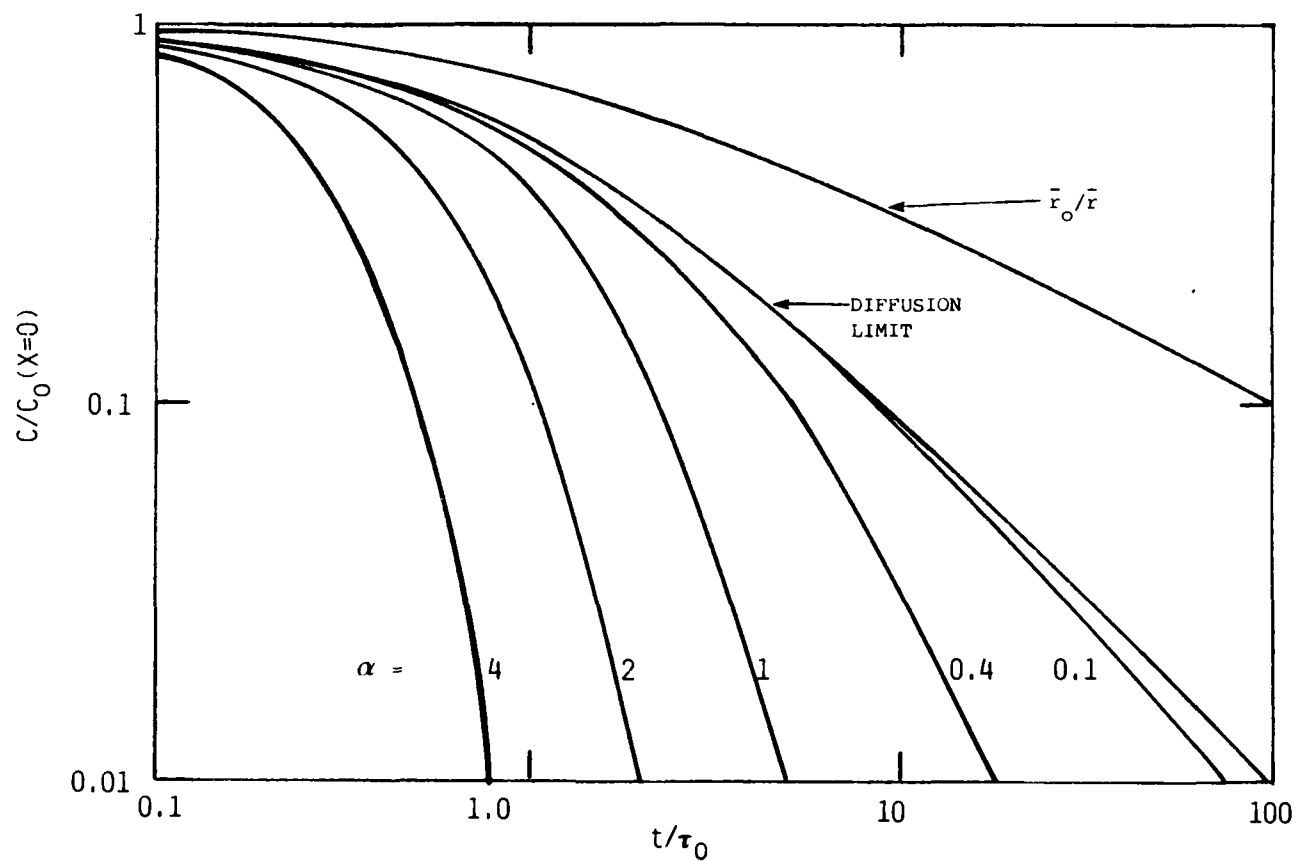
$$\frac{\bar{r}_0^2}{4D\ln 2} = \tau_0 = 3.6 \times 10^{-5} p(\mu) \bar{r}_0^2 (\text{cm}), s$$

$$\bar{r}_0 = \text{HWHM}$$

$$\frac{u\bar{r}_0}{4D\ln 2} = \alpha = \frac{u\tau_0}{\bar{r}_0} = 10^{-5} \bar{r}_0 (\text{cm}) F(\text{sm})$$

$$T = 90 \text{ K}$$

$$D = 2 \times 10^4 / P(\mu), \text{ cm}^2 \text{ s}^{-1}$$



A-1758

Figure 12. Beam excited species concentration gradients as a function of time for several flow velocities. Convection dominates over diffusion for $\alpha > 0.4$.

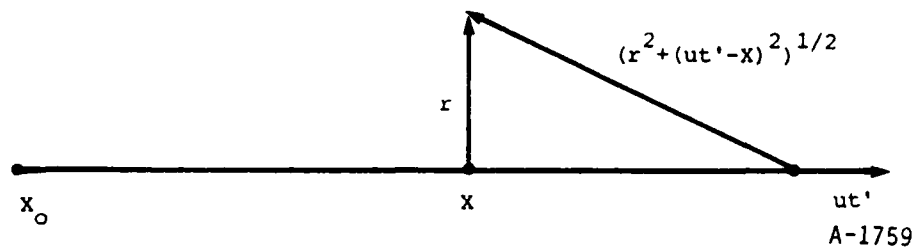


Figure 13. Geometry for determining concentration, C , of species at a given position at time t' after delta function excitation.

The field of view is a cone down the axis of a flow with two dimensional symmetry. In Figure 14 the flow is symmetric with the X axis and does not vary into the paper. The field of view at X' is shown in Figure 15. Here the flow is uniform perpendicular to the r vector. The integral over this disc gives

$$C_3(X, t) = \int_0^{\rho} 4(\rho^2 - r^2)^{1/2} C_2(X, r, t) dr$$

where $\rho = (X - X_{\infty}) \tan \theta/2$.

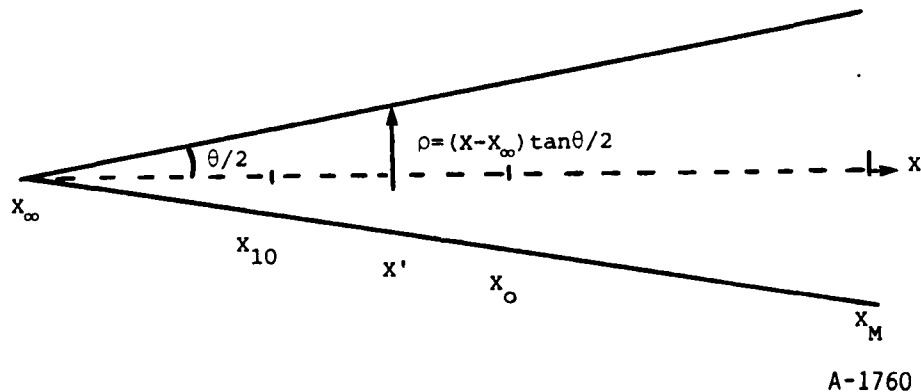
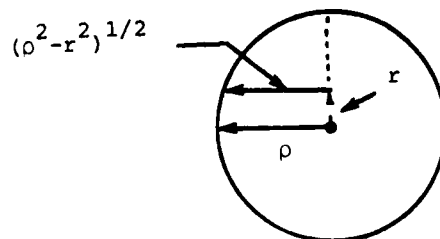


Figure 14. Field of view along optical (x) axis.



A-1761

Figure 15. Cross-section of field of view at position x' .

The integral over X is then,

$$C_4(t) = \int_{X=X_{10}}^{X_m} C_3(X,t) dx.$$

In detail,

$$\begin{aligned} C_3(X,t) &= \int_0^t \int_0^{\rho} 4(\rho^2 - r^2)^{1/2} \frac{\tau_0}{\tau_0 + t'} \exp\left(\frac{-(r^2 + (ut' - X)^2)}{4D(\tau_0 + t')}\right) \exp(-t'/\tau_D) dr dt' \\ &= \int_0^t 16\tau_0 D \exp(-t'/\tau_D) \exp\left(-\frac{(ut' - X)^2}{4D(\tau_0 + t')}\right) M\left(\frac{((X - X_\infty)\tan\theta/2)^2}{4D(\tau_0 + t')}\right) dt' \end{aligned}$$

Now $M(\tau)$ can be written as

$$M(\tau) = \int_0^{\pi/2} T \sin^2 \theta \exp(-T \cos^2 \theta) d\theta$$

or

$$M(\tau) = \int_0^1 \tau \exp(-\tau v^2) (1 - v^2)^{1/2} dv$$

$M(\tau)$ is given in Figure 16. At small T , $M(\tau) = \frac{\pi}{4} T$, at large T , $M(\tau) = \sqrt{\frac{\pi}{4}} T$.

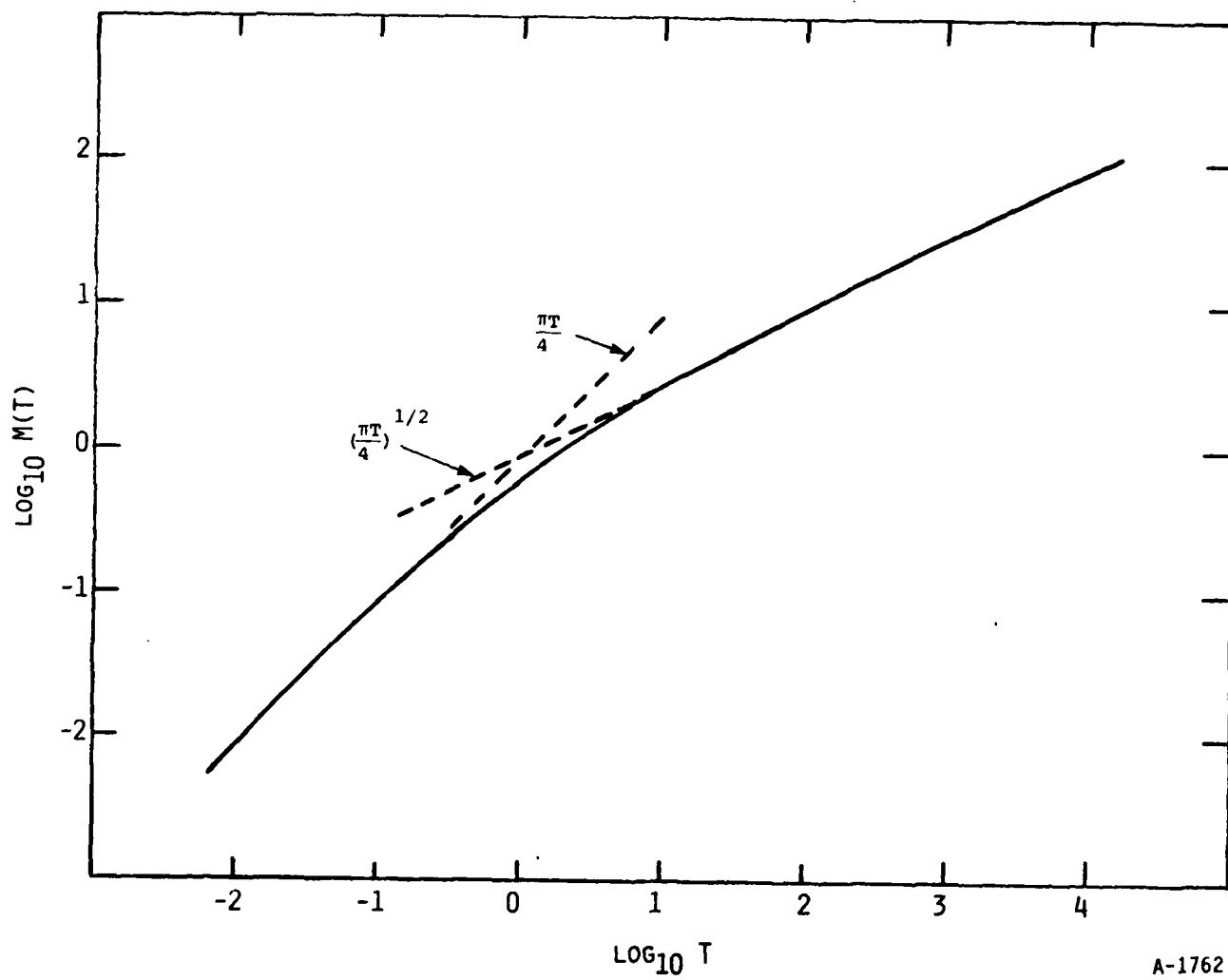
A very good fit is $M(T) = \frac{\pi}{4} T \left(1 + \left(\frac{\pi}{4} T\right)^{5/4}\right)^{-2/5}$. Further we are really interested in $\frac{dC_4}{dt}$ which can be written as

$$\frac{dC_4}{dt} = 16 \tau_0 D X_D \exp(-t/\tau_0) \int_{V_{10}}^{V_M} \exp(-v^2) M((V - V_\infty)\tan\theta/2)^2 dv$$

where

$$X_D = (4D(\tau_0 + t'))^{1/2}$$

and



A-1762

Figure 16. $M(T)$ Versus T .

$$v_1 = \frac{x_1 - ut}{x_D}$$

Now

$$x_\infty = -150 \text{ cm}, x_{10} = -70 \text{ cm}, x_m = 70 \text{ cm}, \theta = 2 \text{ deg}$$

$$D = 2 \times 10^4 / P$$

$$u = 0.6 F/P$$

$$p \text{ in } \mu\text{Hg} \equiv \text{mtorr}$$

$$F \text{ in sccm.}$$

Figure 17 shows $C_4(t)$ at $P = 0.25\mu$. Clearly diffusion dominates over convection for this low flow rate. This is indicated by the approximate square root slope. Figure 18 shows $C_4(t)$ at $p = 1\mu$. Here we see some slight effect due to flow rate at the longest times. Figure 19 shows results for $p = 6\mu$. Here we see some significant effect of flow rate at the longest times.

In Figures 17 through 19 the curves are clearly dominated by diffusion and decay of excited states. This as would be expected from the analysis of the delta function source which gave the condition that $F_0 \bar{x}_0$ had to be greater than 4×10^4 for convection to dominate. However, the effect of decay time is clearly seen and could be extracted if decay time is not too long (i.e., longer than the time between pulses). If the decay time is longer than the pulse time an analysis is necessary to determine clearing of the tank before the next pulse (see below).

The next step is to look at the fall of the concentration after the pulse is turned off, again, in a tank with no walls but with the proper field of view. This solution is simply

$$\frac{C}{C_0} = \int_{t_0}^t \frac{dC_4}{dt'} dt'$$

where $t_0 = 0$ when the pulse is still on and $t_0 = t - \tau_p$, the time where the pulse is turned off.

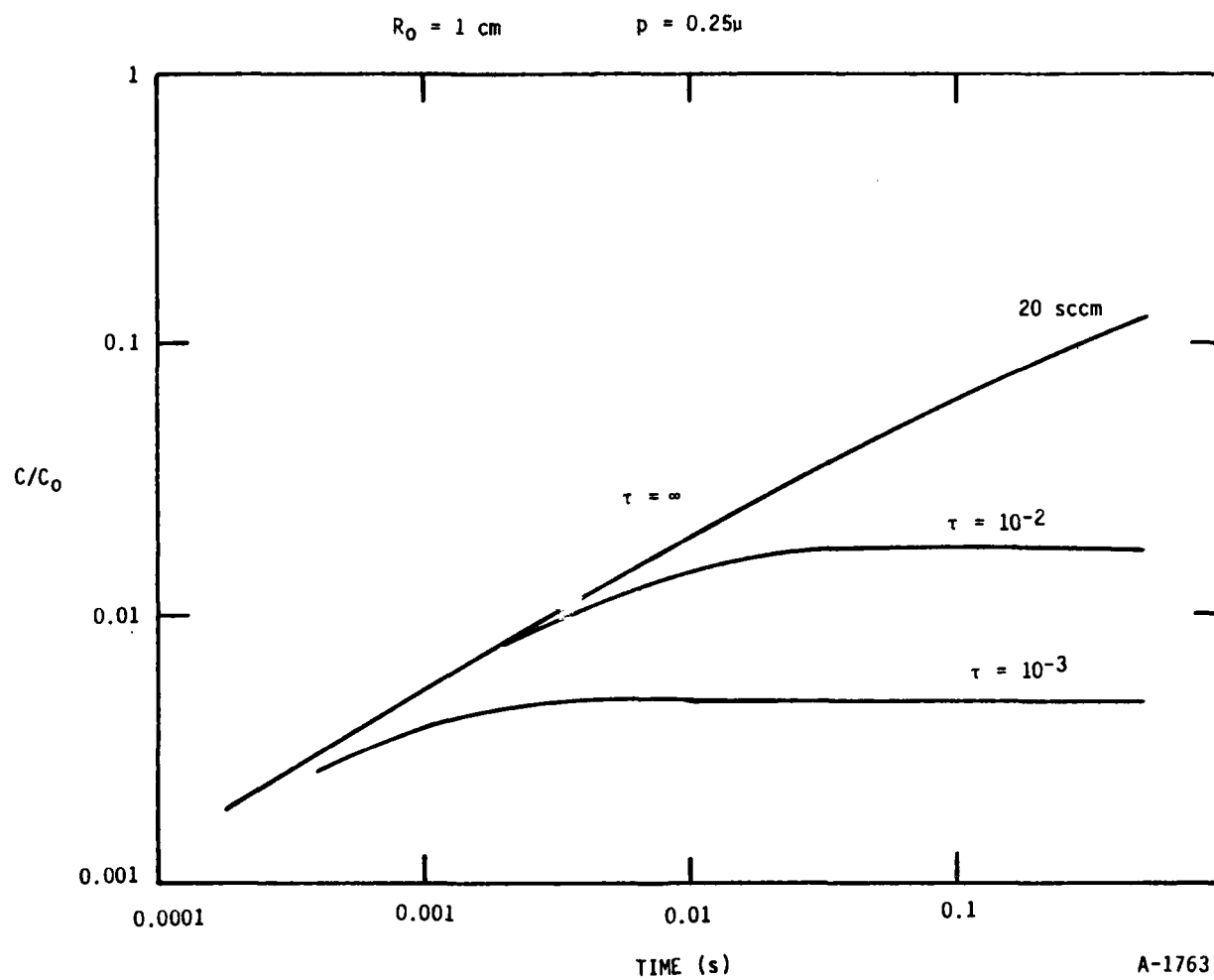


Figure 17. The integrated concentration along the line of sight at 1/4 mtorr pressure as a function of time for several excited state lifetimes, τ .

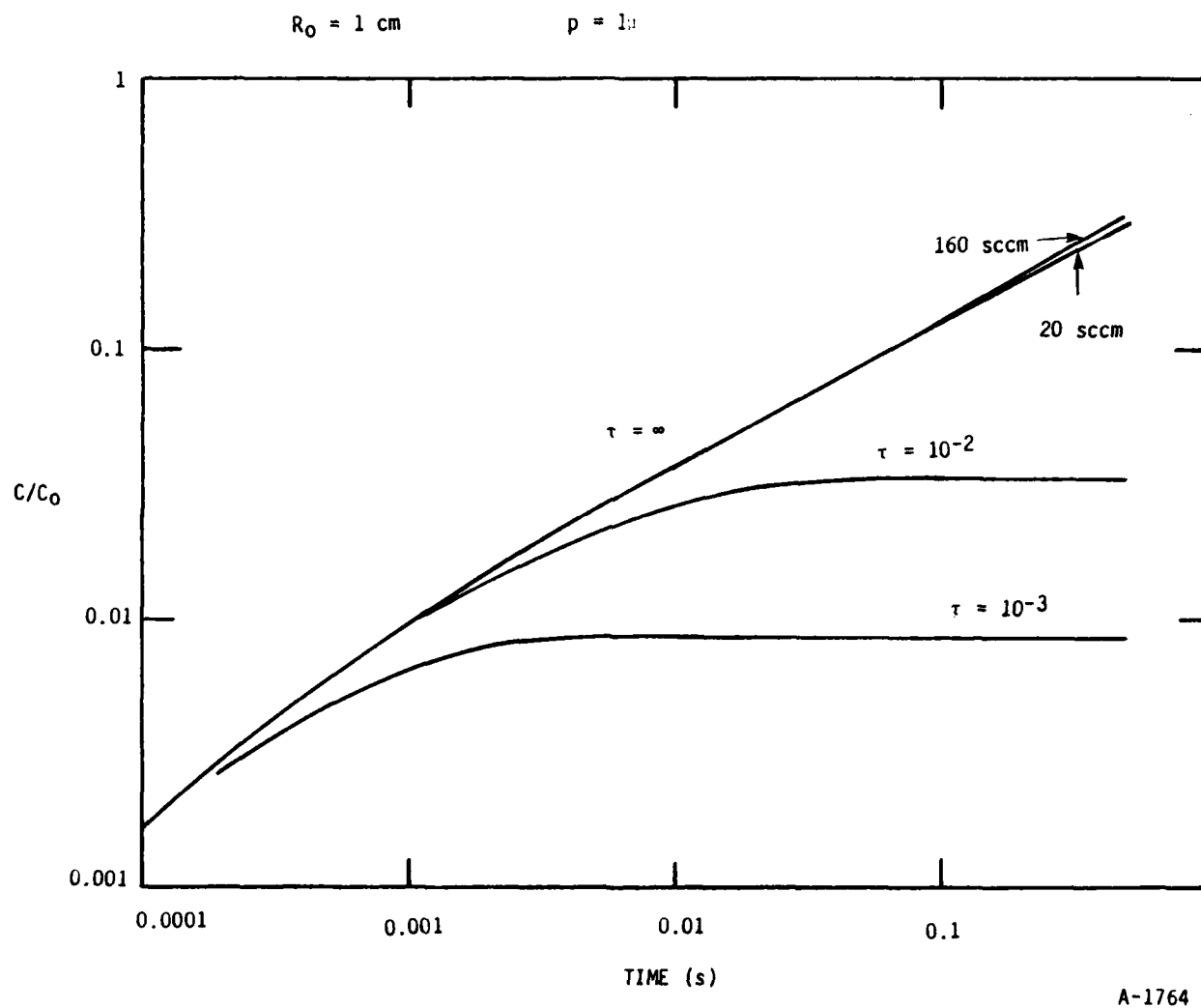


Figure 18. The integrated concentration along the line of sight at 1 mtorr pressure as in Figure 17.

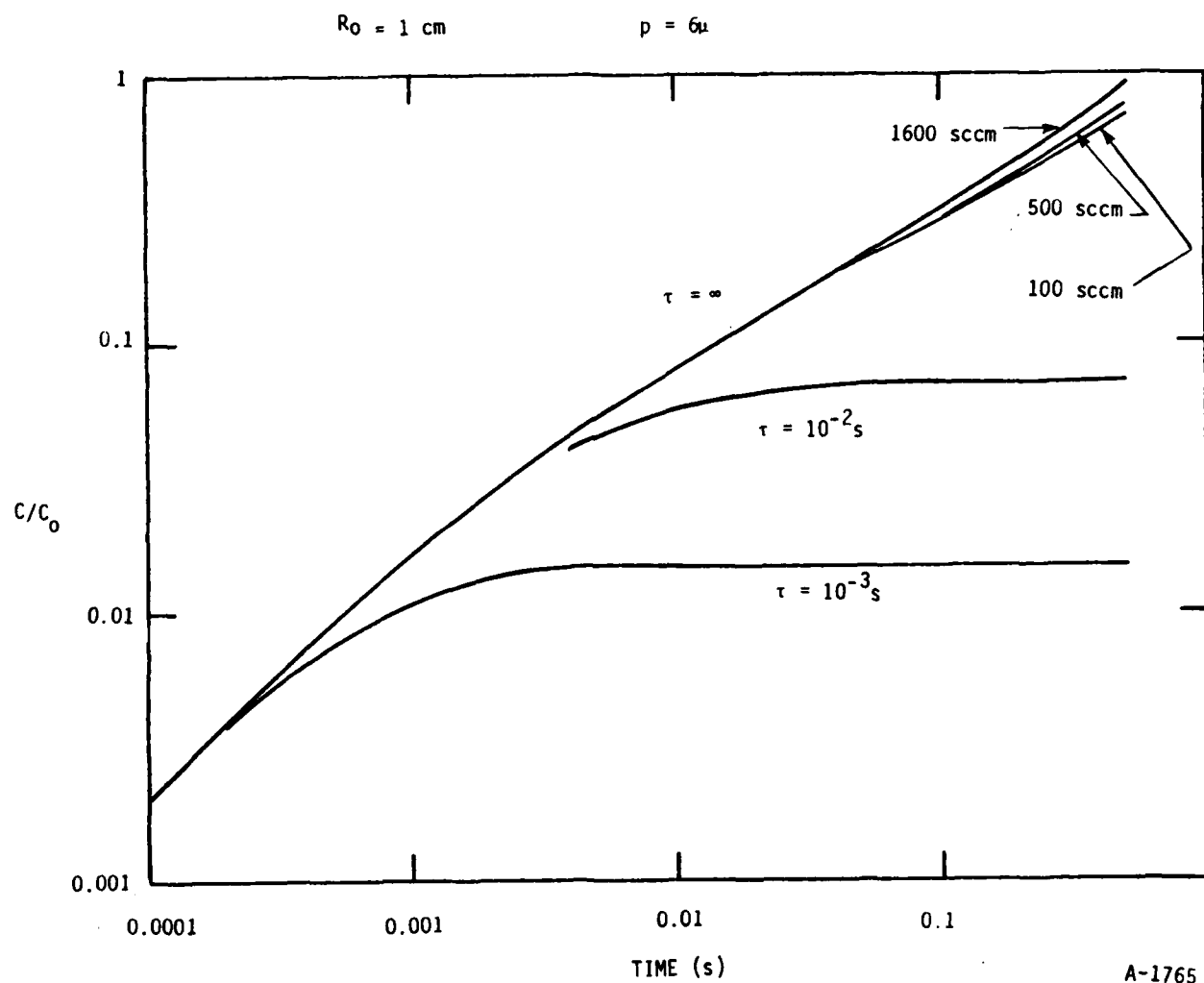


Figure 19. The integrated concentration along the line of sight at 6 mtorr pressure for several flows and radiative lifetimes.

These results are shown in Figures 20 through 22 for various cases. The effect of diffusion on this decay is most at lower pressure and longer decay time constant. There is an initial decay which is more rapid than the decay time constant and is presumably due to diffusion of the just made species out of the field of view. The later, slower decay is only slightly different from the decay time constant. This behavior is the same as seen in the rise time plots (Figures 17 through 19) where an initial square-root rise is seen due to settling of a diffusion profile followed by rise depressed by the decay time constant.

C. Clearing of the Tank

We can look at the time to clear the tank of species produced in a pulse by looking at the problem as a semi-infinite cylinder filled to a constant level from $x = 0$ to $x = \infty$ with flow of velocity u in the x direction. This is a one-dimensional problem defined by

$$\frac{\partial C}{\partial t} + u \frac{\partial C}{\partial x} = D \frac{\partial^2 C}{\partial x^2}$$

with $D \frac{\partial C}{\partial x} = uc$ at $x = 0$; and $C_0 = C = 1$ for $x > 0$ at $t = 0$.

This problem can be solved by the Laplace transform method. The transformed equation is

$$\frac{\partial^2 \bar{C}}{\partial x^2} - \frac{u}{D} \frac{\partial \bar{C}}{\partial x} - \frac{P}{D} \bar{C} = -\frac{C_0}{D}$$

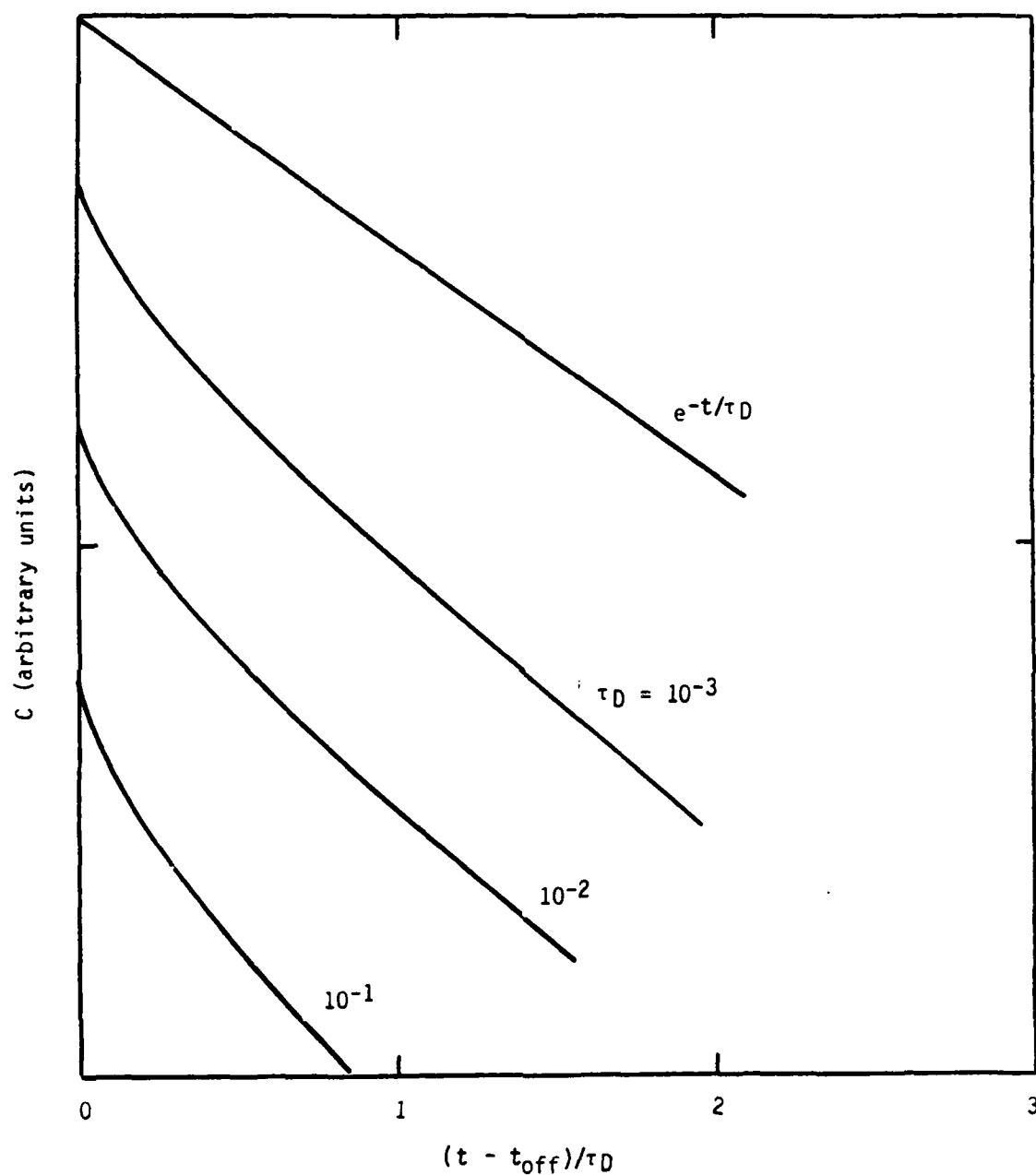
with

$$\frac{\partial \bar{C}}{\partial x} = \frac{u}{D} \bar{C} \text{ at } x = 0.$$

The solution is

$$\bar{C} = \frac{C_0}{P} \left\{ 1 - \frac{u/D \exp \left\{ x \left(\frac{u}{2D} - \left(\frac{u^2}{4D^2} + \frac{P}{D} \right)^{1/2} \right) \right\}}{\left(P/D + u^2/4D^2 \right)^{1/2} + u/2D} \right\}$$

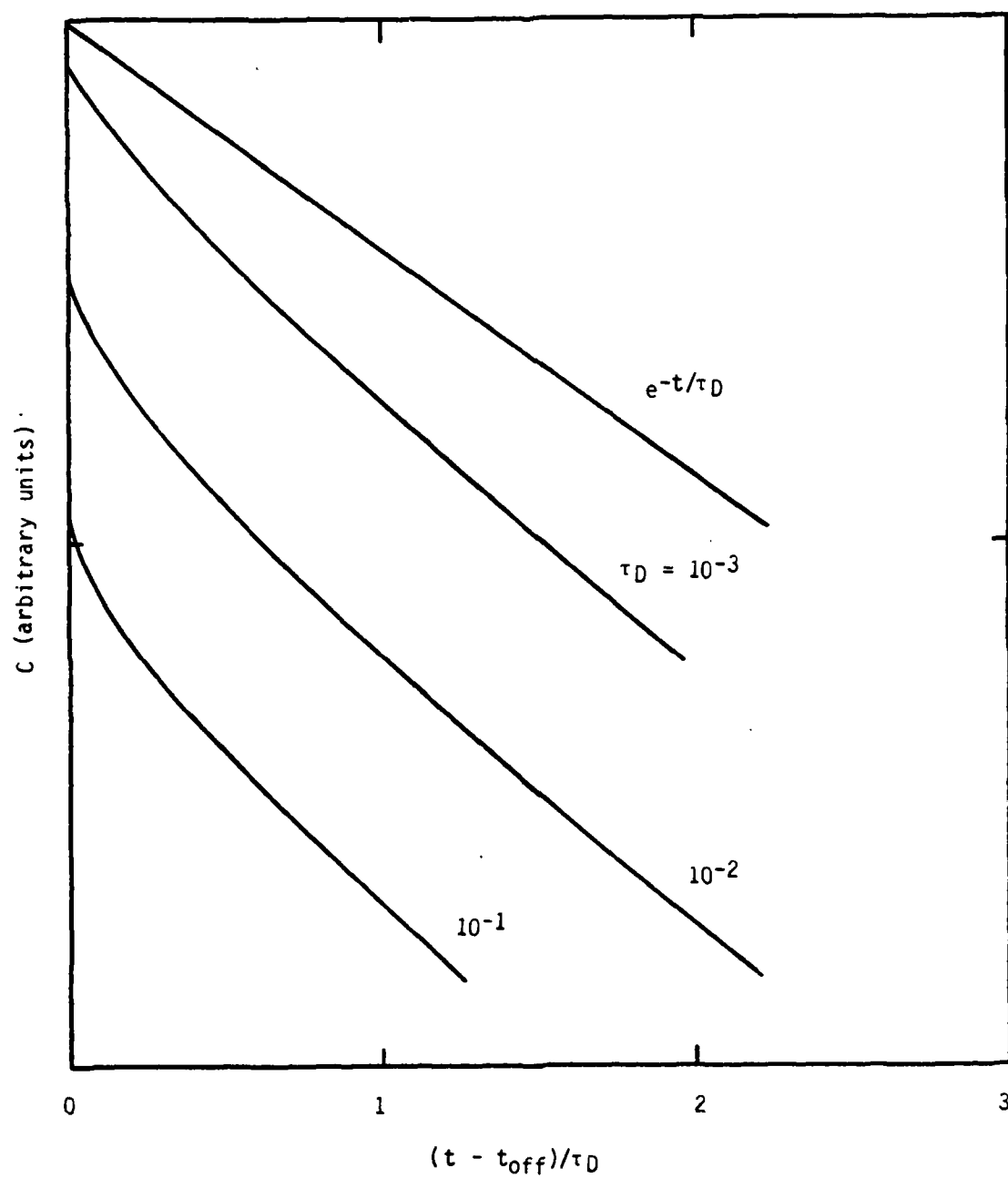
$$R_0 = 1 \text{ cm}, p = 0.25\mu, t_{\text{off}} = 0.5\text{s}$$



A-1766

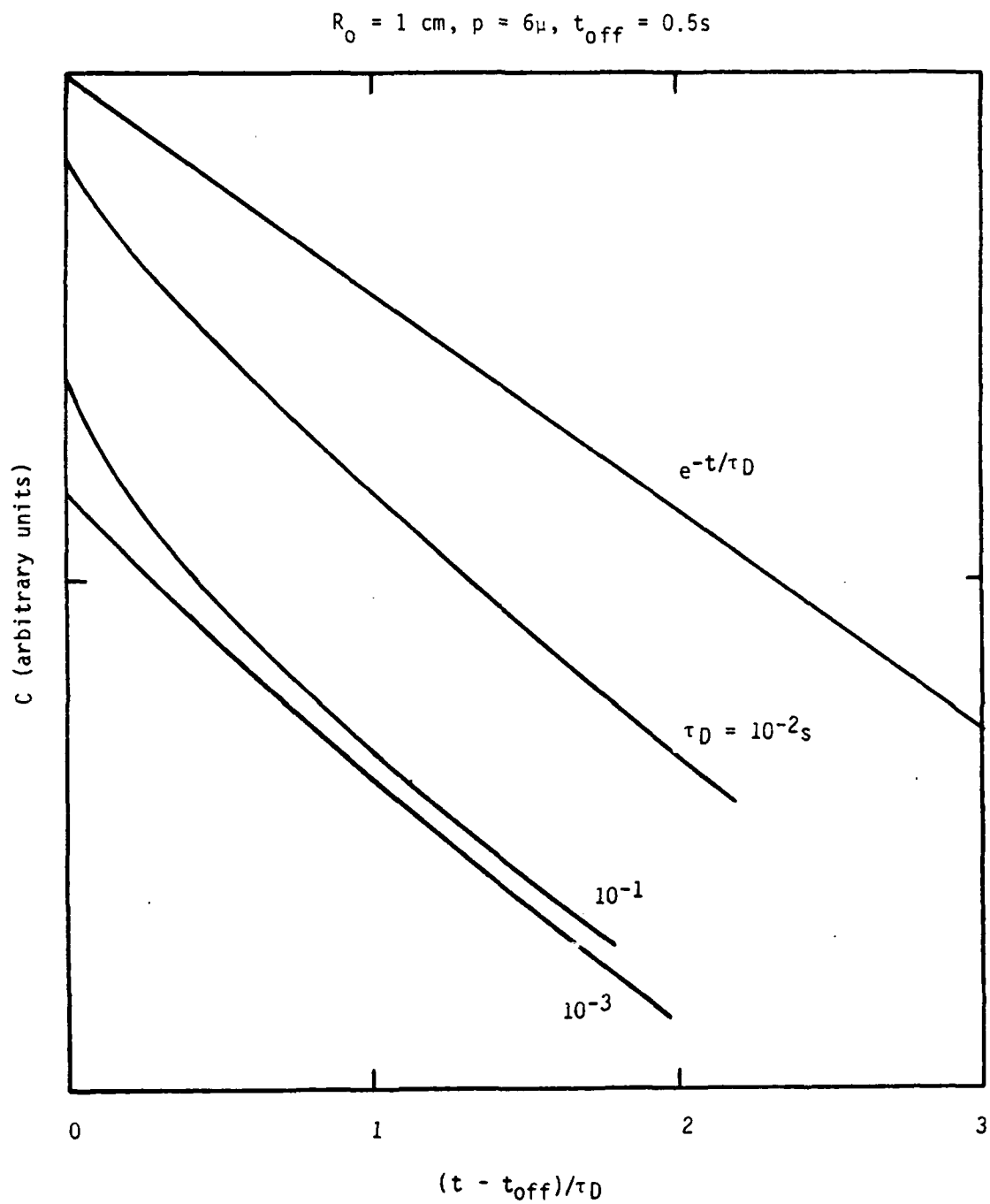
Figure 20. Line of sight concentration after beam termination of several excited state lifetimes at 1/4 mtorr.

$$R_0 = 1 \text{ cm}, p = 1\mu, t_{\text{off}} = 0.5\text{s}$$



A-1767

Figure 21. Line of sight concentration after beam termination for several excited state lifetimes at 1 mtorr.



A-1768

Figure 22. Line of sight concentration after beam termination for several excited state lifetimes at 6 mtorr.

by taking $p' = p + u^2/4D$, $q'^2 = P'/D$, $a = u/2D$ we can write this as

$$\bar{C} = C_0 \left\{ \frac{1}{p} + \frac{e^{ax}}{u} \exp(-q'x) \left(\frac{1}{q'+a} - \frac{1}{q'-a} + \frac{2a}{(q'+a)^2} \right) \right\}.$$

The inverse transform gives

$$C = C_0 \left\{ 1 + \frac{a}{2} (x + ut) e^{ux/D} f^+ - \frac{f^-}{2} - a \left(\frac{Dt}{\pi} \right)^{1/2} \exp(-(x - ut)^2/4Dt) \right\}$$

where

$$f^{\pm} = \operatorname{erfc} \left(\frac{x \pm ut}{\sqrt{4Dt}} \right).$$

Now

$$\operatorname{erfc}(y) = g(y) \frac{1}{\pi^{1/2}} \frac{e^{-y^2}}{y}$$

with

$$g(y) \sim 1 \text{ for } y > 2.$$

Then

$$C = C_0 \left\{ 1 + a \left(\frac{Dt}{\pi} \right)^{1/2} e^{-(x-ut)^2/4Dt} \left(g(x + ut)/\sqrt{4Dt} - 1 \right) - \frac{f^-}{2} \right\}$$

since we are interested in what happens at

$$x = O(10^2), t = O(1), D = O(10^4), \text{ then } g \text{ is near unity and}$$

$$C = C_0 \left\{ 1 - \frac{f^-}{2} \right\}.$$

We are looking for the conditions that $C \approx C_0/10$ which corresponds to $f^- = 1.8$ or an argument of about negative unity. (Note that this means that the argument of g is at least $+1$ and the assumption that g is near unity holds.) We thus want $(x - ut) = - (4Dt)^{1/2}$.

In terms of flow rate and pressure for $x = 100$ this gives

$$t = \frac{P}{F^2} 5.5 \times 10^4 (1 + \sqrt{1 + 0.003 F})^2$$

This result is plotted in Figure 23. Clearing times are, for example, 2.6 sec 10 microns and 1600 sccm, and 25 sec at 1 micron and 100 sccm. These are long times and indicate that care must be taken not to accumulate products in the tank.

D. Approximate Model for LABCEDE Device

An approximate model for the device is that it is a rectangular tank with the same internal length and surface area as the real tank. For simplicity, we pick it to have square cross-section of side $2b$. We take the origin to be the center of the electron source which represents the z -axis. Flow is in the x -direction. The partial differential equation for primary excited states is thus:

$$\frac{\partial C}{\partial t} + u \frac{\partial C}{\partial x} = D \nabla^2 C + \dot{C}$$

where $\dot{C} = A(t)f_x(x^2)f_y(y^2)f_z(z^2)$ with $f_x = f_y = f$ and $f_z = 1$.

The solution of this equation can be written as

$$C = \int_0^t F_x(x, t-\tau) F_y(y, t-\tau) F_z(z, t-\tau) A(\tau) d\tau$$

where

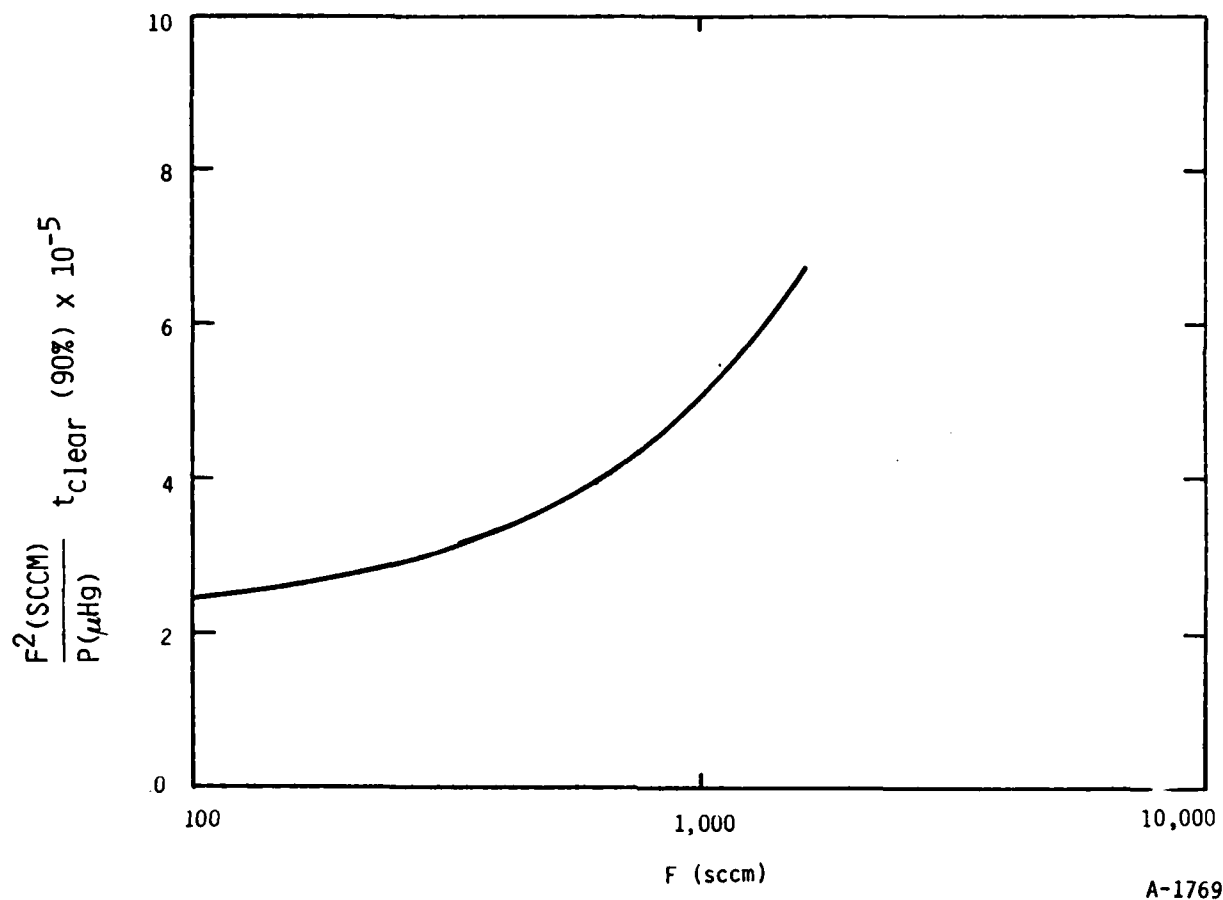


Figure 23. Tank clearing time (90%) as a function of flow.

$$C_1(\xi) = \int_0^t F_1(\xi_1, t-\tau) A(\tau) d\tau$$

is the solution of

$$\frac{\partial C_1}{\partial t} + u_1 \frac{\partial C_1}{\partial \xi_1} = D \frac{\partial^2 C_1}{\partial \xi_1^2} + A(t) f_1(\xi_1^2) \quad .$$

Solution for $C=0$ at Walls

For the case where the boundary conditions are perfectly catalytic walls except at the exit, we can write down the solutions with some ease.

$$F_y(y, t-\tau) = \frac{1}{b} \sum_{n=0}^{\infty} \cos\left\{\frac{(2n+1)\pi y}{2b}\right\} \exp\{-D\pi^2(t-\tau)(2n+1)^2/4b^2\} a_{yn}$$

where

$$a_{yn} = \int_{-b}^b \cos\left\{\frac{(2n+1)\pi y'}{2b}\right\} f_y(y'^2) dy'$$

For $f(z^2) = a$ constant we get the equation

$$a_{zn} = \frac{4b}{\pi} \frac{(-1)^n}{2n+1}$$

$$F_z(z, t-\tau) = \frac{4}{\pi} \sum_{n=0}^{\infty} \frac{(-1)^n}{2n+1} \cos\left\{\frac{(2n+1)\pi z}{2b}\right\} \exp\{-D\pi^2(t-\tau)(2n+1)^2/4b^2\}$$

(see Carslaw and Jaeger (Ref. 9) p. 131 and p. 97). If the source is close to a line source, then we can approximate $f(x^2)$ or $f(y^2)$ as a delta function. Thus $a_{yn}=1$ and

$$F_y(y, t-\tau) = \frac{1}{b} \sum_{n=0}^{\infty} \cos\left\{\frac{(2n+1)\pi y}{2b}\right\} \exp\{-D\pi^2(t-\tau)(2n+1)^2/4b^2\}$$

The solution in the x-direction can be found with the help of the method of images. Since the upstream end of the device is at x_{10} (a negative number) and the source is at $x=0$, we need a sink at $2x_{10}$ to make $C=0$ at x_{10} . The medium can then be considered of infinite extent in the x-direction. The solution is related to solutions to moving source problems like that discussed in Section B above. We can write down the solution

$$F_x(x, t-\tau) = \int_{x_{10}}^{\infty} \frac{f(x'^2)}{(4\pi D(t-\tau))^{1/2}} \{g(x, x'+u(t-\tau), t-\tau) - g(x, -x'+2x_{10}-u(t-\tau), t-\tau)\} dx'$$

with $g(x, \xi', t-\tau) = \exp\{-(x-\xi')^2/4D(t-\tau)\}$. If $f(x'^2)$ is a delta function we get

$$F_x(x, t-\tau) = \frac{1}{(4\pi D(t-\tau))^{1/2}} \{g(x, u(t-\tau), t-\tau) - g(x, 2x_{10} - u(t-\tau), t-\tau)\}$$

General Boundary Conditions

The general wall boundary conditions for the y and z equations can be written as

$$D \frac{\partial C}{\partial y} = \pm \alpha \frac{\bar{C}}{4} C$$

where the plus sign is for the negative y boundary, \bar{C} is the mean thermal speed and α is the accommodation coefficient. The solution for this problem for $\alpha \neq 0$ is found by comparison with Carslaw and Jaeger⁹ p. 360. With $h = \alpha \bar{C}/4$ and

$$Z_n(\xi) = \frac{(\cos \alpha_n \xi) (2(D^2 \alpha_n^2 + h^2))^{1/2}}{(b(D^2 \alpha_n^2 + h^2) + Dh)^{1/2}}$$

where $\tan \alpha_n b = h/\alpha_n D$ gives α_n . Then

$$F_i(\xi_i, t-\tau) = \sum_{n=1}^{\infty} Z_n(\xi_i) e^{-D \alpha_n^2 (t-\tau)} \int_0^b Z_n(\xi') f_i(\xi'^2) d\xi'_i$$

for $i=y$ or z . For the z-direction we get

$$\int_0^b Z_n(\xi') d\xi' = \frac{(2h^2)^{1/2}}{(b(D^2 \alpha_n^2 + h^2) + Dh)^{1/2}}$$

For the y-direction

$$\int_0^b Z_n(\xi') \delta(\xi) d\xi = \frac{(2(D^2 \alpha_n^2 + h^2))^{1/2}}{(b(D^2 \alpha_n^2 + h^2) + Dh)^{1/2}}$$

The solution in the x-direction requires finding the solution for a point source at x' with a boundary condition at $x=x_{10}$ of

$$D \frac{\partial C}{\partial x} = (u + h) C$$

We first translate the equation to $\xi = x - x_{10}$ so that the boundary condition is at $x=0$. We assume that the solution is the sum of a solution, C_1 , that has

$$\frac{\partial C_1}{\partial \xi} = 0 \text{ at } \xi=0$$

and another that has

$$D \frac{\partial C_2}{\partial \xi} = (u + h)(C_1 + C_2)$$

C_1 is known as the sum of a point source at $\xi' + ut$ and one at $-(\xi' + ut)$ and

$$C_1 = \frac{1}{\sqrt{4\pi Dt}} \{g(\xi, \xi' + ut, t) + g(\xi, -(\xi' + ut), t)\}$$

Now we go to the Laplace transform plane. First, we note that

$$L(e^{-\alpha t}) = \bar{v}(p + \alpha)$$

$$g(\xi, \xi' + ut, t) = g(\xi, \xi', t) e^{-(u^2/4D)t} e^{(\xi - \xi')u/2D}$$

$$g(\xi, -\xi' - ut, t) = g(\xi, -\xi', t) e^{-(u^2/4D)t} e^{-(\xi + \xi')u/2D}$$

so

$$\bar{C}_1 = \frac{1}{2Dq'} \{e^{-q'|\xi - \xi'|} e^{(\xi - \xi')u/2D} + e^{-q'|\xi + \xi'|} e^{-(\xi + \xi')u/2D}\}$$

$$q' = \sqrt{(p + u^2/4D)/D}$$

We now look for \bar{C}_2 as a sink at negative ξ'

$$\bar{C}_2 = \frac{-A}{2Dg'} e^{-q'|\xi + \xi'|} e^{-(\xi + \xi')u/2D}$$

so that $D \partial \bar{C}_2 / \partial \xi = (u + h)(\bar{C}_1 + \bar{C}_2)$ at $\xi=0$. We find

$$A = \frac{2(u+h)}{D} / (q' + u/2D + \frac{u+h}{D})$$

$$\bar{C}_2 = \frac{(u+h)}{q'D^2(q' + \frac{3}{2}\frac{u}{D} + \frac{h}{D})}$$

Taking the inverse transform (Carslow and Jaeger appendix V#13), with

$$L^{-1}(\bar{v}(p + \alpha)) = e^{-\alpha t} L^{-1}(\bar{v}(p))$$

$$\begin{aligned} C_2 &= -\frac{u+h}{D} e^{-(u^2/4D)t} e^{-(\xi+\xi')u/2D} \exp\left\{\left(\frac{3u}{2D} + \frac{h}{D}\right)(\xi+\xi')\right. \\ &\quad \left.+ Dt\left(\frac{3}{2}\frac{u}{D} + \frac{h}{D}\right)^2\right\} \operatorname{erfc}\left\{\frac{(\xi+\xi') + Dt\left(\frac{3}{2}\frac{u}{D} + \frac{h}{D}\right)}{\sqrt{4Dt}}\right\} \\ &= -\frac{u+h}{D} \exp\left\{\left(\frac{u+h}{D}\right)\{\xi+\xi'\} + (2u+h)t\right\} \operatorname{erfc}\left\{\frac{\xi+\xi' + t\left(\frac{3}{2}u+h\right)}{\sqrt{4Dt}}\right\} \end{aligned}$$

To transform back to $x=\xi+x_{10}$ replace $\xi+\xi'$ by $x+x'+2x_{10}$ and $\xi-\xi'$ by $x-x'$. If the source is C delta function at $x'=D$ we get

$$\begin{aligned} F_x(x, t-\tau) &= \frac{1}{(4\pi D(t-\tau))^{1/2}} \{g(x, u(t-\tau), t-\tau) + g(x, 2x_{10}-u(t-\tau), t-\tau)\} \\ &\quad - \frac{(u+h)}{D} \exp\left\{\frac{(u+h)}{D}(x+2x_{10}) + (2u+h)(t-\tau)\right\} \operatorname{erfc}\left\{\frac{x+2x_{10} + t\left(\frac{3}{2}u+h\right)}{\sqrt{4D(t-\tau)}}\right\} \end{aligned}$$

We thus can find $C(x, z, t)$ by a time integral of products of readily calculable functions.

2.4 Electron Transport/Primary Beam Characteristics and Secondary Electron Spatial Distribution

2.4.1 Introduction - In order to remove spurious radiators from the observed fluorescence spectrum, the flow system was improved as described in Subsection 2.3. However, at the higher pressures where flow velocity is lowest, the electrons in the beam undergo sufficient collisions that beam spreading occurs. Molecular residence time in the beam and the possibility for irradiation of beam-created species is increased. Also because the beam expands beyond the field of view, quantitative determination of the excitation efficiencies of various transitions is more difficult. It was suggested in the previous system study¹¹ that the beam be magnetically confined. The design and performance of the magnetic coils which accomplish this is described in Subsection 2.4.2. The after implementation of the coils, various improvements to the electron source appear possible, such as simplification and streamlining of the gun. These changes are still in progress but will be briefly discussed in Subsection 2.4.3.

2.4.2 Magnetic Confinement Coils - The applied magnetic field must be roughly uniform along the beam path and be of sufficient strength to prevent an electron from having a trajectory which leaves the field of view after a collision. In LABCEDE electrons are accelerated through a potential of between 2 and 5 kV prior to introduction into the experiment. At these voltages the mean free path of the electron, λ , is given by the relation

$$\frac{1}{\lambda} = \frac{N}{v_e} \int_0^\infty f(v_e) C \quad (19)$$

where N is the gas density, v_e is the electron velocity (2.6×10^9 and 4.2×10^9 cm/s for 2 and 5 kV electrons, respectively), $f(v_e)$ is a complex logarithmic velocity dependence, and C is a constant depending on nuclear and electron charge (e) and electron mass. For 2 (and 5) kV electrons, the mean free paths at 100 μ m pressure are 1m (4.5m) at room temperature and 30 cm (135 cm) at 90K. Thus the electrons will undergo at most only a few collisions in their transit across the tank. When an electron which is

traveling along a magnetic field line undergoes a collision with a neutral, it is restricted to travel within a Larmor radius, r_L , of its original trajectory, where

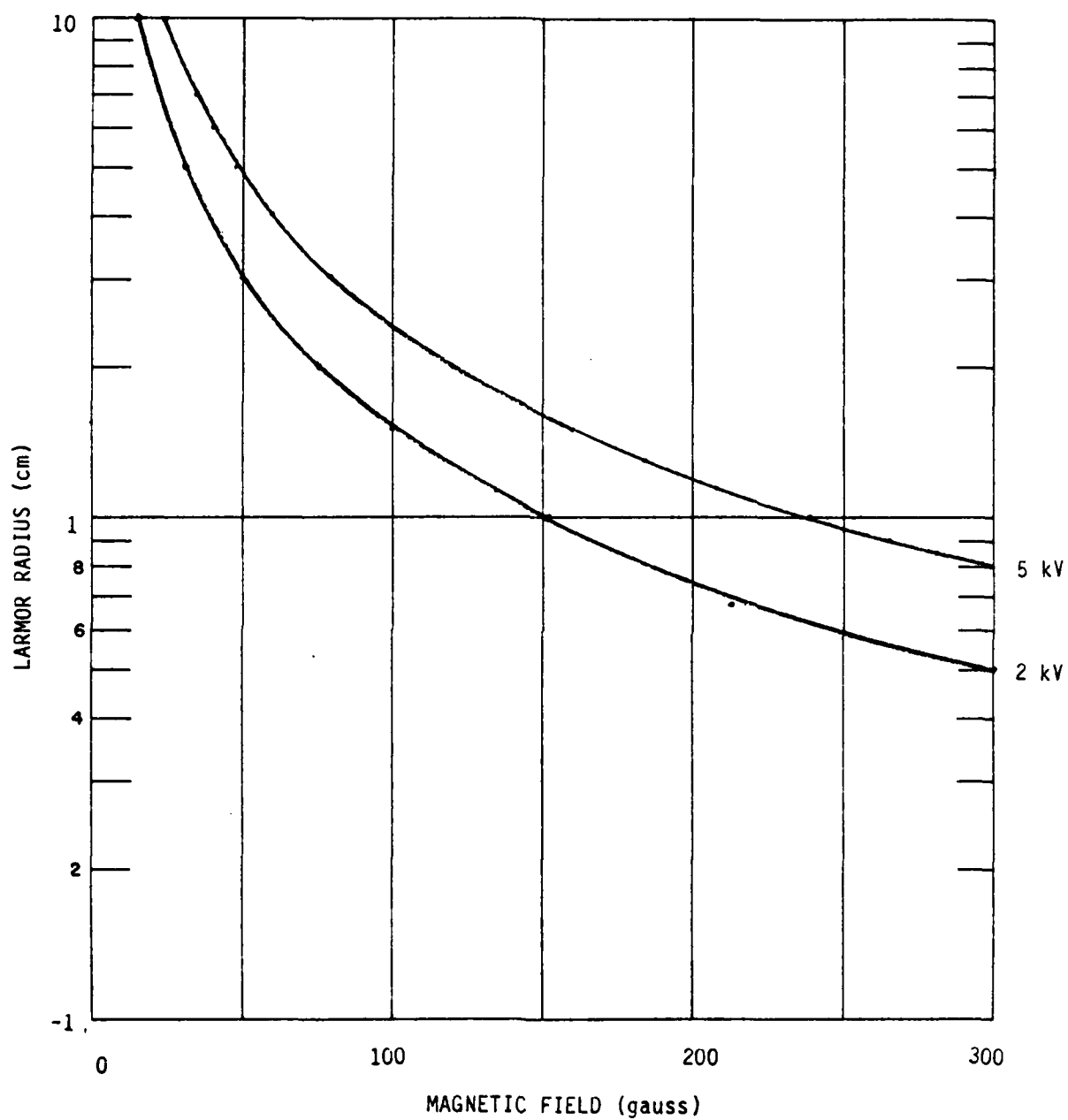
$$r_L = \frac{mV_e}{eB} \quad (20)$$

In Eq. (20) m is the relativistic electron mass and B is the applied magnetic field in Gauss. Thus if a B is applied which restricts r_L to less than 2 cm, then the electron beam will not spread out of the detection system field of view even at the highest operational pressures. Larmor radius is plotted as a function of magnetic field strength in Figure 24 for both 2 and 5 kV electrons. Magnetic fields in the 75 to 150 Gauss range will be sufficient to ensure beam containment.

The shape of the magnetic field between a pair of coils depends on the coil diameter (D) to separation (L) ratio. As the coils are moved further apart the strength of the field between the coils drops. For a given separation, the larger the coils the more homogeneous the field. To insure a uniform field along the entire beam path the magnetic coils must be positioned outside the vacuum enclosure (about 1.2m apart). Thus coil diameters must be very large to achieve uniform fields across the tank. The design chosen has coils of over 1m diameter but even so the magnetic field at the mid-point between the magnets will drop to one-half the value at the center of each coil. These coils required multiple turns of wire and large current flows. Water cooling was required to prevent meltdown so copper tubing was chosen as the current carrier. The magnetic field generated by a pair of coils of radius R at any point Z between them is given by

$$B = \frac{2\pi nI}{10 R} \left\{ 1 + \left(\frac{Z}{R} \right)^2 \right\}^{-3/2} \quad (21)$$

where I is the product of current and turns of conductor. For our geometry, to achieve 150G at the mid-point between the coils 2.3×10^4 amp-turns are required. From the known resistivity, cross-sectional area of the tubing, an



A-1770

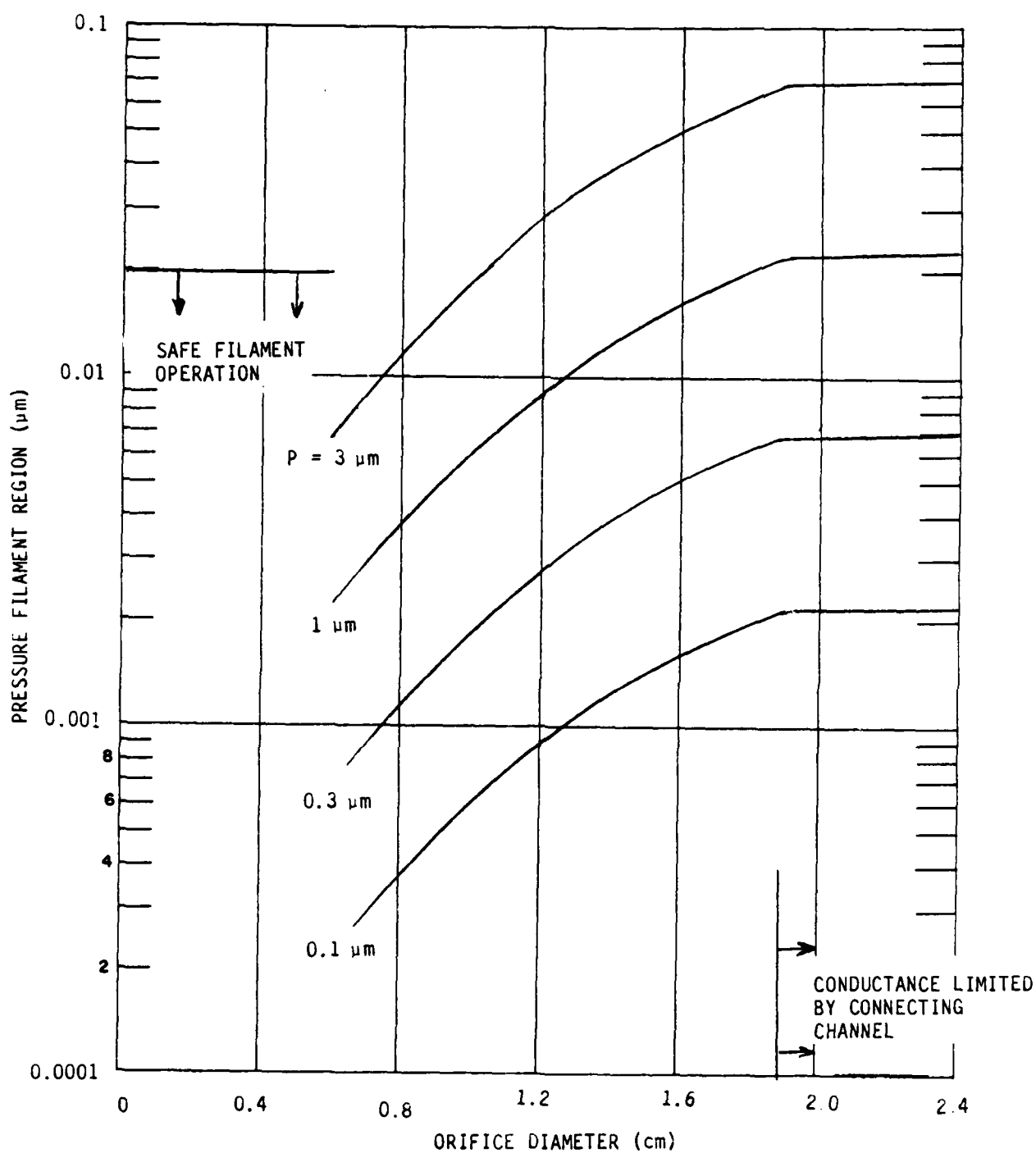
Figure 24. Larmor radius of 2 and 5 kV electrons as a function of magnetic field strength.

optimum design was implemented. Circular wooden coil races were constructed and copper tubing (insulated using plastic shrink tubing) was spooled onto the 1m diameter forms 14 turns to a layer, 17 layers deep (238 turns). These layers were broken into four equal length sections connected electrically (and with cooling water) in parallel. The length of the tubing in each section was about 750 ft. The second coil was wired in series to the first and a 60V welding supply was connected across the coils. A total current of 320A is drawn from the welder supply, for a total $nI = 1.9 \times 10^4$ amp-turns. The observed resistance of the coils was higher than calculated. As a result less current was drawn before reaching the voltage limit of the supply. Over 23 kW are dissipated in the coils and a 0.2 gal/min flow of chilled water through each tubing section was required to prevent overheating. Because the flow is marginally turbulent in the small diameter tubing, a pressure drop of about 70 psi is expected across each tubing length. A booster pump was added to the recirculation system and total flows of nearly 2 gal/min were observed in the eight parallel sections. As a result the exit water from the coils reaches a steady state temperature of 46°C at maximum power dissipation. This is very acceptable temperature. The coils have been in use for many hours and appear to be operating very stably and satisfactorily.

The observed magnetic fields are smaller than design goals, but still adequate for beam confinement. The magnetic field strength was observed to scale linearly with current up to a value of 178G at the center of each coil. The maximum value at the mid-point between the coils was measured to be 77G. The field was observed to increase smoothly along the beam axis away from the mid-point toward the coils. The field was observed to smoothly fall off perpendicular to the beam axis in both directions with a half-power point width of about a coil diameter (1.1m). No modulation or ripple on the field due to the power supply has been observed. From Figure 24 it can be seen that the electrons should be confined to a beam of less than 3 cm radius for this field strength. Actual measurements of beam shape and confinement will be undertaken once the 391.4 nm diagnostic (see Subsection 2.5.6) is implemented.

2.4.3 Electron Source Modifications - During the rebuilding project, mild (ferromagnetic) steel was removed from the apparatus wherever possible (this included bolts and small flanges). Some of the large door and support flanges could not be replaced however and the coils left a residual magnetization in these materials. A small residual field (few G) is present inside the experiment. The electron gun assembly and electronics were mounted inside a mild steel frame. Because this framework had to be replaced, changes in the gun pumping network were made at the same time. The previous gun assembly included two stage differential pumping with an aperture slide bar and a gate valve to allow filament isolation so that repairs could be made during system operation. At least initially none of the electronics were modified. It was felt, however, that the filament should be positioned as close as possible to the experiment. By removing one of the diffusion pumping stages and incorporating the aperture and gate valve into a single compact assembly, the filament was moved to within 30 cm of the magnetic coil/experiment plane. (Previously it had been located well over a meter from the experiment.) Calculations of the pressure in the filament region using a single diffusion pump revealed that quite large orifices between the experiment and the filament were possible. These calculations based on Dushman³ are plotted in Figure 25. For a given diffusion pump speed (1500 l/s) and experimental pressure outside the shroud (0.1 to 3 mT) the pressure in the filament region will be determined by the orifice between the experiment and diffusion pump chamber. It was felt that pressures up to 0.03 mT will not degrade filament performance, and pressures of 0.1 mT will still permit filament operation (although its lifetime will be shortened due to oxidation or its temperature will be decreased by conductional heat losses).

At present no apertures have been inserted between the diffusion pump and experiment. Routine operation with the open 2.5 cm diameter, cylindrical connection has resulted in excellent system performance. No decrease in filament lifetime has been observed. The electron beam has been directed into the experiment at all field strengths. In practice no orifice has been installed. The limiting conductance of the channel is sufficient that the filament chamber pressure remains sufficiently low that stable operation is possible even at the highest flow, valve-closed conditions in the experiment. When the



A-1771

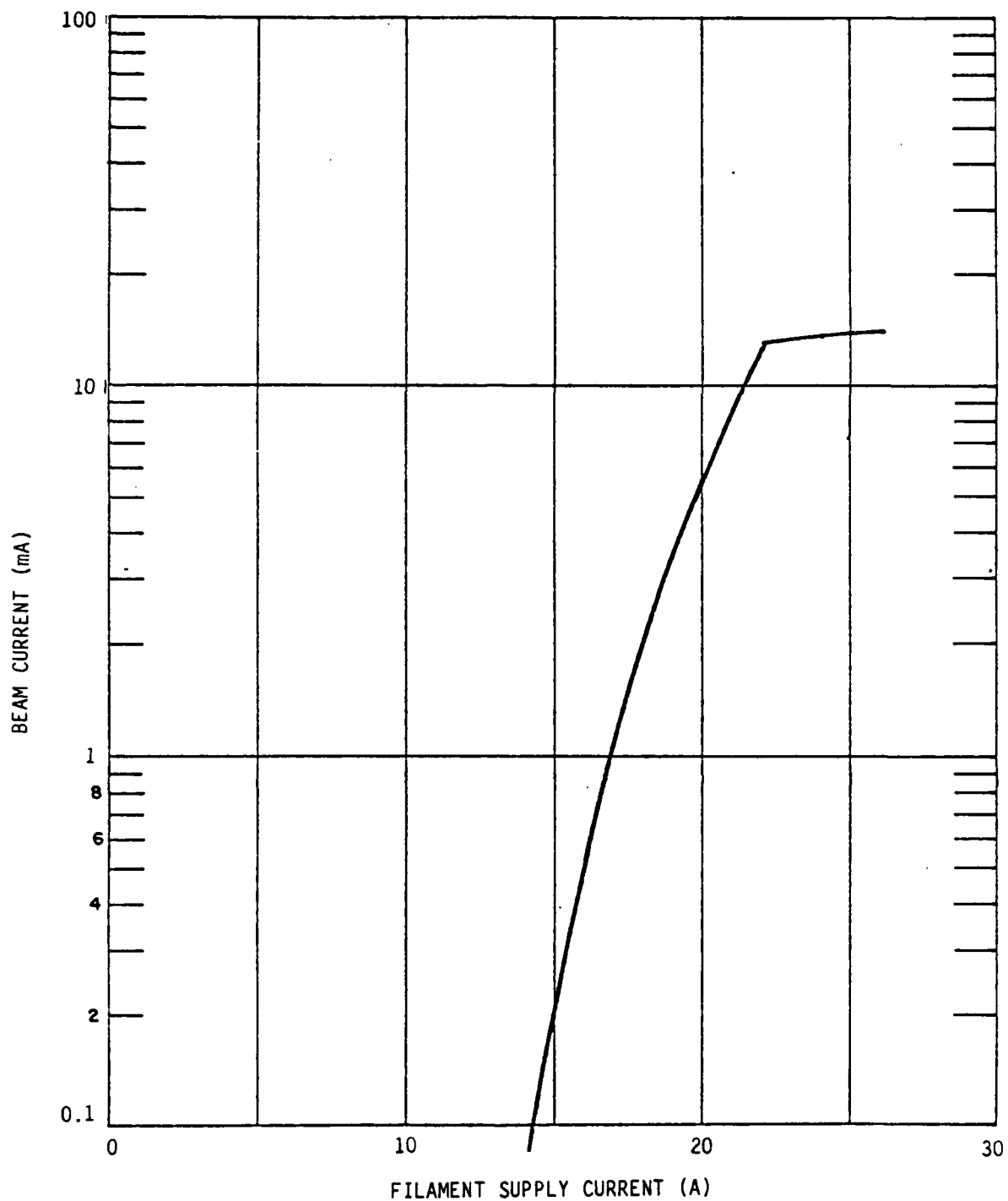
Figure 25. Filament region pressure as a function of restrictive orifice size for several exo-shroud pressures.

throttle valve is closed, shroud pumping is exclusively through the beam entrance port. In practice at the highest mass loadings the filament chamber approaches 8×10^{-5} torr, the backing vacuum pump is audibly pumping gas, but the filament is unharmed. In fact contrary to expectations, the extracted beam current increases slightly under these conditions. There is some evidence that the filament is degraded when pure oxygen is the test gas under these high flow conditions. Either our calculations of the conductance or our estimate of the exo-shroud pressure were wrong, and the severity of the problem was overestimated.

The increased level of filament thermal emission entering the shroud with the simplified gun geometry proved to be a groundless concern. No radiance from the filament has been detected either in the visible or in the infrared (out to $15 \mu\text{m}$). The small steering coils surrounding the beam path were removed as part of the modification but the beam could still be reproducibly introduced into the shroud without an applied magnetic field from the large coils. A small permanent magnet was used to "steer" the beam into the shroud. When the large magnetic coils were energized, the beam was constrained to enter the shroud and "steering" was not required (or even possible at the largest applied fields.) When the magnetic coils were off, the beam rose and curved slightly as it crossed the shroud, not hitting the wall opposite the beam but down-flow closer to the valve. This is the result of the residual magnetic fields present in the shroud due to the earth's field and the magnetized soft steel present as support rings on the vacuum enclosure. When a strong external magnetic field was applied by the coils, the electron beam spiraled across the tank forming nodes at focusses. The spiral dimensions were a function of pressure and the applied field strength. It was felt that the spiraling results from the filament not being aligned along the applied field lines, thus forcing the electron to process around the field lines across the shroud. An additional coil was constructed to extend the applied field lines uniformly out the filament. This coil was capable of generating 50 gauss and was adjusted to minimize beam spiral. Marginal success was achieved. It was found that the large coils could be adjusted to minimize spiraling. This adjustment was carefully undertaken and good spatial uniformity was achieved.

2.4.4 Electron Beam Characteristics - The current-voltage characteristics of the modified electron gun were explored. The filament temperature (as controlled by current flowing through the filament ribbon) was varied to establish the onset of space charge limitations of the extracted beam current. A typical plot of electron beam current as a function of filament supply current is given in Figure 26. The beam current rises rapidly with filament temperature until 22 amps are passing through the filament. Further increases in temperature result in only slight increases in beam current, but considerably shorten the filament lifetime. Consequently, the ideal operational conditions are just onto the space charge limited plateau. At lower filament currents, the observed beam currents (and fluorescent intensities) will be very sensitive to power supply drifts. Figure 26 is for 3 keV of applied acceleration voltage. As voltage is increased, the beam current also rises (almost linearly) so that at 5.5 keV, 24 mA have been obtained. Fluorescent intensities do not increase as drastically, since electron excitation cross sections drop off as voltage increases. Consequently, few experiments have been performed above 6 keV. The experimental apparatus is capable of operation of up to 11 keV in its present configuration. Above that voltage, corona and arcing begins to occur, and beam stability is decreased. Modification of the system to operate at higher voltages should be straightforward, but is not of interest at present.

The beam currents of Figure 26 are the currents drawn from the high voltage supply. Not all of those electrons will enter the shroud. A calibrated Pearson coil was positioned around the beam entrance aperture into the shroud. The Pearson coil will detect the modulation of electron current (AC) passing through its center. The beam was pulsed by applying a bias voltage to a grid to cut off beam current flow. Up to 90 percent of the initial beam current was found to enter the shroud - an excellent throughput attributable in part to the simplified gun geometry. Unfortunately, it was found that it became more and more difficult to bias the beam off. Inspection of the filament area revealed that a black impurity was forming on the surface of the ceramic filament insulating support. The impurity was conductive, forming a resistive path prohibiting complete biasing of the grid. The impurity was, of



A-1772

Figure 26. Electron beam current as a function of filament current for 3 keV acceleration voltage. The beam current rises rapidly with filament temperature until the space charge limit is reached.

course, of unknown origin and could not be removed by manual abrasion or solvents. At present, no cure is known and more ceramic supports are being ordered. Fortunately, impurity buildup appears to have slowed with time, and with maintenance of cryogenic trapping between filament and pump.

The applied magnetic field was found to produce large non-linearities in detected fluorescent intensity as a function of field strength, pressure, and current. This results from the magnetic field affecting the interaction of the primary and created secondary electrons with the gases. In the presence of the field, the secondary electrons are trapped and their energy distribution drastically changed. The result is a collective phenomenon loosely called beam plasma discharge (BPD), which will be discussed later in this report - both in terms of its fundamental physics and its effect on the fluorescent data.

At present filament lifetimes are several hundred hours, permitting weeks of experimental measurements without filament failure. The proposed electron beam collectors have not been designed because of our desire to perform experimental measurements rather than continue apparatus improvement.

2.4.5 Secondary Electron Density Distribution - In order to assess the importance of primary/secondary electron excitation processes we undertook modeling of the electron transport in LABCEDE.

The production of secondary electrons along the beam is given by

$$\frac{d}{dx} \frac{de_s}{dt} = \int J N_{\text{gas}} S(\epsilon, T) dT \quad (\text{electrons/s/unit length}) \quad (22)$$

The number of secondary electrons in a unit volume a distance r away from this source point, x , is this production rate, over $4\pi r^2$, integrated

over the time to pass through the volume element by the secondary electron, $\frac{dr}{u_s}$, and integrated over the elemental area perpendicular to r .

This leads to the concentration of secondary electrons in a volume given by

$$\begin{aligned}
 N_{e_s} &= \int \int dx \frac{d}{dx} \frac{de_s}{dt} \frac{dV}{4\pi r^2} u_s \\
 &= \int_{\text{energy}} dT \frac{S(E,T) J N_{\text{gas}}}{u_s} \int_{\text{beam}} dx \int_{\text{cyl}} \frac{dV}{4\pi r^2} \\
 &= \int_{\text{energy}} \frac{dT S(E,T)}{u_s} J N_{\text{gas}} G (\text{geometry})
 \end{aligned} \tag{23}$$

The geometry integral is

$$\begin{aligned}
 G &= \int dx \int \frac{dV}{4\pi r^2} \\
 &= \int_{-\ell}^{\ell} dx \int_{-h}^h dz \int_0^a \rho d\rho \int_0^{2\pi} d\theta \frac{1}{4\pi(z^2 + (x - \rho \cos\theta)^2 + (\rho \sin\theta)^2)}
 \end{aligned}$$

Taking ℓ , the e-beam length, to be infinite gives

$$G = \int_0^h dz \int_0^a \rho d\rho \int_0^{\pi} d\theta \frac{1}{(\rho^2 \sin^2 \theta + z^2)^{1/2}} \tag{24}$$

This is the solution to an infinite line source radiating radially.

Integrating over the cylinder radius, a , gives

$$\begin{aligned}
G &= \int_0^\pi d\theta \int_0^h dz \frac{\sqrt{a^2 \sin^2 \theta + z^2} - z^2}{\sin^2 \theta} \\
&= 2 \int_0^{\pi/2} d\theta a^2 \int_0^{h/a} dz' \frac{\sqrt{\sin^2 \theta + z'^2} - z'^2}{\sin^2 \theta} \\
&= a^2 \int_0^{\pi/2} d\theta \left[\frac{h/a (\sqrt{\sin^2 \theta + (h/a)^2} - h/a)}{\sin^2 \theta} + \ln (h/a + \sqrt{\sin^2 \theta + (h/a)^2}) \right] \\
&\quad + \pi/2 a^2 \ln 2 \approx \frac{1}{4h} \left(\frac{1}{2} + \ln(4 h/a) \right) \pi a^2 2h \quad (25)
\end{aligned}$$

with

$$h = 100 \text{ cm and } a = 5 \text{ cm}$$

this gives

$$G = 200 \text{ cm}^2$$

As an example, let us consider the production of secondary electrons in CO. The differential cross-section from forming secondaries is taken from T. Sawada et al.,¹² and is given as

$$S(E, T) = 10^{-16} \left(\frac{K}{E} \ln E/J \right) \frac{\Gamma^2}{(T - T_0)^2 + \Gamma^2} \quad (26)$$

with $J = 12.6$, $T_0 = 1.76$, $\Gamma = \frac{12 E}{E - 13.5}$ for CO and E and T in eV. At $E = 3000$ eV this gives

$$S(E, T) = 6.38 \times 10^{-19} \frac{145}{(T - 1.76)^2 + 145}$$

which is constant for $T < 12$.

Let us now consider the production rate of CO(v) in the field of view. This process should be most sensitive to the secondary electron distribution.

$$\begin{aligned}\frac{dCO(v)}{dt} &= \int N_{eS}(T) N_{CO} u_S(T) \sigma(T) dT \\ &= G J N_{CO}^2 \int \sigma(T) S(E,T) dT, s^{-1}\end{aligned}\quad (27)$$

where $\sigma(T)$ is the cross-section for exciting CO(v) by electrons. The resonant cross-section is taken from Kieffer¹³ and is zero beyond 4eV so that the integral term $S(E,T)$ is constant and the approximate integral is $7.5 \times 10^{-16} \text{ cm}^2 \text{ eV}$ giving

$$\frac{dCO(v)}{dt} = G J N_{CO}^2 6.38 \times 10^{-19} \times 7.5 \times 10^{-16}$$

which for $J = 6 \times 10^{16} \text{ electron/s}$, $N_{CO} = 10^{14}$ gives

$$\frac{dCO(v)}{dt} = 5 \times 10^{13} s^{-1}$$

The non-resonant cross-section, $\sigma(T)$ is estimated by Caledonia as

$$\sigma(T) = \frac{2.6 \times 10^{-14}}{T} \ln(14.815T) \quad (28)$$

At large T, the differential cross-section becomes

$$S(E,T) = 6.38 \times 10^{-19} \frac{145}{T}$$

Comparing the resonant integral,

$$\int \frac{\sigma(T)}{10^{-16}} \frac{\sigma(E,T)dT}{6.38 \times 10^{-19}} = 7.5 ,$$

with the corresponding non-resonant integral,

$$\int_{13}^{\infty} \frac{2.6 \times 10^{-2} \ln(14.815T)}{T^3} 145 dT = \frac{3.8}{4(13)^4} \ln(14.815(13)) ,$$

shows that the non-resonant process is a small contribution.

The direct excitation by primary electron is found from the non-resonant cross-section.

$$\begin{aligned}
 \frac{dCO(v)}{dt} &= \int_{-a}^a \sigma(E) N_{CO} J d\ell \\
 &= 2a \sigma(E) N_{CO} J \\
 &= 10 \frac{2.6 \times 10^{-18}}{3000} \ln(14.815 \times 3000) 10^{14} \times 6 \times 10^{16} \\
 &= 5.5 \times 10^{11} s^{-1}
 \end{aligned}$$

The scaling of the two processes (secondaries and primaries) is:

$$\begin{aligned}
 \left. \frac{dCO(v)}{dt} \right|_{sec} &= \left(\frac{I}{10^{-2}} \right) \left(\frac{N_{CO}}{10^{14}} \right)^2 \left(\frac{a}{5} \right) \left(\frac{1+\ln 400/a}{1+\ln 20} \right) 5 \times 10^{13} s^{-1} \\
 \left. \frac{dCO(v)}{dt} \right|_{pri} &= \left(\frac{I}{10^{-2}} \right) \left(\frac{N_{CO}}{10^{14}} \right) \left(\frac{a}{5} \right) 5.5 \times 10^{11} s^{-1}
 \end{aligned} \tag{29}$$

and the secondaries will be two orders of magnitude more important in exciting CO vibrations than the primary electrons in the beam. Let us next consider visible emission involving electronically excited molecular states.

The pressure dependence of the 391.4 nm emission (and thus $N_2^+(B^2\Sigma_u^+)$ concentrations) when no magnetic field was applied was linear at low pressures and less than linear at higher pressures (see Section 3). On the other hand, second positive (N_2C state) emission increased faster than linearly with pressure. The ionic states are formed dominantly by interactions with primary electrons (see Table 3). The N_2C state is formed for the most part by secondaries. In order to quantitatively understand these effects and because the 391.4 nm emission is required for normalization of the Meinel band quenching studies we undertook a simple modeling effort to describe the behavior of the secondary electrons in molecular nitrogen under conditions when beam plasma discharge was not occurring.

TABLE 3. ELECTRON EXCITATION EFFICIENCIES^a IN ABSENCE OF
BEAM PLASMA DISCHARGE AND QUENCHING EFFECTS

Molecular State	Excitation by Primary ^b		Efficiency ^c	
	Total Excitation			
	N ₂ (100%)	N ₂ /O ₂ /O ^d (78,19,3%)	Pure N ₂	N ₂ O ₂ O
N ₂ B 3π _g	0.10	0.10	0.031	0.028
N ₂ C 3Π _u	0.13	0.12	0.029	0.025
N ₂ ⁺ A 2Π _u	0.79	0.77	0.086	0.068
N ₂ ⁺ B 2Σ _u ⁺	0.80	0.78	0.049	0.039
O ₂ +b 4Σ _g ⁻	--	0.80	--	0.016

a - Calculations using code described in Ref. 18.

b - Calculation for 900 eV primaries and assumes total degradation of electron energy into gas. Reasonable approximation for 3 kV primaries because cross section asymptotes with voltage.

c - Fraction of deposited (input) energy which appears in that electronic state. Sum over all states equals 1.

d - Represents estimated atmospheric composition at 100 km.

The energy distributions and angular dependence of secondary electrons in the 4 to 200 eV range which are generated by the impact of up to 2.0 keV electrons on N_2 (and O_2) have been measured by Opal, Beaty and Peterson.^{14,15} Their observed cross sections as a function of secondary energy, E_s , are plotted in Figure 27 for N_2 and O_2 . These curves roughly follow the classical Thomson scattering theory for collision cross sections - asymptoting to a constant value for secondary energies less than the ionization potential and falling off as $(\text{secondary energy})^{-2}$ at sufficiently high energies. Multiple scattering effects (further degrading the electron distribution) are considered later in this section. The results of Opal et al. can readily be extended to electron voltages of interest to us, because above 1 to 2 eV the shape of the secondary electron distribution does not change, although the total cross section decreases slowly with increasing voltage. The total 391.4 nm cross section has been shown to reflect the decreasing stopping power of the gas with increasing voltage.^{16,17} Opal et al.¹⁴ also present the angular distributions of the secondary electrons as a function of their energy. Secondaries with the lowest energies are isotropically scattered. As their energy increases, a peak in the angular distribution forms at 75 deg, just forward of perpendicular to the primaries, and is roughly symmetric about this peak. For 40 eV secondaries, the cross sections at 45 deg from this peak (30 and 120 deg) are down by 2.5; for 160 eV secondaries they are down by 5. Thus, although the secondary distribution will be isotropic to first order, scattering is slightly forward and secondaries in the field of view will have some "up-beam" (toward gun) component.

The N_2^+A and N_2^+B states have thresholds at 16.7 and 18.7 eV, respectively. Thus, secondaries with energies below this cannot give rise to Meinel or first negative band emission. The electron excitation cross sections used in Ref. 18 and in our calculations are plotted in Figure 28 for several electronic states of interest. The N_2^+A and N_2^+B cross sections are seen to parallel each other, with the N_2^+A state excitation cross section being roughly a factor of two greater than N_2^+B for electron energies above 40 eV. Below this value, the differences are greater due to the lower threshold for

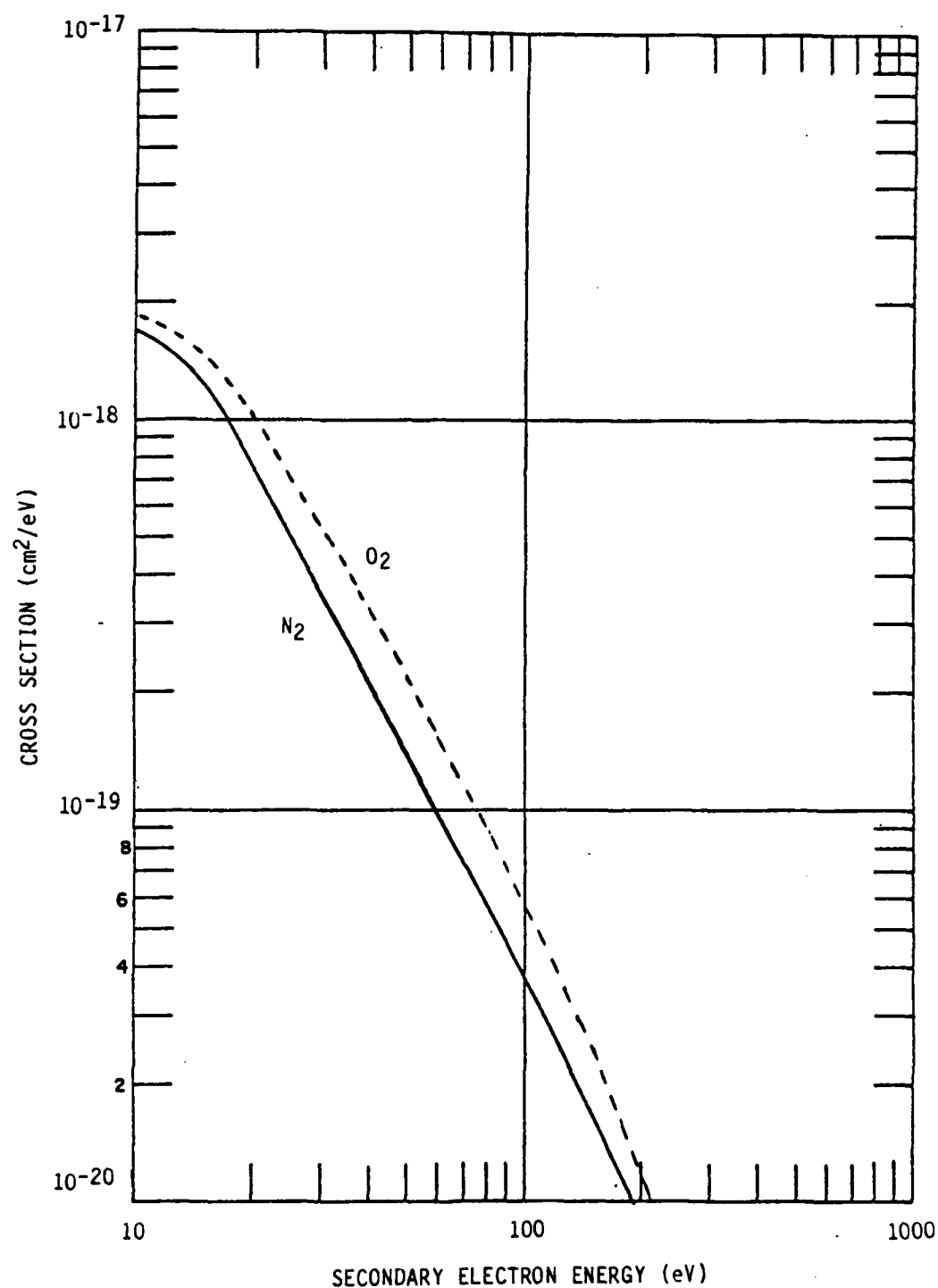
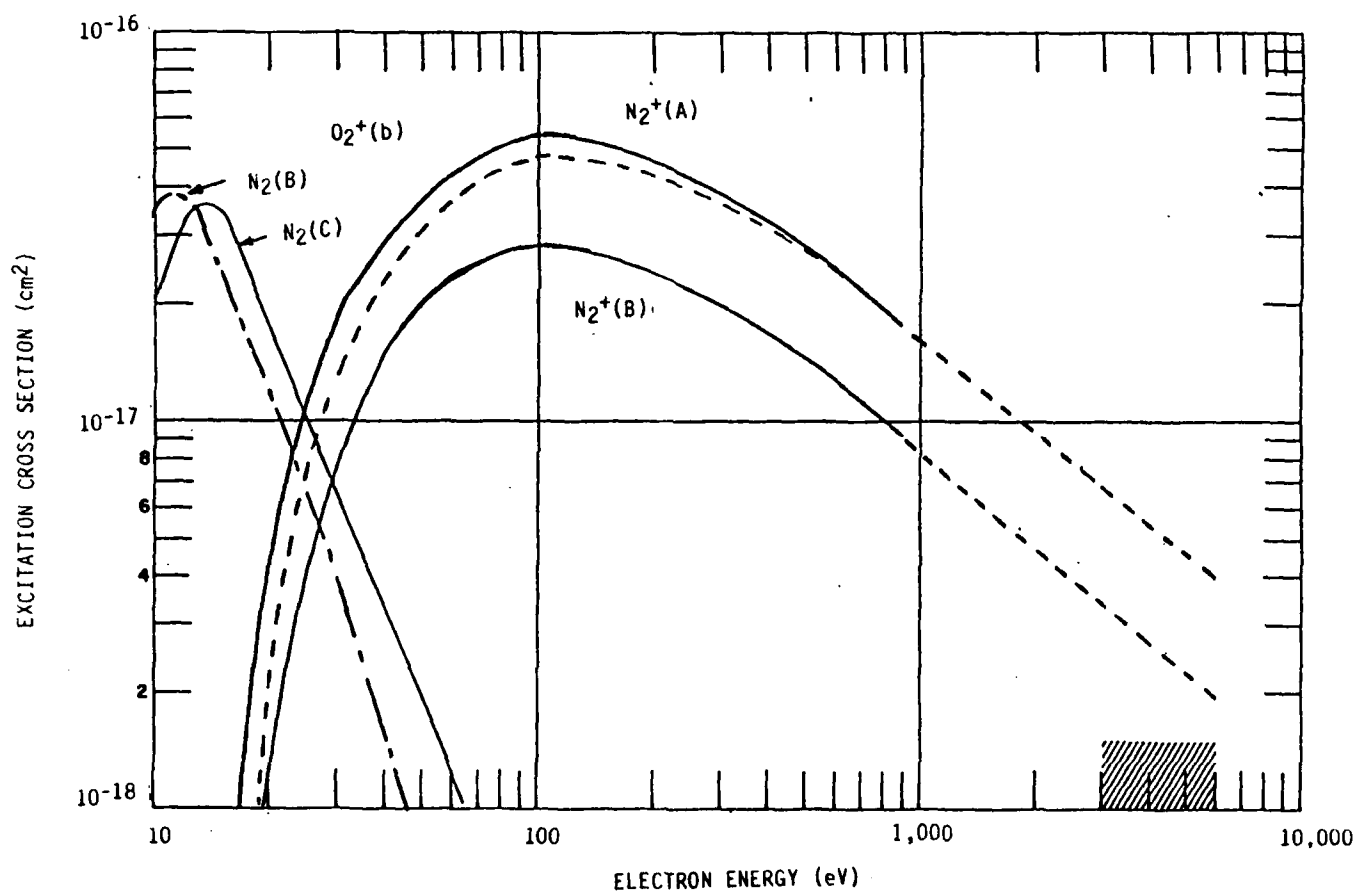


Figure 27. Secondary electron distribution from 2 keV primary electrons for scattering from N_2 and O_2 . As voltage increases, cross section slowly decreases but shape of curve is unchanged.



A-1774

Figure 28. Excitation cross sections for several excited molecular states using values from Ref. 18. Ionic states exhibit > 16 eV threshold. Neutral $N_2(B)$ state accessible by lower energy secondaries.

N_2^+A excitation. Both peak for 100 eV electrons and fall off slowly at higher energies to the Born-Bethe asymptotic dependence. Also plotted are the $O_2^+(b^4\Sigma_g^-)$ excitation cross sections, which are seen to closely follow the N_2^+A values were above threshold. The cross sections for the N_2B (first positive) and N_2C (second positive) states are also displayed. It is seen that lower energy secondaries (10 to 14 eV) will predominantly excite those states, and they have comparable excitation cross section to the ionic states for 20 to 30 eV electrons. Total production of an electronic state reflects both the excitation cross sections and the available secondary electron distribution (as well as cascade from higher lying electronic states). For example, considering only secondary electrons above 16 eV (those capable of ionic excited electronic state production) from the curve of Figure 27, one-third of all secondary electrons produced by 2 to 6 kV primaries have less than 24 eV, two-thirds have less than 44 eV, and 90 percent less than 90 eV. Coupling this to the excitation cross sections leads to the result that 35 eV electrons are most probably responsible for the $N_2^+(A \text{ or } B)$ state excitation. At low energies the excitation cross section is low while at higher energies there are fewer secondaries. Under low pressure conditions with no applied magnetic field, the primary electron excitation will dominate over secondary electron excitation for these states. Although secondary excitation has a larger cross section, the number of primaries far exceeds the secondaries due to small beam attenuation. The neutral $N_2(B \text{ and } C)$ states are most probably excited by 11 and 14 eV secondaries, respectively. Moreover, the product of secondary production cross section per eV and electronic state excitation cross section is an order of magnitude larger for the neutral states than for the ionic states.

The final input required to estimate the spatial distribution is the electron range, the effective distance an electron can travel before it is degraded to the point where it can no longer excite N_2^+A (or B) states. This distance is calculated from electron energy loss, $1/N \, dE/dx$, plots versus electron energy.¹⁶ This energy loss correlates well with the N_2^+B state excitation. The range is found by setting

$$\left[\frac{1}{N} \frac{dE}{dx} \right] NL = E_g \quad (30)$$

and solving for NL. Secondaries between threshold 16 and 90 eV have ranges of 160 ± 40 mtorr-cm. For example, a 25 eV secondary electron will have a range of 16 cm when the pressure in the shroud is 10 mtorr. At higher electron energies, the stopping power asymptotes to an $E^{1.5-1.75}$ dependence and thus NL grows rapidly for E_g above 100 eV, being 55 cm at 10 mtorr for 200 eV electrons. This range is really the vector distance from the scattering event, and a more careful analysis would include the scattered electron angular distribution. For this analysis it is sufficient to note that the secondary electron ranges are greater than the 10 cm high by 0.1 cm wide field of view until pressures approach 30 mtorr. Thus the fraction of the secondary electrons which interact with N_2 to form N_2^+A or B states will vary as a function of operating pressure. Thus, for our thin-target conditions, the N_2^+B emission due to primary electrons will vary linearly with pressure (for constant electron current), but the fraction of the N_2^+B emission arising from secondary electron excitation which falls within the field of view will vary from practically zero at $p < 1$ mtorr to nearly 100 percent above 30 mT - all the secondary electrons are degraded before they can escape from the field of view. This is illustrated more clearly in Figure 29 where the fraction of the secondary electrons stopped (hence total fluorescence excitation) are plotted versus distance from their formation point for several pressures. This calculation contains the secondary electron distribution, the range of each electron, and its excitation cross section for the N_2^+A (or B) state, integrated over all electron energies. A corresponding plot for the neutral states (which are more sensitive to lower energy secondaries) would be quite similar since the range of the secondaries is not strongly dependent on their energy below 100 eV.

If we assume that the detection system field of view is centered on the electron beam, then from Figure 29 we see that in the 5 cm extent of the field of view (fov), only 3 percent of the secondary electrons are stopped in the fov at 1 mtorr, 30 percent at 10 mtorr, and 60 percent at 20 mtorr. In actuality, because the electron scattering is into 4π steradians, the stopping

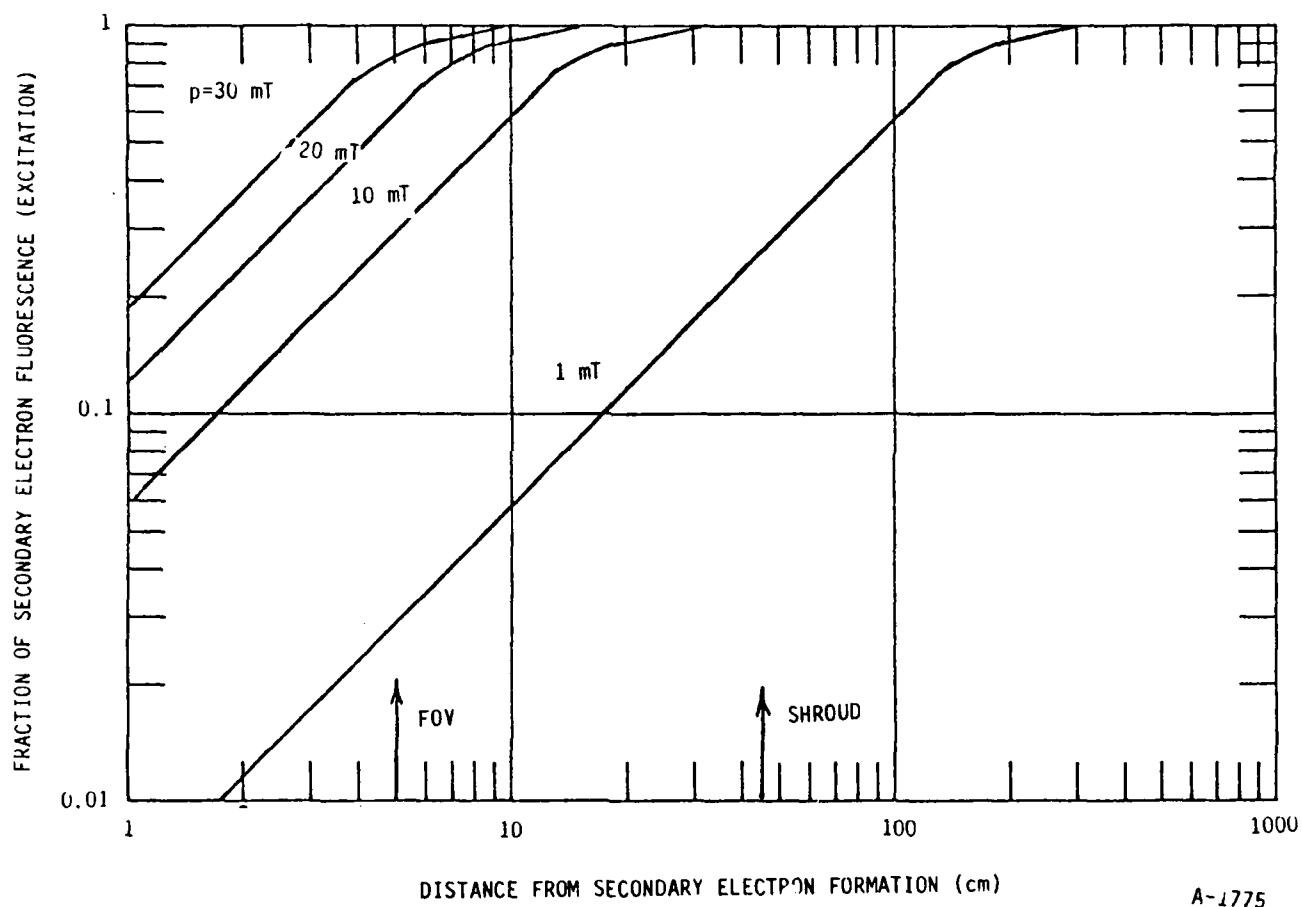


Figure 29. Spatial distribution of molecular-ionic excited states as a function of chamber pressure. Calculation contains secondary electron energy distribution, their range and molecular excitation cross section integrated over electron energy.

AD-A161 674

FLUORESCENCE FROM ELECTRON IRRADIATED GASES IN
REFURBISHED LABCEDE(U) PHYSICAL SCIENCES INC ANDOVER MA
B D GREEN ET AL SEP 85 PSI-TR-433 AFGL-TR-84-8218

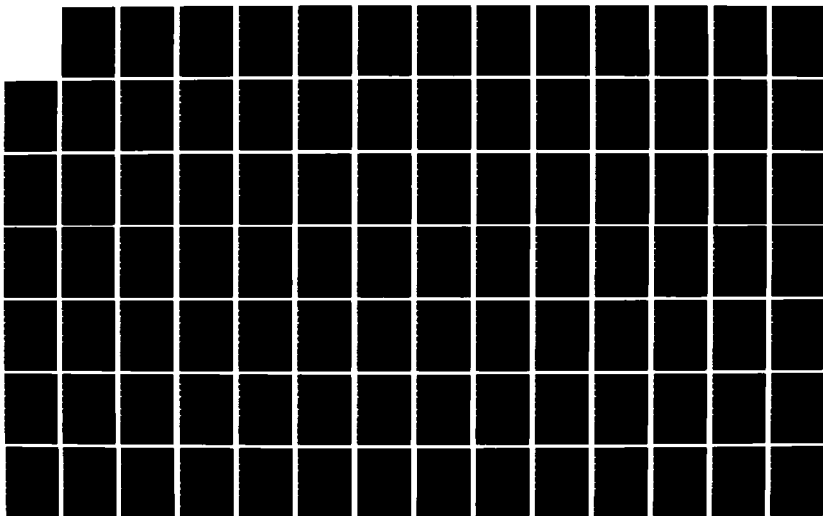
2/4

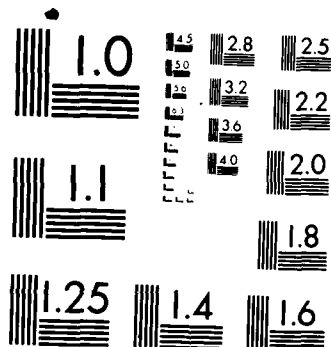
UNCLASSIFIED

F19628-88-C-0168

F/G 4/1

ML





MICROCOPY RESOLUTION TEST CHART
NATIONAL BUREAU OF STANDARDS 1963-A

distance from the primary electron beam will be less than if it were all perpendicular (radially out from the beam), and a greater fraction of the fluorescence will fall within the fov. This behavior is in best agreement with the observations of Section 3, where neutral N_2 second-positive intensity grows faster than linearly with pressure up to 30 mtorr. Figure 29 predicts that all the secondary electrons are stopped in the field of view at this point and further increases in pressure should result in, at most, linear intensity increases as observed. The observed intensity at 20 mtorr is ~48 percent greater than linear and Figure 29 claims that 60 percent of the total secondary fluorescence is responsible for this increase, meaning that in total, secondary electrons would be responsible slightly less than half of the total excitation. Table 3 based on Ref. 18 predicted that totally degraded secondaries would be responsible for 87 percent of the total fluorescence, primaries for only 13 percent. The N_2C fluorescence data at least qualitatively supports our understanding of beam spatial distribution even though collisional cascade processes are neglected. On the other hand, the 391.4 nm emission should behave in a similar but less extreme manner. It should exhibit a slight increase above linear as a function of pressure since secondary electrons contribute less to its total fluorescent intensity. The observed pressure dependence is markedly less than linear. This effect must be modeled more accurately before the Meinel quenching studies can be completed. One potential explanation is small angle scattering of the primaries "up-beam" removing them from the field of view and giving rise to the observed depletion as pressure is increased. Both these opposing trends cannot be explained on the basis of our simplistic modeling. A detailed understanding of LABCEDE conditions must be gained before quantitative measurements programs are possible. However, because the Meinel studies rely on relative excitations of two ionic states, the following approach was attempted.

In addition to gaining an understanding of our fluorescence observations, this modeling pointed out the possibility of performing our Meinel band studies with an applied magnetic field to trap the secondaries in the field of view. First-order cancellation of the effects of electron spatial distribution occurs by ratioing N_2^+B and N_2^+A intensities. However, as can be seen in

Figure 28, at energies near threshold the excitation cross section ratio is no longer constant. For example, the stopping of 17 eV secondaries will affect Meinel band but not first negative intensities. Thus all secondaries must be contained in the field of view at all pressures to eliminate this effect. Application of an external magnetic field constrains the electrons to trajectories of Larmor radii off the beam axis. The electron Larmor radius will be less than 5 cm for magnetic fields in excess of 40 Gauss (Figure 24). Our modeling does not include the effects of the dramatically different secondary electron distribution when beam plasma discharge occurs, but as long as all secondaries are contained in the field of view at all pressures, accurate Meinel band quenching measurements as described in the next section should be possible. Alternately, very small fields of view observing just the primary beam will tend to emphasize primary electron excitation relative to secondary. This approach was finally used in our Meinel studies. This approach becomes less desirable as the secondary electron energy (and thus range) decreases as was the case for CO(v) above. Accurate relative excitation efficiencies will depend on a basic understanding of a primary and secondary electron spatial distribution. The results of this section form only a first step toward that understanding.

2.5 Detection Capabilities

2.5.1 Refurbishment - One of the major aims of the refurbishment project was to decrease background levels and increase optical access to the experimental volume. This will permit simultaneous measurement of fluorescence and energy deposition so that excitation efficiencies may be determined. The new shroud included pairs of ports at right angles to the beam in the beam plane; at a small angle (19 deg intersection angle) to the beam in the horizontal plane; at increasing distances downstream in the directed flow to permit the study of long lived radiators; and on the door either side of center to permit the study of energy deposition along the beam path. Access flanges for these ports were welded into the walls of the vacuum enclosure (see Appendix A for more details.) The ports on the shroud were 1 in. thick for heat sinking and threaded on both sides to support optics and/or baffling nozzles to be

simultaneously attached. The ports will be kept covered by aluminum plates when not in use to keep leakage of room temperature emission into the shroud at a minimum.

A constant source of room temperature emission would be through the gas flow exit port. As a result a careful arrangement was devised which allows gas to exit the shroud relatively unimpeded, yet prevents room emission from entering the shroud. This section of the shroud is shown schematically in Figure 4. All surfaces inside the shroud near the exit (beyond the hemispherical radiation baffle/sled) were painted with a black paint (Sherwin-Williams Kemacryl Lacquer) with high infrared emissivity¹⁷ ($\epsilon > 0.9$). This paint was chosen because it exhibited excellent durability. Additionally, we experimentally determined that it was stable up to 530K even after several heating/cooling cycles. Unfortunately, it flaked off the shroud surfaces after a few cycles. Black velvet (3M) which also has high emissivity was substituted and appears to have acceptable longevity and characteristics. Calculations of the transmission of diffusely scattered light through this maze revealed that a 5×10^6 reduction of the original intensity entering the shroud should result. Consequently, at all wavelengths greater than 9 μm the thermal emission by the 77K surfaces will dominate the contribution of room temperature leakage through the throttle valve past the radiation baffle/sled. Care was taken to seal light leaks along the rest of the shroud.

2.5.2 Capabilities - The LABCEDE facility has the desirable ability to widely vary its operating conditions to simulate field and atmospheric phenomena, then investigate their important kinetic and deposition dependent properties by varying individual experimental parameters with a systematic methodology. Fluorescence from gases at pressures ranging from 0.1 to 100 μm is observable. This corresponds to atmospheric altitudes over the 110 to 62 km range - the mesosphere and lower thermosphere where the atmosphere makes the transition from collision to radiation dominated equilibria for all major infrared emitters. Additionally, the electron dosing rates will be up to 10^2 greater than entire auroral columns and electron densities in the confined electron beam can approach levels present in nuclear event radiation clouds.

With the solar simulator attached, daylit aurora and metastable photochemistry can be investigated. Finally, fast kinetic processes (10^{-13} cm³/s to gas kinetic) which could not be measured in the higher pressure 50 kV system can potentially be investigated in the rebuilt cryogenic system.

2.5.3 Detection Networks and Geometries - At the start of the rebuilding program the available infrared spectrometers included: a SWIR-MWIR CVF (InSb detector); a LWIR CVF (As:Si detector); a warm Michelson interferometer and several warm dispersive spectrometers for the SWIR-MWIR; and a cryogenic Czerny-Turner spectrometer. Because LABCEDE experiments will require detection of very weak emission levels, utmost detection system sensitivity is mandatory. Interferometers gain over dispersive spectrometers by a throughput advantage which can easily be in excess of a factor of 100. Although spectrometers have the capability to concentrate on spectral regions of interest in a sparse spectrum (which can somewhat offset this advantage), interferometers also gain a multiplex advantage if the spectrum is rich. As a result interferometers can measure far fainter fluorescence signals or acquire the data $\sim 10^4$ times faster than a spectrometer. If the source is rapidly varying and noisy, the multiplexing ability becomes a disadvantage¹¹ and all throughput gains can be cancelled.

In order to determine the optimum detection network for LABCEDE, OPTRA was subcontracted to perform an analytical sensitivity study. Their draft report is included as Appendix C. The conclusions of their study were that a warm interferometer has a lower NESR than even a cryogenic grating spectrometer, and that some gains could be made by utilizing a cold filter in front of a cryogenic interferometer even with a warm experiment. This gain is about a factor of four at 15 μ m. Cryogenic operation of the experiment results in a factor of 50 signal/noise gain. They recommended a cryogenic interferometer as the optimum instrument and felt that the ailing LWIR spectrometer was not very useful.

At least for the initial experiments envisioned, the detection networks will utilize either the center port on the door of the chamber and look down

the tank axis toward the valve, or the slant path across the beam at 20 deg angle from upflow opposite the electron gun to downflow just adjacent to the electron beam entrance aperture. Both the visible spectrometer and the room temperature interferometer have been used at both locations. The interferometer was found to be affected by the applied magnetic fields (disorienting its position transducer feedback network) and thus could only record spectra from the side (slant path) geometry when the magnetic coils were not in use. The cryogenic circular variable filter (CVF) required a complete optical baffling system (described in Subsection 2.5.6) and was interfaced to LABCEDE only at the door port. The electron beam is 1.1m distant from the door port, 0.7m from the shroud end wall (door), and is perpendicular to the optical axis. Thus, from the door port the beam is viewed through 0.7m of inlet gas, upstream from the beam and through 0.4m of near vacuum in the space between the shroud and the vacuum enclosure. The distance from the other observation port to the center of the tank is 0.7m, 0.5m of which is inside the shroud. Of course, for both geometries the emission is distributed some distance along the optical path as it intersects the electron beam and includes the effects of secondary electron excitation. For both geometries, absorption of the beam excited emission by the inlet gases along the optical path could be a problem. This effect must be considered for each molecular system studied.

The visible fluorescence studies were conducted with a 0.3m McPherson 218 monochromator. Without a lens, its field of view at the center of the electron beam is 20×20 cm from the door port and 14×14 cm from the side port. The fluorescence studies discussed in Section 3 utilized a 2-ft f/2 lens to take a vertical slice of the entire beam, i.e., the monochromator slit was imaged at the beam plane and a 10 cm high, 0.1 cm wide slice of the beam was observed. The room temperature interferometer has been used in a number of past studies and its field of view accurately determined¹¹ as a radially symmetric gaussian with a 3 deg half angle field of view (0.008 sr). The interferometer would thus have a circular field of view 12 cm in diameter at the beam plane when viewing from the door port. From the side port, the roughly 7 cm diameter circular field of view would intersect the electron beam at an acute angle. At higher pressures, where the beam is larger than the

field of view, the intersection is a parallel piped cylinder. At low pressures when the beam is essentially a line, the intersection is a section of the line source. The CVF has a smaller 2° field of view and the electron beam will be scattered to fill the field of view (and form an extended source) at even lower pressures than for the interferometer. When the external magnetic field is applied, beam growth will be restricted and may never fill the field of view.

2.5.4 Experimental Intensity Predictions - As part of our previous design effort,¹¹ ion-pair creation rates in the rebuilt facility were calculated as a basis for predicting infrared fluorescent intensities. One of the first exercises undertaken on LABCEDE was the estimation of the actual energy deposition from 391.4 nm fluorescence. The estimate is rough due to a number of assumptions, but once the viewing geometry was calculated and the transmission and quantum efficiencies taken into account, it was decided that the phototube-monochromator network viewing from the door port had a responsivity of 10^9 photons/cm³-s per nanoampere of phototube current. Since 1 to 391.4 nm photon is emitted for every 20 ion pairs formed, nanoamperes can be directly related to ion pair formation rate in the field of view. From beam size estimates, energy deposition per unit path length across the tank was estimated. In Ref. 11, we calculated energy depositions of $1-2 \times 10^{12}$ ion pairs/cm-s-mtorr-mA. Our observations of 391.4 nm fluorescence lead to values slightly lower than predicted for the case with no applied magnetic field. When the magnetic field was turned on, the N_2^+B state emission increased by an order of magnitude, yielding an ion pair creation rate well above our estimate. Based on the number of assumptions in extrapolating the experimental observation to the modeling, the agreement is encouraging. Nevertheless, quantitative estimates await implementation of the beam spatial distribution diagnostic described in Subsection 2.5.5.

Having even crude estimates of the ion pair production rates in LABCEDE gives us the ability to update our predictions of the expected infrared fluorescent intensities. The number of vibrationally excited CO₂ molecules

created per ion pair will depend on the gas mixture irradiated. Table 4 gives the $\text{CO}_2(v_2)$ production rate for a variety of gas mixtures. These estimates are based on an electron deposition code described previously.¹⁸ The number of molecules which are excited to the v_2 state also depends on the degree of energy degradation and primary voltage. For very thin targets, the primary electrons are scattered to create secondaries which travel out of the field of view before they interact further with the target gas. The column labeled primary best describes this situation. At higher chamber pressures, the secondaries are stopped in the observation volume. The column labeled total v_2 /ion-pair models totally degraded electron energy deposition. It should be noted that this code does not take cascade (collisional or radiative) processes into account or the stopping power of each gas mix. An air mixture is seen to have the lowest excitation efficiency listed. Removal of oxygen quadruples $\text{CO}_2(v_2)$ production. Further increases result if argon is used as the target gas and CO_2 fractional composition is increased. These numbers are

TABLE 4. $\text{CO}_2(v_2)$ MOLECULES EXCITED PER ION PAIR

Gases	Composition	Primary v_2 /Ion Pair	Primary Voltage	Total v_2 /Ion Pair
$\text{N}_2/\text{O}_2/\text{CO}_2$	0.79/0.2097/0.0003	0.04	900	0.92
N_2/CO_2	0.9/0.1	0.18	1000	3.88
	0.99/0.01	0.14		3.24
Ar/CO_2	0.999/0.001	0.28	900	5.49
	0.99/0.01	0.29		5.58
	0.9/0.1	0.33		6.64
	0.7/0.3	0.42		8.76
Ar/CO_2	0.7/0.3	0.06	6000	8.52
CO_2	1.0	0.79	900	15.70

useful as an indication of potential gas mixtures to be used if $\text{CO}_2(\nu_2)$ emission is observed only weakly in air. As was noted for $\text{CO}(\nu)$ excitation above, secondary electron excitation is expected to dominate primary and the degraded columns are more appropriate.

Our best estimates of the expected radiances suggest that the $15\ \mu\text{m}$ features will be easily observed by the CVF and possibly even by a warm interferometer viewing the experiment through a narrow pass filter at 77K. Calculations were made for 330 ppm of CO_2 in air at a range of total pressures between 1 and 75 mtorr for the apparatus at room temperature and 100K. Ion pair creation rates in a 11 cm diameter field of view were estimated as $0.6\text{--}8 \times 10^{14}$ I.P./s-mtorr depending on the presence of a beam plasma discharge. From Table 4, it is seen that up to 0.9 $\text{CO}_2(\nu_2)$ molecules will be created per ion pair. Only a fraction of these will radiate in the detection system field of view. Diffusional and quenching losses were taken into account to determine a fluorescence quantum yield, which was further partitioned across the band's spectrum. This spectral radiance was then compared to the NESR values for various detection networks to establish detectability limits as a function of pressure, temperature, and energy deposition. The results of these calculations are plotted in Figure 30. The $\text{CO}_2(\nu_2)$ Q-branch has 40 percent of the total bandstrength in a $2\ \text{cm}^{-1}$ region (667 to $669\ \text{cm}^{-1}$). The expected radiance (degraded to $10\ \text{cm}^{-1}$ resolution) is plotted versus the total pressure of a mixture of 330 ppm CO_2 in air for the apparatus under cryogenic conditions (both with and without a beam plasma discharge) and for the apparatus at room temperature. The expected noise equivalent spectral radiances of various detection networks are listed along the right hand axis. For example, the CVF looking into the cold experiment is predicted to be able to detect emission at total pressures above 3 mtorr when there is no BPD, and above $1/2$ mtorr when a beam plasma discharge is occurring in the shroud. The other systems were generalized detection networks considered in Appendix C. Thus, it appears that $\text{CO}_2\ 15\ \mu\text{m}$ emission will be observed in LABCED. Alteration of the gas mixture to remove oxygen, or use of argon as the bath gas, will raise the curves accordingly, making detection even more likely. These predictions will be compared with observations in Section 3.

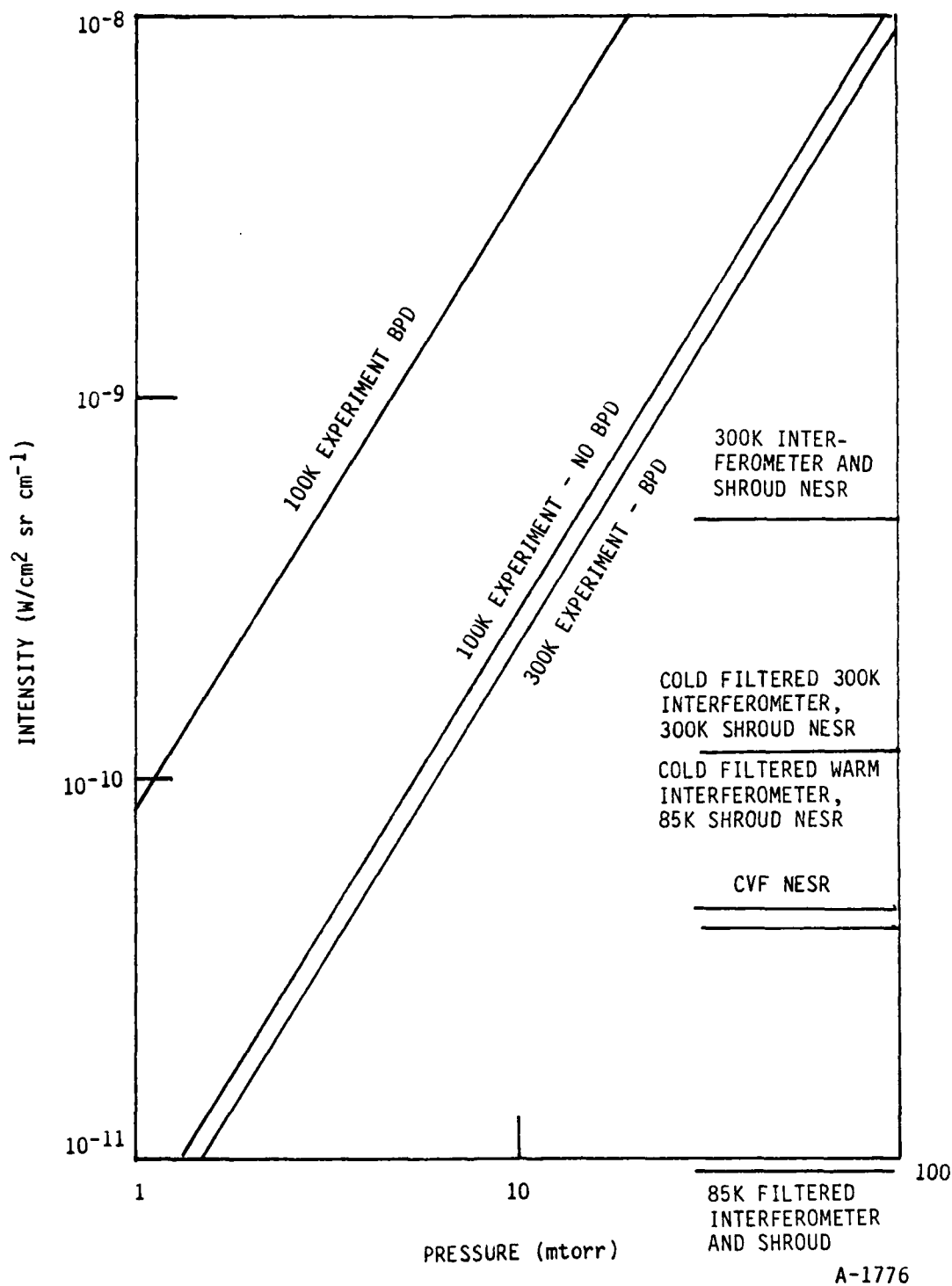


Figure 30. Estimated $\text{CO}_2(\nu_2)$ Q-branch intensities for various experimental operating conditions as compared with expected detection system noise equivalent spectral radiances (NESR). A gas mixture of 330 ppm CO_2 in N_2 is irradiated by 6 mA of 3 keV electrons should produce those intensities. Detection systems have a 1 Hz bandpass.

2.5.5 391.4 nm Scanning Photometer - In order to verify these predictions, the energy deposited by the electron beam, its spatial extent, and its position in the shroud (over the range of experimental conditions must be carefully measured. One of the major goals of the refurbishment project was to also increase and stabilize the electron beam current density.

Scattering of the electrons by the target gas causes the primary beam to grow as it traverses the tank,¹¹ and CVF or interferometer detection networks will not view a uniform source. Spatial characterization of the beam is thus necessary to relate observed fluorescent intensities to electron dosing levels within each system's field of view.

Emission from N_2^+B molecules at 391.4 nm is an accepted measure of ion pair creation rates in the irradiated gas. These excited states are formed dominantly by the high energy primary electrons (see Table 3), and therefore can be used as a probe of the local primary electron density or ion pair creation rates.

A scanning 3914 nm radiometer system was constructed to spatially resolve this N_2^+ emission, and define the electron beam profile and volumetric deposition rates as a function of pressure, applied magnetic field and gas composition. This monitoring system consists of a gimballed f/8 telescope a limiting aperture to determine spatial resolution, a narrow band pass 391.4 nm interference filter, and an x-y motor-driven scanning platform. The system was designed for maximum flexibility - the diagnostic wavelength can be shifted to any emission of interest between 0.2 and 8 μm .

The radiometer is located on the large observation port directly above and perpendicular to the beam path through the vacuum chamber. The telescope system consists of a $f = 8$ in. CaF_2 lens with a clear aperture, of 1 in. The lens is located ~24 in. from the tank centerline, yielding a f/24 collection efficiency. The demagnification ratio for imaging a portion of the beam emission to the image plane 36 in. from tank centerline is ~2:1. The telescope is mounted on two gimbals, which allow its body to tilt about the lens plane.

This is accomplished by fixing the telescope lens on the lower gimbals and allowing the body to slide through a bearing in the upper gimbal. The vertical separation between the gimbals is fixed: the lower gimbal is mounted on the window flange; and the upper gimbal mounted on a movable x-y table. Linear x-y motions of the carriage are then transformed into a tilt of the telescope, by the gimbal, which, in turn, produces a linear change in the field of view coordinates.

A universal mounting plate is provided at the image plane of the telescope to permit the mounting of an aperture (or detector) which defines the spatial resolution of the system. After the optical stop, the 391.4 nm interference filter is mounted along with either a photomultiplier tube or photodiode detector. The advantage of a tilting telescope arrangement over a fixed lens system with an image plane scanner is that with a telescope, the cone angle through the filter remains constant and therefore, the central wavelength does not shift due to angle of incident effects. These effects would be significant for the narrow bandpass filters and spatial scan ranges needed for this system.

The field of view of the radiometer is changed by translating the gimbal carriage with two low speed, high torque 12V DC motors. The motor control system has been designed to allow manual positioning, scanning, or computer controlled scanning. The diagnostic may be shifted to other wavelengths of interest simply by changing the filter/detector combination, since the telescope system will transmit from 180 nm to beyond 8 μm .

The window isolating the vacuum chamber from the radiometer is a standard 5 in. O.D. glass plate, and is perfectly adequate for the 3914Å wavelength of interest, however, other window materials can be substituted if the radiometer is used at other wavelengths.

Since a large port on the shroud is required to allow for scanning of the e-beam emission, some form of window must be used in the cryoshroud to prevent

gas loss through the aperture and to prevent room temperature background radiation from destroying the low LWIR background. This may be accomplished in two ways. The window may be constructed of a Schott glass that transmits UV/VIS visible radiation and absorbs the IR. Thus the window would have an IR emissivity of 1 at the 77K cryoshroud temperature. The second alternative is to obtain a dielectric mirror that reflects the IR and allows transmission in the visible and UV. Both are available but the Schott glass system should be less expensive and much less susceptible to thermal effects than the dielectric filters and is therefore recommended.

Two alternatives for detectors were considered. For the extremely high spatial resolution desired, we required use of a photomultiplier. For moderate resolution, a simple photo diode detector can be used, eliminating the need of a high voltage supply and a bulky housing. In addition, the telescope assembly was designed to support a 1/4m scanning spectrophotometer and, if the need arises, the filter can be removed and a monochromator substituted.

Below are listed some important specifications, calibration factors, and remaining questions concerning the LABCEDE scanning photometer. These should serve as a guide in the use and interpretation of data from the photometer.

- a. In the object plane of the photometer (at the beam), the scan range is 305 mm (12 in.) for a travel from -65 to +65 panel meter units. The calibration constant is $2.34 \text{ mm unit}^{-1}$. One panel meter unit corresponds to 10 mV from the rear panel position readout port. When fixed in a specific position, the photometer holds that position to within ± 0.1 meter unit or about 0.2 mm in either axis. When scanning the photometer, there is about a 2 unit backlash upon reversing direction; hence one should always scan in the same direction. If operated in this manner, the reproducibility of a position setting is better than ± 0.5 units or ± 5 mv.
- b. The proper orientation of the elements in the optical train which match the calibration conditions are:

1. Aperture in tray and mounted closest to lens.
2. 3914Å interference filter on top of aperture with reflective surface facing aperture and marked edge of filter on same side of tray as red mark.
3. Ground glass scatter screen, labeled #2, on top of filter with label facing down and on side of red slash.
4. Red slash on PMT housing aligned with red slash on filter tray.

The tray that holds the filters (etc.) allows little room for the filters to slip (± 0.5 mm). If smaller or thinner filters are used, an O-ring or gasket should be placed in the stack to prevent slippage during scanning. When small apertures are used only a comparably small portion of the filter and ground glass are actually illuminated. As a result, the overall responsivity of the system is very susceptible to dirt, smudges, and to local transmission properties at the point of illumination; i.e., overall transmission properties of a filter or scatter screen may not hold in this application. The system was calibrated using components that were rigorously cleaned and consistently positioned according to the above description; deviations from this arrangement could produce errors as large as 100 percent in the responsivity.

- c. The standard bias voltage chosen for the PMT is 1 kV. All quantities were measured at this bias when possible. I have measured the gain at other bias voltages relative to 1 kV for scaling purposes. They are given in Table 5. The PMT is an EMI 9956B with a maximum bias voltage of 1150V. It has an S-11 type photocathode; see the attached data sheet for spectral response curves and other data on the tube.
- d. If the beam is 24.8 in. from the lens, the proper distance of the resolution defining aperture from the top of the lens is 11.2 in.

TABLE 5. RELATIVE GAINS FOR EMI9956B PMT

Voltage	Gain
1100	1.84
1050	1.35
1000	1.00
950	0.68
900	0.46
850	0.32
800	0.21
750	0.13
700	0.081
650	0.046
550	0.014
500	7.0(-3)
450	3.2(-3)
400	1.4(-3)
350	4.9(-3)
300	1.4(-4)

The magnification ratio for the aperture, imaged at 24.8 in. from the lens, is 2.22. The proper aperture-to-lens distances and magnification ratios for other wavelengths, calculated from the refractive index of BK-7 and the lens makers formula, are given in Table 6. The actual resolution measured for various apertures is listed below:

<u>Aperture Diameter (mm)</u>	<u>Expected Resolution (mm)</u>	<u>Measured Resolution (mm)</u>
2.5	5.55	6.0 \pm 0.4
1.0	2.22	2.35 \pm 0.1
0.5	1.11	1.12 \pm 0.05

TABLE 6. APERATURE-TO-LENS DISTANCES AND MAGNIFICATION RATIOS
FOR WAVELENGTHS OTHER THAN 391.4 nm

Wavelength (nm)	BK7 Refractive Index	Focal Length (in.)	Aperture Distance (in.)	Magnification	Comments
346.1	1.529988	7.56	10.86	2.29	
350.0	1.539164	7.58	10.90	2.28	
391.4	1.532034	7.68	11.11	2.24	N(² p)
427.8	1.527524	7.74	11.24	2.21	
450.0	1.525321	7.78	11.32	2.20	N ₂ ⁺ (B-X)(0,0)
500.0	1.521415	7.83	11.43	2.18	N ₂ ⁺ (B-X)(0,1)
540.0	1.519039	7.87	11.51	2.16	
580.0	1.517121	7.90	11.58	2.15	
600.0	1.516295	7.91	11.60	2.14	N ₂ (B-A)(ΔV=5)
650.0	1.514521	7.94	11.66	2.13	N ₂ (B-A)(ΔV=4)
700.0	1.513066	7.96	11.71	2.12	
750.0	1.511839	7.98	11.75	2.12	
762.0	1.511572	7.98	11.75	2.12	
800.0	1.510780	8.00	11.79	2.11	
850.0	1.509845	8.01	11.81	2.11	O ₂ (b-x)

The quoted resolution corresponds to the baseline crossing points of the cosine function which closely approximates our spectral resolution function, which was experimentally measured using calipers opening across a uniform light source.

- e. If we have a narrow beam running parallel to the mounting plate of the photometer, the distance from the lens to the beam increases with increasing tilt of the optical train. For the worst case, this increases the lens-to-object distance by ~0.7 in. or 1.8 cm. This will degrade the resolution of the photometer by ~5 percent, but should have a negligible effect on collection efficiency due to good depth of field.

- f. The photon collection efficiency for the photometer, when positioned anywhere from +55 - 55 units in either the x or y axis, varies less than 1 percent.
- g. The photon collection efficiency of the photometer changes by less than 6.5 percent when a diffuse source is positioned anywhere between 50 and 80 cm from the lens. The focus of the system is at 63.5 cm and the deviation is ± 3.2 percent from the efficiency at this point. This is a good upper limit on the deviation and the actual figure is probably much less.
- h. The response of the detection system is not uniform across the full field of view of the system but varies in a manner which is nearly symmetric about the optical axis when ground glass is employed as a scatter screen. Uniformity of bare tube is very poor, showing asymmetries of ± 50 percent. For the full field of view of the photometer (38 ± 2 mm), the response varies by 21 percent ($\Delta R/\bar{R}$). For our largest aperture (5 mm), the field of view is restricted such that the variation in response is less than 3 percent. The average response increases by ~ 10 percent in going from full field to the restricted fields we anticipate using. Our full field absolute response determination must be corrected for this effect.
- i. Rejection of light from outside the viewing region appears to be good. Scans taken using the full field of view of the photometer looking at a small light bulb showed a sharp drop-off in intensity at the edge of the field and no increase over the dark baseline at large angles from the vertical position. This would define a lower limit on the off-axis rejection ratio of about 100:1. This rejection was achieved in part by lining walls of photometer with black paper, thus decreasing off axis background light levels.

- j. The linearity of the system response was checked using a series of calibrated neutral density filters to attenuate an Optronics Laboratories calibrated irradiance source. At a bias of 1 kV the system response was linear to within 2 percent over a range of photocurrents from 2×10^{-6} to 2×10^{-8} A.
- k. The absolute response of the detector/scatter screen combination with one window and the lens in the optical train was determined. The transmission function of the 3914Å filter was removed as part of the calibration analysis. The full field of view was employed.

Two light sources were used to do the calibration, the Optronics Laboratories quartz-halogen irradiance source and the blackbody. The quartz-halogen lamp is a more reliable source in this wavelength range. This is due to the steep dependence of the UV emission intensity on source temperature at the highest temperatures our blackbody could attain. The blackbody calibration provides a cross-check for the standard lamp calibration. The calibration constant, R_{3914} , gives the expected photocurrent per $3925 \pm 12\text{\AA}$ photon hitting the scatter screen with the transmission of the lens and spectrometer window folded in. This value, for a 1000V bias on the PMT, is $(1.02 \pm 0.21) \times 10^{-14}$ A photon $^{-1}$ s.

The quoted uncertainty in the calibration comes from a linear propagation of errors analysis. The value for R_{3914} is bounded by calibrations done using the blackbody which assume either a 1250 or 1300K source temperature. Our best estimate of the actual source temperature is 1290K. These bounds provide an extreme upper limit on the uncertainty in the calibration of about ± 40 percent.

Several issues remain before R_{3914} can be applied to determine volume emission rates:

1. The emission profile of the 3914Å band must be passed through the transmission function of the interference filter to get the transmission for the band. (This can be done using a monochromator and measuring filter in/filter out signals for wide slit settings).
 2. We must determine or estimate the transmission at 3914Å of the glass window on the shroud.
 3. We must also correct the calibration for the change in average response on going to the restricted field of view of the tube.
1. At light intensities approaching 2×10^{11} photons s^{-1} incident on the photocathode the PMT becomes very noisy. This may be evidence of the onset of saturation for the photocathode. For 1 kV bias the corresponding photocurrent would be $\sim 2.5 \times 10^6$ A.

2.5.6 Liquid He-cooled CVF - Based on the intensity predictions of Sub-section 2.5.4, it was decided that the first long wavelength measurement attempted would be the study of $CO_2(v_2)$ emission at 15 μm . Previous field measurements during the HIRIS mission²⁰ contained some evidence that there was a considerable enhancement of this feature (including increased excitation of other vibrational modes). The LWIR CVF is presently the most sensitive and thus best capable of performing this measurement. This instrument has been shipped to Utah State University for electronics modification and fabrication of a new segmented filter wheel from existing components. Due to a mix up with OCLI, the wheel was incorrectly cut and only partial coverage of the 15 μm band was available on the segmented wheel. The CVF was recalled to AFGL where it was used to successfully measure $CO_2(v_2)$ fluorescence (see Section 4). A cryogenic interferometer has been purchased to allow LABCEDE to be utilized to its full capabilities. This instrument should be able to scan slowly to permit time resolved Fourier spectroscopy, and should be external to the apparatus for ease of interfacing, cooling, and repair.

PSI interfaced the liquid helium-cooled CVF mounted outside the vacuum chamber, to the inner shroud via a vacuum tight, cryocooled optical baffle. This LWIR baffle system has been designed so that it can be used when the present CVF is replaced by a cryogenic interferometer.

The CVF is located outside the LABCEDE vacuum chamber, mounted on the vacuum chamber door on the tank center line. A cold, light tight path is required to prevent room temperature blackbody emission from entering either the CVF or the LABCEDE cryoshroud. Vacuum integrity is required to prevent cryopumping of the test gases by the LHe cooled CVF which would, at a minimum, cause a deterioration of the sensitivity of the radiometer or, at worst, cause a freezeup of the filter wheel. These design criteria are met by a triaxial baffle arrangement. The inner most baffle is made from CDA Grade 101 copper and is attached directly to the front of the CVF. In its design configuration, the baffle was ~15 in. long and extending to the inner cryoshroud of the main test chamber. This baffle is 2 in. I.D. and constructed with 1/8 in. thick walls. The heavy construction is intended to provide a temperature gradient along this baffle of less than 1K at 4K CVF temperature. The thermal load is due to radiation from an outer (77K) cryobaffle. This inner baffle is constructed from copper (instead of aluminum which is much lighter) for reasons of thermal conductivity. At 77K, CDA 101 copper has approximately the same thermal conductivity as aluminum by weight, but below this temperature, copper is a substantially better conductor. This baffle also prevents scatter radiation from entering the CVF, even though the field of view of the CVF is less than 2 in. in diameter at the LABCEDE cryoshroud. In the actual installation this baffle was shortened to ~7 in. with no detrimental results.

To minimize the heat load on the 4K CVF baffle, a second 77K copper baffle extends out from the LABCEDE cryoshroud towards the CVF. An adaptor flange of aluminum mates the 77K baffle to the LABCEDE cryoshroud end plate. A KRS-5 window is located between the adaptor flange and the baffle tube, to maintain separation between the LABCEDE and radiometric vacuum systems. Either a 2 or 3 in. window can be accommodated, and will withstand a 1 atm pressure differential in either direction. Silicon O-rings are used to make

the seal. The adaptor flange has eight small gas injection ports to allow the injection of a noncondensing purge gas over the inner surface of the window to prevent condensation of test gases such as CO_2 on the window surface. The 77K baffle is constructed of 2-1/2 in. I.D. CDA grade 101 copper tubing with 1/4 in. walls. Copper is used here to allow for leak tight soldering of the tubing to the mounting flange. The wall thickness is required to maintain a 20K temperature differential from the shroud to the end of the baffle. The thermal load arises from room temperature radiation and conduction from the outer stainless vacuum baffle. The second copper baffle is ~16 in. long and is made in two pieces to allow the tank door to be opened without removing the baffle.

The outer vacuum baffle connects the outer vacuum chamber to the cryo-baffle, and isolates the two vacuum chambers. This baffle is constructed of stainless steel to minimize the thermal conduction from the vacuum vessel to the 77K baffle. Multilayer insulation was used to cover the exposed helium dewar face and baffle to the greatest extent possible. This further reduced thermal loads and resulted in >2 hr liquid helium hold times during routine operation.

Installation of the baffle system has proven to be very simple. The tank door is opened and the 77K baffle, with window and adaptor flanges attached, is simply bolted on to the inner LABCEDE cryoshroud. The tank door is closed, and the stainless steel vacuum baffle slides over the protruding copper baffle. The vacuum seal on the cold end of the stainless steel baffle is a silicon O-ring. This seal must be free to move, since the shroud contracts approximately 1 in. in cooling. Once the vacuum baffle is installed, an aluminum flange is mounted over the port to complete the vacuum isolation of LABCEDE chamber and the system can be evacuated. When the CVF is used, the inner baffle is attached to the CVF and the radiometer bolted to the window flange, evacuated and cooled. Helium leak checks of the system confirmed the vacuum integrity of the baffle system.

The limited resolution of the CVF, hampers detailed molecular emission and excited state kinetic investigations. Consequently, a cryogenic interferometer is expected to be available for future experiments. The baffling system can be used without major modification. The only changes required will be a new adaptor plate to couple the interferometer to the vacuum chamber and the fabrication of a LHe baffle extending from the interferometer.

Preliminary experiments using the system are very promising. The baffle system appears to be successful in maintaining the low LWIR background of the reconstructed LABCEDE apparatus. However, a CVF system calibration was required to quantitatively assess background radiances. Molecular emission from CO₂ at 15 μm and from O₃ at 9.6 μm were observed. These observations will be described more fully in Section 3.

2.5.7 Cryogenic LABCEDE IR Optical Environment - Measurements of radiative intensities of the background environment inside the LABCEDE chamber were performed using the HS-1B model CVF available after refurbishment at Utah State University. The CVF was carefully calibrated at the AFGL Calibration Facility by Blumberg, Wolnik, Condrón, and Austin to determine transmission wavelength as a function of filter position and voltage response as a function of incident radiance level. Both resolution and shape of the field of view changed substantially between and within mask segments. These quantities were also accurately determined.

The spectral radiance, L_{λ} (in W/cm² sr μm), is related to the voltage level generated by the arsenic-doped silicon detector by the formula

$$L_{\lambda} = C_{\lambda} f(v) \quad (31)$$

where C_{λ} , the spectral response function for the CVF used in our studies is plotted in Figure 31, and $f(v)$ is the term which corrects for the non-linear response to intensity. For the signal levels we observe, $f(v)$ is $3.261 \times 10^{-2} v^{0.9816}$ when the signal voltage generated is between 0.01 and 0.245V, and $f(v) = 4.245 \times 10^{-2} v^{1.169}$ when output is between 0.245 and 0.93V.

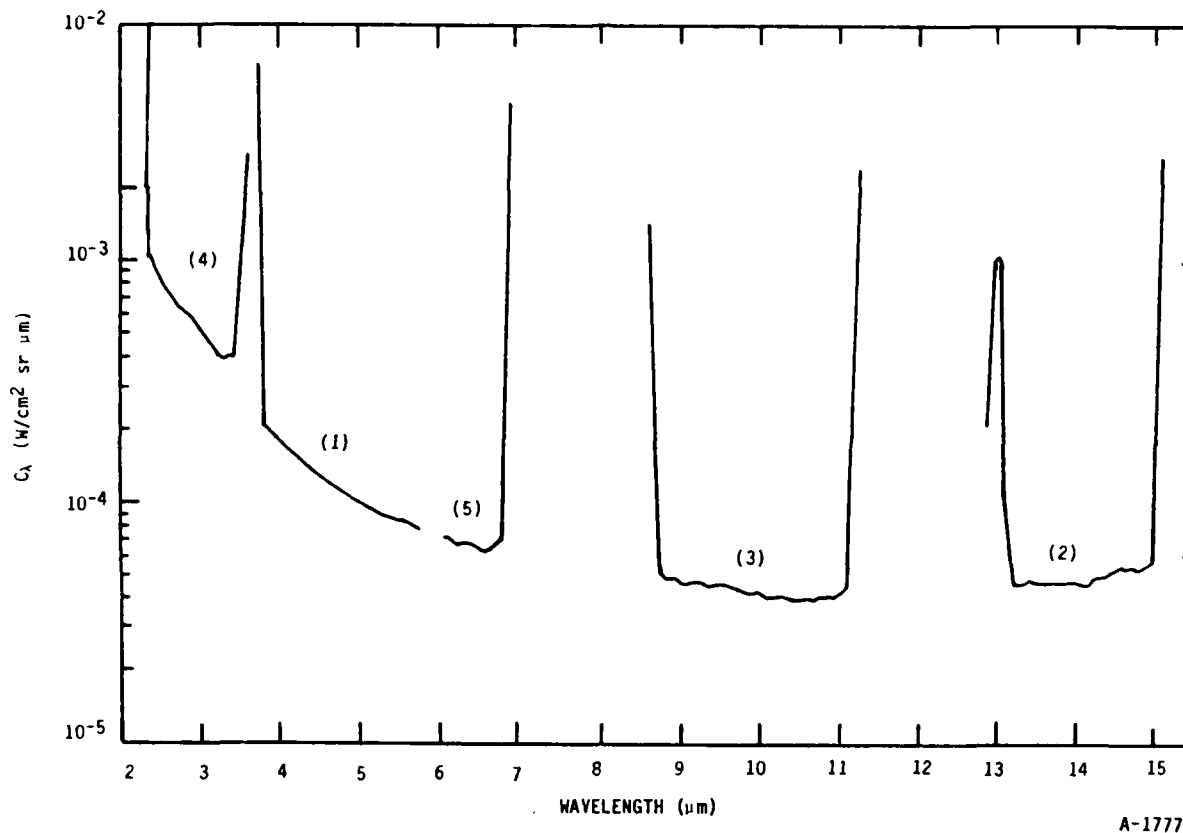


Figure 31. Spectral response function for CVF HS-1B.

We conducted a series of runs using the CVF to determine the ultimate radiative background levels which can be achieved at every wavelength and to relate these observations to the thermocouple temperature measurements. We also investigated the effects of CVF cooling time and shroud cooling time on the background levels and looked for effects of glow from the electron beam filament and beam heating of the walls. The general conclusions reached are:

- a. The filter wheel is the slowest cooling part of the optical system requiring 3 hr after the CVF dewar is filled with liquid helium to cool sufficiently to allow the detector to come out of saturation. Thus the CVF dewar should be kept at liquid nitrogen temperatures overnight and filled with liquid helium as early as possible. By late afternoon (after 5 hr of cooling), the filter wheel has cooled sufficiently that it does not dominate background levels.

- b. The shroud cools relatively rapidly in 1-1/2 to 2 hr; however, the sled assembly cools somewhat more slowly due to radiative loading from the valve area taxing its conductional cooling capacity. The sled, which fills the CVF field of view, is the prime factor in the radiative environment in LABCEDE and its ultimate temperature determines LWIR background levels. The sled asymptotically approaches its equilibrium value and is still slowly cooling by mid-afternoon. Thus the shroud should also be cooled as early as possible to maximize experimental time.
- c. The CVF dewar hold time for liquid helium is 1-3/4 to 3 hr depending on thermal loads and quality of fill. The signal levels increase at the end of a fill as the dewar is warming. However, as long as dewar has not warmed substantially before it is re-cooled, the signal levels return to their equilibrium values in only a few minutes after liquid helium transfer.
- d. Several sets were taken in rapid succession to look for effects of filament glow (beam port valve open and closed), and electron beam heating of the shroud walls. No changes were observed.

A typical spectrum acquired to investigate background signal levels is shown in Figure 32. This spectrum was taken on 9 June 1983; run L at 5:16 p.m. The experiment had been cooling since 8:08 a.m. and had reached an equilibrium temperature of 85 to 90K as monitored by the thermocouples. All ports into the shroud were blanked off with Al flanges except for the beam entrance aperture and CVF observation port. For this data the electron gun filament was hot and a beam of 19.6 mA of 5.9 keV electrons was entering the shroud. It was 1-3/4 hr since the last transfer of liquid He into the CVF, so that the dewar was warming very slowly. Another transfer of liquid He would not be required for another hour after the run. The data of Figure 32 is quite interesting. The large spike at 9 μ m is an artifact of the filter wheel masking. It is believed that the mask at the end of a filter segment moved so as to transmit the LWIR emission (at all wavelengths) from the experiment.

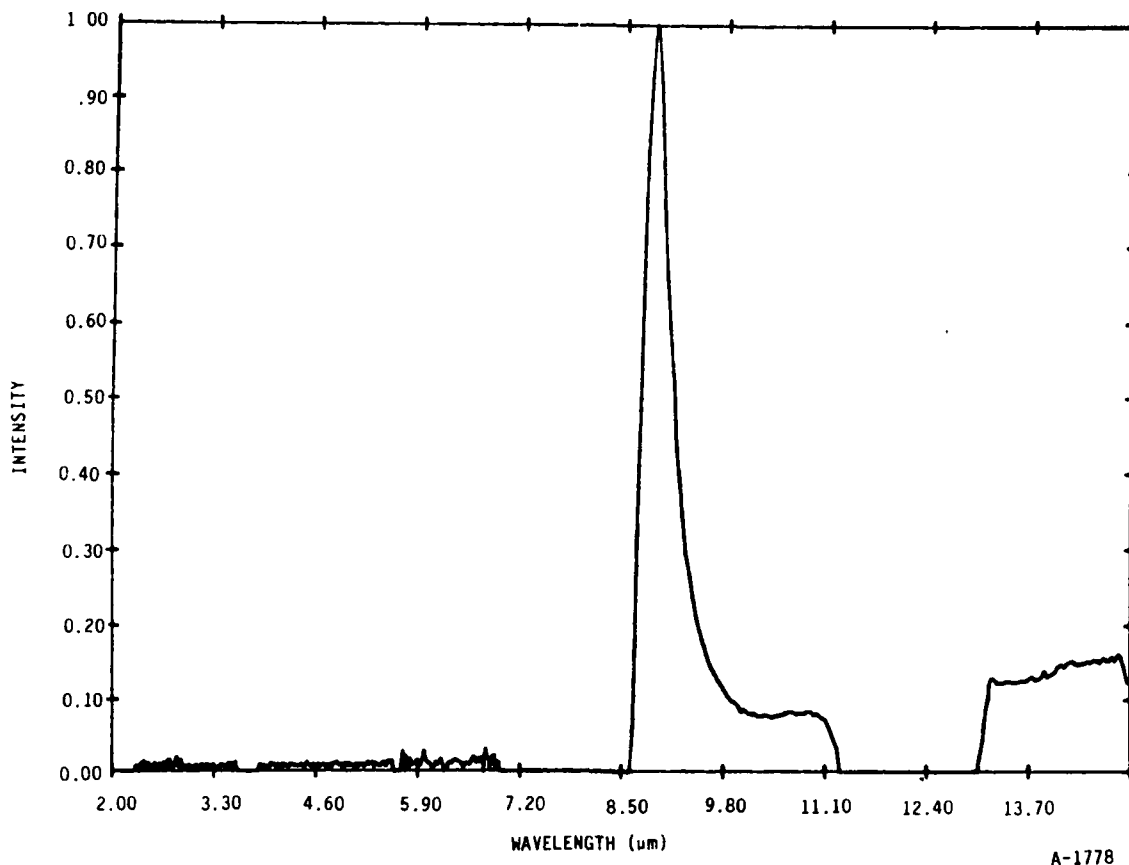


Figure 32. DC background signal levels in cryogenic LABCEDE as acquired by CVF. Maximum intensity is 0.89V (see text for details).

The rest of the scan is smoothly varying. Figures 33 and 34 show expanded segments of this same scan showing the MWIR and 13 to 15 μm segments in greater detail. Clearly noise dominates the MWIR spectral region in Figure 33. The LWIR region by contrast exhibits a smooth plateau with intensities falling off to shorter wavelengths as would be expected for a $\sim 100\text{K}$ blackbody. The signal level voltages of Figures 32 through 34 are converted into radiances using Eq. (31) and C_λ from Figure 31. The resulting radiances, L_λ , are plotted versus wavelength in Figure 35. The data between 8.5 and 10.5 μm has been excluded. The detected radiance levels are within a factor of 3 of $10^{-7} \text{ W/cm}^2 \text{ sr } \mu\text{m}$ between 2 and 15 μm . The failure to observe any changes in background levels due to filament glow or beam heating implies that those radiances would be below the $10^{-8} \text{ W/cm}^2 \text{ sr } \mu\text{m}$ level. Generally, the radiances decrease to shorter wavelengths as would be expected, until they fall into the noise at 6 μm . The rise in the SWIR is due to the rise in C_λ . The shape and magnitudes of L_λ can be attributed to three separate sources.

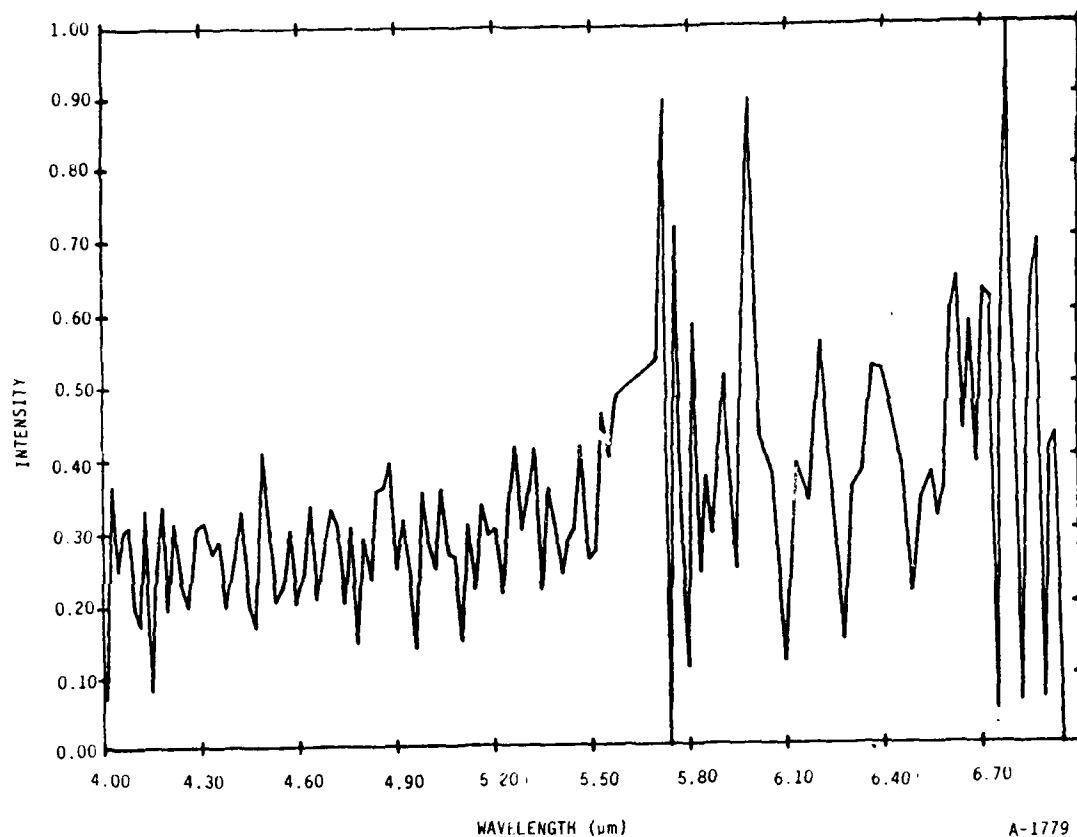


Figure 33. MWIR segment of data of Figure 32. Noise dominates spectrum. Maximum intensity is 0.0273V.

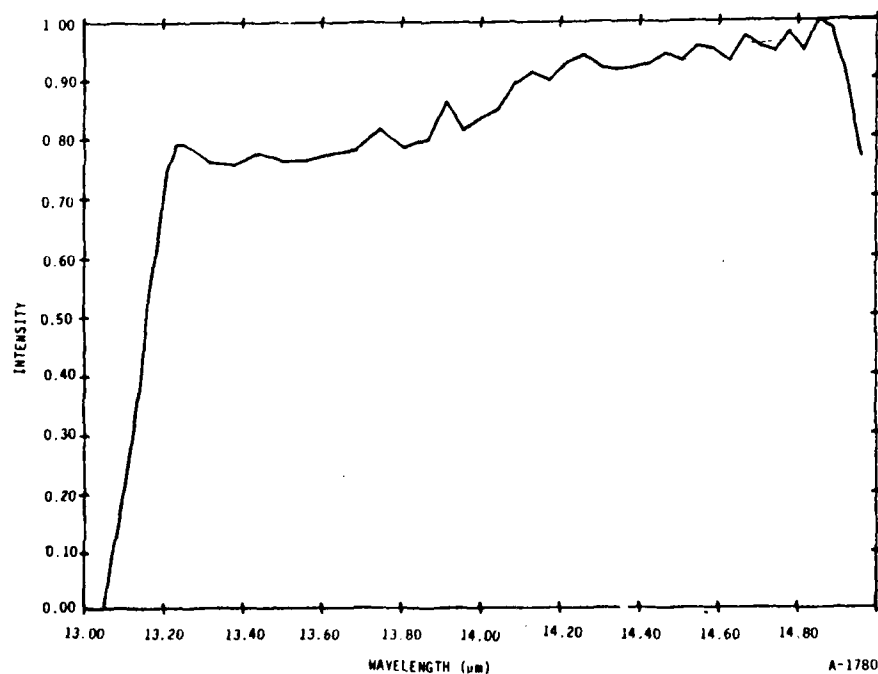
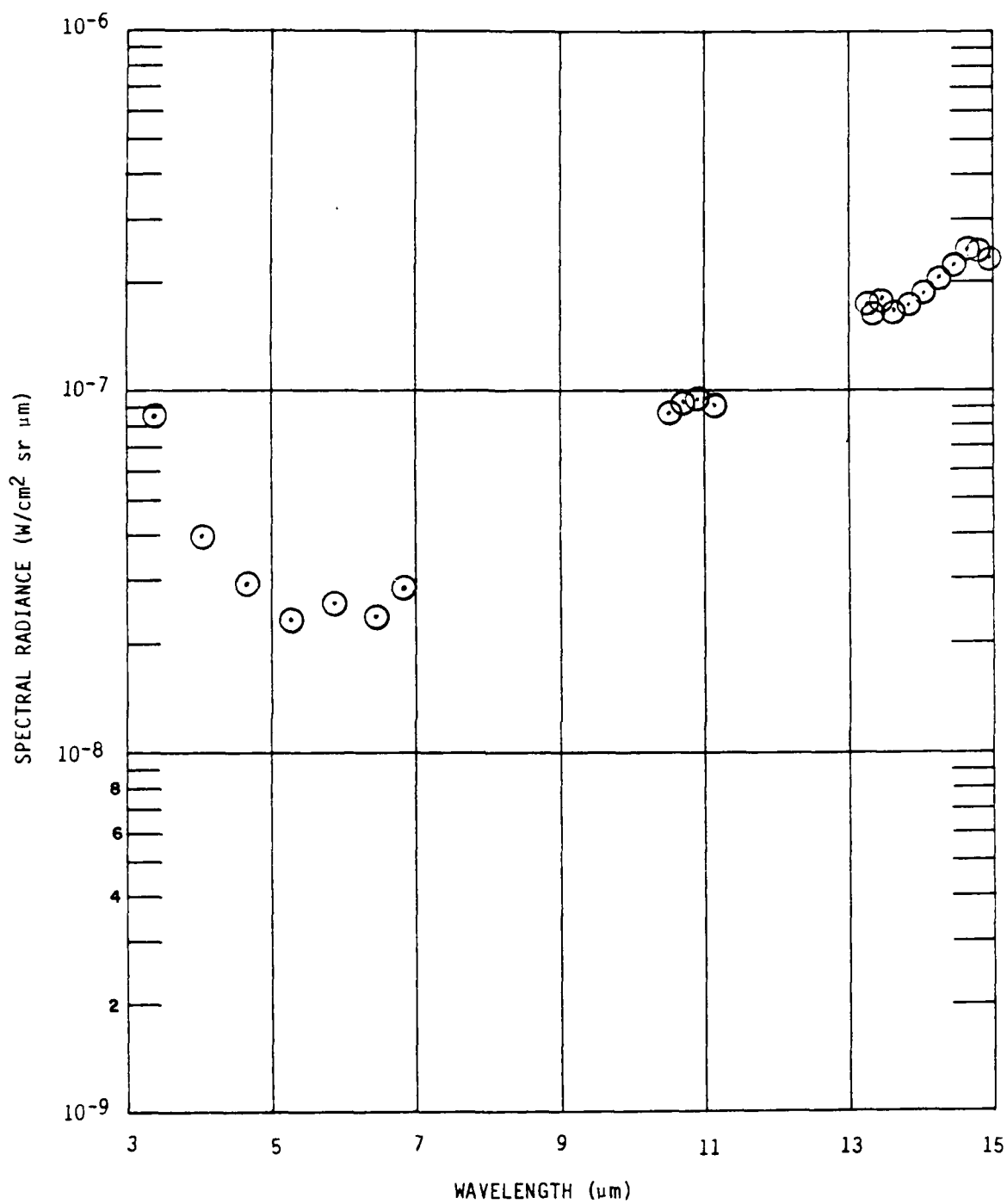


Figure 34. LWIR portion of 9 June 1983 data of Figure 32. In this region signal level is real and decreases to shorter wavelengths as expected for cryogenic blackbody emission. Maximum intensity is 0.143V.



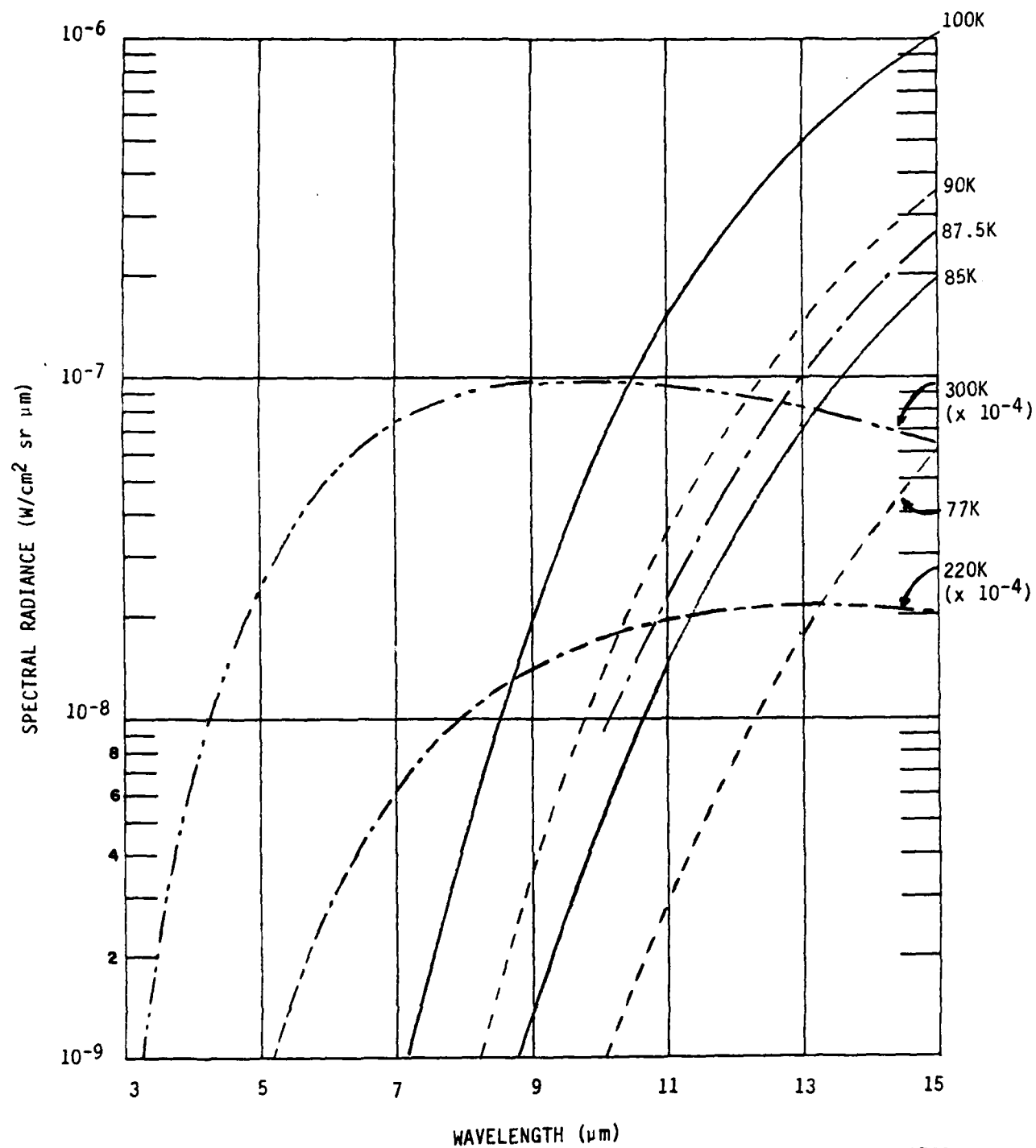
A-1781

Figure 35. Radiances at a number of discrete wavelengths as calculated from data of Figure 32.

The LWIR portion appears to be dominated by blackbody emission at 85K. The radiances of blackbodies as a function of wavelength for a range of temperatures are given in Figure 36. By comparison of Figures 35 and 36, it can be seen that between 13 and 15 μm , the observed radiances correspond to blackbody emission of 88 to 90K both in terms of shape and intensity. We believe this to be the emission from the radiation baffle ("sled") which fills the CVF field of view at the opposite end of the shroud. The radiation baffle temperature was monitored using thermocouples to be 85 and 90K in good agreement with the observed optical temperature. The optical temperature determination is not very sensitive to emissivity of the surface. As can be seen from Figure 36, radiance at 15 μm varies strongly with temperature. Thus neglecting other contributions (see below), the sled appears to asymptotically approach 87K assuming unit emissivity. If its emissivity were 0.9 (quoted emissivity is 0.92), the asymptotic optical temperature would be 88K.

By observing the LWIR emission in several sets of data we observed a small drop in the LWIR emission corresponding to a 2K decrease between 7 and 9 hr of shroud cooling. (This change was attributed to an increased liquid nitrogen coolant flow to the shroud and correlates perfectly with observed temperature change profiles at the rear of the shroud.) During that 2-hr period, there were no detectable radiance fluctuations only the smooth trend downward. Earlier in the day when the LWIR optical "temperature" was 100K, the experiment cooled at the 7 min/deg K rate. When liquid nitrogen flow was suspended, the optical "temperature" rose quickly with little temporal lag - a continuous cooling supply is essential. Thus we have achieved one of the major design goals. The LWIR radiative environment is stable over hours, is dominated by the shroud cold wall emission (not reflection, etc.) and is clearly below the emission levels of a 90K blackbody.

At the shortest wavelengths the voltage signal is a constant independent of wavelength (see Figure 32). Sources of noise include detector/amplifier noise, noise pickup in the cable, and digitizing errors, and slow offset drifts. Pick-up noise and digitizing errors are typically at the 2 mV level. Offset drifts can be even larger. The observed DC offset in this spectrum is



A-1782

Figure 36. Blackbody radiances versus wavelength for several temperatures of interest.

about 5 mV and noise about this offset is 3 mV peak-peak. In order to quantify the effects of a constant offset across the spectrum, the signal level (millivolts) at $2.5 \mu\text{m}$ was assumed to contain no blackbody contributions (see Figure 36) and be purely offset errors. This value of voltage was used to generate radiances across the spectrum as plotted in Figure 37. The observed radiances are replotted on this figure also. The rise at short wavelengths mimics the rise in C_λ , and follows the observed L_λ values in the SWIR as expected.

Between 5 and $11 \mu\text{m}$ the observed radiances fall well above the offset and 85K blackbody curves. An acceptable fit to the data is obtained by including a contribution from a $220\text{K} \pm 20\text{K}$ blackbody radiant source (see Figure 36) with only a small emissivity, i.e., a source at this temperature filling 0.04 percent of the field of view. In reality, it is far too simplistic to ascribe a single temperature to this contribution since it is the sum of emissions from various light leaks, from warm surfaces near the valve reflected by the radiation baffle, from window reflections of warm surfaces near the CVF, and from window emissions. The important conclusion, however, is that across the 5 to $11 \mu\text{m}$ range the background levels are reduced by more than four orders of magnitude below a 300K source. Moreover, the fact that we observe no effects due to filament glow or electron beam into vacuum indicates that scattering inside the shroud into the field of view is small, and that changes in these sources (filament temperature variation and pulsing the beam) will not dominate backgrounds.

A curve representing the sum of the three sources (offset, a 85K blackbody, $\epsilon = 1$, and a 220K blackbody, $\epsilon = 0.0004$) is plotted in Figure 37 also. The agreement with the observed radiances is quite good, and the fit is fairly unique. Note that the inclusion of 220K emission required the source of 13 to $15 \mu\text{m}$ emission to be reduced to 85K (if emissivity = 1). This is still within the temperature range monitored by the thermocouples.

Thus, although LABCEDE's optical environment cannot be described by a single "temperature" in the infrared, the far LWIR environment appears to be

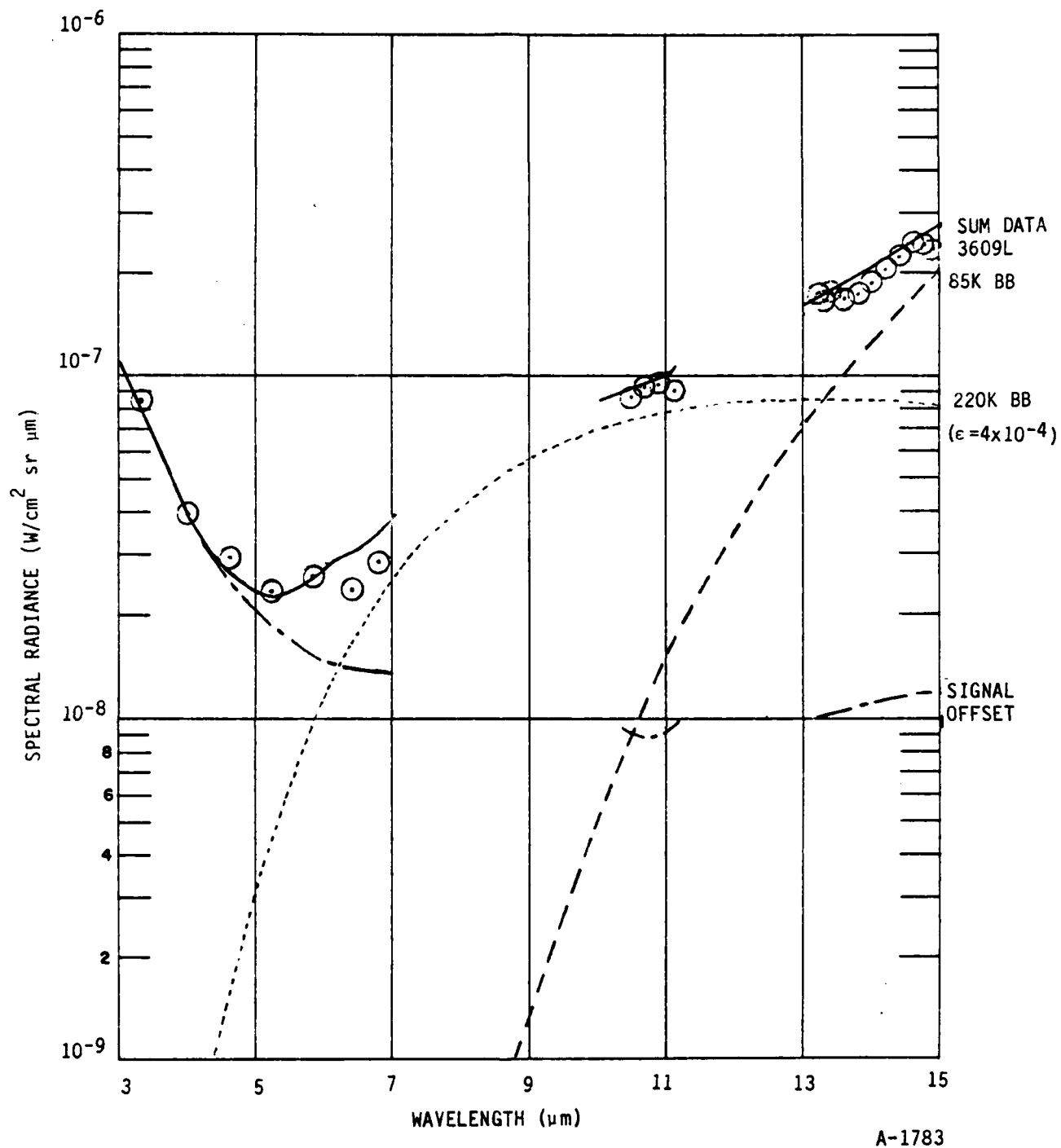


Figure 37. Contributions from three sources to observed radiances: offset level, 85K blackbody emissivity of 1, 220K blackbody emissivity of 4×10^{-4} . Sum of processes agree well with observed values.

equal in temperature to the walls, and the overall background reduction across the MWIR-LWIR is 10^4 below a room temperature device. The offset at short wavelengths is an artifact of DC operation and should be removed in pulsed studies.

Studies of molecular fluorescence will be conducted using a pulsed source and phase sensitive or time resolved detection. This should allow a considerable additional gain in sensitivity/detectability threshold. Very preliminary observations of residual background radiances or noise levels in this pulsed mode indicate that radiances are reduced to the 10^{-10} W/cm² sr μ m across the 2 to 15 μ m region. (This corresponds to another 100-1000-fold gain in sensitivity.) These preliminary estimates will be more carefully defined as techniques are refined in future experiments. The infrared fluorescence levels detected will be given in Section 4, but for this detection network geometry, and for an allowed LWIR transition, this residual background or noise level in a pulsed mode corresponds to the radiance levels of $\sim 10^8$ emitters in the CVF field of view.

3. VISIBLE MEASUREMENTS

3.1 Introduction

In this section we show how UV/visible spectroscopic studies of electron irradiated air and N_2 in the large low pressure LABCEDE Facility demonstrate its effectiveness in simulating the non-equilibrium upper atmosphere. Preliminary laboratory spectra compare well with auroral data and with spectra from the EXCEDE flight. Additionally, the laboratory data can characterize the performance of the refurbished LABCEDE facility. The spectra appear free of spurious radiators, beam intensity is stable, and the effects of electron density variations can be studied using an external, uniform magnetic field. Consequently, LABCEDE is becoming an accurate, efficient tool for interpreting field data: isolating radiating species and important kinetic processes. These are necessary inputs for the accurate extrapolation of field measurements to nuclear environments. Survey spectra were taken first to establish the identity of the major emitting species in the apparatus, and then measurements on the variations in the intensity of isolated spectral features as a function of operating parameters (composition, pressure, current, magnetic field), determine the radiating species' characteristics in more detail.

The next subsection describes the detection system for these experiments. In Subsection 3.3 we show preliminary emission spectra of both air and pure nitrogen between 185 and 900 nm and compare them to field observations. In Subsection 3.4 we present observations of the variations in intensity of the $N_2^+(B^2\Sigma_u^+, v'=0 - X^2\Sigma_g^+, v''=0)$ and $N_2(C^3\Pi_u, v'=0 - B^3\Pi_g, v''=2)$ bands at 391.4 and 380.4 nm, respectively, as functions of pressure, electron-beam voltage and current, and magnetic field strength. A summary is given in Subsection 3.5. This work is ongoing, and is rapidly progressing from qualitative to quantitative.

3.2 Experimental

The fluorescence is observed through one of two observation ports containing BaF_2 windows. One port views the excitation region from the upstream

end of the tank, normal to the electron beam, and about 1.2m from it. The other observation port sits at an angle of about 19 deg from the intersection of the electron beam with the longitudinal axis of the tank and about 0.7m from this junction. (Experimental observation ports were described more fully in Subsection 2.5.1.) A 0.3m monochromator (McPherson 218) equipped with a 1200 groove/mm grating blazed at 500 nm disperses the radiation in studies between 320 and 900 nm, while studies between 180 and 320 nm employ a 2400 g/mm grating blazed at 300 nm. An HTV R955 photomultiplier operated at a gain of 5×10^6 detects the photons, and a picoameter/recorder combination amplifies and displays the photomultiplier output.

The visible survey spectra and variations in 391.4 and 380.4 nm intensities with operating parameters were made with the monochromator butted up to the window at the end of the tank. In these studies, the field of view was a square approximately 20×20 cm. The UV spectra and the Meinel-quenching studies used a 5 cm diameter, 10 cm focal length lens to collect the fluorescence and focus it upon the entrance slit of the monochromator. In these latter studies, the image of the monochromator slit at the excitation region determined the detector's field of view. This image is about 10×0.1 cm for viewing from the end of the tank, and 7×0.07 cm for viewing from the side port. The field of view of the detector, therefore, was a rectangular slice through the electron beam whose height is larger than the diameter of the beam but whose width is narrow compared to the length of the irradiated volume. Because the mean molecular velocity of nitrogen at 300K is 4.8×10^4 cm s⁻¹, the N₂⁺(A) molecules can travel no more than 5 mm during the molecule's effective lifetime (≈ 10 μ s).^{21,22} This distance is too short to allow significant diffusive losses out of the field of view in its long dimension. Diffusion out of the field of view along the axis of the irradiated volume is balanced by diffusion into the field of view along the e-beam axis from species excited outside the monochromator field of view.

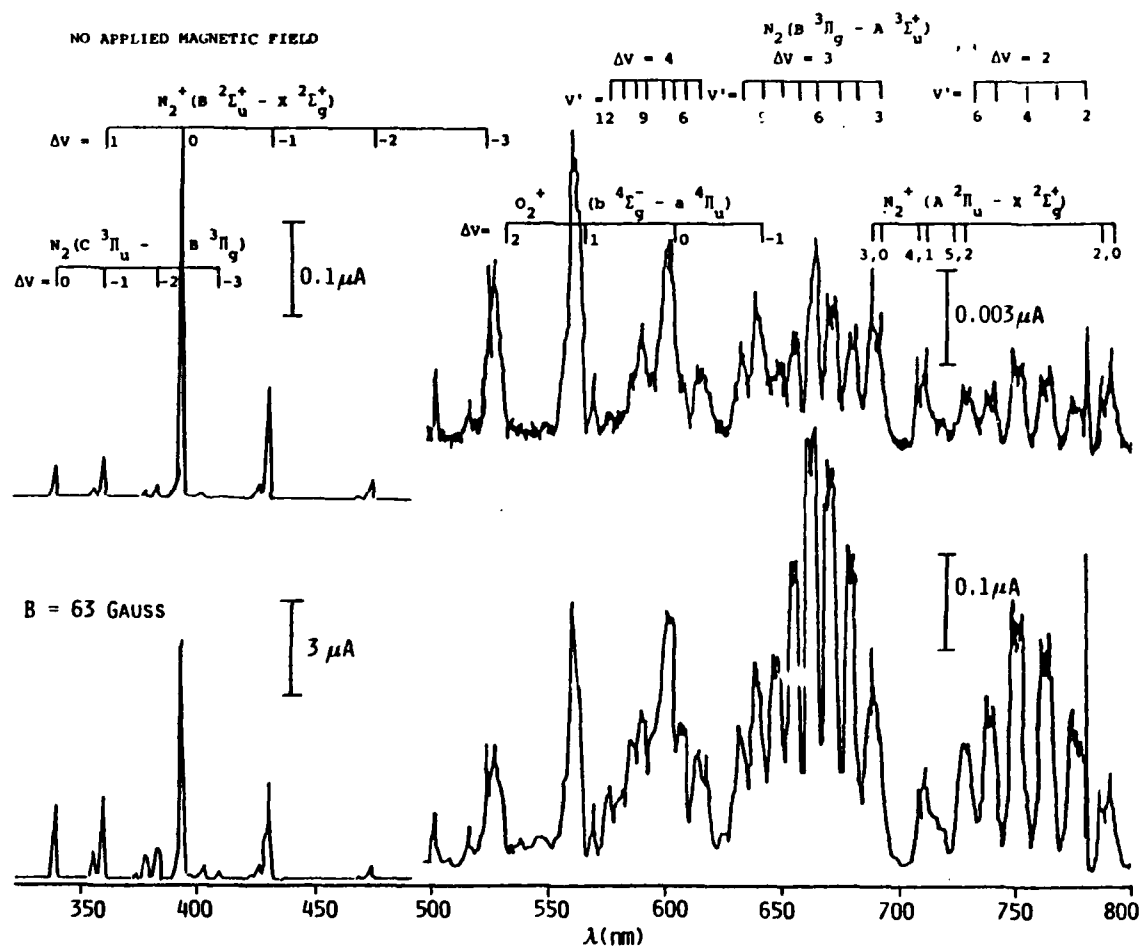
A Corning 3-71 colored glass filter rejects second-order spectra for measurements made to the red of 500 nm. Because the second order of the very

strong nitrogen first-negative band at 391 nm ($N_2^+ B^2\Sigma_u^+, v' = 0 - X^2\Sigma_g, v'' = 0$) coincides with the Meinel 2,0 band at 782 nm, we checked the rejection ratio of this filter in the second order by scanning several strong uv mercury lines emitted from a pen lamp to ensure that second-order leakage did not contaminate Meinel-band intensity measurements. The rejection ratio was about 10^{-6} compared to a ratio of the intensities of the Meinel 2,0 band to the first order 391 nm band of $\sim 5 \times 10^{-3}$.

Most of the Meinel bands are overlapped with nitrogen first-positive ($N_2 B^3\Pi_g - A^3\Sigma_u^+$) emissions. The Meinel (2,0), (3,1), and (4,2) bands are relatively free from this overlap at low pressures where the Meinel band excitation is stronger relative to that of the first-positive bands than is the case at higher pressures. This difference in apparent excitation efficiencies results both from the efficiency with which the Meinel bands are quenched at higher pressures and from the fact that secondary electrons excite the first-positive bands more efficiently than do primary electrons. For the Meinel bands the reverse is true. The flux density of secondaries in the reactor chamber increases with pressure. Thus, to avoid interference from first-positive emission, we used a narrow bandpass (0.26 nm) and limited our measurements to pressures below 20 mtorr. We also set our spectrometer wavelengths to regions between potentially interfering first-positive transitions. Over the pressure region investigated, we could not detect any evidence of interference from the first-positive bands. At much higher pressures, however, pressures reaching 100 mtorr, the first-positive bands did begin to overlap some of the Meinel bands we studied.

3.3 Spectral Surveys and their Comparison with Field Observations

3.3.1 Visible Results - Figure 38 shows the spectrum excited in 2 mtorr of air between 320 and 800 nm with and without the presence of a magnetic field. The field both focusses the electron beam (increasing current density) and contains the scattered secondary electrons near the beam axis. Most of the observed emission features are molecular band systems, the principle ones



A-1784

Figure 38. Visible spectrum of 2 mtorr of air irradiated by 8 mA of 3 keV electrons for two values of magnetic field. Note that intensities in presence of applied field are ~30 times upper values. Additionally, neutral species transitions are enhanced relative to ionic bands.

being the nitrogen first-positive, $N_2(B^3\Pi_g - A^3\Sigma_u^+)$, second positive, $N_2(C^3\Pi_u - B^3\Pi_g)$, first-negative, $N_2^+(B^2\Sigma_u^+ - X^2\Sigma_g^+)$, and Meinel, $N_2^+(A^2\Pi_u - X^2\Sigma_g^+)$, and the oxygen first-negative, $O_2^+(b^4\Sigma_g^- - a^4\Pi_u)$, systems. Higher resolution scans also show a number of emission lines from neutral and ionic nitrogen and oxygen atoms. Under these conditions, species which are excited predominantly by primary electrons, such as $N_2^+(B^2\Sigma_u^+)$ are enhanced by about a factor of 20 in the presence of the magnetic field. Species such as $N_2(B^3\Pi_g)$ and $N_2(C^3\Pi_u)$, for which a major fraction of the excitation results from interactions with secondary electrons, are enhanced by two orders of magnitude in turning on the magnetic field. The magnetic-field enhancement is pressure dependent, being stronger at lower pressures. In addition the ratio of the enhancement for species excited mainly by secondary electrons to that for primary-electron excitation changes with pressure. For example, nitrogen second-positive emissions are enhanced about a factor of four more than nitrogen first-negative emissions when the magnetic field is turned on at 2 mtorr, but both the second-positive and first-negative emissions are enhanced about the same amount when the magnetic field is turned on at 40 mtorr, about a factor of five enhancement for both. Thus one can vary the relative intensities of the various band systems by varying pressure and magnetic field. Subsection 3.4 discusses these points in more detail. The expected excitation efficiencies and fraction due to primary electron scattering are given in Table 3 for the case of no applied magnetic field.

A comparison of the spectra in Figure 38 with published auroral spectra²³ reveals that all allowed emissions which are observed in aurorae are present in the LABCEDE spectra. In the 500 to 900 nm region, with the magnetic field off, the oxygen first-negative, and nitrogen Meinel bands, and the atomic lines are excited more strongly relative to the nitrogen first-positive bands than is the case for Gattinger and Vallance Jones' auroral spectrum.²³ With the magnetic field on, on the other hand, excitation of the first-positive bands in LABCEDE is stronger than the other bands as compared to the auroral case. Proper adjustment of pressure and magnetic field in LABCEDE should bring the laboratory and field spectra into fairly close congruence.

The short residence time in LABCEDE precludes the observation of the important forbidden auroral emissions. Some of these, such as the auroral green line, O I ($^1S - ^1D$, $\lambda = 557.7$ nm), and the atmospheric oxygen bands, $O_2(b^1\Sigma_g^+ - x^3\Sigma_g^-)$, are readily observable in the higher pressure, small LABCEDE system.²⁴ We plan to search for some of these emissions in future studies after modifying the system to allow higher pressure operation.

3.3.2 Ultraviolet Results - Figures 39 and 40 show LABCEDE spectra in the ultraviolet for 1 mtorr air and nitrogen, respectively, as contrasted with a spectrum from EXCEDE shown in Figure 41. All are taken with 0.8 nm resolution. Both LABCEDE spectra match the EXCEDE spectrum fairly well, although the nitrogen spectrum gives a better match to the relative band intensities (except in the region between 280 and 290 nm). We have sufficient signal intensity to rescan the spectrum at higher resolution, and with varying gas mixtures. Consequently, spectral assignment is easier and more definite. Figure 42 shows the LABCEDE air spectrum with 0.2 nm resolution. We have recorded some sections of the spectrum with 0.05 nm resolution.

Molecular nitrogen bands are the major ultraviolet emissions: Lyman-Birge-Hopfield (LBH) $N_2(a^1\Pi_g - x^1\Sigma_g^+)$; Herman-Kaplan, $N_2(E^3\Sigma_g^+ - A^3\Sigma_u^+)$; fourth-positive, $N_2(D^3\Sigma_u^+ - B^2\Pi_g)$; and second-positive, $N_2(C^3\Pi_u - B^3\Pi_g)$. In addition, the NO γ -bands ($A^2\Sigma^+ - X^2\Pi$) appear weakly in the LABCEDE air spectrum. At higher air pressures and longer residence times, the γ -bands become quite strong, thus showing that secondary chemical reactions form the NO in LABCEDE. The nitric oxide emissions are completely absent in higher resolution nitrogen scans in LABCEDE, even at the higher pressures and longer residence times, demonstrating gas handling system purity. The LABCEDE nitrogen spectral intensities more closely resemble the EXCEDE data than LABCEDE air spectra at the locations of strong NO γ -bands (e.g., 226.5, 236.5, 247.5, and 259 nm). We interpret this as evidence that NO γ -band emission is absent in the EXCEDE measurements. This is not surprising as it would require the chemical reaction of a beam-created species to form NO while still in the irradiated volume so that subsequent electron excitation to NO(A) could occur.

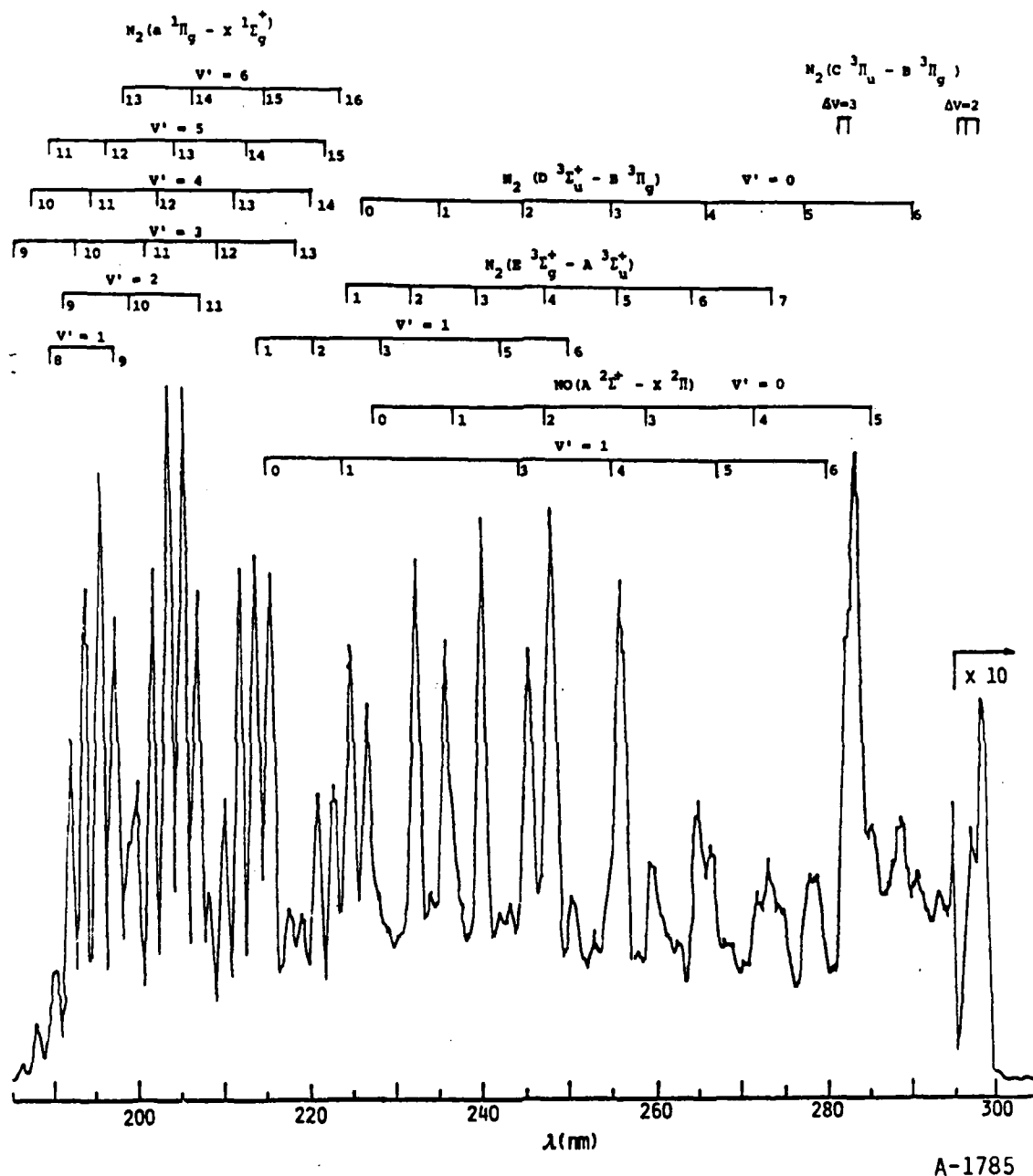


Figure 39. LABCEDE UV spectrum of 1 mtorr air irradiated by 15 mA of 6 keV electrons, with an applied magnetic field of 26 Gauss. Resolution of data is 0.8 nm. Numbers under brackets are transition lower-state vibrational quantum numbers.

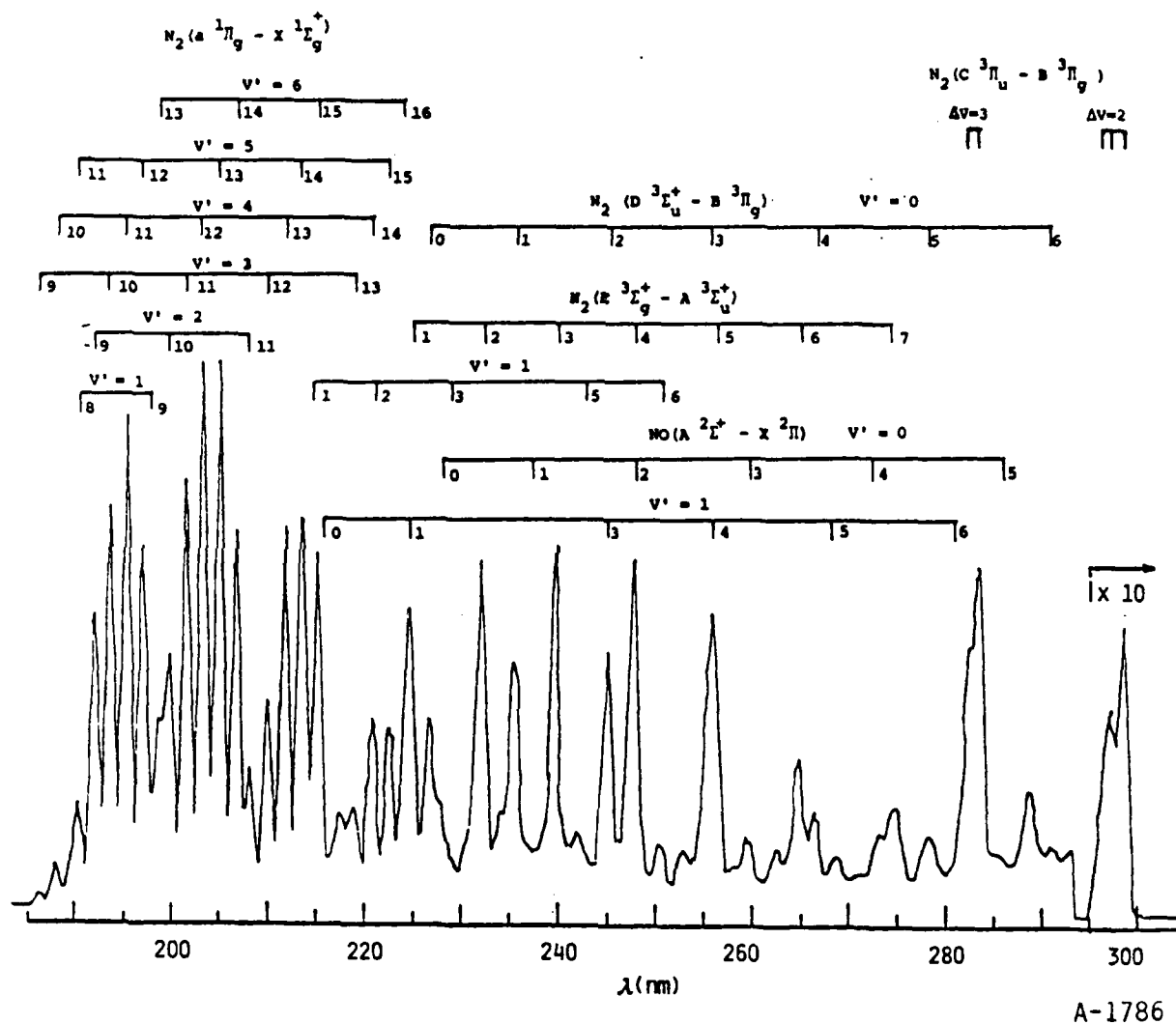


Figure 40. LABCEDE UV spectrum of 1 mtorr nitrogen irradiated under the same conditions as Figure 39. Comparison with Figure 39 reveals most features in air spectrum as attributable to molecular nitrogen. The NO (A-X) bands are not present in this spectrum.

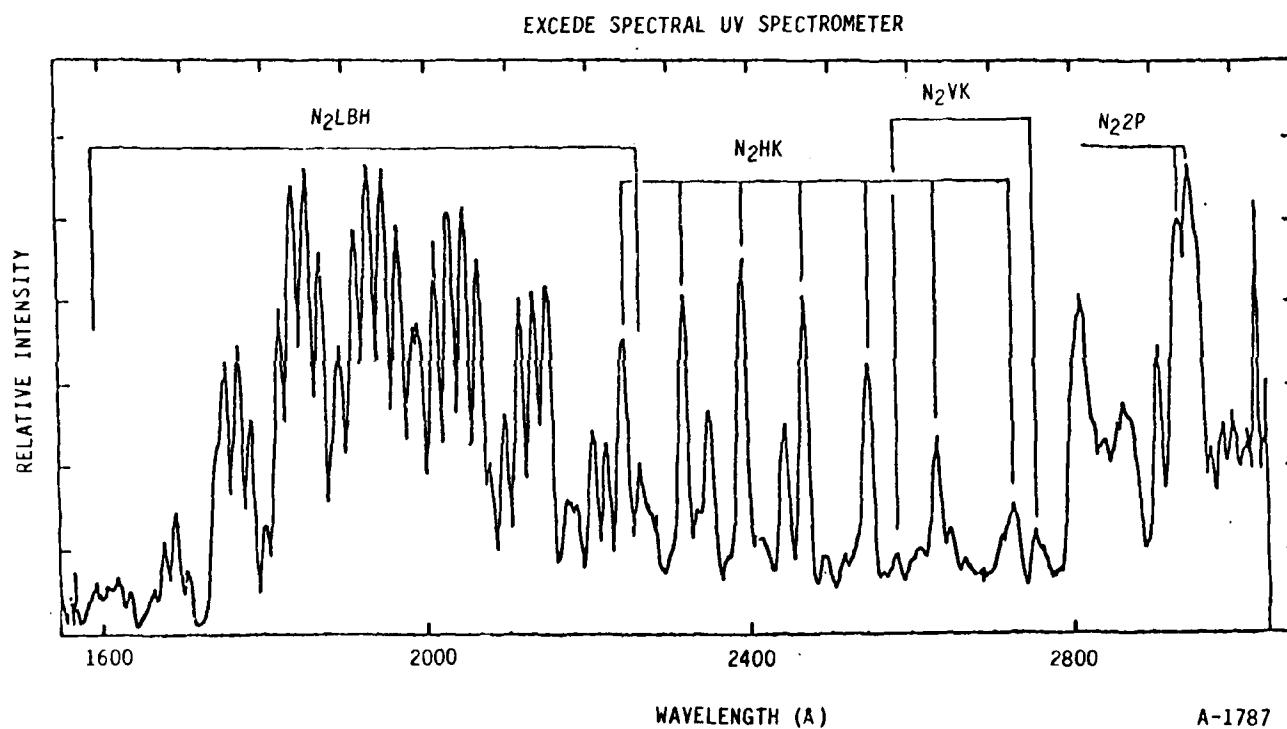


Figure 41. EXCEDE UV spectrum of the upper atmosphere irradiated by 3 keV electrons. Nominal resolution is 0.8 nm. LBH = Lyman-Birge-Hopfield (a - X); HK = Herman-Kaplan (E - A); VK = Vegard-Kaplan (A - X); and 2P = second-positive (C - B). Agreement of laboratory and field data is quite good. Spectrum provided by R. R. O'Neil (AFGL).

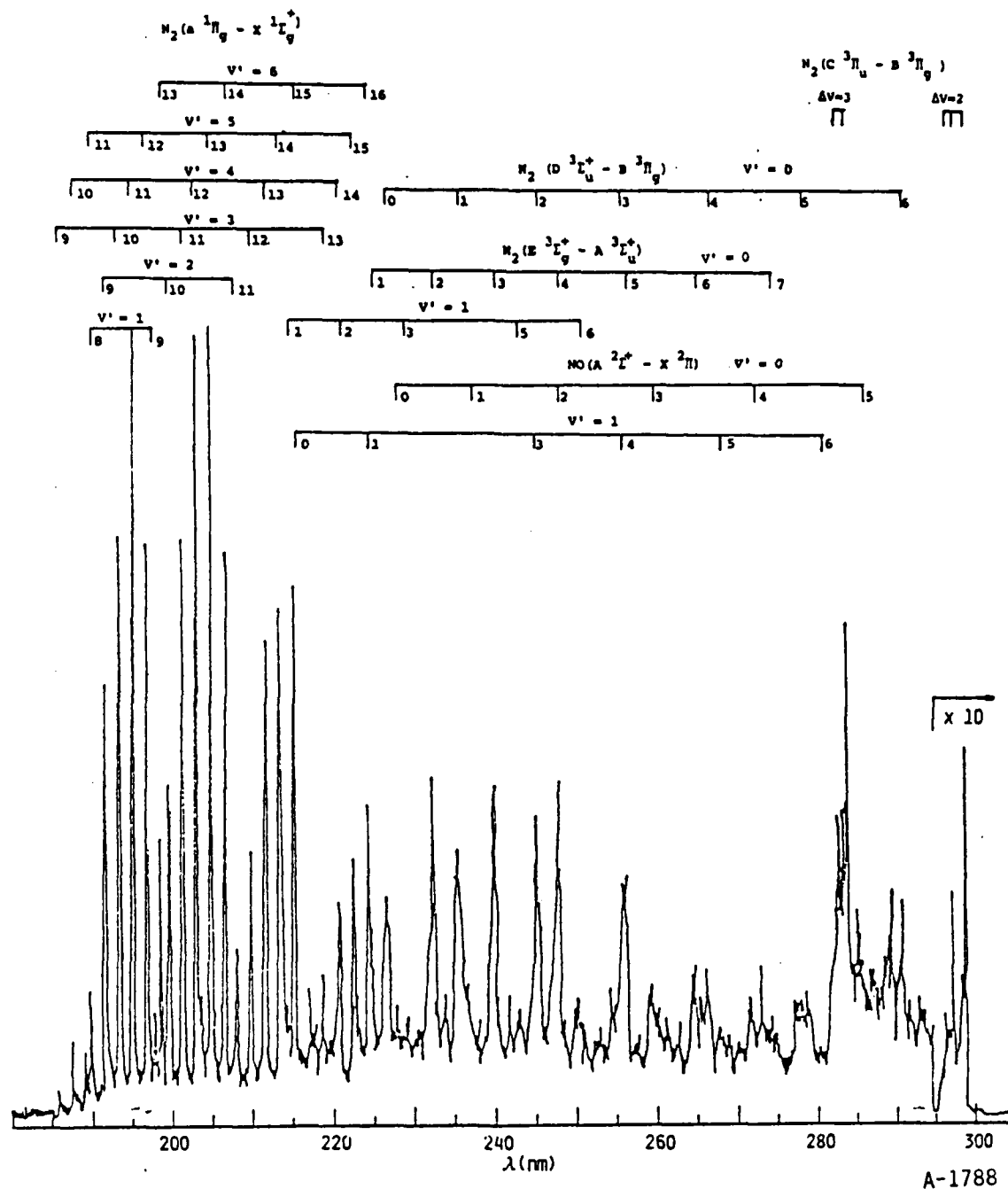


Figure 42. Higher resolution (0.2 nm) LABCEDE UV spectrum of air for the same conditions as Figure 39. Several spectral features are revealed as composites of overlapping transitions at this resolution.

The higher resolution scans in LABCEDE reveal that the tentative identification of bands in the EXCEDE spectrum²⁵ at 260 and 276 nm as being nitrogen Vegard-Kaplan emission is incorrect for LABCEDE conditions. The bands have neither the correct shapes nor positions to be from that system. The feature at 276 nm is predominantly the 0,5 band of the fourth-positive system at 277.5 nm. We have not yet assigned the feature at 260 nm, but note that the band head is at 258.6 nm and the band is blue degraded whereas the Vegard-Kaplan 0,5 band is red degraded and has a band head at 260.4 nm. Presumably this band belongs to one of the ubiquitous nitrogen singlet systems in the 200 to 300 nm spectral region.²⁶

The features between 280 and 290 nm are a composite of the 0,3 and 1,4 bands of the nitrogen second-positive system at 282.0 and 281.4 nm. Several other nitrogen bands are observed, the strongest having heads at 282.6, 282.7, 287.3, 287.9, and 288.6 nm. Also seen is an extensive system of emission features from 281 nm to at least 294 nm which is most likely an oxygen system. These latter bands appear most strongly in low pressure air at short residence times, so could not arise from a secondary species such as nitric oxide. We plan to study this system more extensively in the future to obtain an unambiguous assignment.

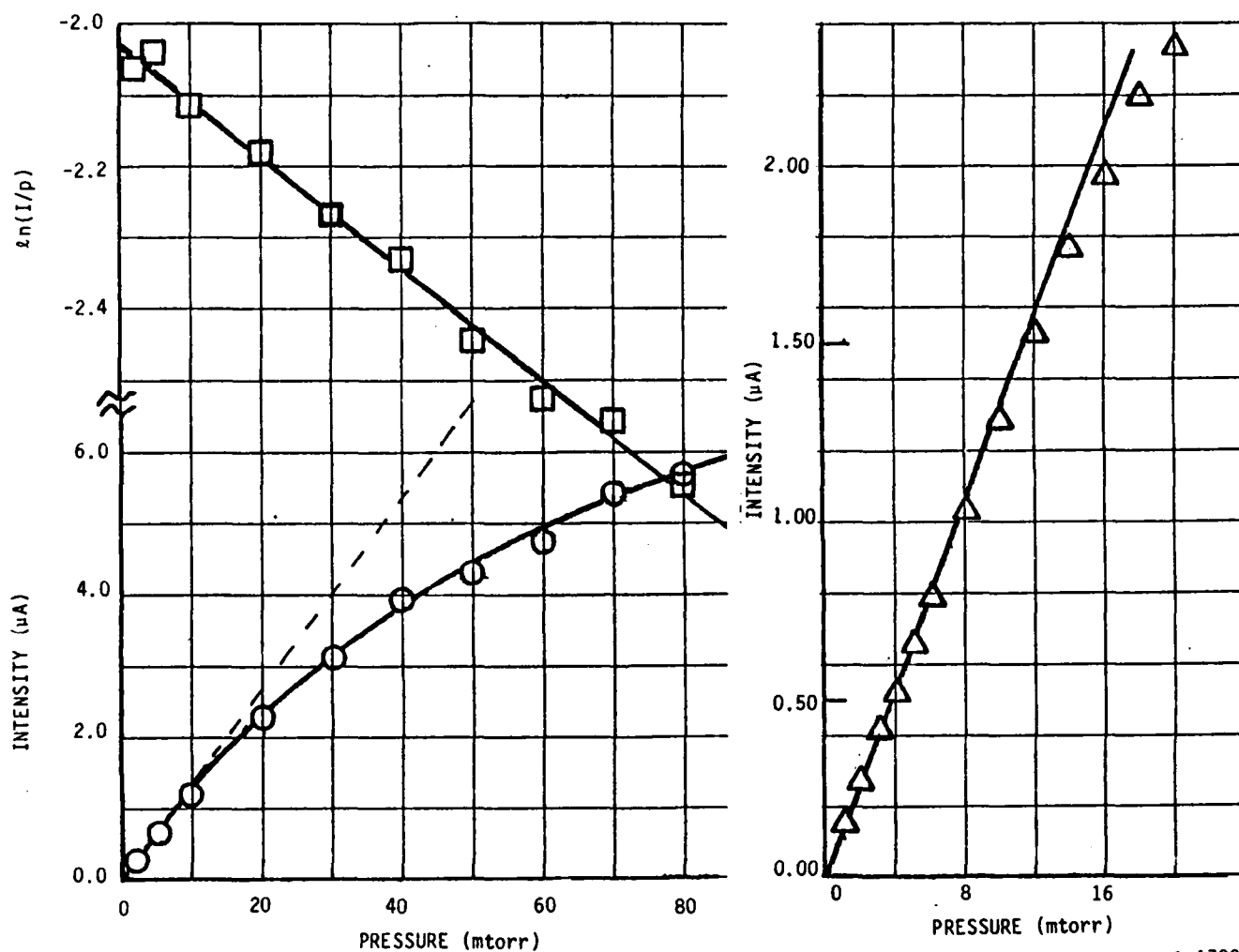
At high pressures in the apparatus, the intensities of the LBH and Herman-Kaplan systems are reduced relative to the much shorter lived fourth-positive system. In addition, the LBH vibrational distribution changes so that lower vibrational levels are populated more strongly relative to the higher levels than is the case at low pressure. These observations indicate that the LBH and Herman-Kaplan systems are quenched electronically and vibrationally. We have also observed the effects of quenching of the nitrogen Meinel and first-positive and oxygen first-negative systems in the region below 500 nm. We studied the quenching of the Meinel bands in some detail (see Section 7), and plan to extend these quenching studies to other systems, including the ultraviolet systems, in the future. Such quenching studies will permit accurate atmospheric modeling and a determination of accurate excitation efficiencies.

3.4 Variation in Intensities of Several Features as Functions of Operating Parameters

After surveying the spectra as described above, we investigated the variation in the intensity of several emission features as functions of pressure, electron-beam current, and magnetic field. In this section we will describe measurements on the $N_2^+(B^2\Sigma_u^+ v' = 0 - X^2\Sigma_g^+ v'' = 0)$ transition at 391.4 nm and the $N_2(C^3\Pi_u v' = 0 - B^3\Pi_g v'' = 2)$ transition at 380.4 nm. These two transitions represent band systems which are excited predominantly by primary and by secondary electrons respectively (see Table 3).²⁷ The data also begin to map out operating regions in which beam-plasma discharge is important and those in which it is not. Both of these transitions are short lived (62 ns for the 391.4 nm transition and 37 ns for that at 380.4 nm)²⁶ so that electronic quenching is unimportant over the range of pressure investigated.²⁸ The $N_2^+(A^2\Pi_u - X^1\Sigma_g^+)$ system has a radiative lifetime of about 10 μ s, and thus collisional quenching of this state may be studied at mtorr pressures. That series of measurements is described in Section 7.

Figure 43 shows how the intensity of the 391.4 nm transition varies with pressure of air in the test chamber for the case of no confining magnetic field and for an e-beam energy and current of 3.0 kV and 8 mA respectively. Because the spectral system was uncalibrated, the intensity scale in units of μ A of photomultiplier current, is only relative. The intensity increases linearly with pressure up to about 10 mtorr, after which it continues to increase with pressure but at an increasingly less than linear rate. This fall-off from linearity results from attenuation and scattering of the e-beam as it traverses the reaction chamber from the electron gun to the observation region.

The observed emission comes from molecules excited electronically in collisions between the gas in the chamber and the electrons in the e-beam. Because the gas in the chamber is essentially static and the lifetime of the emitting molecules in the field of view is short compared to the time the molecules are within the field of view, steady-state conditions obtain in the



A-1789

Figure 43. Variation in intensity of $N_2^+(B^2\Sigma_u^+, v'=0 \rightarrow X^2\Sigma_g^+, v''=0)$ at 391.4 nm as a function of pressure of air in absence of a magnetic field. Also shown is an e-beam attenuation plot ($\ln(I/p)$ versus p). e-beam current is 8 mA; beam voltage is 0.3 kV. Right-hand plot shows quasi-linear region with an expanded scale.

chamber. Thus the emission intensity is directly proportional to the number density of excited species created in unit time within the detector's field of view. The number density of excited species within the field of view is the ratio of the number of electrons in the e-beam stopped within the field of view to the volume of the field of view:

$$I_{A*} \propto [A*] = \frac{i_o - i}{\pi r^2 \ell} = \frac{i_o}{\pi r^2 \ell} (1 - e^{-\sigma \ell p}) \quad (32)$$

where r and ℓ are the radius of the E-beam and length of the field of view, respectively, i_o is the e-beam current, and σ is the electron-excitation cross section. If the attenuation is very weak, the exponential in Eq. (32) can be expanded with all terms save the first two dropped, and thin-target conditions obtain:

$$I_{A*} \propto i_o \sigma p \quad (33)$$

Thus, the observed emission intensity should be linearly proportional to the e-beam current, the excitation cross section, and the chamber pressure. Figure 43 shows the linearity with pressure below 10 mtorr.

At higher pressures the E-beam is attenuated before reaching the observation region:

$$i_o = i_o' e^{-\sigma' \ell' p} \quad (34)$$

where i_o' is the initial e-beam current at the exit of the electron gun, σ' is the total cross section for attenuation of the e-beam, and ℓ' is the effective distance between the electron gun and the observation region. If the width of the observation region, ℓ , is sufficiently small that the e-beam attenuation is insignificant over that length, then thin-target conditions still hold for describing the observed emission intensity, but the e-beam current, i_o in Eq. (32), is no longer constant, but instead is a function of pressure as given in Eq. (34). Combining Eqs. (33) and (34) gives

$$I_A \propto \sigma p i_0' e^{-\sigma' l' p} \quad (35)$$

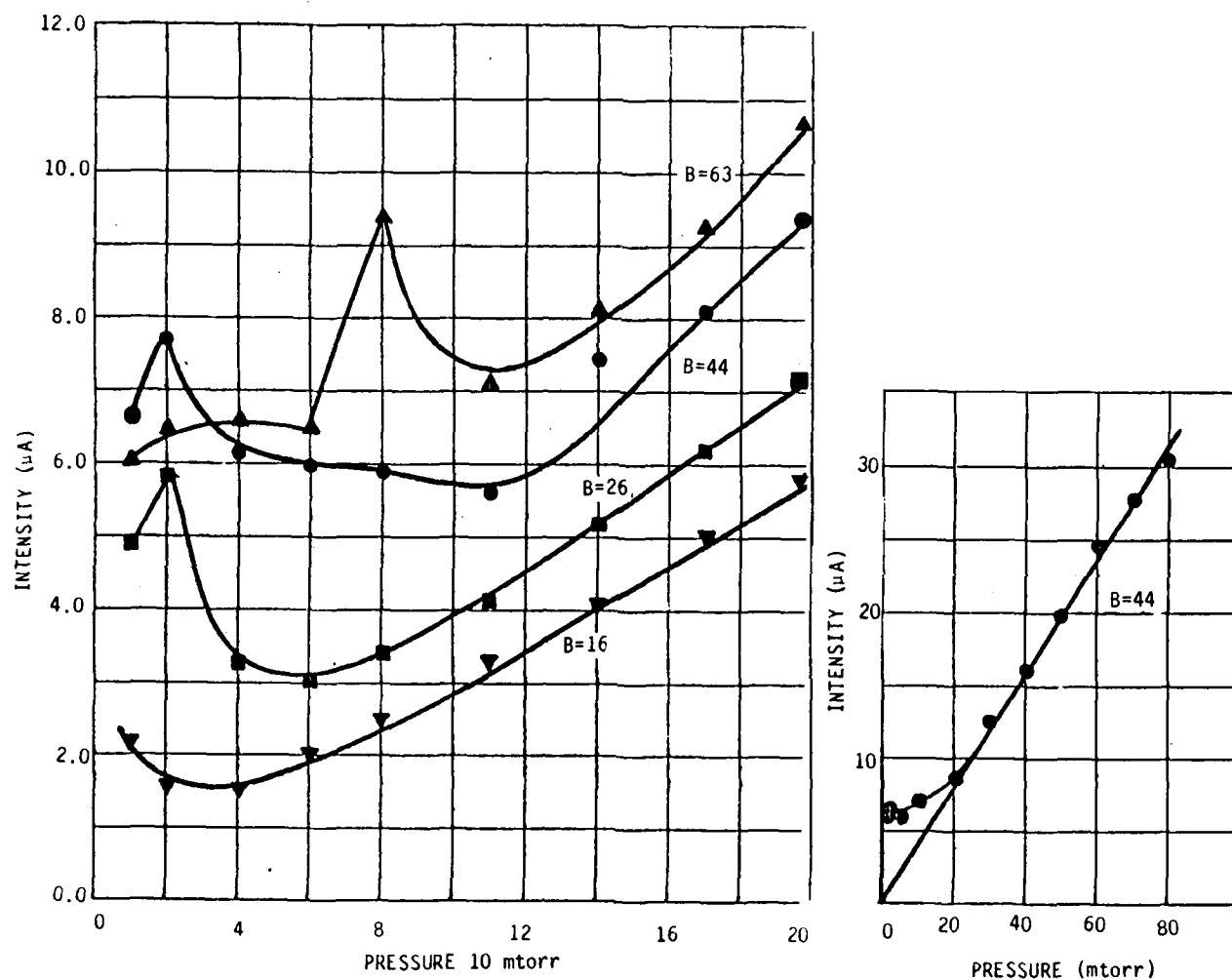
Dividing through by p and taking the natural log of both sides gives the attenuation equation:

$$\ln(I/p) \propto \ln(\sigma i_0') - \sigma' l' p \quad (36)$$

Thus a plot of $\ln(I/p)$ versus p should be linear. Figure 43 shows such a plot. The cross section one can derive from this attenuation plot is not physically significant because the attenuation depends not only on inelastic scattering collisions, but also elastic scattering of the electrons out of the beam so that they never enter the field of view of the detection system. The observed attenuation, σ' , is therefore strongly dependent on viewing geometry.

Figure 44 shows how the intensity of the 391.4 nm band changes with pressure when the magnetic field is turned on. The inset for the case of $B = 44$ Gauss, shows that at pressures above 20 mtorr, the intensity rises linearly with pressure up to the highest pressures studied, 80 mtorr. Furthermore, the linear portion of the curve extrapolates to the origin. At lower pressures, however, the variation in intensity with pressure is non-linear, and in fact the dependence is not even monotonic. The greatly enhanced intensity at low pressures results from striking a beam-plasma discharge. Presumably, if we were to investigate pressures below 1 mtorr, the discharge would extinguish at some point and the intensity would drop precipitously. These effects will be considered in Section 9.

The reason that the intensity-versus-pressure plot is linear up to 80 mtorr with the magnetic field on as contrasted with the case of no magnetic field is that the magnetic field constrains all electrons, both elastically scattered primaries as well as secondaries, to a small region around the primary electron-beam axis. Thus the whole of the electron beam remains within the detector field of view at all pressures. The range of the 3 kV beam at 80 mtorr is about 2-1/2 meters,²⁹ so that the actual attenuation of the primary electron beam between the electron gun and the observation region



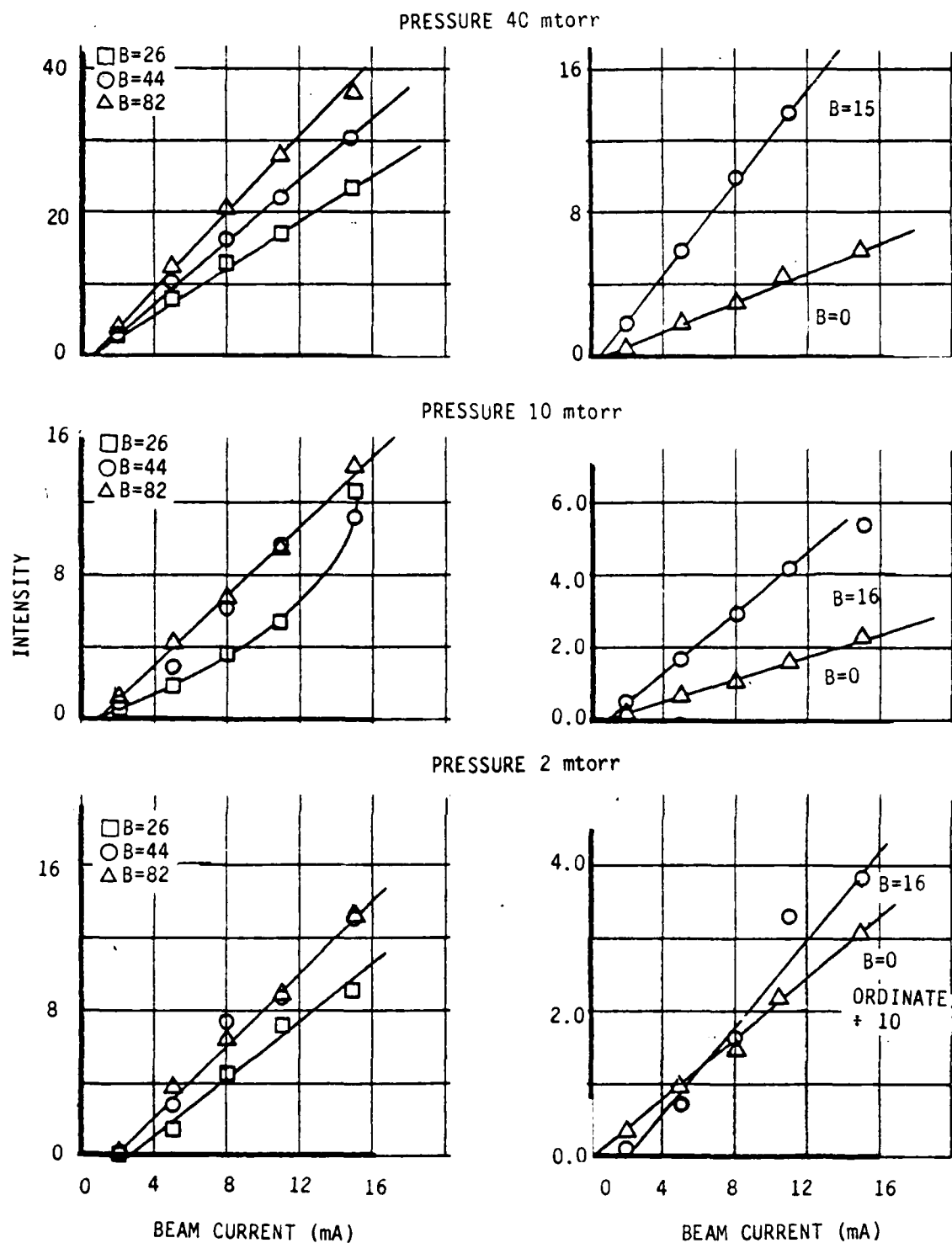
A-1790

Figure 44. Variation in intensity of $N_2^+(B^2\Sigma_u^+, v' = 0 - X^2\Sigma_g^+, v''=0)$ band at 391.4 nm as a function of pressure of air for four different magnetic field strengths for a 3.0 kV, 8 mA beam. Magnetic field strengths are in units of Gauss.

will be less than 20 percent. Thus the majority of the apparent attenuation observed in the case of no magnetic field results from electrons leaving the detector field of view either as elastically scattered primary electrons, or else as unstopped secondary electrons. With the magnetic field on, all scattered electrons are constrained to gyrate around the primary electron beam at their Larmor radius. Thus scattered primary electrons still pass through the field of view and secondary electrons are eventually degraded to thermal velocities by subsequent collisions while still within the field of view.

Figure 45 shows how the intensity at 391.4 nm varies with electron beam current at several different magnetic field strengths for each of three different pressures. Except for the measurements at intermediate magnetic field strengths at a pressure of 10 mtorr, the intensity appears to vary linearly with e-beam current just as would be expected based upon the considerations involved in deriving Eq. (35). The curves with no magnetic field extrapolate to the origin at all pressures. In the presence of a magnetic field at 2 mtorr, however, the signal apparently vanishes at a beam current of about 2 mA. This probably indicates a necessary current-density threshold before the beam-plasma discharge ignites.

Figure 46 shows how the signal at 391.4 nm varies with electron-beam current at several different primary-electron energies. The plotted slopes are actually averages of the ratio of intensity to e-beam current, essentially a force fit through the origin. The differences between these slopes at different e-beam energies result from the variation in the cross section for 391.4 nm excitation with electron energy. The ratios of the slopes of the lines normalized to that at 3.0 kV are 1.3:1.16:1.0:0.79:0.58 for e-beam energies of 2.0, 2.5, 3.0, 4.0, and 5.0 kV respectively. The ratios of the cross sections for excitation of the 391.4 nm band by electrons³⁰ are 1.39:1.17:1.0:0.78:0.61 respectively for the same ordering of electron energies as above.



A-1791

Figure 45. Variation in intensity of the $N_2^+(B^2\Sigma_u^+, v'=0 - X^2\Sigma_g^+, v''=0)$ transition at 391.4 nm as a function of e-beam current for five different magnetic fields at each of three different pressures. All plots have a common abscissa; all intensities are in μA ; all magnetic field strengths are in Gauss. e-beam energy = 3.0 kV.

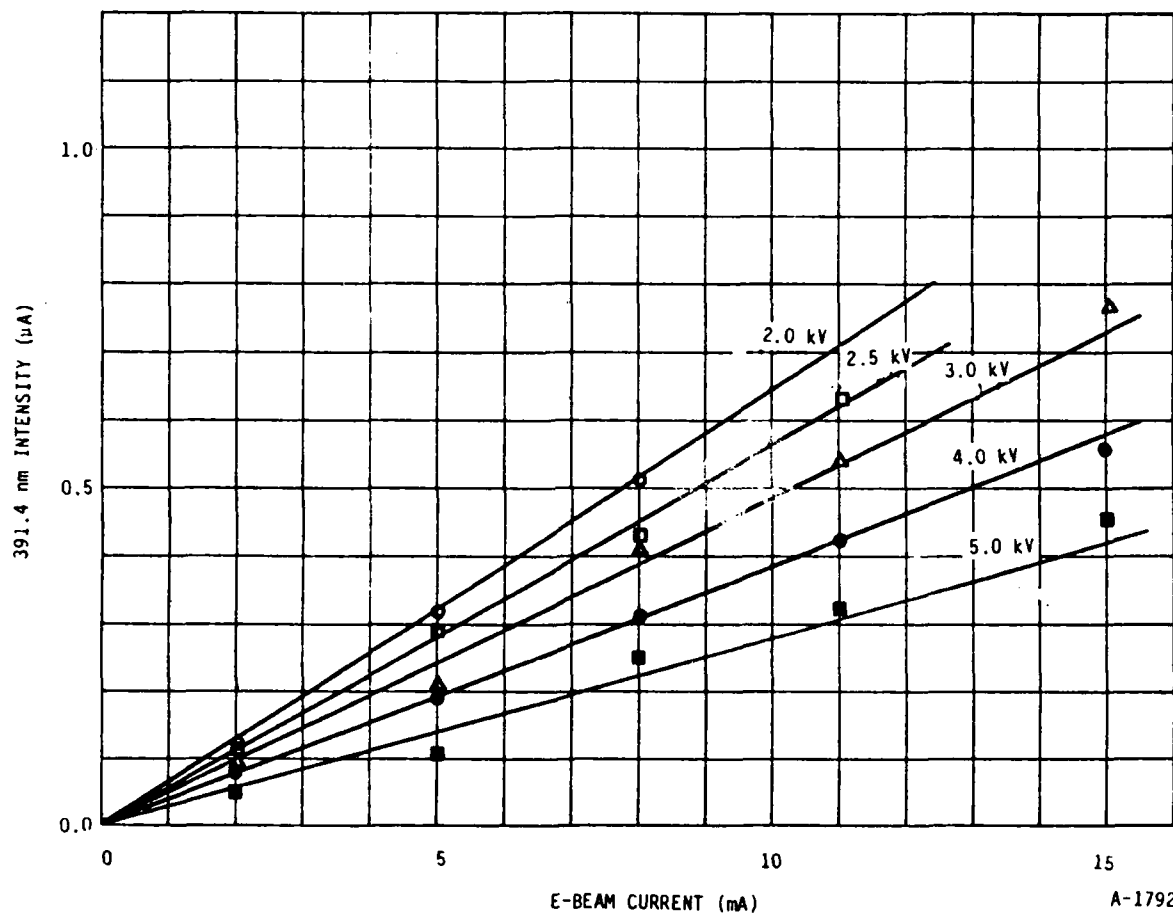
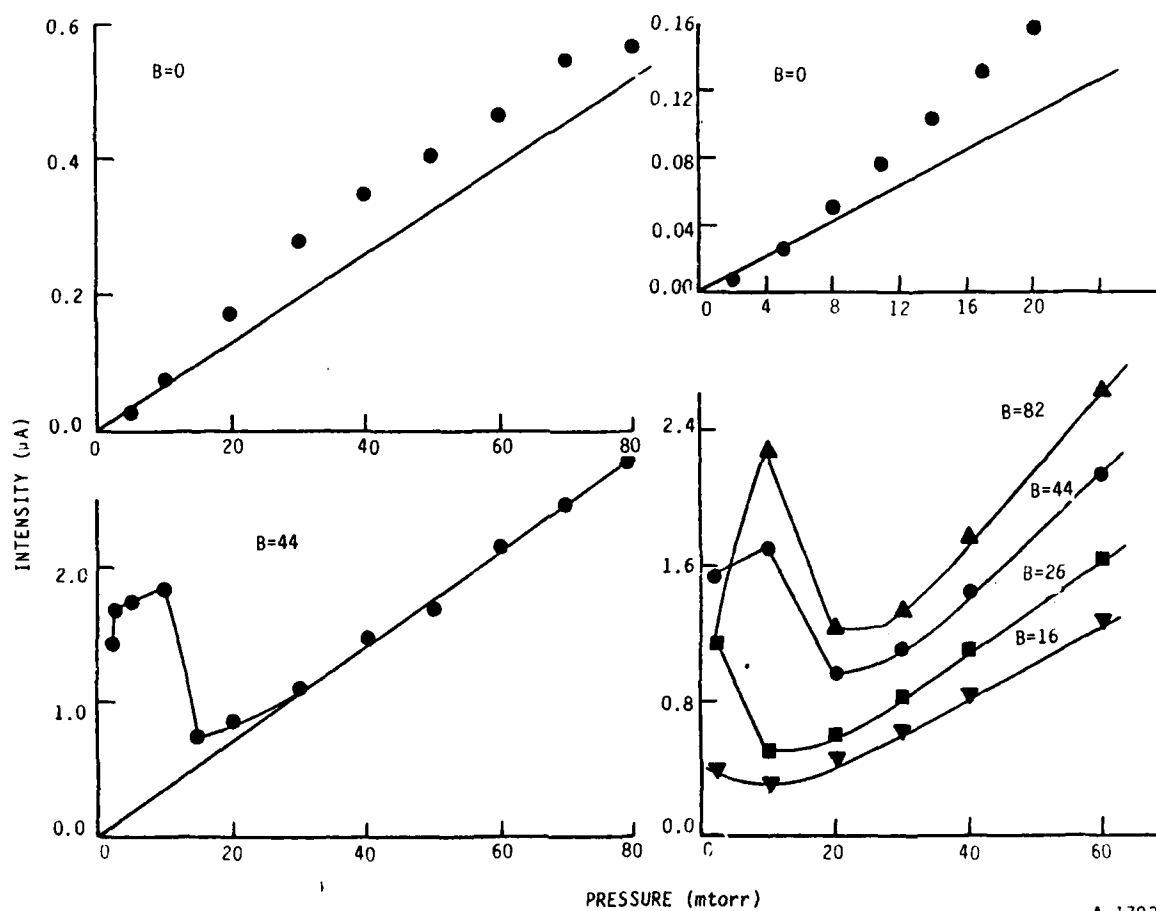


Figure 46. Variation in intensity of $N_2^+(B^2\Sigma_u^+, v'=0 - X^2\Sigma_g^+, v''=0)$ transition at 391.4 nm as a function of e-beam current for five different values of e-beam energy. $B = 0$, pressure = 4 mtorr of air.

Figure 47 shows how the signal of the $N_2(C^3\Pi_u, v' = 0 - B^3\Pi_g, v'' = 2)$ transition at 380.4 nm varies with pressure both in the presence and in the absence of a magnetic field. This state is excited predominantly by secondary electrons unlike the 391.4 nm transition, so that the pressure dependence in the absence of the magnetic field is much different from the 391.4 nm case. Even at low pressures, the intensity does not vary linearly with the pressure, and furthermore, the deviation from linearity at low pressure is positive: the intensity grows at a greater-than-linear rate. Our observations indicate that the intensity grows as $p^{1.3}$ at pressures below about 20 mtorr. The greater-than-linear increase of 380.4 nm emission with pressure results from an increased secondary-electron flux as the pressure increases, thus effectively rendering the excitation current, i_0' Eq. (34) a function of pressure. This observation was qualitatively modeled in Subsection 2.4.4. At higher pressures with the magnetic field off, the signal intensity begins to turn over and to grow at a less-than-linear rate, because of the effective attenuation of the primary electron beam already noted above for the 391.4 nm emission.

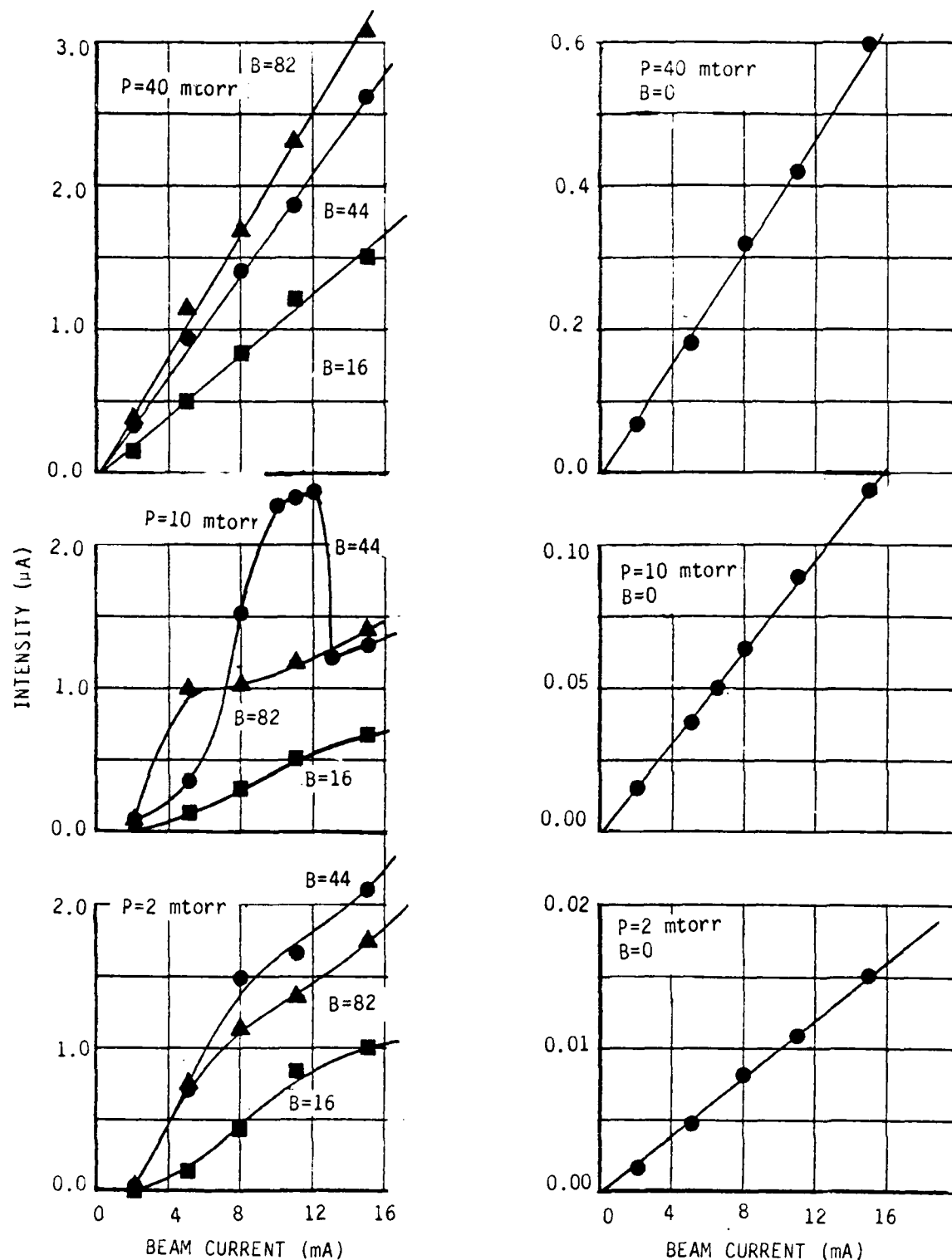
In the presence of a magnetic field, the intensity grows linearly with pressure, at pressures above about 30 mtorr, and extrapolates to the origin as in the case of the 391.4 nm emission. At low pressures in the presence of a magnetic field, the pressure dependence is complex, and again not even monotonic. This again results from the effects of beam-plasma discharge. We plan to investigate the region below 1 mtorr carefully to determine thresholds for the beam-plasma discharge. In our system we know that the discharge exists down to at least 0.5 mtorr. The apparent quenching of the discharge at 30 mtorr pressures will also be examined more thoroughly.

Figure 48 shows the dependence of the 380.4 nm emission on e-beam current for several magnetic-field strengths at each of three different pressures. In all cases the 380.4 nm emission intensity varies linearly with current when no magnetic field is present, and all B-off curves extrapolate to the origin. In the presence of the magnetic field, however, the data at both 2 and 10 mtorr



A-1793

Figure 47. Variation in intensity of $N_2(C^3||_u, v'=0 - B^3||_g, v''=2)$ band at 380.4 nm as a function of the pressure of air for several different values of magnetic field. e-beam energy = 3.0 kV, e-beam current = 8 mA.



A-1794

Figure 48. Variation in intensity of $N_2(C^3\Pi_u, v'=0 - B^3\Pi_g v''=2)$ band at 380.4 nm as a function of e-beam current at four different magnetic fields for each of three different pressures of air. All ordinates are in units of μA ; all plots have a common abscissa; $V = 3.0$ kV.

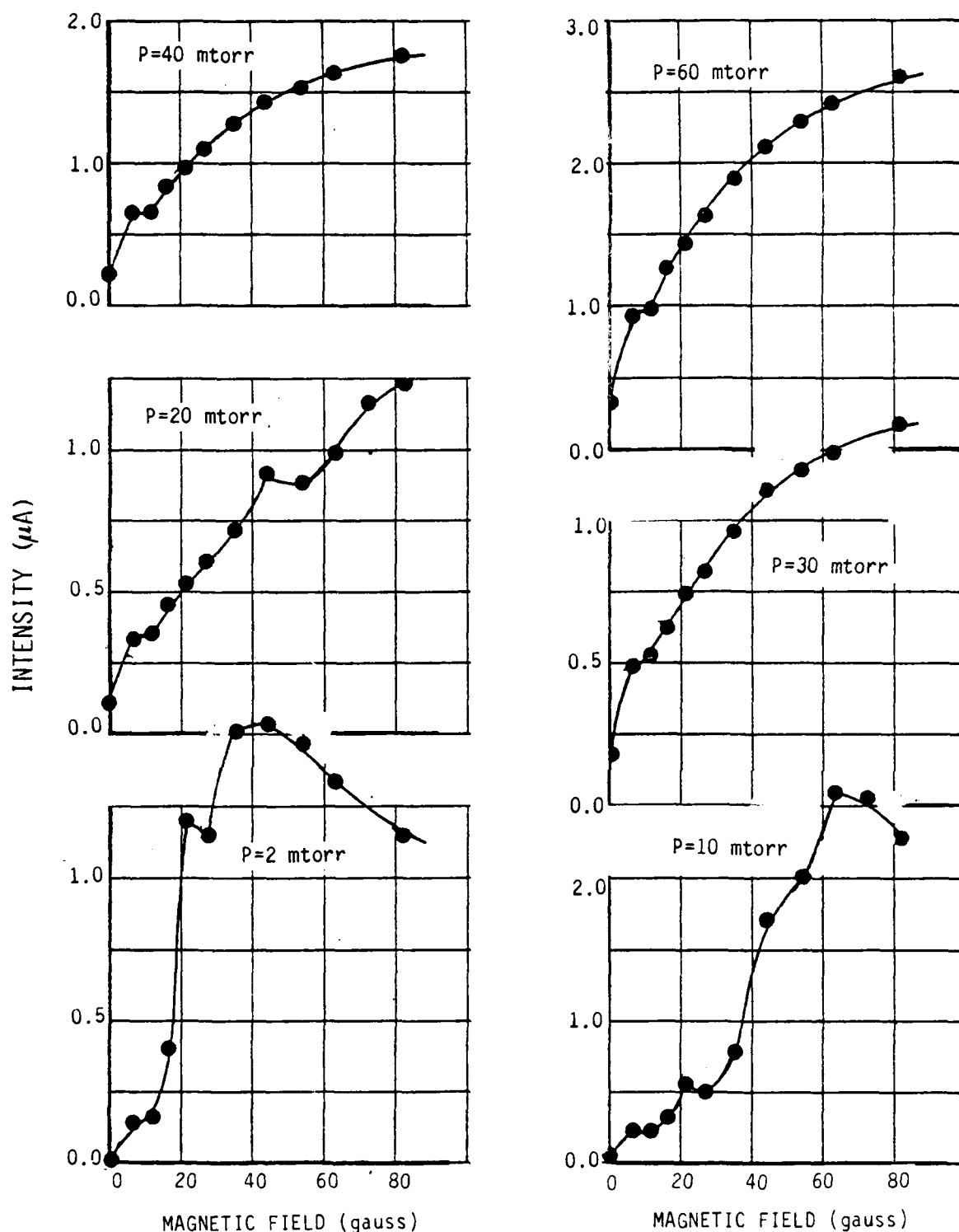
vary non-linearly with e-beam current, and furthermore seem to vanish at currents of about 2 mA. At 40 mtorr, even with the magnetic field on, the intensity varies linearly with current, and vanishes at the origin. This strange behaviour undoubtedly relates to the effects of beam-plasma discharge.

Figure 49 shows the variation in the 380.4 nm intensity as a function of magnetic field at six different pressures of air for a 3.0 kV, 8 mA electron beam. At the higher pressures the intensity increases smoothly as the magnetic field strength increases, but at the two lowest pressures, the intensity variation with magnetic field is neither smooth nor monotonic. Understanding this behavior requires further study.

Some important theoretical aspects of the beam-plasma discharge phenomenon are discussed in Section 9 to provide a framework for understanding the observations in this subsection.

3.5 Summary of the Visible Measurements

The broad spectral coverage of the UV-near IR measurements in LABCEDE described in this section, provide abundant data useful in understanding a variety of issues important to atmospheric science. We have shown that our visible and ultra-violet spectra do compare well with field spectra of electron-irradiated air and have been able to aid the assignment of some of the spectral features observed in the EXCEDE field program. We have presented measurements of the variations in intensity of emissions from $N_2^+(B^2\Pi_u^+)$ and $N_2(C^3\Pi_u)$ at 391.4 and 380.4 nm respectively as functions of a number of operating parameters of the apparatus. These two species are representative of species excited predominantly by primary and by secondary electrons respectively. Preliminary theoretical considerations will use these measurements to illuminate the characteristics of beam-plasma discharge. These observations provide the groundwork for quantitative quenching and excitation measurements (such as the N_2^+A state) by illuminating experimental capabilities and constraints.



A-1795

Figure 49. Variation in intensity of $N_2(C^3\Pi_u, v'=0 - B^3\Pi_g v''=2)$ band at 380.4 nm as a function of magnetic field at six different pressures of air. All plots have a common abscissa; all ordinates are in μA e-beam energy = 3.0 kV, e-beam current = 8 mA.

4. INFRARED OBSERVATIONS

4.1 Operational Considerations

Two very different instruments were used to spectrally resolve the infrared fluorescence from LABCEDE: a room temperature Michelson interferometer which has been the main detection network during our past laboratory measurement programs; and a liquid helium temperature circular variable filter (CVF) system. The operating regimen for these two instruments is given in the next two subsections. In Subsection 4.1.3 our current understanding of gas transport and intrinsic observation times is given. This understanding arose from interpretation of IR time histories.

4.1.1 Michelson Interferometer - This instrument,³¹ its application to time-resolved Fourier Spectroscopy,³² and its capabilities to perform kinetic studies³³⁻³⁵ have all been documented. However, it had not previously been successfully applied to the observation of fluorescence from gases at 1 mt pressures representative of the refurbished LABCEDE apparatus. Spectroscopy, not kinetics, was the goal of these preliminary observations. Consequently, the beam was pulsed with 50 percent duty cycle and the total AC component of the interferogram was used. Traditional time-resolved measurements were only attempted in passing. Fluorescence was observed both from the end of the tank and from the side observation port. Both lead selenide (PbSe) and indium antimonide (InSb) detectors were utilized for different measurements. The InSb detector was found to be three times more sensitive than PbSe, but our needs for observing fluorescence beyond 5.3 μm (InSb cutoff) forced the use of the PbSe detector in most of our studies. Both detectors were found to be operating near D^* limits. Both were 3 mm diameter round (InSb detector is circular, PbSe detector is 3 mm square masked to 3 mm round). Consequently, the maximum achievable resolution³⁶ is 9.7 cm^{-1} :

$$\delta\sigma = \frac{\pi^2 \sigma_{\text{max}}}{2\pi} \quad (37)$$

where $\delta\sigma$ is the resolution, $\pi\alpha^2$ is the detector collection steradiancy, and σ_{\max} is the maximum detectable wavenumber (7901 cm^{-1}). The PbSe detector was found to have a spectral response comparable to its value originally, i.e., its long wavelength ($1/e$) response cut-off was at 1430 cm^{-1} . Adsorbed water vapor did not affect the observed response function. The weak fluorescent signals in LABCEDE forced detection bandpass reduction. Typical PbSe operating conditions were 90V bias with $4 \times 10^6\text{ ohm}$ series resistance (intrinsic detection system response time of $100\text{ }\mu\text{s}$), with the resulting signal amplified by an AC coupled PARC113 preamplifier on the 5K gain scale with bandpass of 10 to 300 (or 10 to 100) Hz. This resulted in a time constant of 0.5 to 1.6 ms. The beam was pulsed with a 30 ms period so that this bandpass did not reduce the AC fluorescence component. Viewing the fluorescence from the side port increased signal levels by a factor of two, not three as calculated. This was due to the beam overfilling the interferometer's field of view in this configuration. Additionally, beam wander caused the signals to have a long-time drift. The large magnetic coils for beam confinement could have reduced drift, confined the beam, and increased signal levels substantially. However, it was found empirically that the interferometer would not operate when positioned in the center of the energized coils. The interferometer's mirror position sensor was simply overwhelmed by the external field and the instrument became catatonic.

As a result, fluorescence observations were performed from the gas-inlet end of the chamber both with coils on and off. It was found that the small vibrations from the large Kinney pump propagate through the entire apparatus (although at a much reduced level as a result of the pumpline bellows and vibration pads described in Section 2). Thus a vibration-isolation table (NRC $1 \times 1.5\text{m}$) was utilized since vibrations will seriously degrade interferometer performance. This degradation results from mirror position instabilities resulting in errors in laser fringe zero-crossing points which propagate as spectral noise in the transformed interferograms.³⁶ Finally, rejection of out-of-band ($\sigma > 7900\text{ cm}^{-1}$) emission was also critical. The FFT cannot accurately treat this emission, both reflecting it around 7901 cm^{-1} (i.e., an

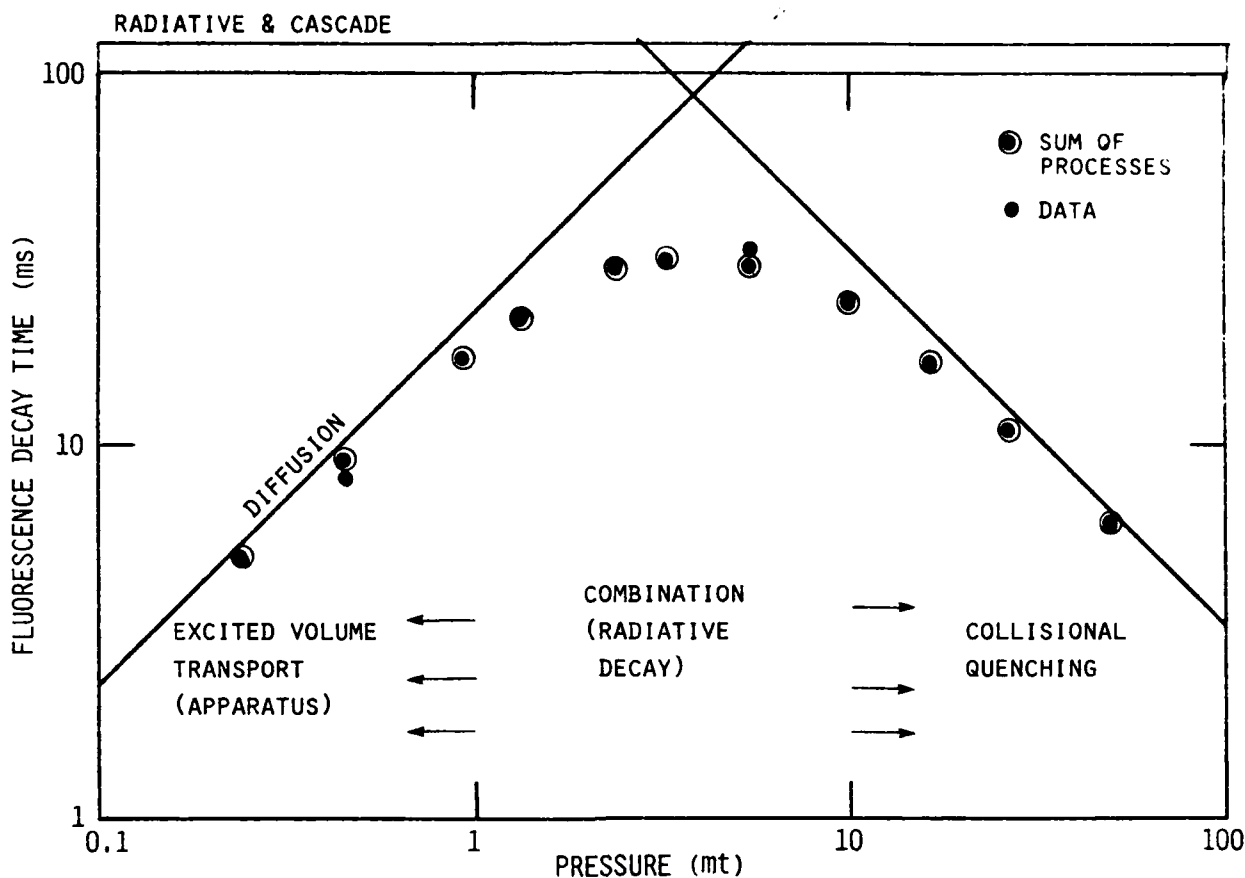
emission line at 8901 cm^{-1} would appear in the spectrum at 6901 cm^{-1}) and increasing noise at all frequencies. A germanium cutoff filter, which transmits frequencies less than $\sim 5500\text{ cm}^{-1}$ was positioned across the entrance aperture when out-of-band emission is strong. The filter was used only as required due to the associated loss of a factor of two in signal levels due to its low transmission.

Data was acquired on the PDP11 using program @LAB0 with inputs of the beam pulse into Schmidt Trigger 1, the fringe sensor into the DR11C card and the data into Channel 0. These inputs could be separately checked using LABT 3,4 and 1, respectively. Program BLAB sorts and subtracts data from different times to generate a single interferogram. IP2K is used to display and transform this data. After the data is acquired, it can be transferred (in toto) to the Apollo node using the companion programs PASLAB/XFER.BIN. The LABCEDE program (developed by PSI) then processes data on the Apollo to create time-resolved spectra.

4.1.2 The Cryogenic CVF - The cooling times and response function of CVF HS1B have been described in Section 2, Subsection 2.5.7. This detection system was interfaced to the apparatus at the gas-inlet end observation port. Initially the CVF could only continuously scan completing 1 rev in 2 to 35 sec. This continuous scanning mode was not suited for our experiment. Moreover, because the intrinsic time response of the instrument is 5 ms, at these scan rates, the signals lagged into subsequent spectral elements. Blurring and distortion occurred. Our first modification included a momentary contact scan button. The motor could not be easily adjusted to scan slower. Thus, most of the early scans were performed by slowly, manually turning the drive motor shaft and CVF wheel. Initial observations were of the steady-state (DC) fluorescence. Two spectra (beam on, beam off) were subtracted to remove the background radiance and thus determine the beam-induced fluorescence. This approach is sensitive to long term drifts in the system. The next step involved pulsing the beam and using a lock-in amplifier to extract the in-phase component of the beam-induced fluorescence, and is considerably more

sensitive than the approach above. It, however, is a time-averaged fluorescent signal and distorts signal decays at different rates. At the end of the period of performance a computer code was developed (CVFTR) to step the filter wheel. The size of the wavelength step and dwell time were completely flexible. Time-resolved data was acquired by synchronization of fluorescence signal with beam pulse at a fixed wavelength. After averaging over an arbitrary number of beam pulses, the wheel was moved to the next wavelength and the time-resolved fluorescence monitored there. This approach is quite satisfactory. It gives a true picture of the fluorescence decay histories and was capable of performing kinetic relaxation studies of $\text{NO}(v)$ by NO (see below). Each of the steps described above resulted in increased sensitivity and accuracy. We are still exploring signal averaging and amplification improvements, and do not feel we have yet reached our ultimate sensitivities.

4.1.3 Gas Transport and Kinetic Regimes in LABCEDE - In order to understand the gas transport properties empirically, a series of experiments were conducted using the CVF looking into LABCEDE under cryogenic conditions. An external magnetic field was applied to minimize beam growth effects. The beam was pulsed 500 ms on and off. Fluorescence decay times were followed on an oscilloscope or using the computer. The observed decays were found to be independent of gas inlet method (porous tube array or jet), applied magnetic field, beam current. A number of molecular radiators were used to separate physical and chemical decays. The key set of observations were on Ar/trace NO mixtures. The decay time of $\text{NO}_{v'=1, v''=0}$ fluorescence as a function of pressure is shown in Figure 50. At the lowest pressures, the time for fluorescence to decay to $1/e$ of its steady-state value increases (takes longer) as pressure increases. At the highest pressures, the fluorescence decays more rapidly after beam termination as pressure is increased. Between 1 and 10 mt a transition between these opposing trends occurs. We believe that this behavior represents the sum of several processes occurring inside the apparatus. The low pressure rise scales roughly as P and reflects a transport of the beam-excited species to the walls out of the field of view. This trend with pressure should not depend on molecular system but to first order should only be a characteristic of the apparatus. Identical low pressure scalings



A-1796

Figure 50. NO(1 + 0) fluorescence decay times in Ar/NO mixtures at 77K using CVF.

were observed for CO(v) in N₂ and pure CO, CO₂(v₂) in Ar and N₂, and O₃(v₃) in Ar/O₂. At the highest pressures the fluorescence decays of Figure 50 scale as p⁻¹. Under these conditions molecular quenching is responsible for loss of excited state species, the molecules are collisionally relaxed before they are transported to the walls or out of the field of view. In addition to NO(v), evidence of CO₂(v₂) by Ar and O₃(v₃) by O₂ quenching has been observed. Unlike the transport, the pressure that quenching becomes important and forces the decays to occur more rapidly depends on molecular excited state and quenching partner concentration and is different for different spectral bands. Indeed, if quenching is negligible, a plateau corresponding to radiatively limited decay is observed. CO₂(v₃) emission ($\tau = 4$ ms) exhibits this plateau at all pressures. CO(v) decays in N₂ show the low pressure rise corresponding to reduction in transport out of the field of view until the radiative lifetime (30 ms) is reached at 3 mt. At N₂ pressures above this, quenching appears to be negligible and the decay is nearly independent of pressure.

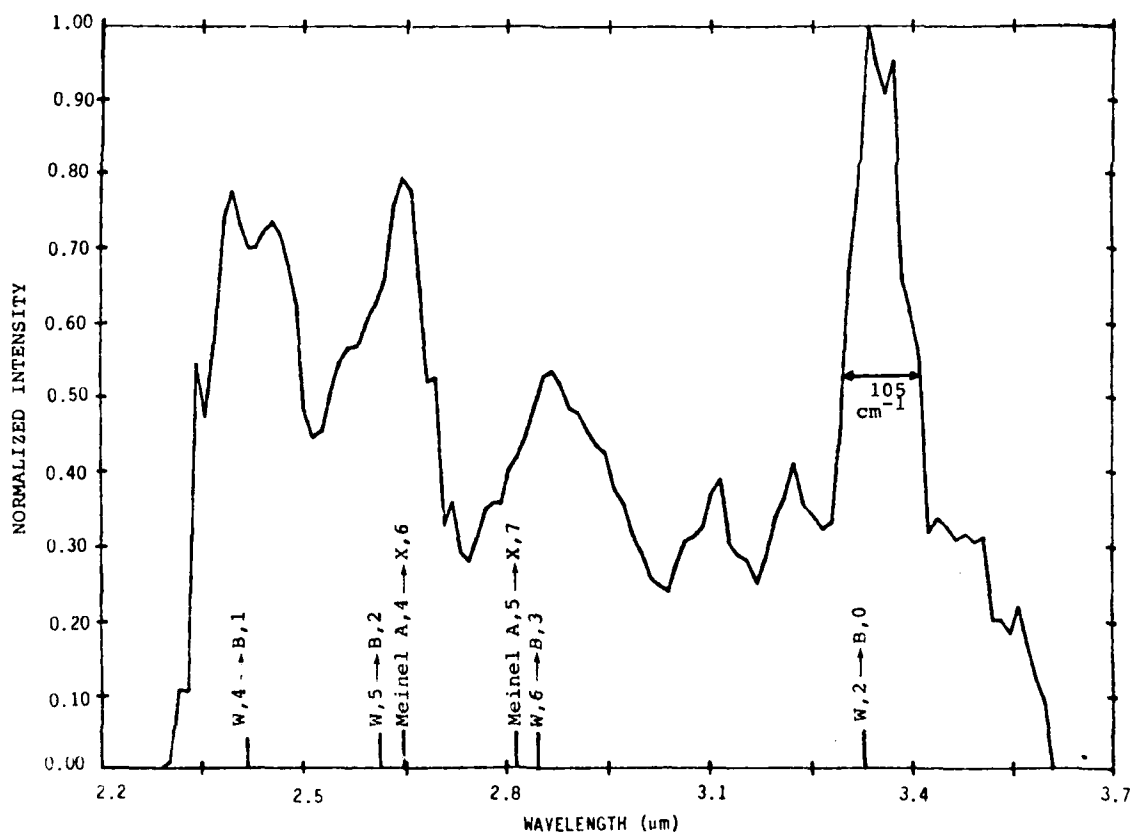
The ramifications of these observations are very important for defining the ability of the refurbished LABCEDE to explore various molecular processes in a systematic manner. At the lowest pressures, the excited molecular states created by the electron beam or chemistry will be transported out of the field of view before relaxation (either radiative or collisional) can occur. Thus, the fluorescence at those pressures will reflect the "nascent" distributions created by electron-irradiation or chemiluminescent reactions. We can measure these distributions and even attempt to isolate the formation mechanism by varying experimental parameters. Secondly, at the highest pressures we can detect the vibrational-level-dependent quenching coefficients of the excited species. Finally, in the absence of significant quenching, the excited state radiative lifetimes can be extracted from data which reflects the entire radiative cascade. Thus LABCEDE has the potential for performing a variety of kinetic and spectroscopic studies of low pressure gases. The preliminary results of these studies are given in the next section.

4.2 Molecular Systems

Several molecular band systems were investigated using the two detection networks described above. These results are preliminary in nature and are presented here to catalog our observations and to point the way for future, more detailed measurements. Our understanding of the conditions inside the apparatus developed as these measurements proceeded and even as a result of the analysis of these data. Thus optimum conditions for performing a given set of experiments were not used and most of these systems will have to be reexamined in light of our growing understanding of the apparatus.

4.2.1 Electronic Transitions of N_2 and O_2 - Infrared radiative transitions between electronically excited states N_2 or O_2 have been studied for years. However, it was felt that they would be too weak to play a significant role in the disturbed upper atmosphere. Under discharge conditions they appear quite brightly. Initially in EXCEDE, and recently in LABCEDE, COCHISE, and possibly in the aurora observed by HIRIS, N_2 electronic $W \rightarrow B$ transitions have been

identified as important SWIR-MWIR radiators. In LABCEDE, beam plasma discharge conditions were optimized to produce infrared emissions in pure N_2 and O_2 which were detected by the CVF as shown in Figures 51 through 53. The features in N_2 have been tentatively identified as $W \rightarrow B$ transitions, especially in the $\Delta V = -2$ sequence. The observed intensities in the $2 \rightarrow 0$, $3 \rightarrow 1$, $4 \rightarrow 2$, and $5 \rightarrow 3$ bands are in rough agreement with Cartwright's³⁷ calculated auroral W state vibrational distribution and transition probabilities based on Franck-Condon factors and λ^{-2} scaling. For nitrogen, the radiant intensities observed are in the 10^{-7} W/cm² sr μ m range (10^{-10} W/cm² sr cm⁻¹) in the SWIR, and about a factor of five less in the MWIR. No fluorescence (above the 10^{-9} W/cm² sr μ m level) was observed in the LWIR. The intensities do depend on flow rates indicating metastables (especially $N_2(A)$) may play a role in emitter state formation. Different features show different flow dependences, indicating that emission from several different electronic states is being



A-1797

Figure 51. SWIR spectrum of 1.83 mt of N_2 under slow flow conditions. Only $W, 2 \rightarrow B, 0$ transition is clearly identified.

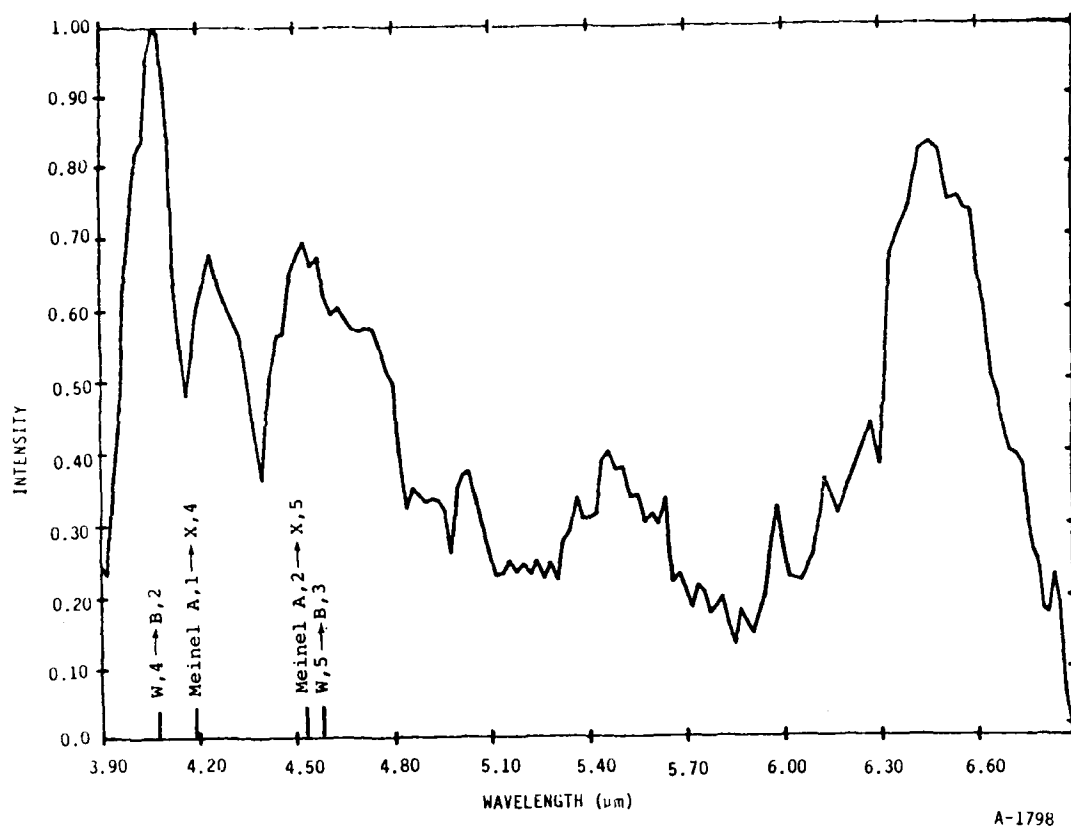


Figure 52. MWIR spectrum of 1.8 mt of N_2 under medium flow conditions. Intensity scale is $\sim 1/2$ of Figure 51. Structure is reproducible.

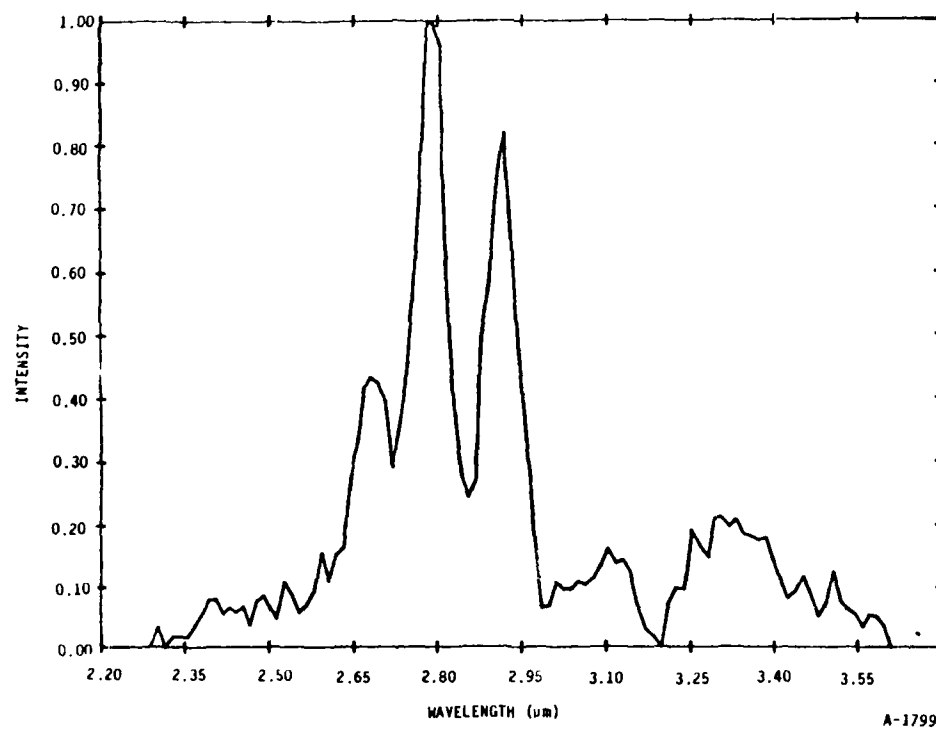


Figure 53. SWIR spectrum of 2.7 mt of O_2 when beam plasma discharge is occurring. Intensity maximum is 7% of Figure 51.

observed. In N_2 a number of features have not been assigned. The resolution ($\sim 45 \text{ cm}^{-1}$) prevents unambiguous assignment, although Meinel ($N_2^+ A \rightarrow X$) and first-positive transitions should be expected. Interferometric spectra with improved resolution and an electronic state spectral synthesis code will permit more accurate analysis in the future.

The spectrum from electron irradiated O_2 under beam plasma discharge conditions is dominated by $O_3(\nu_3, \nu_1 + \nu_3)$. No LWIR features other than $O_3(\nu_3)$ were observed. None of the O_2 SWIR features has been identified as yet, but ionic and the 4.5 eV states are likely radiators. We are planning interferometric scans in the near future. In general fluorescence from oxygen electronic states is weaker than N_2 under comparable experimental conditions.

4.2.2 N_2O MWIR Fluorescence - $N_2O(\nu_3)$ fluorescence at $4.5 \mu\text{m}$ may be an important radiator in auroras or in the disturbed atmosphere. Zipf claims that N_2O is the dominant product of the $N_2(A) + O_2$ reaction. Inside LABCEDE $N_2O(\nu_3)$ fluorescence was observed using the interferometer. In N_2/O_2 mixtures, ν_3 fluorescence increased as the flow decreased, hinting that metastables play a role in its formation. When pure N_2O was irradiated, a number of vibrational bands were observed: $00^{\circ}1$, $12^{\circ}0$, $02^{\circ}1$. Peak fluorescent intensities were $10^{-7} \text{ W/cm}^2 \text{ sr cm}^{-1}$. In pure N_2O , $NO(\nu)$ fundamental band fluorescence is also observed as shown in Figure 54. When He or Ar buffer gas is added, excitation of the various N_2O modes changes and NO fluorescence disappears. When N_2O is just a trace (0.5 percent) in argon a broader pedestal surrounding the ν_3 emission is observed as shown in Figure 55. The intensity of the pedestal scales differently than ν_3 as N_2O concentration is varied. This broad emission has been tentatively identified as $NO^+(\nu)$, but a cleaner formation method must be found. Observations using the CVF also indicated the presence of this emission band along with $NO(\nu)$ emission. The coarser resolution of the CVF makes assignment of this emission even more difficult.

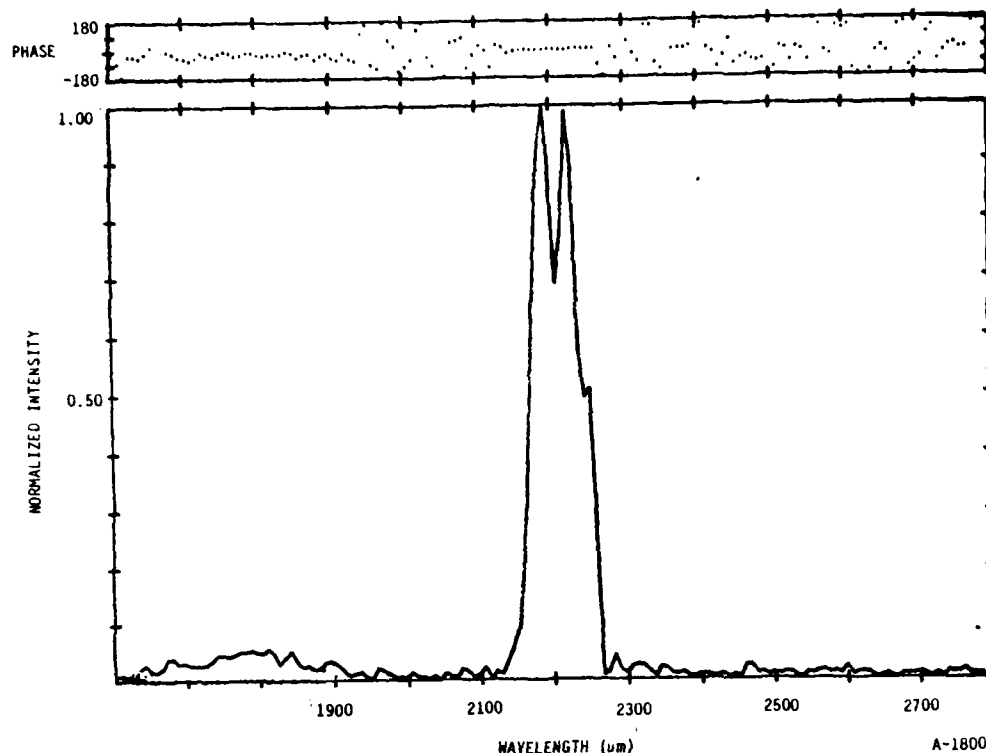


Figure 54. Emission from 24 mt of N_2O as irradiated by 7 mA of 3 kV electrons with an applied field of 85 Gauss. ν_3 emission is very optically thick. NO fundamental band emission is also evident.

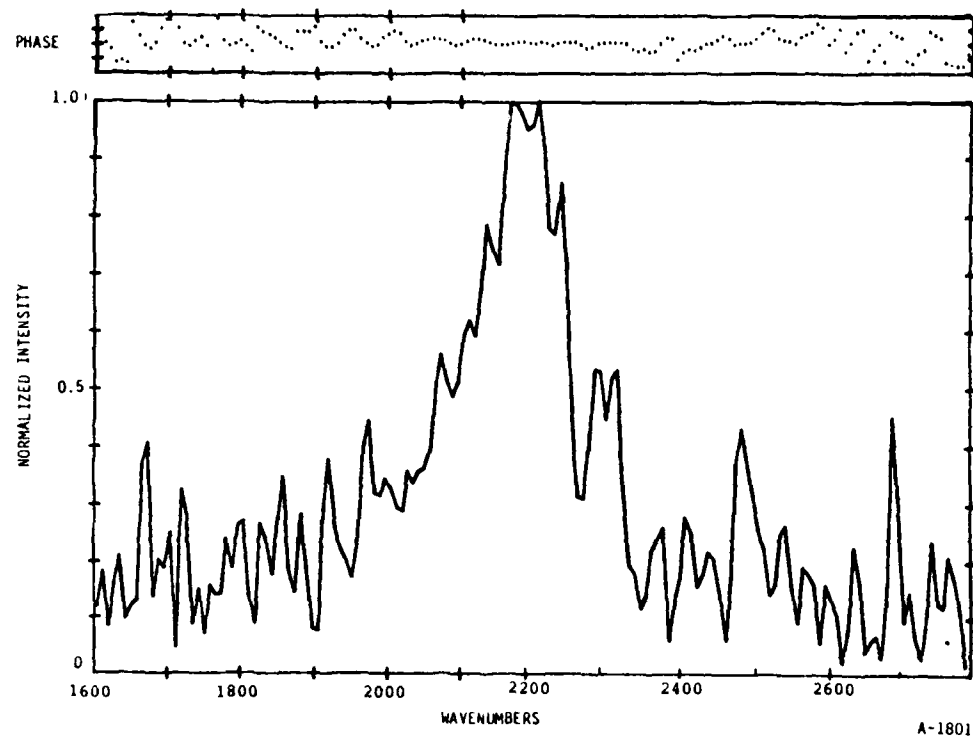


Figure 55. Emission from 0.5 mt N_2O in 43 mt of Ar when irradiated by 6 mA of 3 kV electrons under an applied field of 80 Gauss. No evidence of $N_2O(\nu_3)$ is present in the broader pedestal tentatively assigned as $NO^+(v)$ fundamental band emission.

4.2.3 Excitation Efficiency of NO and CO - Nitric oxide fluorescence has often been observed previously in N_2/O_2 mixtures.^{34,35} Using the CVF in cryogenic LABCEDE, we were able to observe complete fundamental and overtone bands of NO as shown in Figure 56. That spectrum was taken while irradiating a 20 mt of $N_2/0.8$ mt O_2 mixture with 8 mA of 6 kV electrons. No external field was applied and BPD did not appear to be occurring. Using the CVF calibration data (both for spectral response and field of view which slightly differs for the two mask segments) we can measure a relative luminous efficiency of the fundamental and overtone band to be

$$\frac{I_{\text{overtone}}}{I_{\text{fundamental}}} = 16\%$$

This value is in excellent agreement with the value of 15 to 20 percent calculated from the model of Kennealy and Caledonia³⁸ which is based on the

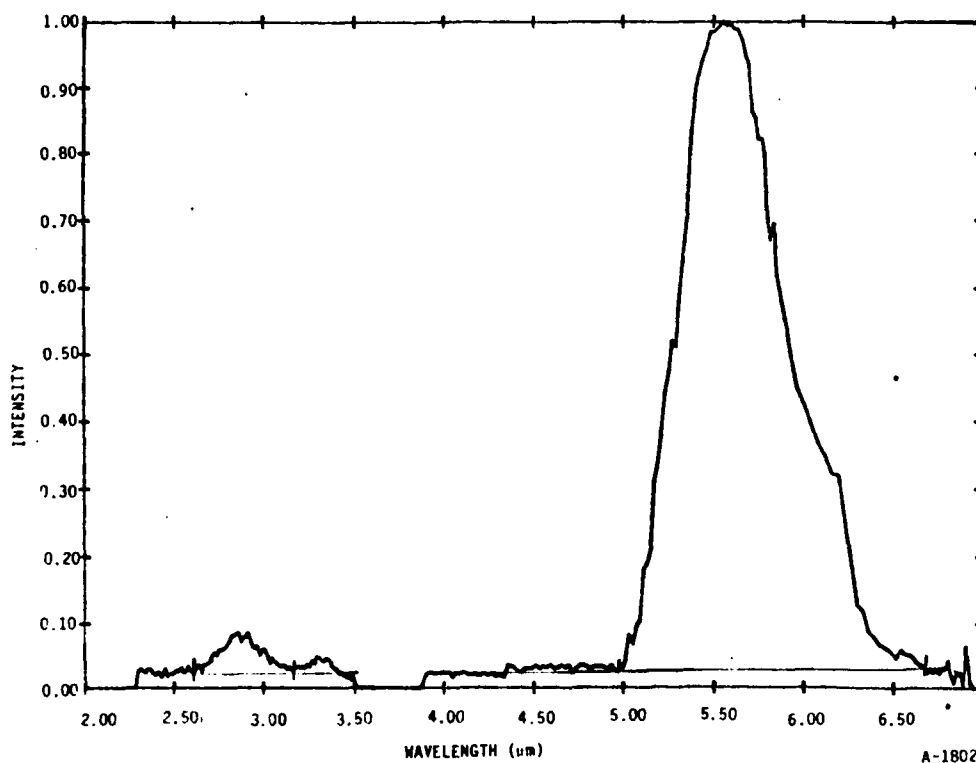
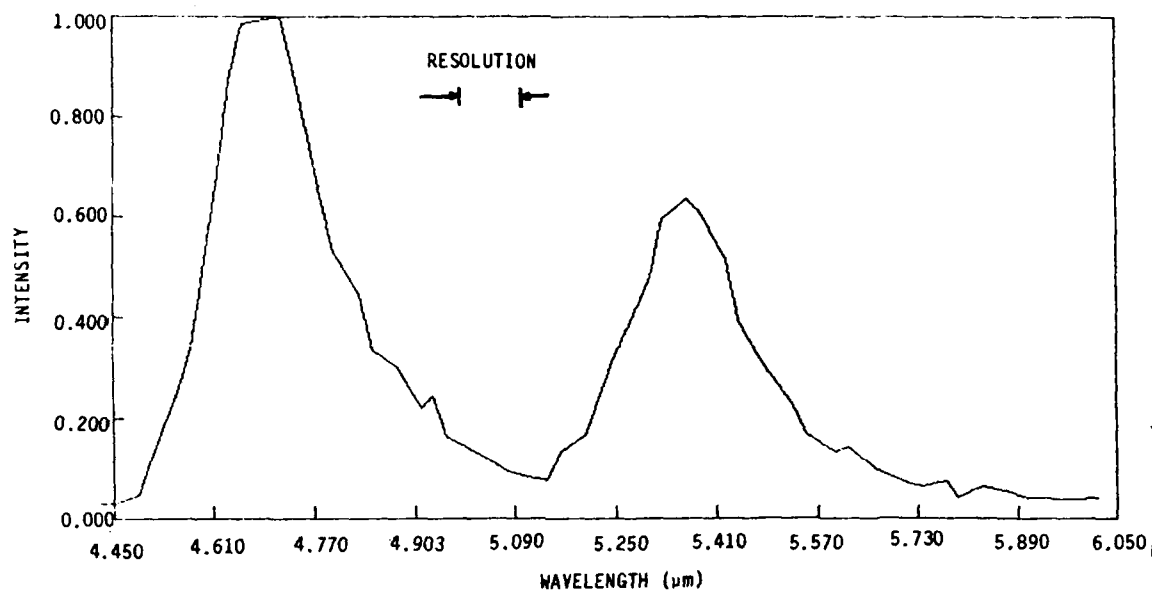


Figure 56. Fluorescence from 4% O_2 in N_2 at a total pressure of 20 mtorr with no applied field. NO overtone and fundamental bands are observed.

COCHISE chemiluminescent nascent vibrational distribution,³⁹ and Billingsley's⁴⁰ Einstein coefficient's ratios, as verified by LABCEDE observations.³⁴ Quenching is expected to be negligible in the spectrum of Figure 56, with radiative cascade expected to be dominant over diffusion.

We also attempted to measure direct excitation efficiencies of NO. When pure NO was irradiated both NO fluorescence and $N_2O(v_3)$ emission was observed indicating that dissociation of NO must be occurring. The NO fluorescence changed both in magnitude and in spectral distribution as an external magnetic field is applied and BPD occurs. In the presence of BPD higher vibrational levels (up to $v' < 6$) are observed, while only molecules with $v' < 3$ are observed under single particle scattering conditions. This indicates that either the numerous secondary electrons are pumping vibrationally excited NO up its manifold or that electronic states are being formed which cascade to high vibrational levels of the ground state. When N_2 is added as the bath gas, the NO fluorescence is less sensitive to magnetic field changes.

A variety of other gases were mixed with NO, including CO. A spectrum from an NO/CO mixture is presented in Figure 57. Fundamental band fluorescence from both molecules is clearly present. It seemed that the relative vibrational excitation efficiencies for direct electron impact could be measured in this manner. Several series of experiments were performed. The interferometer proved incapable of detecting fluorescence from these mixtures at pressures below 1 mt. At pressures above 1 mt optical thickness becomes severe. The integrated intensities in each band do not scale linearly with pressure, indicating serious cross-talk between the molecules. This interaction may be due to an alteration of the secondary electron energy distribution or to vibrational energy transfer. In an attempt to work at low pressures, the CVF was used to monitor fluorescence down to 0.05 mt. At these low pressures, the integrated intensities smoothly increase with pressure, but NO fluorescence is enhanced when CO is added, and CO is slightly diminished in intensity when NO is added to the reaction zone. We have performed mixing tests and feel concentration inhomogeneities are small. The relative intensities depend on time during the beam pulse and it is likely that gas



A-1803

Figure 57. Spectrum of 0.5 mt NO, 0.5 mt CO mixture irradiated by 6 mA of 6 kV electrons. CVF resolution scales linearly with wavelength but is shown at 5 μm .

transport is affecting our observations. At these low pressures excited volume transport times are less than 10 ms (see Figure 50) while radiative lifetimes are considerably longer, and differ by a factor of three for CO and NO. Quantitative measurements of relative excitation efficiencies must await more data with good time resolution to minimize transport losses.

4.2.4 NO(v) Relaxation by NO - In order to test our understanding of the kinetic regimes accessible inside refurbished LABCEDE, we undertook a set of measurements which fully demonstrated device capabilities. Relaxation of NO(v) by NO has been measured to be rapid at room temperature (on the order of $10^{-12} \text{ cm}^3 \text{ molecule}^{-1} \text{ s}^{-1}$). Our measurements were performed under cryogenic (90K) conditions using the CVF to monitor NO fundamental band fluorescence arising from 5 percent NO in argon over a range of total pressures when irradiated by 3 kV electrons (pulsed on for 10 ms, off for 150 ms). This data was acquired in the time-resolved mode. The emission intensity is recorded at

32 times at 5 ms intervals during and following the electron beam pulse, while the CVF wheel was at a fixed position. The intensity at each time interval is averaged over many (25) electron beam pulses and then the filter is moved to a new position corresponding to a different wavelength. The wavelength difference between successive filter positions is a small fraction of the spectral resolution. The signal from CVF is amplified by a PAR 113 (gain 10-200, band-pass 0.1 to 30 Hz) and given to the computer. NO fluorescence peak intensities are on the order of 10^{-7} W/cm² sr μ m.

The first step in data analysis was to normalize the intensities for the gain of external amplifiers and then correct them for the variable wavelength response of the detector/filter system. The data is then corrected for the presence of a time-independent background emission by subtracting the signal recorded during the final time interval, when all electron-beam-induced emission has decayed away, from the data at all other times. The data is then formatted into arrays, corresponding to complete emission spectra recorded at each time interval, in order to fit the spectra to vibrational populations.

The spectral fitting routine assumes a Boltzmann rotational equilibrium and fits the magnitudes of vibrational basis functions to the observed spectra. These basis functions are unit intensity rotational manifolds, calculated assuming a rotational temperature of 90K, normalized by the Einstein coefficient appropriate to that vibrational level, and smoothed using a triangular integration function which coarsely simulates the resolution function of the circular variable filter. Typically, 8 to 16 vibrational basis functions are required to fit an NO spectrum. The output of the routine is a list of relative populations in each vibrational level, scaled by the peak signal intensity in order to compare populations at different time intervals.

The spectrum at each time interval is fit in this manner, enabling us to generate an array of vibrational populations as a function of time during and following the electron beam pulse. By studying the behavior of these vibrational levels as a function of pressure, gas composition, and excitation conditions the influence of diffusion, quenching, and radiation on the observed infrared emission was unraveled.

These initial studies were of Ar/NO mixtures. Mole fraction was held constant while total pressure was varied between 1 and 50 mtorr. The vibrational distribution was strongly quenched at the highest pressures, exhibiting only $v' = 1$ emission. At the lowest pressures emission from $v' < 16$ was observed at beam termination.

As an example, the fluorescence spectrum of 5 percent NO in argon at 6 mtorr (6×10^{14} molecules/cm³) total pressure at 90K is given in Figure 58. CVF intensity is plotted against infrared wavelength. Emission persists to 7 μ m. A spectral fit to that data is shown in Figure 58. Contributions from 16 vibrational basis functions are indicated. The heavy line is the sum of the contributions and represents a best, least-squares fit to the data. Populations (proportional to spectral intensity) determined from Figure 59 and another spectrum at a time well after beam termination are plotted in

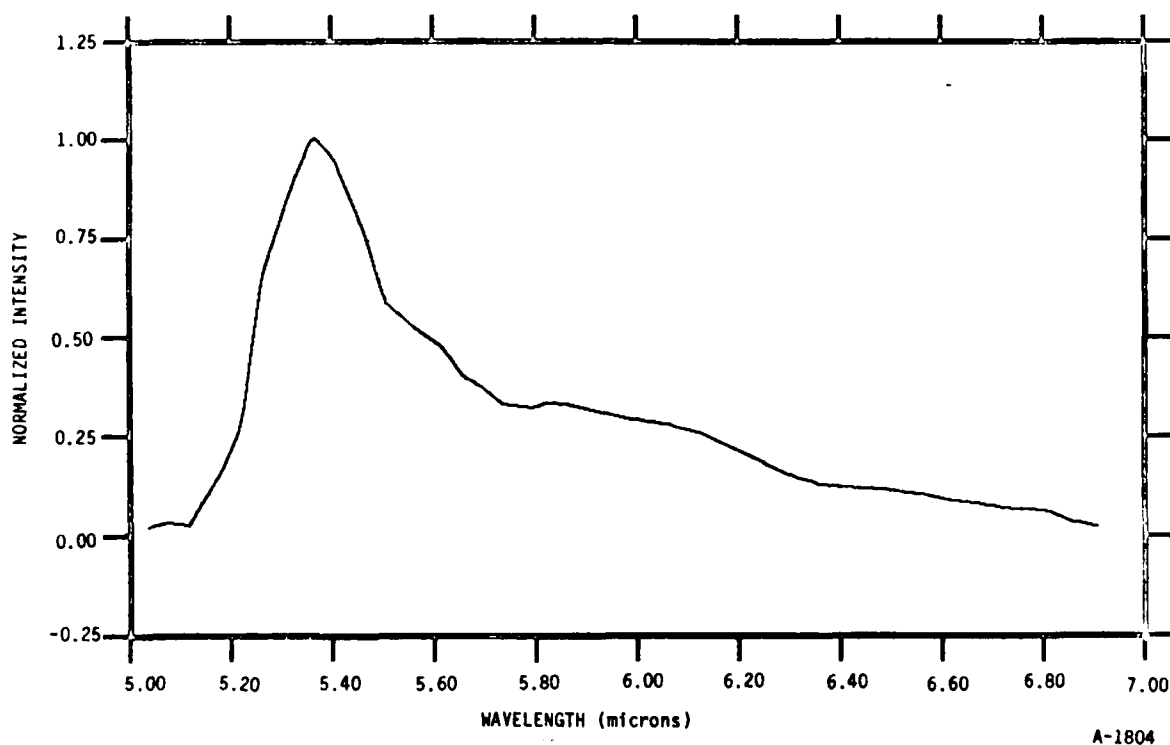


Figure 58. NO fundamental band fluorescence at beam termination from an Ar/NO (5%) mixture at 6 mt total pressure.

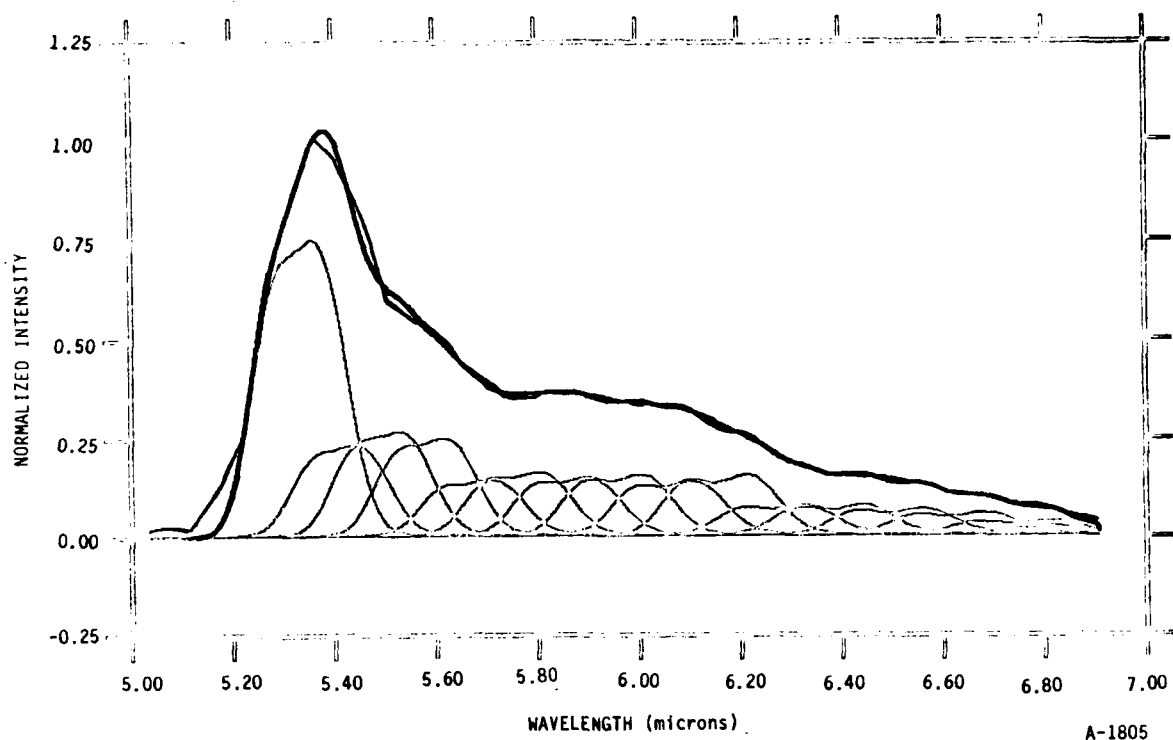
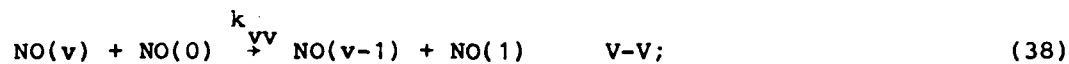
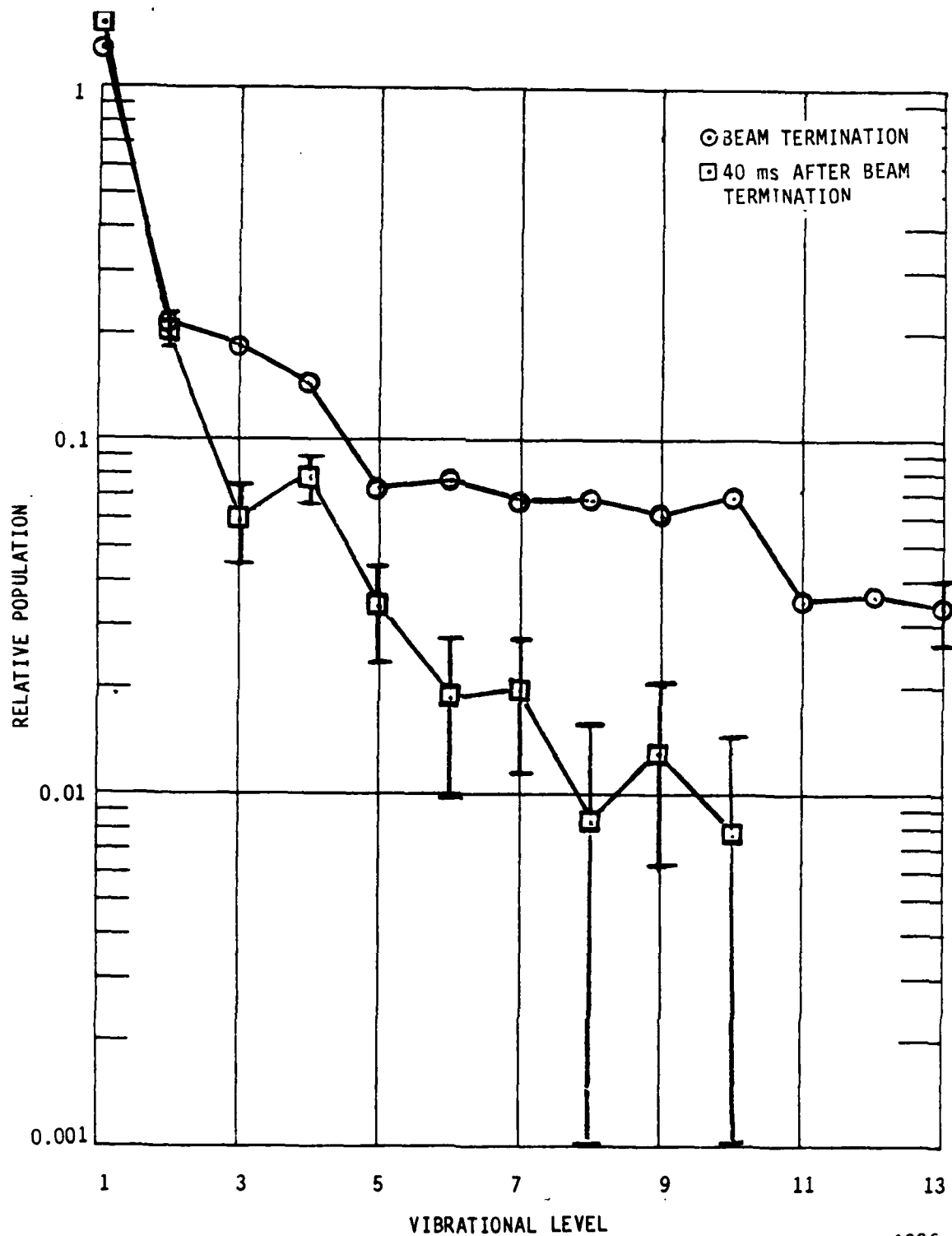


Figure 59. Synthetic spectrum comprised of emission from $\text{NO}(v < 16)$ which is best fit to the data of Figure 58. Rotational temperature is 90K.

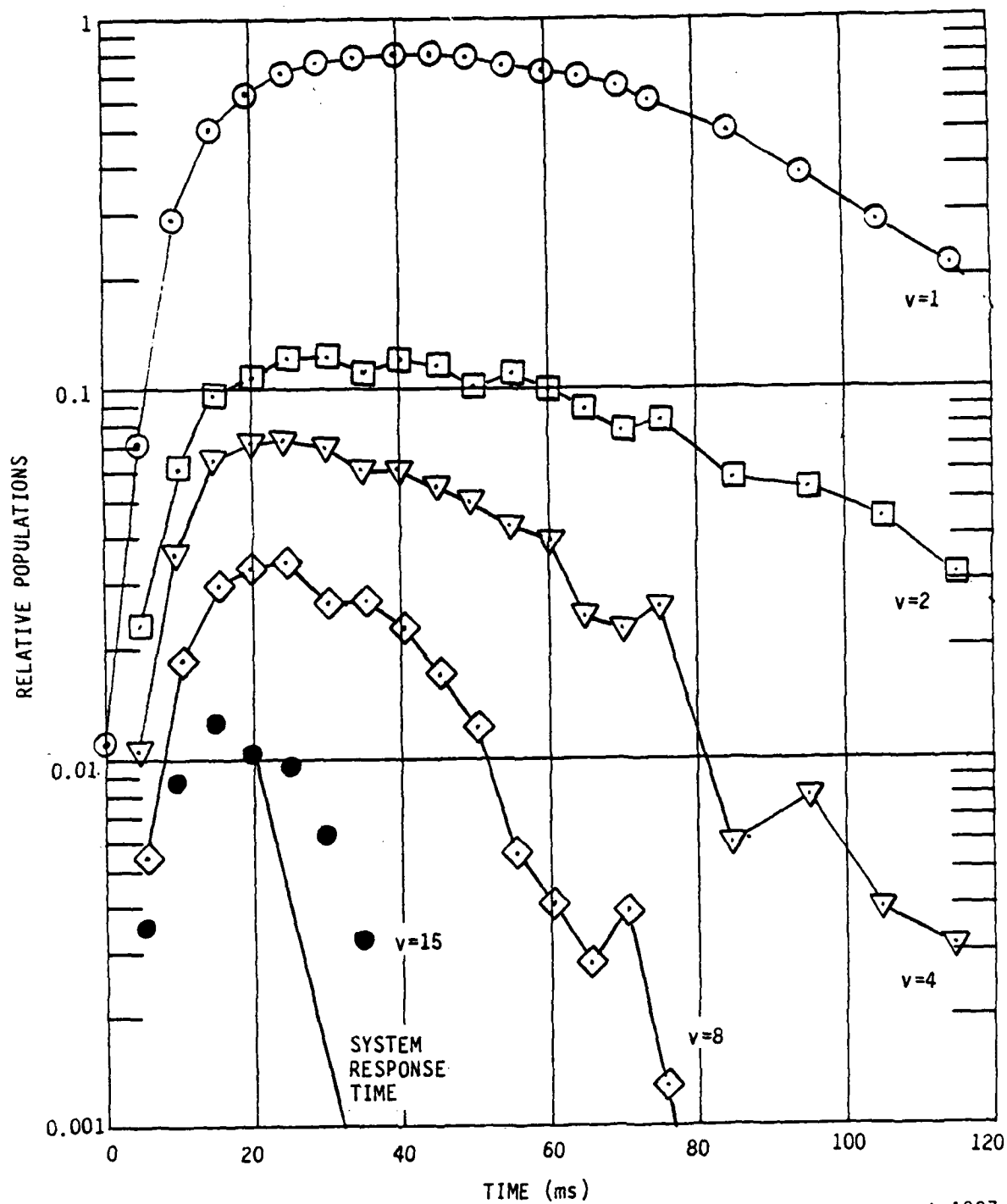
Figure 60. Spectra at 5 ms time intervals were analyzed. The resulting population histories of the vibrational levels are shown in Figure 61. The levels are coupled by several relaxation processes. V-V and V-T quenching as well as radiation and diffusion, all result in loss of $\text{NO}(v)$ molecules in the field of view. Our approach is to relate the time integrated population history to loss processes and feed from levels above via a set of master equations. The relevant kinetic processes considered include:





A-1806

Figure 60. NO vibrational distributions at beam termination and 40 ms later for Ar/NO data at 6 mt pressure.



A-1807

Figure 61. Vibrational population histories for representative vibrational levels. Noise rise during (and after pulse for lower v) as excitation and cascade occurs.

After excitation stops, the populations of the coupled levels can be written

$$\frac{dn_v}{dt} = R_{v+1}n_{v+1} - R_v n_v - Dn_v \quad (42)$$

or

$$R_v(s^{-1}) = - \sum_{i=v}^N \Delta n_i / a_v - D \sum_{i=v}^N a_i / a_v \quad (43)$$

where

$$R_v = k_{vv} NO(0) + k_{vT} M + A_{v+v-1}.$$

By choosing appropriate experimental conditions, diffusion can be minimized and we can determine the role of quenching.

Calculated kinetic deactivation rates, R_v , due to all processes are given in Figure 62 for levels 1-7. Estimates of diffusion losses and radiative decay rates are also plotted for comparison. The residual decay rate is attributed to quenching. Quenching by argon will be negligible under these conditions and from the known NO concentration, quenching coefficients for the process $NO(v) + NO(0) \rightarrow NO(v-1) + NO(1)$ can be determined as plotted in Figure 63. Literature values for room temperature quenching are shown for comparison. The results are preliminary, but agreement is quite good. This exercise certainly demonstrates the ability of LABCEDE to perform kinetic measurements. In the future we will acquire and analyze data from other NO partial pressures to more accurately remove the effects of other loss processes through a Stern-Volmer analysis.

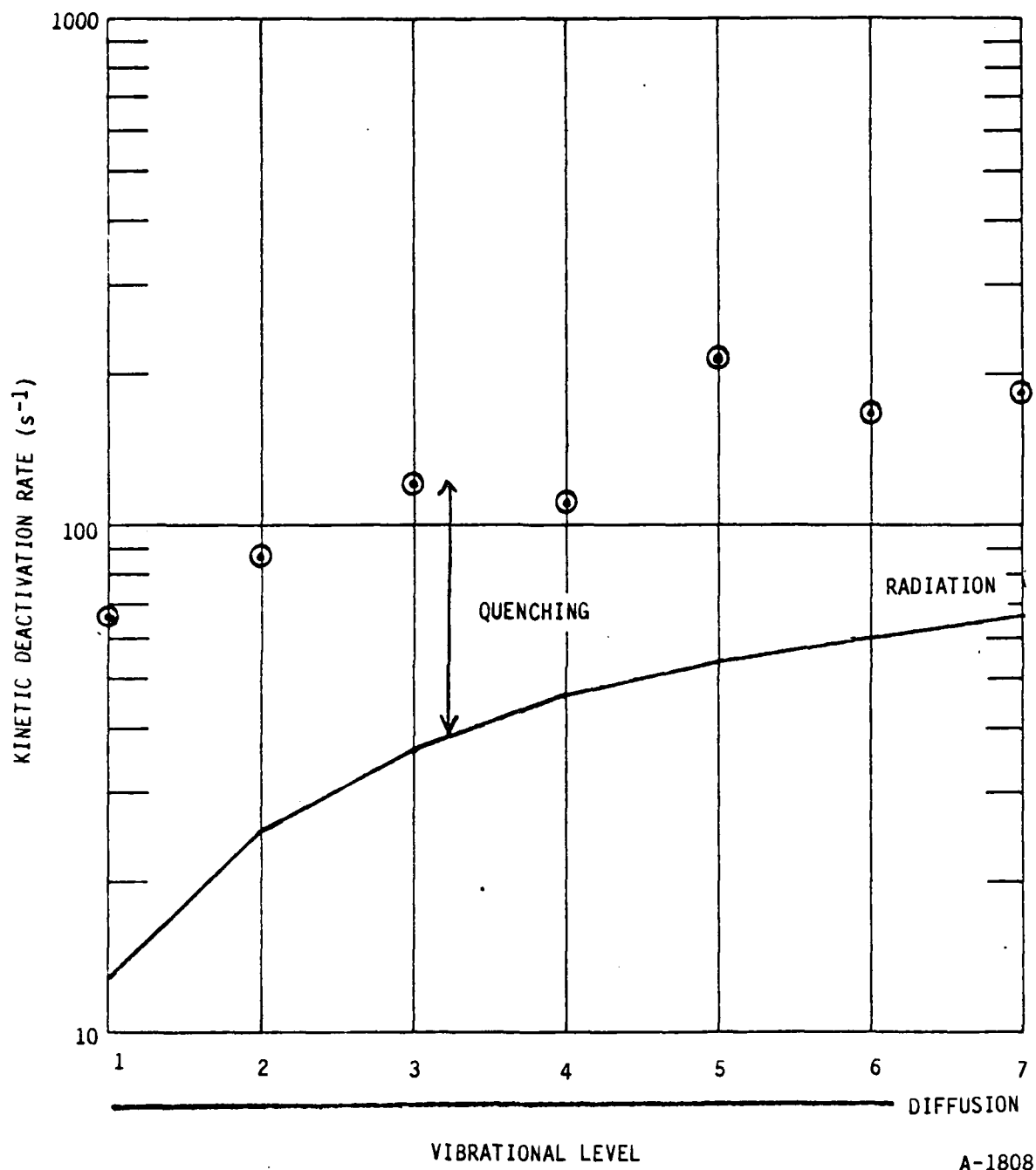
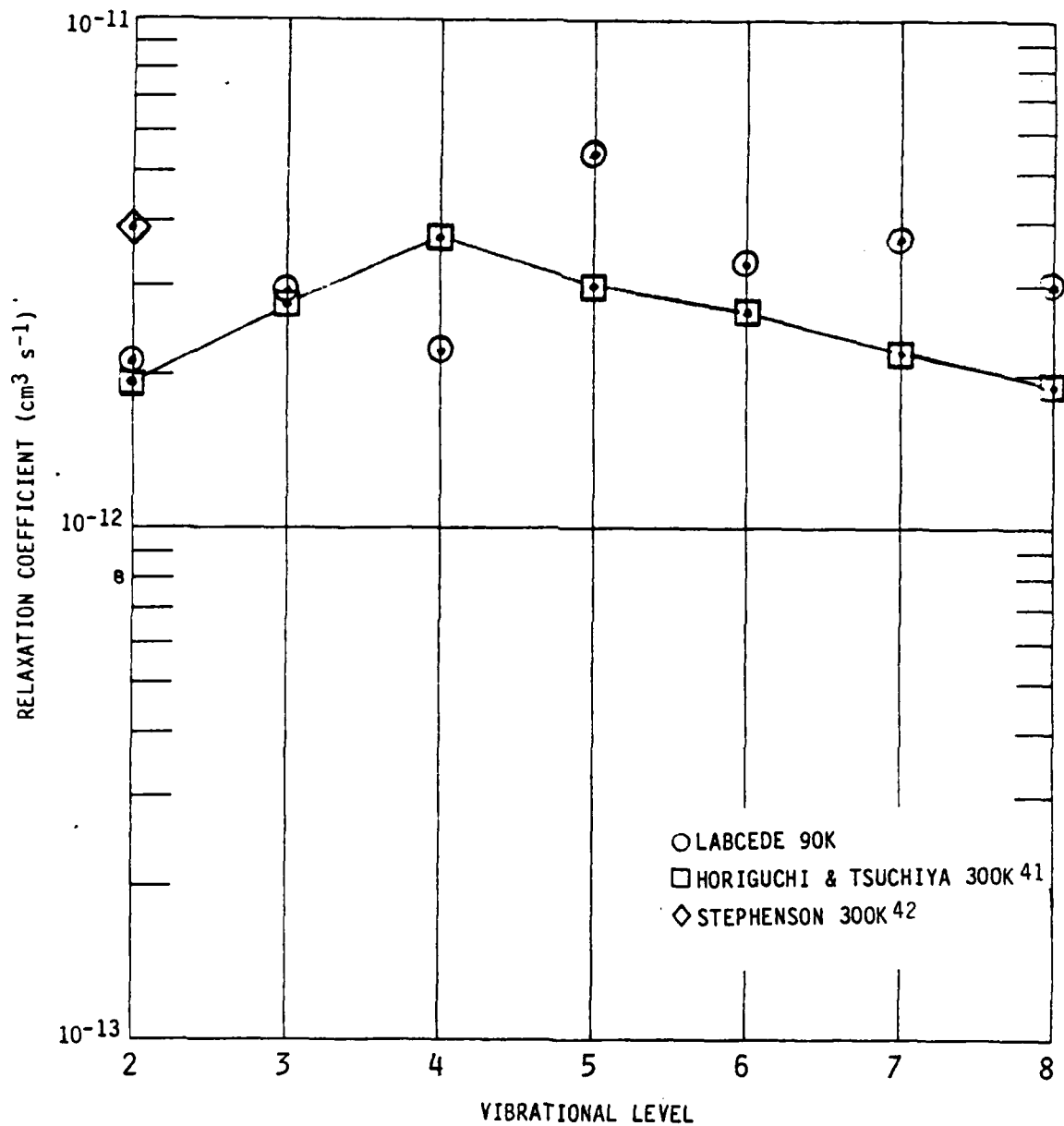


Figure 62. Total relaxation rates for Ar/NO 6 mt data. Estimates of radiative decay and diffusion are indicated for comparison.



A-1809

Figure 63. Preliminary relaxation rate coefficients for $\text{NO}(v)$ by NO at 90K. Values of room temperature measurements are shown for comparison.

4.2.5 Ozone Fluorescence - When pure oxygen or oxygen/N₂, Ar mixtures were irradiated, O₃(ν_3) fluorescence was clearly observed between 9.2 and 10.4 μm as illustrated in Figure 64. That spectrum was taken observing pure O₂ at 6.3 mt under moderate flow conditions. Due to the presence of the large spike in the signal at 8.5 μm (due to a faulty mask in the filter wheel), care had to be taken when collecting data around 9 μm . Even in the pulsed mode, complete rejection of the large DC component was difficult and the best data was acquired by manually scanning the wheel away from the spike region. The $\nu_1 + \nu_3$ band was also observed at 4.7 μm . Ozone ν_3 fluorescence was detected at significant intensities down to 0.35 mt when BPD was occurring (1.5 mt when it was not) and persisted up to the high pressure limit of the apparatus. Integrated band intensities covered the range of 10^{-10} - 2×10^{-9} W/cm² sr.

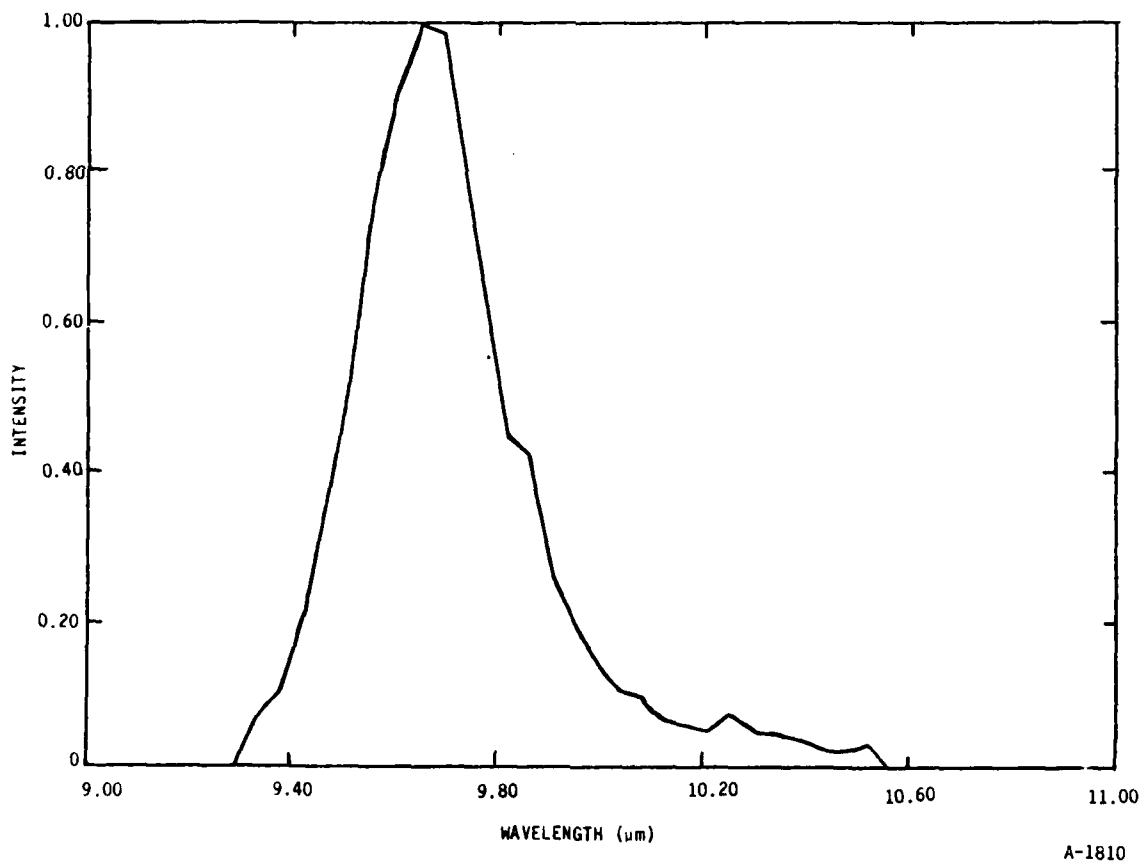
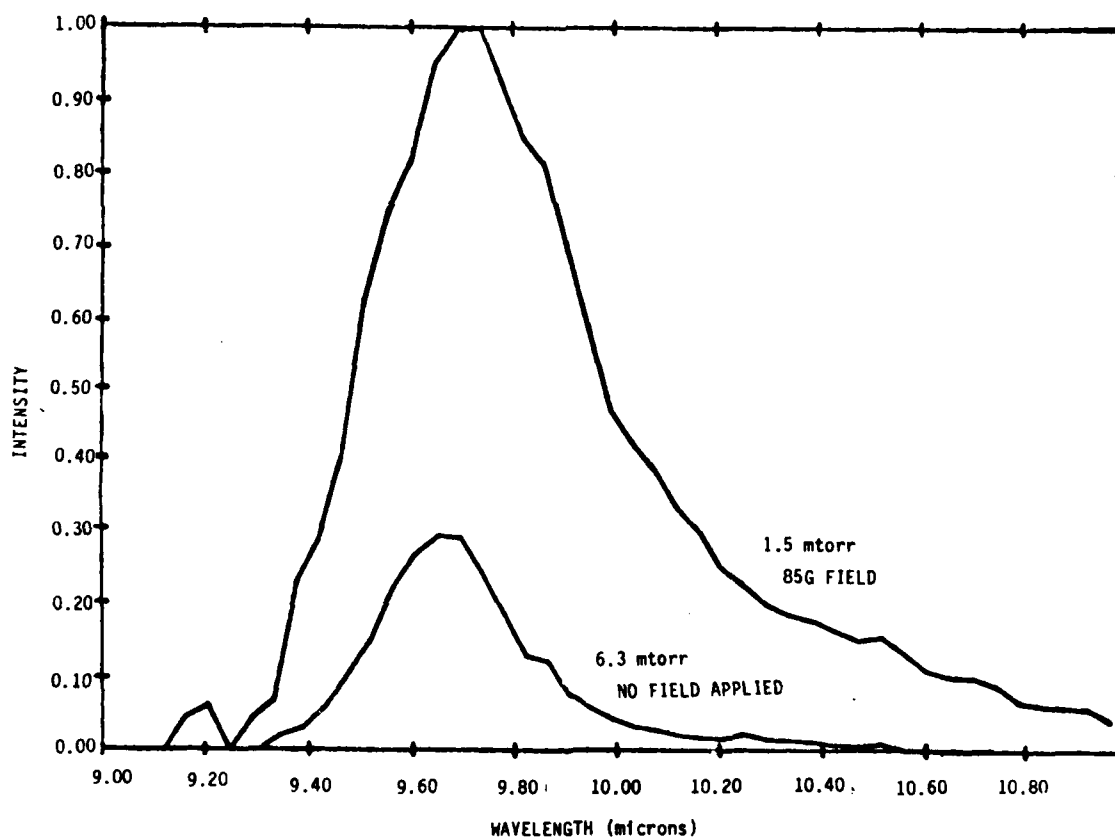


Figure 64. Ozone ν_3 band fluorescence from 6.3 mt of O₂ flowing at 250 sccm as irradiated by 6 mA of 5.5 kV electrons with no applied magnetic field.

At moderate dosing levels, the LWIR fluorescence observed had a relatively cold vibrational distribution, similar to that observed in the aurorally excited thermosphere as observed by the HIRIS flight.⁴⁰ When BPD occurred, both the intensity and vibrational distribution were enhanced as demonstrated in Figure 65. In that figure, the more intense "BPD" spectrum arose from O₂ at one-quarter the pressure of the field off spectrum, yet is three times as intense. When no field is applied, O₃ fluorescent intensity scales greater than linearly (almost quadratically) with pressure yielding a "BPD" enhancement of ~50. From the figure, it is also evident that the "BPD" spectrum has an enhanced LWIR tail; i.e., relatively higher vibrational levels are excited. The "BPD" vibrational distribution is less excited - "colder" - than the ones observed in the sunlit mesosphere or in COCHISE which are the product of the $O + O_2 + M \rightarrow$ chemiluminescent reaction.



A-1811

Figure 65. Scans of O₂ irradiated by 6 mA of 5.5 keV electrons. Two spectra correspond to 6.3 mtorr of O₂ with no magnetic field applied and 1.5 mt of O₂ with an 85 Gauss applied field demonstrating BPD intensity enhancement and shift in vibrational distribution.

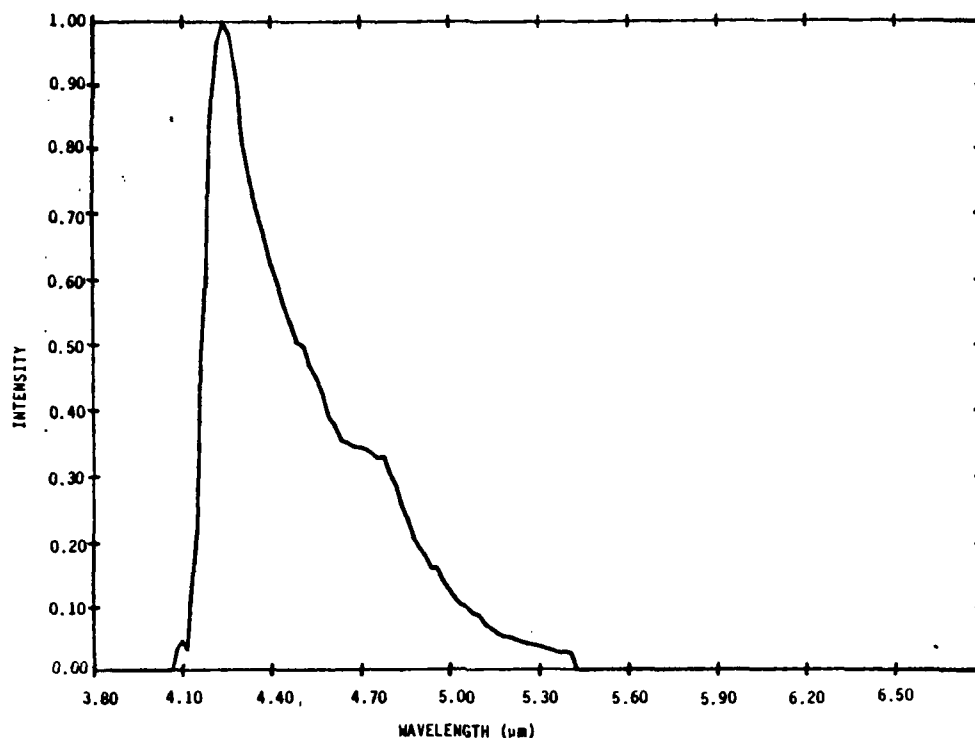
As pressure is increased to 10 mt, the discharge is quenched and no enhancements can be realized using applied fields. As pressure was increased further, the fluorescence bandwidth decreased, indicating that either another excitation mechanism was responsible for the vibrational distribution or that relaxation of $O_3(v_3, v > 1)$ was occurring. Argon and nitrogen diluents were observed to affect the distribution less than pure O_2 at comparable pressures, perhaps indicating O_2 is a more effective collisional relaxation partner than the others.

Several possible mechanisms could be occurring in LABCEDE to create/-excite $O_3(v_3)$ molecules. Recombination is a likely source. If the electron beam is efficient at dissociating O_2 even at the one percent level, then the residence time in the apparatus is sufficient to create O_3 concentrations which would radiate at the observed intensities. Moreover, the strong dependence of observed intensity on flow highlights the role of beam-created species such as O-atoms. The BPD enhancement could also result from enhanced O-atom production. The observed v_3 vibrational distribution does not match the known recombination chemiluminescence distribution at any chamber pressure. Additionally, the observed fluorescence decays upon beam termination. Such would not be the case if recombination were the source. Possibly the recombination reaction creates O_3 outside of the field of view. Ozone has a vapor pressure of 50 mt inside cryogenic LABCEDE, so that the only physical loss process will be pumping. Ground-state ozone created by recombination can recirculate back to the beam irradiated volume and be excited by direct electron impact. An alternative source might be the creation of O_2 high lying metastables (such as the $A^3\Sigma_u^+$, $A'^3\Delta_u$, or $c^1\Sigma_u^-$ states) which are energetic enough to promptly react with O_2 in a two body reaction to create $O_3(v_3) + O$.

Future investigations will employ time-resolved techniques to identify O_3 mechanism(s) operational in LABCEDE, by varying dosing, composition, diluent and flow in a systematic manner. Measurement of quenching rates also appears to be possible for $O_3(v_3)$ by O_2 .

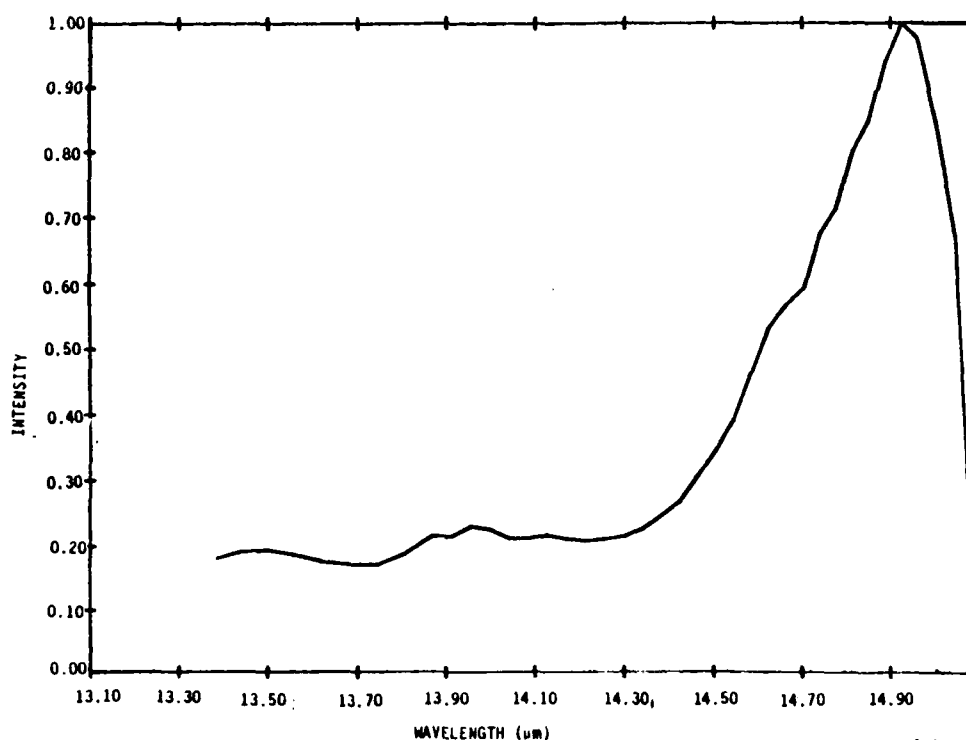
4.2.6 CO₂ Fluorescence - Fluorescence from several bands of CO₂ was observed under cryogenic experimental conditions using the CVF spectrometer. Because CO₂ has a very low vapor pressure ($< 10^{-7}$ torr) at 77K, it was not introduced into the shroud via the porous tube array, but rather through the jet inlet which is not in equilibrium with the shroud. The maximum CO₂ flows possible were ~50 sccm. Use of the jet inlet and condensation on the walls prevents quantitative absolute measurements since CO₂ concentrations (radial and absolute) are unknown and concentrations in the excitation/observation volume have only been modeled crudely (see Section 2). Determination of relative excitation efficiencies however, does not depend on knowledge of absolute concentrations. Series of runs on eight different days yielded a wealth of intriguing observations.

CO₂ ν_2 (15 μm) and ν_3 (4.3 μm) bands were observed under optically thin conditions when no beam plasma discharge was occurring, as shown in Figures 66 and 67. These spectra were taken using a lock-in amplifier to monitor the signal from 5 mt of Ar irradiated by 7 mA of 6 kV electrons. The CO₂ flow was 1.2 percent of the Ar flow. No external magnetic field was applied. Emission at 2.7 μm was also observed. Both Ar and N₂ were used as diluent gases for these observations. CO₂ fluorescence was seen in both gases, but Ar produced brighter CO₂ intensities. In Ar, chemistry is minimized. CO fundamental band fluorescence is present at wavelengths greater than 4.7 μm in Figure 66, and is responsible for the long wavelength tail of the observed spectrum. In Figure 67, the small maximum at 13.9 μm is reproducible and is thought to be the Q-branch of the $\nu_1 \rightarrow \nu_2$ transition previously observed by HIRIS. Due to incompetence (as described in Section 2), this segment of the CVF wheel cut off at ~14.98 μm and so misses the CO₂ ν_2 P-branch and possibly the entire Q-branch. If this is the case, the fluorescence detected represents only 30 percent of the total bandstrength. Thus exact determination of excitation efficiencies is not possible. Given these caveats, the ν_1 band intensity suggests an excited state concentration [CO₂(ν_1)] which is ~ 2 percent of the ν_2 concentration. This corresponds to an intermode vibrational temperature of 250 to 300K. Peak radiance levels observed are weak ($\sim 10^{-10}$ W/cm² sr μm) but well above the noise level.



A-1812

Figure 66. CO_2 v_3 and CO fundamental band fluorescence as detected by the CVF. Gases are optically thin and no BPD is present.

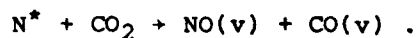


A-1813

Figure 67. CO_2 (v_1) and partial (v_2) features under some conditions as shown in Figure 66. Intensity is a factor of five weaker in this region.

In nitrogen, the calculated v_2 concentrations are two orders of magnitude greater than the v_3 concentrations under low dosing conditions at low pressures. These concentrations reflect the overall balance between direct electron excitation, energy transfer, radiative cascade and collisional quenching. Fluorescence spectra were also acquired in the time-resolved mode. $\text{CO}(v_2)$ signals were found to decay more slowly than v_3 (as expected from lifetime arguments). When 6 mt of N_2 /trace CO_2 (optically thin) were irradiated, the v_3 decay times were many times slower than its 2.3 ms radiative lifetime - energy transfer must be occurring (possibly $\text{N}_2(v) + \text{CO}_2(v_3)$). Under these conditions v_2 decays more slowly than v_3 , but is limited by excited volume transport not its radiative lifetime. The observed decays are substantially different when BPD is occurring. The v_2 decay is much faster indicating that the composition of the gas has been altered and quenching (perhaps by O-atoms) is increasing the decay.

A final intriguing observation in N_2/CO_2 irradiated mixtures is the presence of vibrationally excited NO and CO in the MWIR spectrum region, as shown in Figure 68. Both molecules are created with considerable ($v > 10$) vibrational excitation and continue to be produced after beam termination. Because at least one metastable nitrogen atom is created per ion pair in the gas, a likely mechanism is



When BPD is present, the observed vibrational distributions are colder, reflecting the fact that direct electron impact cross-sections for CO and NO may favor colder vibrational distributions than the chemiluminescent reactions. Several future measurements programs are planned to investigate this observation more carefully.

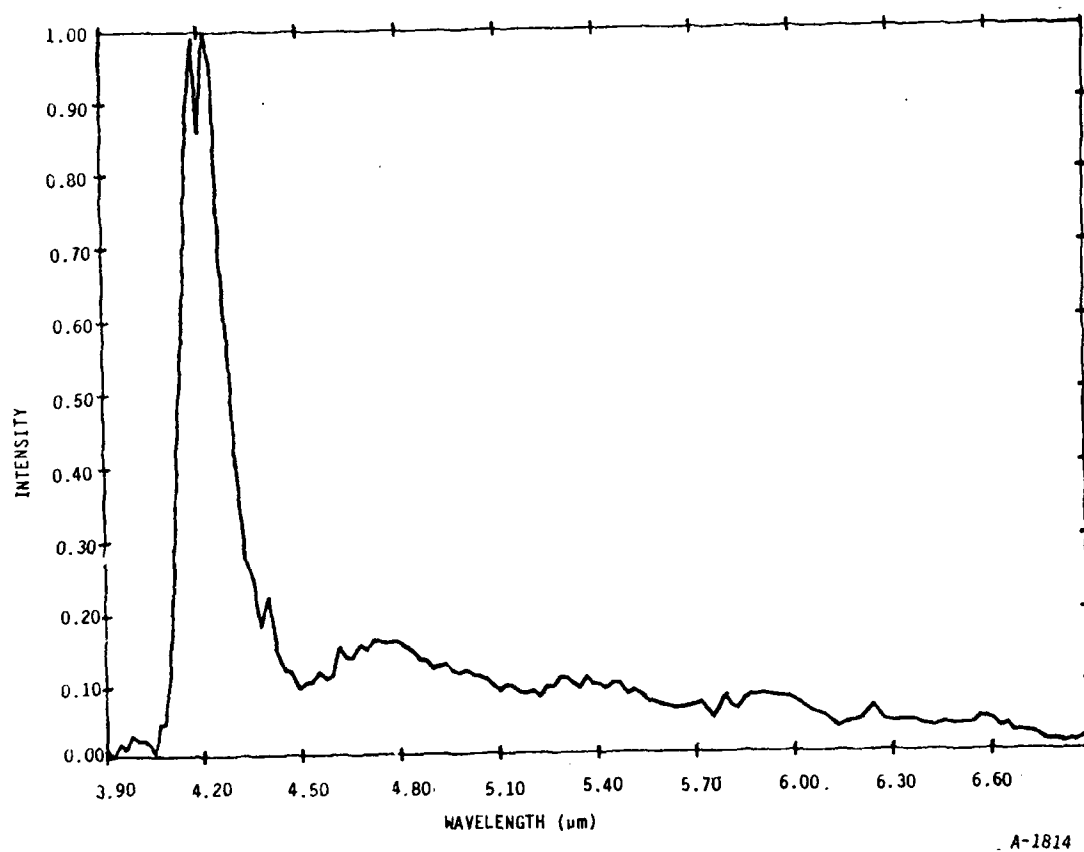


Figure 68. MWIR fluorescence from N_2 200 sccm/ CO_2 mixture at 1.7 mt total pressure when irradiated by 3.8 mA of 5.9 kV electrons. No field is applied. $CO_2(v_3)$, CO, and NO fundamental bands are observed.

5. OBSERVATIONS OF NH INFRARED CHEMILUMINESCENCE

5.1 Introduction

The reactions between metastable $N(^2D)$ nitrogen atoms and a variety of diatomic and triatomic molecules have undergone considerable study in the last decade and the rate constants for a number of these reactions have now been well established.^{43,44} Little attention has been directed to the products of these reactions, however. The one exception appears to be the reaction between $N(^2D)$ and O_2 which has been shown⁴⁵ to produce NO, vibrationally excited up to at least $v = 12$. The purpose of this paper is to present experimental evidence that the reaction between $N(^2D)$ and H_2 produces vibrationally excited $NH(v < 3)$.

5.2 Experiment Description

These experiments were performed on the LABCEDE facility situated at the Air Force Geophysics Laboratory. In this device a constant pressure, continually flowing gas is irradiated by a well-collimated electron beam. The infrared radiation produced by the electron/gas-target interaction is viewed at right angles to the beam by a Michelson interferometer computer-interfaced to allow time dependent Fourier spectroscopy.⁴⁶ The details of this facility have been previously described⁴⁷ and will not be discussed further here. In the present experiments mixtures of 8 torr N_2 /0.0-0.3 torr H_2 were irradiated with an ~ 1 mA beam of 40 keV electrons. The beam pulse duration was 3 ms with a 30 percent duty cycle. The irradiated gas had a total chamber residence time of 2.5 sec; the test gases used were greater than 99.99 percent pure. The interferometer was equipped with an InSb detector operated at 77K. The detection network had a total response time of 100 μs and the instrument provided a spectral resolution of 10 cm^{-1} .

5.3 Experimental Results and Interpretation

A typical spectrum arising from this gas mixture, in the 3000 cm^{-1} region, is shown in Figure 69. No other spectral features were observed in

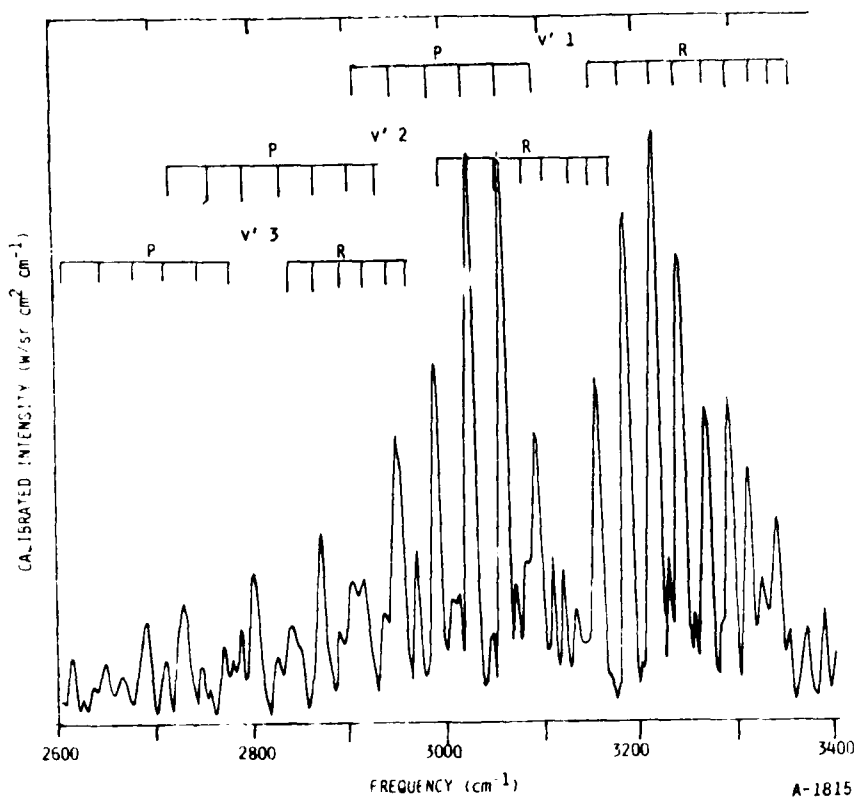


Figure 69. $\text{NH}(\Delta v=1)$ emission observed in a mixture of 7.5 torr N_2 0.05 torr H_2 . Beam conditions of $I = 1.1$ mA, $V = 40$ keV. Spectral resolution 10 cm^{-1} .

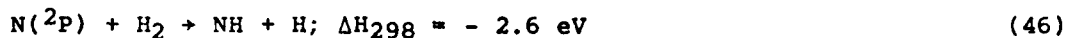
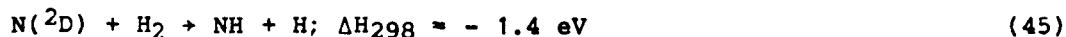
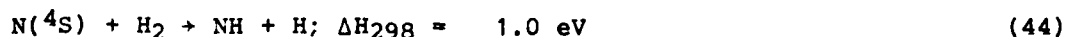
the 1800 to 6500 cm^{-1} system bandpass. This data has been corrected for detector responsivity and exhibits a relatively good S/N. The observed radiation is clearly identified as due to $v = 3 \rightarrow 2$, $2 \rightarrow 1$, and $1 \rightarrow 0$ fundamental vibration/rotation band transitions of ground state NH . No evidence of transitions arising from $\text{NH}(v > 3)$ are observed. The rotational assignments shown in the figure are based on previous identifications of Sakai⁴⁸ who has examined NH fundamental band fluorescence under high spectral resolution in a discharge experiment. The observed radiation signatures, such as shown in the figure, remained relatively invariant while the beam was on and upon beam termination were found to decay with a time constant only slightly longer than that of the system. The implication is that $\text{NH}(v)$ is primarily produced only when the beam is on and undergoes a rapid decay.

The radiation intensity of each v, J transition is proportional to the product of the population of the upper state of the transition and the respective Einstein coefficient. The vibrational level dependent Einstein coefficients for NH ⁴⁹ were used to determine the vibrational populations from the

individual line intensities. It is found that the observed rotational distributions are consistent with those for $T_R = 300$ K and that the vibrational populations of levels $v = 1-3$ are in the ratio 0.82, 0.13, 0.04, respectively. This corresponds to a Boltzmann vibrational temperature of approximately 3000K. Although these observations are affected by quenching phenomena, they suggest that the nascent distribution of NH states is high vibrationally excited.

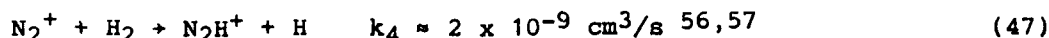
It is possible to speculate on the NH formation mechanism under these conditions. The primary neutral species formed during the electron irradiation are $H(2S)$, $N(4S)$, and the metastable states $N(2D)$, $N(2P)$ and $N_2(A)$. It has been shown experimentally⁵⁰ that ground state hydrogen atoms do not react with N_2 . Tanaka and McNesby⁵¹ have shown that $H(2P)$ reacts with N_2 with ultimate formation of NH_3 ; however, the $(2P)$ state corresponds to the strongly allowed Lyman α transitions and any $H(2P)$ formed by electron irradiation would most probably decay prior to chemical reaction under the present conditions. It is unlikely that the quenching of $N_2(A)$ state by H_2 would lead to an NH product, as this requires a highly improbable four center reaction. Three body recombination of N and H atoms could provide vibrationally excited NH; however, the rate for this reaction is expected to be small given the low atomic species concentrations in the system and the fact that $k_1 < 6.4 \times 10^{-32} \text{ cm}^6\text{s}$.⁵² Moreover, if this reaction occurred, it would proceed even after beam termination because of the anticipated slow decrease in the concentration of atomic species.

The potential reactions between nitrogen atoms and H_2 which can lead to NH formation are

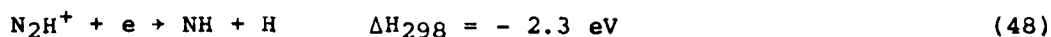


where the NH heat of formation recently specified by Piper⁵³ has been used in evaluating the reaction energetics. The reaction between H₂ and ground state nitrogen atoms is endothermic by 1 eV and will not proceed at room temperature. Furthermore, although both reactions (45) and (46) are exothermic, it can be shown⁵⁴ that there is no adiabatic pathway between the reactants and products of reaction (46). Indeed, there is not even an exothermic adiabatic pathway for producing the products in electronically excited states.⁵⁴ This observation is reflected in the observed low value⁵⁴ for the rate constant for quenching of N(²P) by H₂, 1.9 x 10⁻¹⁵ cm³/s. Alternately, an adiabatic pathway is available for reaction (45),⁵⁴ and the rate constant for this process has been measured^{43,44,55} to be 2.1 x 10⁻¹² cm³/s. This reaction is only sufficiently exothermic to produce NH(v < 3). Lastly, under the present experimental conditions the collisional lifetime for N(²D) varies between 40 and 200 μs. Thus, as observed, NH formation by this process would cease at beam termination when N(²D) production ceases.

There is also a potential ionic pathway for formation of NH. The dominant beam-created ion in this gas mixture is N₂⁺ however this species will rapidly react with H₂ to form N₂H⁺, i.e.,

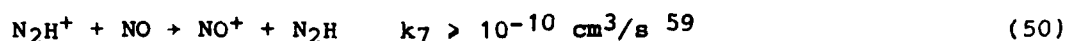
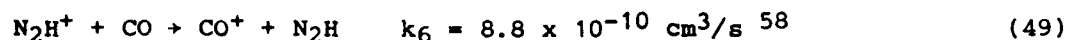


N₂H⁺ does not react further with any of the neutral species in the gas mix and thus becomes the terminal positive ion, being lost only by electron-ion recombination. The products of this latter reaction have never been measured however one of the two possible reaction branches can lead to formation of NH,



The characteristic lifetime for N₂H⁺ under the present conditions is estimated to be 60 μs and reaction (48) is sufficiently exothermic to produce NH(v < 6). Thus, this formation mechanism would also be consistent with the observations.

A series of measurements were performed in order to distinguish between mechanisms (45) and (48). Specifically additional molecular species which would react with N_2H^+ were introduced to the N_2/H_2 gas mix. It has been determined that both NO and CO undergo rapid charge exchange reactions with N_2H^+ , i.e.,



Furthermore, in the gas mixtures of interest, the positive ions CO^+ and NO^+ do not appear to have reaction pathways which would allow reformation of N_2H^+ . Thus, if a sufficiently large concentration of these species is introduced into the gas mix, N_2H^+ will no longer be the terminal positive ion and the effects of reaction (48) will be obviated.

It is to be noted that $N(^2D)$ may also be quenched by the introduction of these species. The rate constant for quenching of $N(^2D)$ by CO is $\sim 2-6 \times 10^{-12} \text{ cm}^3/\text{s}$,⁵⁵ about the same as that for H_2 , whereas the rate constant for quenching by NO is near gas kinetic,⁵⁵ $0.6-1.8 \times 10^{-10} \text{ cm}^3/\text{s}$. Therefore introduction of a sufficient quantity of NO would also act to eliminate reaction (45) as a source of NH.

Measurements were performed with both NO and CO additives in a base mixture of 8 torr N_2 0.2 torr H_2 . The beam conditions were as described previously. From the predicted energy deposition and known rate constants for reactions (49) and (50), it was deduced that CO and NO densities of $> 2 \times 10^{13} \text{ cm}^3$ and $> 2 \times 10^{14} \text{ cm}^3$, respectively, would be sufficient to supplant N_2H^+ as the dominant positive ion. The resulting observations of peak NH intensity are tabulated in Table 7. As can be seen, there is no significant change in NH radiation when CO is introduced, even though the N_2H^+ concentration should be significantly reduced upon this addition. On the other hand, the NH radiation is reduced upon introduction of modest amounts of NO (less than that required to supplant N_2H^+ as the positive ion) and is completely eliminated at higher NO

TABLE 7. OBSERVATIONS OF NH FUNDAMENTAL BAND PEAK INTENSITY

Run	(CO), cm ⁻³	(NO), cm ⁻³	Normalized Peak NH Intensity
1	-	-	1.0
2	9 x 10 ¹³	-	1.1
3	3 x 10 ¹⁴	-	0.9
4	1 x 10 ¹⁵	-	1.0
5	2 x 10 ¹⁵	-	0.8
6	-	8 x 10 ¹³	0.8
7	-	2 x 10 ¹⁵	0.0

concentrations. These observations are consistent with N(²D), rather than N₂H⁺, being the precursor of the NH radiation. Indeed even the slight reduction in NH radiation observed at the highest CO concentration is consistent with this observation.

5.4 Summary

In conclusion, radiation from vibrationally excited NH has been observed in electron irradiated mixtures of N₂/H₂. A preliminary review of the relevant neutral and ionic chemistry in electron irradiated N₂/H₂ mixtures suggests that N(²D) could be the precursor for NH through a chemi-excitation reaction with H₂. This suggestion is reinforced by the fact that reaction (45) is only sufficiently energetic to produce NH(v < 3) in accord with the experimental observations.

6. ABSOLUTE PRODUCTION RATES AND EFFICIENCIES OF NO IN ELECTRON-IRRADIATED N₂/O₂ MIXTURES

6.1 Introduction

Nitric oxide is a prominent infrared radiator in a variety of environments including high temperature combustion processes and the disturbed upper atmosphere. Knowledge of its vibrational distribution resulting from chemical reactions under these conditions is important both for predicting infrared radiances and for gaining some understanding of the reaction surface geometry through product-channel energy partitioning. In particular, the intensity and spectral distribution of vibrationally excited NO is a necessary input to the modeling of non-equilibrium atmospheric processes, such as aurorae. We report here our experimental measurement of the initial vibrational distribution of NO formed by irradiating N₂/trace O₂ mixtures with 36 keV electrons. The mechanism postulated under these conditions is $N(^2D) + O_2 \rightarrow NO(v \leq 18) + O$. By means of an absolute intensity calibration and modeling of electron beam energy deposition we have also determined the number of vibrationally excited NO molecules formed per ion pair created by the electron beam and the fraction of the electron energy deposited in the gas which goes into NO vibrational energy.

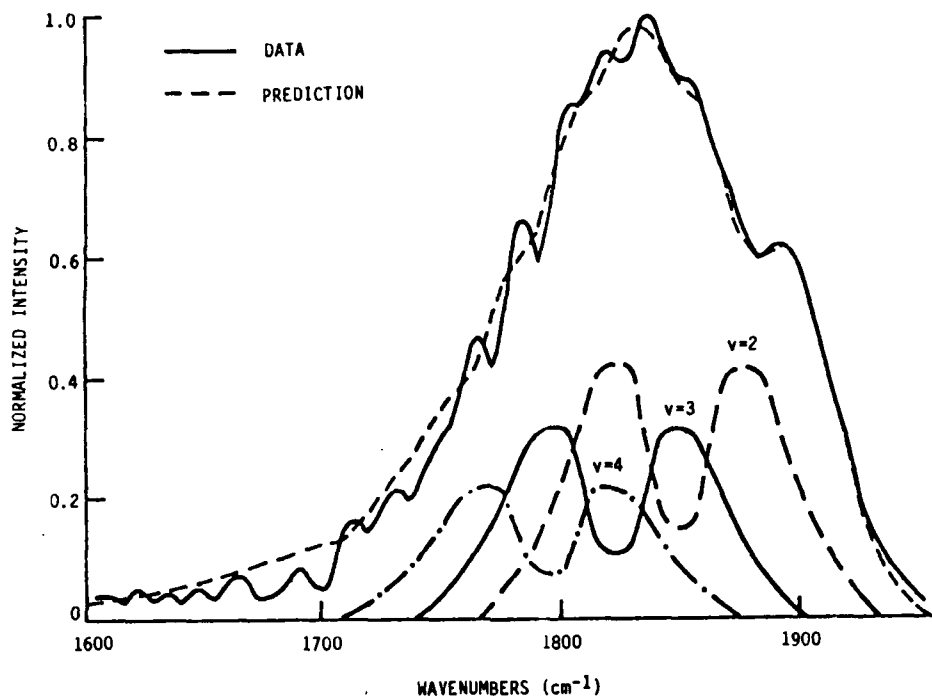
6.2 Experimental and Data Analysis

These experiments were performed at the Air Force Geophysics Laboratory on the higher pressure, higher voltage LABCEDE apparatus.⁶⁰ In this facility, a constant pressure, continuously flowing gas sample is irradiated by a pulsed electron beam. As the electrons pass through the gas mixture, they scatter inelastically with the molecules and deposit energy. When mixtures of N₂ and O₂ are irradiated, a portion of the deposited energy appears as NO vibrational excitation and a fraction of the vibrational energy is subsequently emitted as fluorescence. The emission is viewed perpendicular to the electron beam axis with a computer-interfaced Michelson interferometer operated with a lead

selenide detector. The scan length of the interferometer provides 10 cm^{-1} resolution. The technique of time-resolved Fourier spectroscopy is applied to observe simultaneously the time dependence of the fluorescence from all the emitting molecular vibrational levels.^{60,61} For these experiments 1 ms long pulses of 0.5 to 1.1 mA current of 36 keV electrons were focussed into mixtures of ultrahigh purity N_2 and varying trace concentrations of O_2 . With this apparatus it is not possible to detect vibrationally excited NO at pressures of N_2 and O_2 sufficiently low that the initial vibrational distribution of the NO can be observed prior to relaxation by collisions. Instead, the NO is formed under the collisionally coupled conditions of 50 torr of N_2 and 0.05 to 1.0 torr of O_2 . The temporally and spectrally resolved data acquired during electron irradiation can then be analyzed to determine relative excitation rates into the various vibrational levels if the relevant relaxation rates are known. Diffusion of the excited molecules out of the observation region does not occur on the time scales of these measurements.

Fluorescent intensities were acquired at 100 μs intervals during and after the electron beam pulse to obtain time resolved spectra of the formation and decay of NO. The data from 50 consecutive pulses was averaged to improve the signal-to-noise ratio and then stored on magnetic tape. The beam created contribution to the detected intensities was isolated from the background intensity by subtracting an interferogram acquired just before beam onset from the interferograms for subsequent times. During the electron beam pulse, the spectrally integrated intensity incident on the detector nearly reached steady state, indicating balanced production and loss rates. A typical spectrum is displayed in Figure 70. The observed decays of the spectral components following beam termination have been analyzed to obtain relaxation rates and rate constants for the quenching of the NO population in state v by collisions with O_2 .⁶² With the measured quenching rates, the data taken during NO formation can be analyzed to obtain relative excitation rates.

Several calibrations are required to make quantitative measurements of the amount of NO vibrational excitation produced by the electron beam. To



A-1816

Figure 70. NO fundamental band fluorescence spectrum at beam pulse termination from a 50 torr N_2 , 1.5 torr O_2 mixture. A synthetic spectrum fit to the data is also shown. Emission contributions from individual vibrational levels to the predictions are displayed for $v'=2$, 3, and 4.

obtain relative excitation rates, the spectral response of the detection system was determined using a standard blackbody point source at 1173K. To obtain the absolute amount of excitation produced, it was necessary to account for the nonuniformity of the field of view of the interferometer. In addition, the radiation source varied spatially as the electron beam spread across the field of view in the target chamber.

The blackbody source used for the spectral calibration was also used to map the intensity response across the interferometer's roughly circular field of view at the electron beam plane. The nonuniformity of this response is mainly due to vignetting by the optical system and nonuniform response across the surface of the lead selenide detector. Interferometer misalignment and optical element aberrations could also contribute to this nonuniformity.

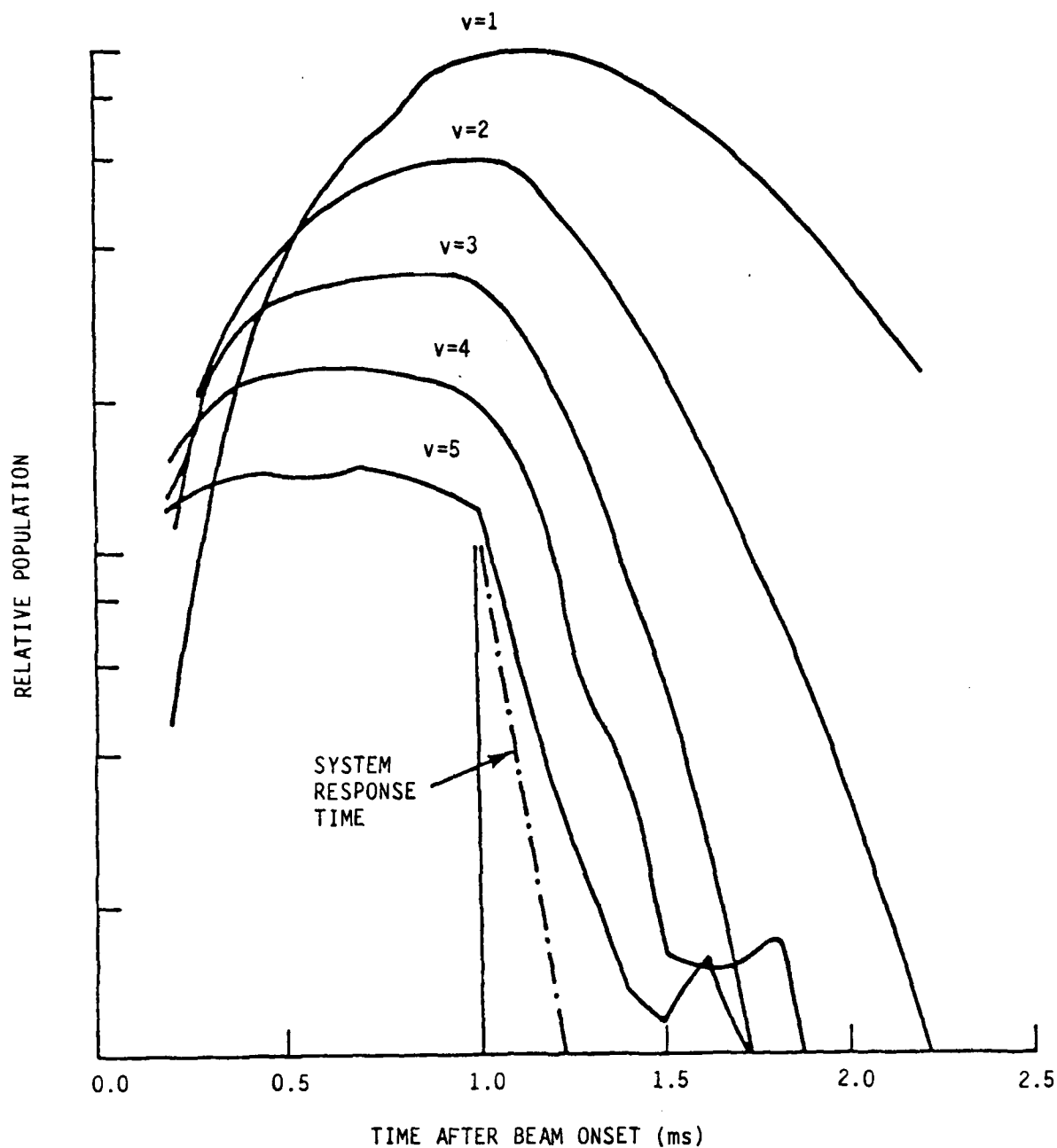
Interferometer alignment was verified by comparison of integrated spectral intensity (measured in volts) and detector signal (measured in volts). Knowledge of these responses permitted the interferogram signal voltages observed at the detector to be accurately related to a uniform illumination across the detection system's field of view in $\text{watts/cm}^2 \text{ sr cm}^{-1}$. In reality, the fluorescing molecules do not uniformly fill the detection network field of view. As the electrons collide with the gas molecules, they are scattered and the beam grows as a function of distance traveled from the entrance into the sample gas mixture. Secondary electrons (arising from scattering events) have a very small range under our conditions and closely follow the primary electron spatial distribution. Center⁶³ has measured the radial beam current density profiles for 20 to 100 keV electrons in thin N_2 targets. His observation was that the beam current distribution is Gaussian about the beam axis. Center's empirical formulas were used to calculate expected beam growth and radial distribution for our conditions of pressure, distance and voltage. The calculated beam shapes agreed well with visual observations. Detection system response was further adjusted to account for this non-uniform fluorescence spatial distribution, permitting the detected intensity to be related to the total intensity emitted by the irradiated gas. This quantity can then be compared with the modeled energy deposition to yield $\text{NO}(v)$ production efficiencies in these mixtures as discussed in Subsection 6.3.

Some specifics are useful in illustrating the calibration process. The detection system had significant spectral response from 1430 cm^{-1} to greater than 4000 cm^{-1} . The entire NO fundamental band was thus observed unclipped by detector response. Nonuniformities of the field of view reduced throughput to 73 percent of the pure geometric level. The interferometer viewed an 8.5 cm path of irradiated gas centered 8 cm from the beam entrance into the chamber. The conical beam grew to several centimeters radius, but about 90 percent of the electron scattering events along the 8.5 cm observed path fell within the circular field of view. Moreover, the fluorescent intensity was greatest along the electron beam centerline where the detection system spatial response was also greatest. Thus the above corrections and calibrations are not large factors, but are necessary for accurate emission intensity determination.

The calibrated experimental spectra were then fit to determine the intensity contribution of each vibrational level to the observed emission. Because NO is created only in trace amounts, self-absorption of the fluorescence is not important, and the observed emission intensity may be written as

$$I_n(\sigma) = \sum_v \frac{N_v A_{v \rightarrow v-1} hc\sigma \xi_v(\sigma)}{4\pi} \quad (51)$$

where N_v is the total number of molecules within the interferometer's field of view which are in vibrational state v , $A_{v \rightarrow v-1}$ is the fundamental band Einstein coefficient, $hc\sigma$ is the energy of the emitted photon of wavenumber σ , and $\xi_v(\sigma)$ is the unit intensity basis function describing the spectral signature of each rotational-vibrational band as it is degraded by the interferometer instrument function ($\sin x/x$ with 10 cm^{-1} FWHM resolution). Details of the construction of these basis functions are given in Ref. 62. Fluorescence is observed from molecules with up to ten vibrational quanta. However, because the emission from these levels is spectrally overlapped, a spectral curve fitting algorithm has been developed to distinguish the individual basis function contributions. The quantities $N_v A_{v \rightarrow v-1}$ are adjusted so that the square of the difference between the data and the fit $I_n(v)$ is minimized. The emitting state populations are then found using Billingsley's Einstein coefficients.⁶⁴ Populations were determined at $100 \text{ }\mu\text{s}$ intervals during and after the pulse. The temporal histories of the lowest five NO vibrational levels are plotted in Figure 71. As can be seen, the lowest levels have not yet reached steady-state during the 1 ms beam pulse. By the end of the electron beam pulse, the population in level 5 is stationary due to the balance between creation of $\text{NO}(v=5)$ and relaxation of higher levels into level 5 and loss by relaxation into lower levels. The temporal behavior of these kinetically coupled vibrational populations provides the information required to extract the rates of formation of NO in each vibrational level. Experimental data were acquired over a range of O_2 concentrations ($0.05\text{--}1 \text{ torr}$) in order to isolate the effects of O_2 quenching of both reactants and products.



A-1817

Figure 71. The temporal behavior of the vibrational populations of NO($v=1-5$) deduced from the spectral fitting of the time resolved fluorescence. Beam termination is at 1.0 ms.

6.3 Kinetic Analysis

The rates for creation of vibrationally excited NO may be determined directly from the deduced vibrational population histories if the competing effects of vibrational relaxation are properly taken into account. The deduced population decays have contributions from several relaxation processes. Quenching by N_2 , O_2 , and beam-created O-atoms dominates radiative decay losses. The total quenching of each level v , R_v , may be written as the sum of these processes

$$R_v = k_{O_2}(v)[O_2] + k_{N_2}(v)[N_2] + k_O(v)[O] + A_{v \rightarrow v-1} \quad (52)$$

For single quantum relaxation, the observed vibrational population changes reflect a balance between losses (collision and radiative relaxation into the next lower level, $v-1$), and feeding by quenching of the level above, $v+1$, and by the creation rate for vibrationally excited NO, $R_e(v)$. The master equations describing the vibrational population histories in terms of these processes may then be written as:

$$\frac{dN_v}{dt} = R_e(v) - R_v N_v + R_{v+1} N_{v+1} \quad \text{for } v=1, M \quad (53)$$

where M is the highest level created. There is no relaxational feeding term in dN_M/dt . The radiative relaxation term, $A_{v \rightarrow v-1}$, in Eq. (53) is by far the smallest component in the sum under our experimental conditions. The contribution of the first overtone transitions, $A_{v \rightarrow v-2}$, to the observed relaxation has been neglected since they are typically even an order of magnitude smaller than the fundamental band values.⁶⁴ A previous kinetic analysis⁶² has indicated that the assumption of single quantum vibrational relaxation adequately represents the experimental observations.

Errors in the calculated N_v values due to noise in the laboratory spectra and fitting uncertainties requires that a time integration form of Eq. (53) be employed to increase the accuracy of the determination of the R_v value. Integrating Eq. (53) over the electron beam pulse duration, $t=0$ to t_p , we obtain

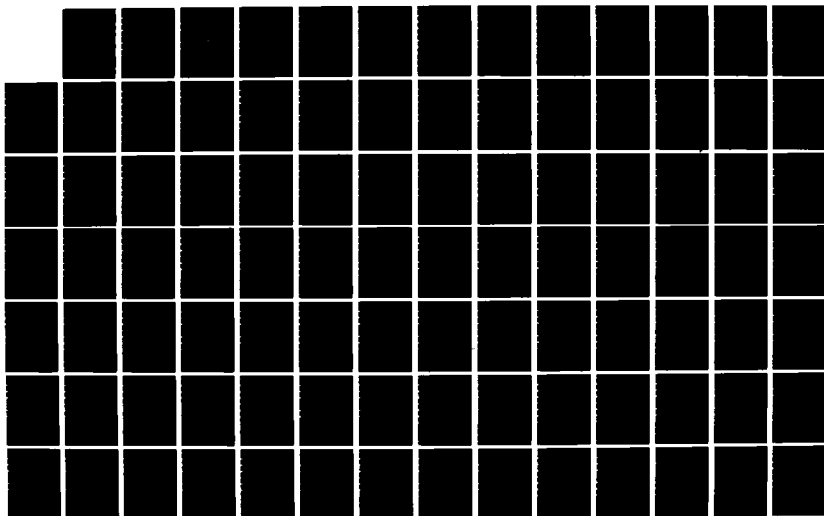
AD-A161 674

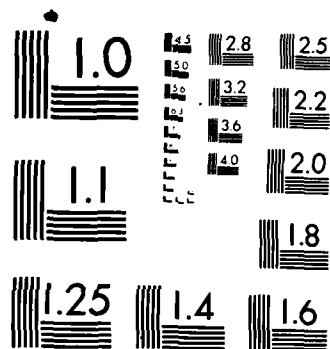
FLUORESCENCE FROM ELECTRON IRRADIATED GASES IN
REFURBISHED LABCEDE(U) PHYSICAL SCIENCES INC ANDOVER MA
B D GREEN ET AL SEP 85 PSI-TR-433 AFGL-TR-84-8218
F19628-80-C-0168 F/G 4/1

3/4

UNCLASSIFIED

NL





MICROCOPY RESOLUTION TEST CHART
NATIONAL BUREAU OF STANDARDS-1963-A

$$N_v(t_p) = R_e(v)t_p - R_v a_v + R_{v+1} a_{v+1} \quad (54)$$

where the quantities a_v are defined by

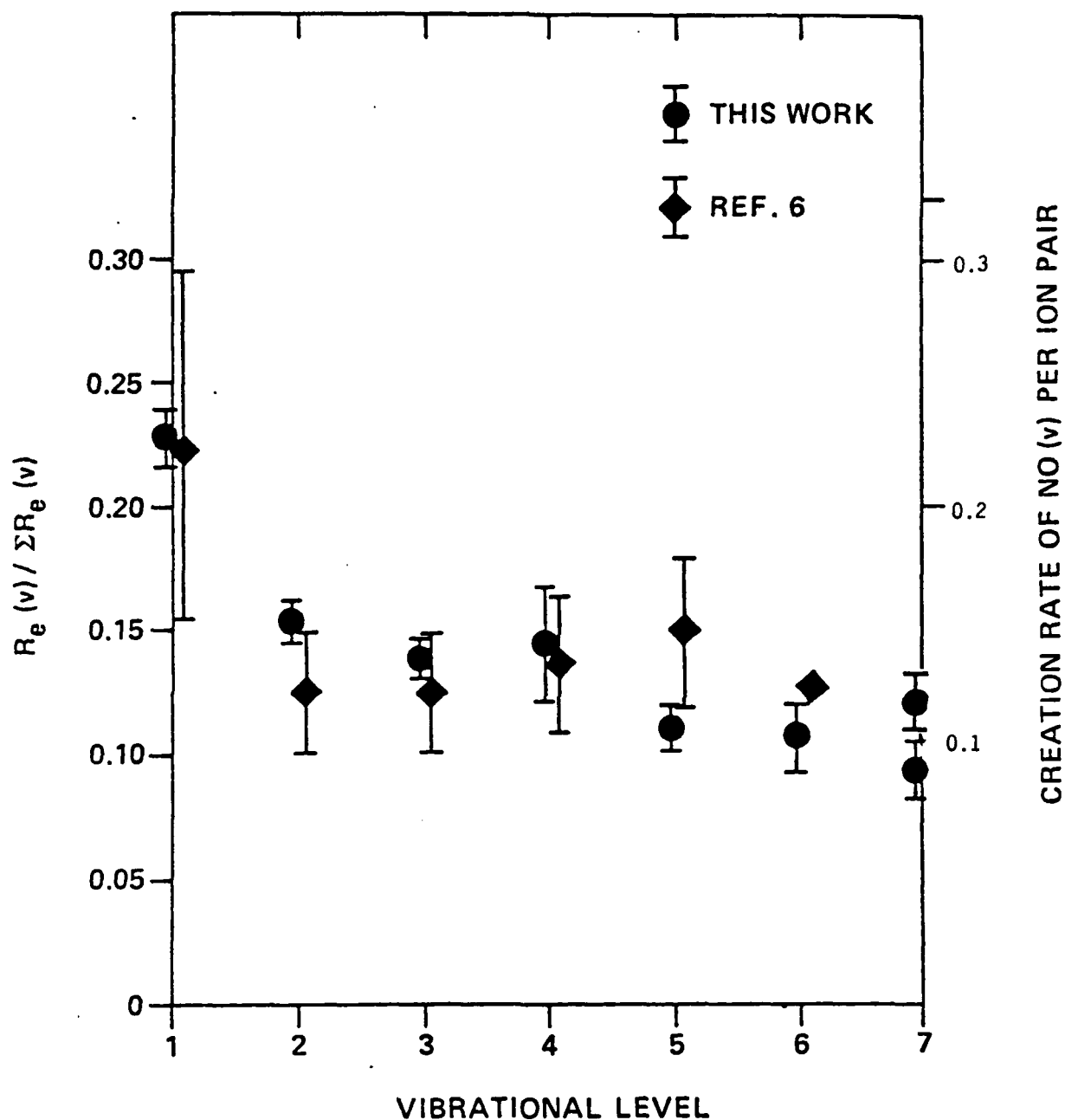
$$a_v = \int_0^{t_p} N_v dt \quad (55)$$

and t_p is 1 ms. Note that the quantities a_v are defined directly from the data and the rates R_v can be determined from an analysis of the relaxation data after beam termination. The populations of the highest vibrational levels tend to be the least accurately determined, primarily due to low emission intensities. Consequently, Eq. (54) can only be evaluated for the first seven levels. The low signal levels for higher vibrational levels are due to small excited state densities, not weaker radiative bandstrengths. Thus the NO molecules created under our experimental conditions are formed primarily with seven or less vibrational quanta. About 10 percent of the molecules are found with eight or more quanta. Because of the rapid relaxation of these levels, their relative formation rates cannot be determined here.

The excitation rates, $R_e(v)$, were calculated from Eq. (54) using the time integrals of the deduced vibrational populations and the case-specific relaxation rates R_v found from the fluorescence data after beam termination.⁶² The normalized values of $\frac{R_e(v)}{\sum R_e(v)}$ are plotted in Figure 72. The values plotted in Figure 72 are the average of nine separate experiments with oxygen concentrations between 0.05 and 0.4 torr. The error bars represent one standard deviation. Although there is a clear trend of decreased production with increasing vibrational level, the production rates into all seven levels are the same within a factor of two.

The average amount of vibrational excitation can be readily deduced from the data. The average number of vibrational quanta per excited NO molecule is defined by

$$\bar{v} = \frac{\sum_{v=1}^M v R_e(v)}{\sum_{v=1}^M R_e(v)} \quad (56)$$



A-1818

Figure 72. Normalized excitation rates for NO(v) compared with observations of Ref. 65. Error bars are one standard deviation. The two sets of measurements agree within error bars for all levels. Absolute creation rates per ion pair are given along right-hand axis.

and is found to be 3.6 ± 0.2 quanta, independent of O_2 pressure and beam current. It should be noted that \bar{v} is dependent only upon the relative vibrational distribution and not the absolute calibration. Our determination of \bar{v} is, however, a lower bound because of the truncation of the sums at $v=7$. Also shown for comparison in Figure 72 are the previously measured relative production rates of Kennealy et al.⁶⁵ for the initial distribution of $NO(v)$ created in the reaction of $N(^2D, ^2P)$ with O_2 . They favored $N(^2D)$ as the reaction precursor, but were unable to discriminate between the two metastable states. The good agreement between the two sets of production rates leads us to believe that the same production mechanism is at work: that the NO produced in these electron irradiated N_2/O_2 mixtures results from the metastable $N^* + O_2$ reaction.

To relate the absolute values of the observed creation rates $R_e(v)$ and the total production rate $\Sigma R_e(v)$ to the rate of production of the metastable nitrogen atom reaction precursor, N^* , it is necessary to consider the effects of competitive quenching of N^* by N_2 and O_2 , due to the reactions:



Since N^* reaches steady state conditions very rapidly during the beam pulse, the observed NO creation rate is equal to the precursor creation rate times the fraction ϕ :

$$\phi = k_{O_2} [O_2] \{k_{O_2} [O_2] + k_{N_2} [N_2]\}^{-1} \quad (58)$$

where k_{O_2} and k_{N_2} are the rate constants for the processes (57a) and (57b), respectively. These rate constants have been determined for both $N(^2D)$ and $N(^2P)$. The quenching rate constant of $N(^2P)$ by N_2 ⁶⁶ is four orders of magnitude slower than by O_2 ^{67,68} and thus, the first term in the denominator of Eq. (58) would be negligible for this precursor. Thus, if $N(^2P)$ were the reaction precursor, no variation in $NO(v)$ production would be expected as a function of O_2 pressure. However, even though the normalized $R_e(v)$ values

exhibit a small standard deviation, their absolute values and the absolute value of the total production rate ($\Sigma R_e(v)$) shows a marked variation with O_2 pressure for experiments performed under similar conditions. The quenching rate constants for $N(^2D)$ by O_2 and N_2 have been measured by several groups.⁶⁶⁻⁷² Although there is some spread in the reported values, we have adopted the recent values of Iannuzzi and Kaufman⁶⁸ for O_2 quenching ($k_{O_2} = 5.3 \times 10^{-12} \text{ cm}^3 \text{ molecule}^{-1} \text{ s}^{-1}$) and a value of $k_{N_2} = 1.6 \times 10^{-14} \text{ cm}^3 \text{ molecule}^{-1} \text{ s}^{-1}$ for N_2 quenching.^{67,69} From these rate constants and the known pressures, values of ϕ were calculated for each experiment. The total excitation rates were then adjusted upward to correct for N_2 quenching, and these adjusted $\Sigma R_e(v)$ values were invariant over the range of experimental O_2 concentrations. We take this as strong evidence that $N(^2D)$ is responsible for production of the observed vibrationally excited NO in our electron-irradiated N_2/O_2 mixtures.

The adjusted total production rates in the field of view (for a beam current of 0.5 mA) were $8 \times 10^{17} \text{ s}^{-1}$. The standard deviation of this value is only $0.3 \times 10^{17} \text{ s}^{-1}$. Previous analyses⁶² have shown that uncertainties due to the spectral fitting process introduce an uncertainty of about 5 percent into the deduced rates. The rate determination using the time integral approach described above introduces very little additional uncertainty. The uncertainties in the calibration process, however, are significant, amounting to as much as 20 percent. Although fluorescence from NO vibrational levels up to $v = 10$ was observed, NO is predominantly formed in the seven vibrational levels included in the analysis. It is estimated that the omitted higher vibrational levels might contribute 10 percent at most to the total creation rate. Thus total error bars of +30 percent, -20 percent are placed on the production rates.

The magnitudes of these production rates are not very instructive inasmuch as they represent the total rate of excitation within the field of view and thus are both specific to the experiment and to the beam current and voltage. All the data can be collapsed to a common scale by normalizing by the total rate of beam energy deposition within the field of view. This deposition "power" is given by the volume integral:

$$P = \int \rho i (\rho^{-1} dE/dx) dV \quad (59)$$

where ρ is the gas density, i is the local current density as calculated from Center's Gaussian distribution.⁶³ $\rho^{-1} dE/dx$ is the beam energy loss per unit axial distance for electrons of energy E and the integral is over the observed beam volume. For our quasi-thin gas target, Eq. (59) may be more simply represented as

$$P = \rho I \bar{L} (\rho^{-1} dE/dx)_{\text{avg}} \quad (60)$$

where I is the total beam current, \bar{L} is the effective length over which deposition is observed (incorporating corrections due to beam growth and the circular form of the field of view) and the quantity in brackets represents the energy loss per unit distance appropriately averaged across the field of view, which must be estimated by computer modeling as described below.

The phenomenology of electron energy degradation in gas targets is well understood. The rate of energy loss is found to depend upon both the composition of the scattering gas and the beam voltage. The energy loss per unit electron pathlength, s , typically written as $\rho^{-1} dE/ds$, has been tabulated for a number of gases.⁷² Unfortunately, the relationship between electron pathlength and distance along the axis of beam propagation, x , is not readily specified and requires evaluation via computer analysis. Two different computer models have been used to predict the axial profile of energy deposition in the test chamber. The first of these is ELTRAN,⁷³ a standard one-dimensional Monte Carlo transport code, which describes electron multiple scattering in terms of the Moliere⁷³ distribution. The second is the Transport Electron Program,⁷⁴ which utilizes various analytic approximations to develop an integral solution of the transport equation. These codes have been exercised for the present experimental conditions and the axial energy depositions predicted by the two models were found to be in excellent agreement and to vary between 18 and 25 MeV-cm²/g across the field of view. These values are three times greater than the tabulated straight electron pathlength values.⁷³

The power deposited in the observation volume as calculated from Eq. (60) can then be related to the creation rate for electron-ion pairs in the field of view by the expression:

$$\dot{X}^+ = P/eW \quad (61)$$

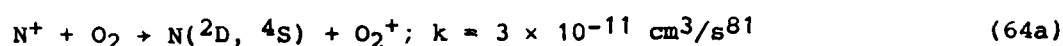
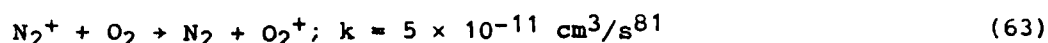
where e is the electron charge and W is the energy required to produce an electron-ion pair in the irradiated gas (34.4 eV in nitrogen).⁷⁵ The excitation rates deduced above were then normalized by the value of \dot{X}^+ for each experimental run to determine the creation rate per ion pair for producing vibrationally excited NO, \dot{NO}^* :

$$\dot{NO}^* = \sum_{v=1}^7 R_e(v)/\dot{X}^+ \quad (62)$$

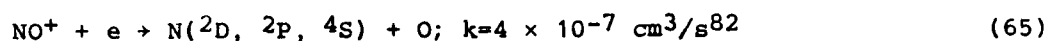
This quantity was found to depend on oxygen pressure through the $R_e(v)$ values. If the adjusted $R_e(v)$ values (which take into account the competition between N_2 and O_2 for $N(^2D)$ quenching) are used in Eq. (61), then the number of vibrationally excited NO molecules created per electron-ion pair is found to be $1.0_{-0.2}^{+0.3}$, independent of oxygen pressure or beam current. Consequently, the normalized excitation rates for each vibrational level as shown in Figure 72 are thus also the absolute creation rates into each level per electron-ion pair as indicated along the right hand axis. For example, approximately 0.14 $NO(v=3)$ molecules are created per electron-ion pair. This also implies that at least 1 $N(^2D)$ precursor must be formed per ion in these experiments since ground state NO molecules (which cannot be detected) are undoubtedly also created.

Metastable $N(^2D)$ atoms are formed by direct electron impact dissociative excitation. In N_2 -trace O_2 mixtures, about 0.67 $N(^2D)$ atoms are produced per ion pair by direct channels.⁷⁶⁻⁷⁸ Other more indirect formation pathways also exist however. For example N_2^+ electron-ion recombination can lead to $N(^2D)$ production.⁷⁹ The dominant ions produced by the electron beam are N_2^+ and N^+ in approximately the ratio 80%:20%. These ions then either recombine or react to form other ions. These reactions act primarily to transfer the positive

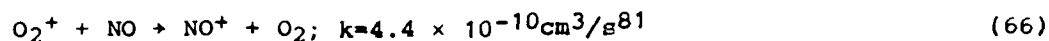
charge to that species exhibiting the lowest ionization potential. For the gas mixtures used, the apparent dominant ion becomes O_2^+ . Characteristic electron densities in LABCEDE are on the order of $10^{11}/\text{cm}^3$ and since the recombination rate constant of diatomic ions is $\sim 2 \times 10^{-7} \text{ cm}^3/\text{s}$,⁸⁰ recombination times will be on the order of 50 μs . The ion-neutral reactions must occur more rapidly than this to be important. Reactions with O_2 are quite fast:



and will thus have characteristic times of less than 10 μs for O_2 pressures greater than 0.1 torr. As a result N_2^+ recombination is not an important source of $N(^2D)$ at the finite O_2 pressures of the present experiment. On the other hand, N^+ reacts to form $N(^2D)$ directly in reaction (64a) or indirectly through reaction (64b) followed by NO^+ dissociative recombination:



for thermal electrons. Thus N^+ produces no more than $\sim 0.2 N(^2D)$ atoms per ion pair. Because NO has a lower ionization potential than O_2 , sufficient build-up of that beam created species from one beam pulse to the next could result in additional $N(^2D)$ formation from N_2^+ , or N^+ ions by reactions (63) or (64a) followed by



and reaction (65). The NO concentration has been roughly bounded by visible afterglow experiments and computer modeling.⁸³ It seems likely that O_2^+ dissociative recombination will dominate over reaction (66). Nevertheless, $N(^2D)$ atoms may be formed from N_2^+ ions through the reaction sequence (63),

(66), (65). Reactions of the primary ions with other beam created species such as O-atoms are not likely; their concentrations are too low to compete with the O_2 reactions even if gas kinetic rate constants are assumed. Thus the production rate of $N(^2D)$ atoms from the ionic reactions is at least 0.2 per ion pair, possibly as much as ~ 0.4 per ion pair, yielding a total production rate of $N(^2D)$ in these mixtures of 0.9 to 1.1 per ion pair. This is in good agreement with our experimental observations which require the creation of at least one $N(^2D)$ per ion pair. This $N(^2D)$ production rate per ion pair is within 50 percent of the value for air. A more detailed description of the creation rates in air is given in Ref. 84.

Finally, the fraction of the deposited beam energy which is converted into NO vibrational energy is defined by:

$$\epsilon_1 = \sum_{v=1}^7 E_v R_e(v) / P \quad (67)$$

where E_v is the difference in energy between level v and the ground vibrational level. Once again the resultant efficiency is a function of O_2 pressure unless the $R_e(v)$ values are corrected for $N(^2D)$ quenching by N_2 . If this is done the average energy efficiency is then found to be $2_{-0.5}^{+0.8}\%$ independent of experimental conditions. This quantity has been evaluated from the data for the lowest seven vibrational levels. In this case the truncation of the sum can produce a larger error than in the creation rate per ion pair (Eq. (62)) because the higher vibrational levels are weighted by larger E_v values. It is estimated that the true efficiency could be as much as 25 percent higher than the value shown due to this effect, as reflected in the non-symmetric error bars. Our observations are consistent with upper atmospheric emission data from the HIRIS Mission,⁸⁵ which revealed an apparent efficiency of $NO(v)$ production in air as 1.5 to 4 percent in the aurorally excited lower thermosphere.^{86,87}

6.4 Summary

The technique of time-resolved Fourier spectroscopy has been applied to the study of the production of vibrationally excited NO in electron irradiated N₂-trace O₂ mixtures. NO fundamental band fluorescence is observed from up to ten vibrationally excited levels. The detection system was carefully calibrated to permit determination of absolute intensities. The absolute vibrational population densities which gave rise to the fluorescence were calculated using synthetic spectra. The variation of these populations with time during and after the beam pulse were used to estimate relaxation and excitation rates for each vibrational level using a time integration technique. The reaction of N(²D) atoms with O₂ has been tentatively identified as the NO(v) formation mechanism. Computer modeling of the energy deposition rates of the electron beam has permitted the total creation rate per ion pair to be set at $1.0^{+0.3}_{-0.2}$ vibrationally excited NO molecules per ion pair. The number of molecules created per ion pair in each of the first seven vibrational levels is found to be 0.23, 0.15, 0.14, 0.15, 0.11, 0.11, 0.09 respectively. Both direct dissociative excitation and ionic reactions give rise to N(²D) metastables with sufficient rates to explain the observed NO production. Approximately $2^{+0.8}_{-0.5}\%$ of the deposited beam energy appears as NO vibrational energy. This efficiency is consistent with the analysis of HIRIS data. These results are critical for relating upper atmospheric radiance observations to actual energy depositions and are a necessary input to models of the disturbed upper atmosphere.

7. ELECTRON EXCITATION AND COLLISIONAL QUENCHING OF $N_2^+(A)$ MOLECULES BY N_2 AND O_2

7.1 Introduction

The $N_2^+(A^2\Pi_u)$ state is one of the major radiators in auroras⁸⁸⁻⁹¹ and the air glow,⁹² giving rise to the Meinel bands in the red and near infrared region of the spectrum (500 to 2000 nm). In addition, ionization of molecular nitrogen by energetic electrons is predominantly through the $A^2\Pi_u$ state.⁹³ Thus, the excitation and de-excitation of $N_2^+(A^2\Pi_u)$ controls the distribution of $N_2^+(v)$ in an aurora or otherwise disturbed atmosphere. Because the lifetime of the $A^2\Pi_u$ state is about 10 μ s, this state quenches readily at pressures above a millitorr. This efficient quenching confounded early laboratory attempts to measure the lifetime of $N_2^+(A^2\Pi_u)$.^{93,94} Ion beam time-of-flight measurements, however, have settled the lifetime issue.^{95,96}

The quenching of this state is still not well understood. Laboratory values for the rate coefficient for quenching $N_2^+(A^2\Pi_u)$ by molecular nitrogen span a range of more than a factor of two.^{94,97-99} To our knowledge, molecular-oxygen quenching of the Meinel bands at room temperature has never been studied, although Pendleton and Weaver⁹⁸ estimated an O_2 -quenching-rate coefficient based upon one measurement in nitrogen-oxygen mixture. Sheridan et al.¹⁰⁰ also published a value for O_2 quenching of $N_2^+(A^2\Pi_u, v'=4)$ but at collision energies of 6 to 11 keV.

Although the relative electron-impact excitation rates of the various vibrational levels of N_2^+A are reasonably well established,^{93,99,101,102} the same is not true for the absolute electron-impact excitation cross-section. Values for this quantity range over an order of magnitude. The difficulty in extracting accurate electron impact cross sections is related in part to the problems associated with the quenching of this state. Thus a good handle on the quenching is required to understand the excitation.

Using a Stern-Volmer formulation, we have determined the rate coefficients for quenching $N_2^+(A^2\Pi_u, v'=2, 3, \text{ and } 4)$ by room air, and in addition, the quenching of $v'=2$ by molecular oxygen and nitrogen. Peterson and Moseley's⁹⁶ measured $N_2^+(A^2\Pi_u)$ lifetimes place our quenching measurements on an absolute basis. We have also measured relative electron-impact excitation rates for vibrational levels 2-7. Relating these relative excitation rates to the rate of excitation of the nitrogen first-negative band, whose absolute excitation cross section is well established, enables us to determine the absolute Meinel-band, electron-impact excitation cross section.

7.2 Experimental

The experimental apparatus is the LABCEDE facility^{103,104} at the Air Force Geophysics Laboratory, operated at room temperature for these experiments. It is a cylindrical vacuum tank, 3.4m long and 1m in diameter in which an electron beam excites numerous nitrogen and oxygen emissions, including the Meinel bands.¹⁰⁵ The gas mixture enters the reaction chamber at one end through a large porous-tube array and flows under essentially plug-flow conditions along the longitudinal axis of the chamber and out through a 32-in. diffusion pump backed by a Roots blower/fore pump combination (effective pumping speed = $2.6 \times 10^4 \text{ l s}^{-1}$). This flow pattern limits the residence time of gaseous species in the electron beam volume to only a few milliseconds at most, so that quenching by electron-beam-created species is negligible.

The electron beam enters the chamber through one side, a little over a meter from the upstream end of the tank. The electron gun provides currents up to 20 mA at energies up to 6 kV.

Fluorescence is observed through one of two observation ports containing BaF₂ windows. One port views the excitation region from the upstream end of the tank, normal to the electron beam, and about 1.2m from it. The other observation port sits at an angle of about 19 deg from the intersection of the electron beam with the longitudinal axis of the tank and about 0.7m from this junction. A 5 cm diameter, 10 cm focal length suprasil lens collects the

fluorescence and focusses it upon the entrance slit of a 0.3m monochromator (McPherson 218) equipped with a 1200 groove/mm grating blazed at 500 nm. An HTV R955 photomultiplier operated at a gain of 5×10^6 detects the photons, and a picoameter/recorder combination displays the photomultiplier output.

The image of the monochromator slit at the excitation region determines the detector's field of view. This image is about 4×0.4 cm for viewing from the end of the tank, and 3×0.28 cm for viewing from the side port. The field of view of the detector, therefore, is a rectangular slice through the electron beam whose height is comparable to the diameter of the beam but whose width is narrow compared to the length of the irradiated volume. Because the mean molecular velocity of nitrogen at 300K is 4.8×10^4 cm s⁻¹, the N₂⁺(A) molecules can travel no more than 5 mm during the molecule's effective lifetime. This distance is too short to allow significant diffusive losses out of the field of view in its long dimension. Experiments in which the length of the field of view was varied by a factor of eight verified this assumption. Diffusion out of the field of view along the axis of the irradiated volume is balanced by diffusion into the field of view along the e-beam axis from species excited outside the monochromator field of view.

A Corning 3-71 colored glass filter rejects second-order spectra for measurements made to the red of 500 nm. In order to ensure that second-order leakage of the very strong nitrogen first-negative band at 391 nm (N₂⁺ B²Σ_u⁺, v'=0 - X²Σ_g⁺, v''=0) did not contaminate the intensity measurements of the Meinel 2,0 band at 782 nm, we checked the rejection ratio of this filter in the second order by scanning several strong uv mercury lines emitted from a pen lamp. The rejection ratio was about 10⁻⁶ compared to a ratio of the intensities of the Meinel 2,0 band to the first order 391 nm band of $\sim 5 \times 10^{-3}$. Concentrations of N₂⁺ x ground state are sufficiently low that self-absorption of both fluorescence bands is completely negligible (optically thin).

Most of the Meinel bands are overlapped with nitrogen first-positive (N₂B³Π_g - A³Σ_u⁺) emissions. The Meinel (2,0), (3,1), and (4,2) bands are

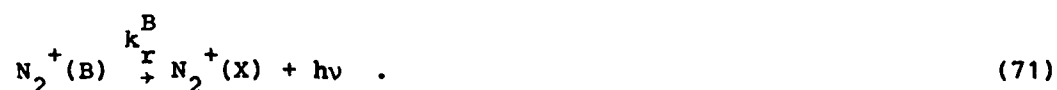
relatively free from this overlap at low pressures where the Meinel band excitation is stronger relative to that of the first-positive bands than is the case at higher pressures, but this overlap still can be a problem. This difference in apparent excitation efficiencies results both from the efficiency with which the Meinel bands are quenched at higher pressures and from the fact that secondary electrons excite the first-positive bands more efficiently than do primary electrons and the flux of secondaries in the reactor increases with pressure. We employed a number of measures to avoid interference from underlying first-positive emission, as described below.

7.3 Measurement Technique

We used a classical Stern-Volmer analysis¹⁰⁶ to extract the quenching rate coefficients of the Meinel bands, using the nitrogen first-negative band at 391.4 nm as the reference transition for the case of no quenching. Except near threshold, the relative cross sections for electron-impact excitation of the $N_2^+A^2\Pi_u$ and $B^2\Sigma_u^+$ states as a function of energy are proportional.¹⁰⁷ In addition, the ratio of creation of both states by primary electrons to that by secondary electrons is identical (about 4:1).¹⁰⁸ Thus, measurements of the intensity of the 391.4 nm transition as a function of pressure will reflect accurately the relative changes in the Meinel band intensities if quenching were absent. Several groups have determined a Stern-Volmer quenching coefficient (defined below) for the 391.4 nm band of $\sim 1 \text{ torr}^{-1}$.^{94,109,111} Thus, at pressures below 10 mtorr, the 391.4 nm intensity is diminished by less than 1 percent, negligible in the case of the present experiments.

The range of the primary electrons is so great^{112,113} ($> 10\text{m}$) at the pressures of our experiments ($< 10 \text{ mtorr}$), that production of significant number densities of such potentially reactive species as oxygen or nitrogen atoms in the observation region is unlikely. Thus, these species are ignored.

Our quenching analysis uses the following reaction scheme:



Steady-state conditions prevail in the observation volume so that

$$\frac{d[N_2^+(A)]}{dt} = k_f^A(p) - \{k_r^A + k_Q[Q]\}[N_2^+(A)] = 0, \quad (72)$$

where the formation rate, k_f , is a function of pressure, p .

The Meinel-band emission intensity is $I_A = k_r^A[N_2^+(A)]$, and Eq. (72) therefore gives

$$I_A = \frac{k_f^A(p)}{1 + \frac{k_Q[Q]}{k_r^A}} \quad (73)$$

Similarly, the emission intensity of $N_2^+(B)$ is

$$I_B = k_r^B[N_2^+(B)] = k_f^B(p) \quad (74)$$

Because the ratio of the electron excitation cross sections for the N_2^+ (A and B) states is constant except near threshold, we can write

$$k_f^A(p) = \zeta k_f^B(p), \quad (75)$$

where ζ is the constant of proportionality between the curves of electron excitation cross section as a function of energy for the A and B states. The ratio of Eq. (74) to Eq. (73) with the inclusion of Eq. (75) gives the working equation for our quenching studies:

$$\frac{I_B}{I_A} = \frac{1}{\zeta} + \frac{k_Q}{\zeta k_r^A} [Q]. \quad (76)$$

Plots of the ratio of the intensities of the 391.4 nm band to a Meinel band versus number density of quencher should be linear, and the ratio of the slope to intercept from those plots (the Stern-Volmer quenching coefficient) gives the ratio of k_Q to k_r^A . Holland and Maier⁹⁵ and Peterson and Moseley⁹⁶ have established values for k_r^A , so that our k_Q values will be absolute.

In order to isolate the effects of quenching by molecular nitrogen from those of quenching by molecular oxygen, we did a series of runs in O_2/N_2 mixtures with mole fraction ratios, X_{O_2}/X_{N_2} , ranging from zero to 1.7. Each run consisted of series of measurements of the ratio I_B/I_A as a function of pressure with a fixed X_{O_2}/X_{N_2} . Analysis according to Eq. (76) then yields a value for k_Q/k_r^A of

$$k_Q/k_r^A = K_{\text{mix}} = \frac{k_{N_2}^A}{k_r^A} X_{N_2} + \frac{k_{O_2}^A}{k_r^A} X_{O_2}. \quad (77)$$

Dividing this equation through by X_{N_2} gives

$$\frac{K_{\text{mix}}}{X_{N_2}} = \frac{k_{N_2}^A}{k_r^A} + \frac{k_{O_2}^A}{k_r^A} \frac{X_{O_2}}{X_{N_2}}. \quad (78)$$

Thus from a linear plot of K_{mix}/X_{N_2} vs X_{O_2}/X_{N_2} we can extract the molecular oxygen quenching-rate coefficient from the slope, and the molecular nitrogen quenching-rate coefficient from the intercept.

7.4 Experimental Results

7.4.1 Quenching Rates - Our initial data showed a distinct curvature in plots of the ratio of the intensities of the nitrogen first-negative to Meinel bands as a function of pressure. We experimentally determined that the problem was not related to diffusion of the Meinel bands out of the field of view by obtaining identical results in a series of measurements in which the detector field of view as varied by a factor of eight. Contamination of the Meinel spectrum by underlying nitrogen first-positive radiation seemed to be the most likely culprit.

At pressures on the order of a millitorr, the majority of the emission observed in the tank is excited by the high-energy, primary electrons in the beam. As the pressure in the chamber rises, secondary electrons created from ionization of the gas in the chamber by the primary electron beam begin to become appreciable. These secondary electrons can collide with and excite the gas in the chamber within the detector's field of view. While the primary electron-beam flux is relatively constant over the range of pressures of this study, the secondary-electron flux increases rapidly as the chamber pressure is increased.

Almost 90 percent of the nitrogen first-positive band excitation is by secondary electrons, whereas nearly 80 percent of the Meinel and first-negative band excitation will be by primary electrons.¹⁰⁸ Thus at the lowest pressures where the number of secondary electrons created is small and where the mean free path of these secondaries is relatively great, the nitrogen first-positive excitation will be negligible compared to the Meinel-band excitation. As the pressure increases, however, the number of secondary electrons rapidly increases, and their mean free path decreases so that the effects of secondary excitation within a restricted field of view grows in a much greater than linear fashion, while the growth in the nitrogen first-negative band intensity grows essentially linearly.

The Meinel band intensity would grow linearly with pressure, like the first-negative bands, if they were not quenched. Because they are quenched, they grow less than linearly. When the Meinel bands are overlapped by other bands which grow much more rapidly than linearly with pressure, the effect of Meinel quenching on the total intensity within a given band pass around the Meinel bands will be underestimated due to the growing underlying radiation.

We employed several measures to reduce the effects of underlying first-positive radiation to the point where our measurements of the Meinel band intensities are free from the interference of underlying first-positive radiation. The measurements are made with a field of view restricted to the central portion of the primary electron beam, are restricted to pressures below 7.5 mtorr, and employed a monochromator to restrict the detector band pass to narrow regions of the spectrum over which the Meinel-band intensities are strongest compared to neighboring first-positive emissions.

The purpose behind restricting the detector's field of view to the central portion of the electron beam is to discriminate against regions of the apparatus in which emissions are excited predominantly by secondary electrons. The primary electrons are confined to a fairly narrow, and well defined field of view. The secondary electrons on the other hand are scattered almost isotropically out of the primary beam so that excitation events involving secondary electrons are more likely to occur outside the primary beam. The field of view was maintained sufficiently large, however, that we could observe no effects of diffusion of the $N_2^+(A)$ out of the field of view prior to radiation.

Figure 73 defines a safe upper limit to the pressure before the effects of underlying radiation become too great. It is a plot of the fraction of the total integrated intensity under the Meinel 2,0 band which can be attributed to emission from the first-positive 7,6 band as a function of pressure in air and in nitrogen. The integrated intensity of the 7,6 band was calculated by scaling the intensity of the first-positive 7,4 band by the appropriate transition probability¹¹⁴ and monochromator response function. An interesting

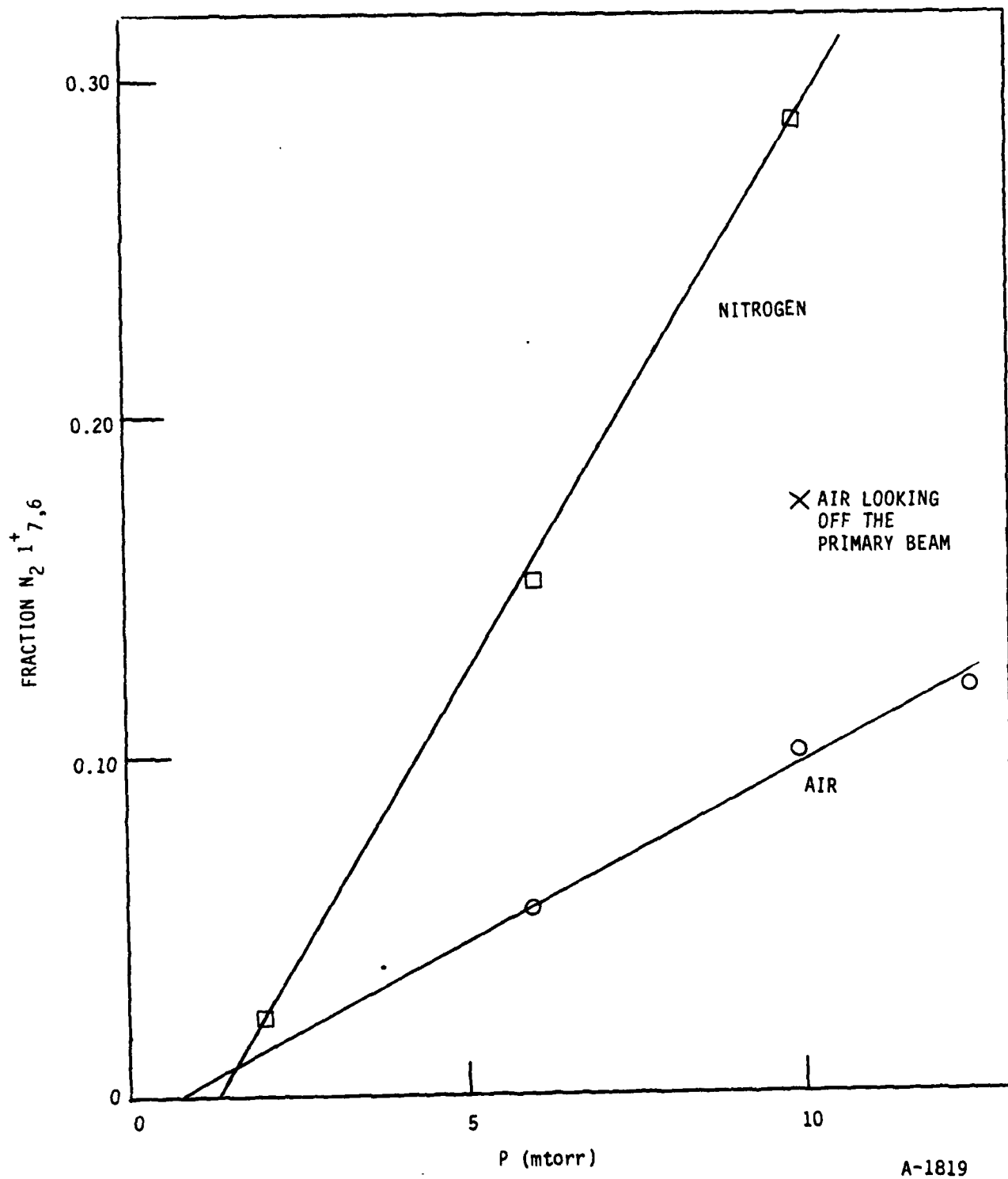


Figure 73. The fraction of total integrated intensity in the 780 to 795 nm region that can be attributed to $N_2(B^3\Pi_g - A^3\Sigma_u^+, 7,6)$ band.

feature of the plot is that the presence of the oxygen in the air seems to reduce the importance of secondary-electron excitation at least with respect to excitation of the nitrogen first-positive bands. Note also the point taken in air at 10 mtorr, but with the monochromator's field of view set to look somewhat above the central portion of the primary electron beam. The first-positive excitation for this setting has almost doubled in relation to the Meinel band intensity. This figure shows that if interference by the 7,6 band of as much as 10 percent can be tolerated, then measurements in air can proceed up to 10 mtorr, whereas in nitrogen, the maximum pressure must be kept below 5 mtorr. In practice, the restrictions will not be so great because we can restrict the monochromator band pass to a region of the spectrum where the contribution of the first-positive band emission in that band pass is somewhat less than its contribution to the observed emission over the whole emission band. For example, one of the most intense portions of the Meinel 2,0 band is the region about the R_2 head at 782.6 nm. The 7,6 first-positive band on the other hand is strongest in the region between 785 and 790 nm and is falling off to the blue of 785 nm.

Figure 74 shows the effect of varying the band pass on the ratio of the intensity of the first-negative band at 391.4 nm to the Meinel 2,0 band at 782.5 nm as a function of pressure of air. The data taken with band passes between 0.25 and 1.0 nm all match up quite well at all pressures up to 10 mtorr. The data taken with a 2.0 nm band pass, however deviates markedly from linearity above 5 mtorr, and the effect of this deviation from linearity is even worse when the data are taken with a 2 nm band pass which is centered at 785 nm, right in the center of the band where the first-positive contribution will be stronger. Although the data in Figure 74 indicate that the safe region for measurements extends up to 10 mtorr with a 1 nm bandpass, we restricted the bulk of our measurements to be below 7.5 mtorr.

With these restrictions in mind several series of quenching measurements were made. Figure 75 shows a representative quenching plot for laboratory air. Runs in air at a number of different electron-beam currents and beam energies determined the independence of the quenching parameter upon these variables. Figure 76 summarizes these results.

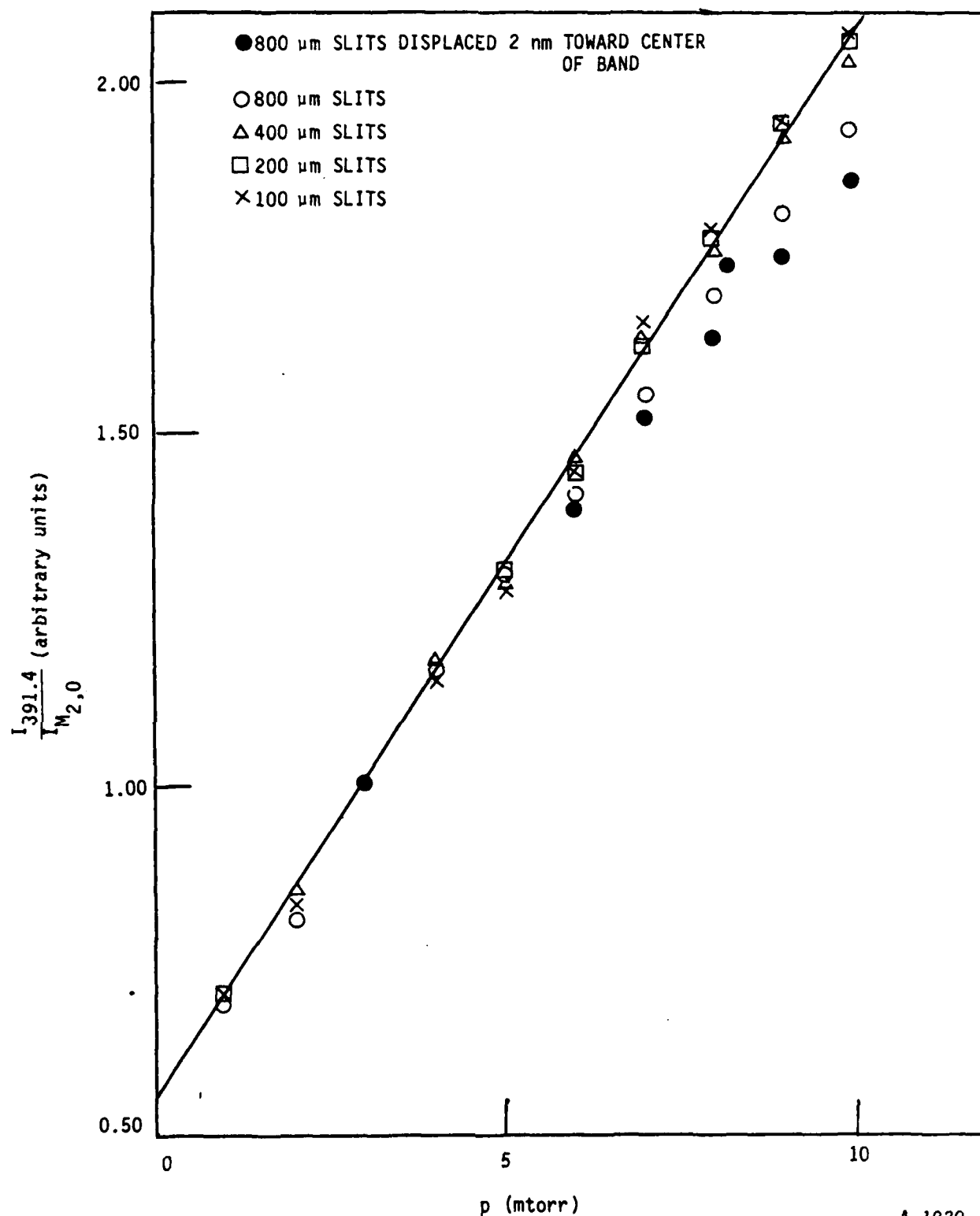
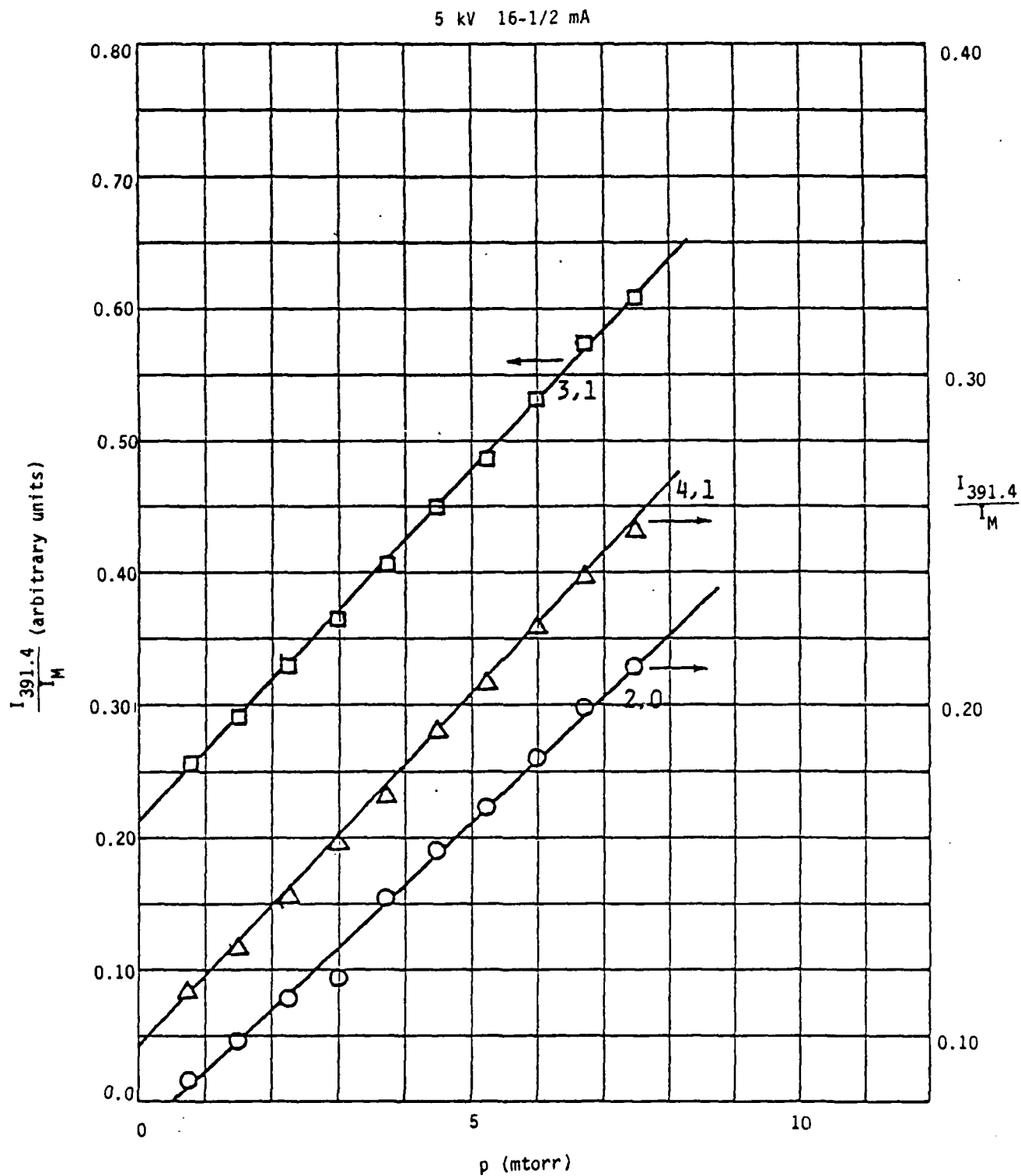
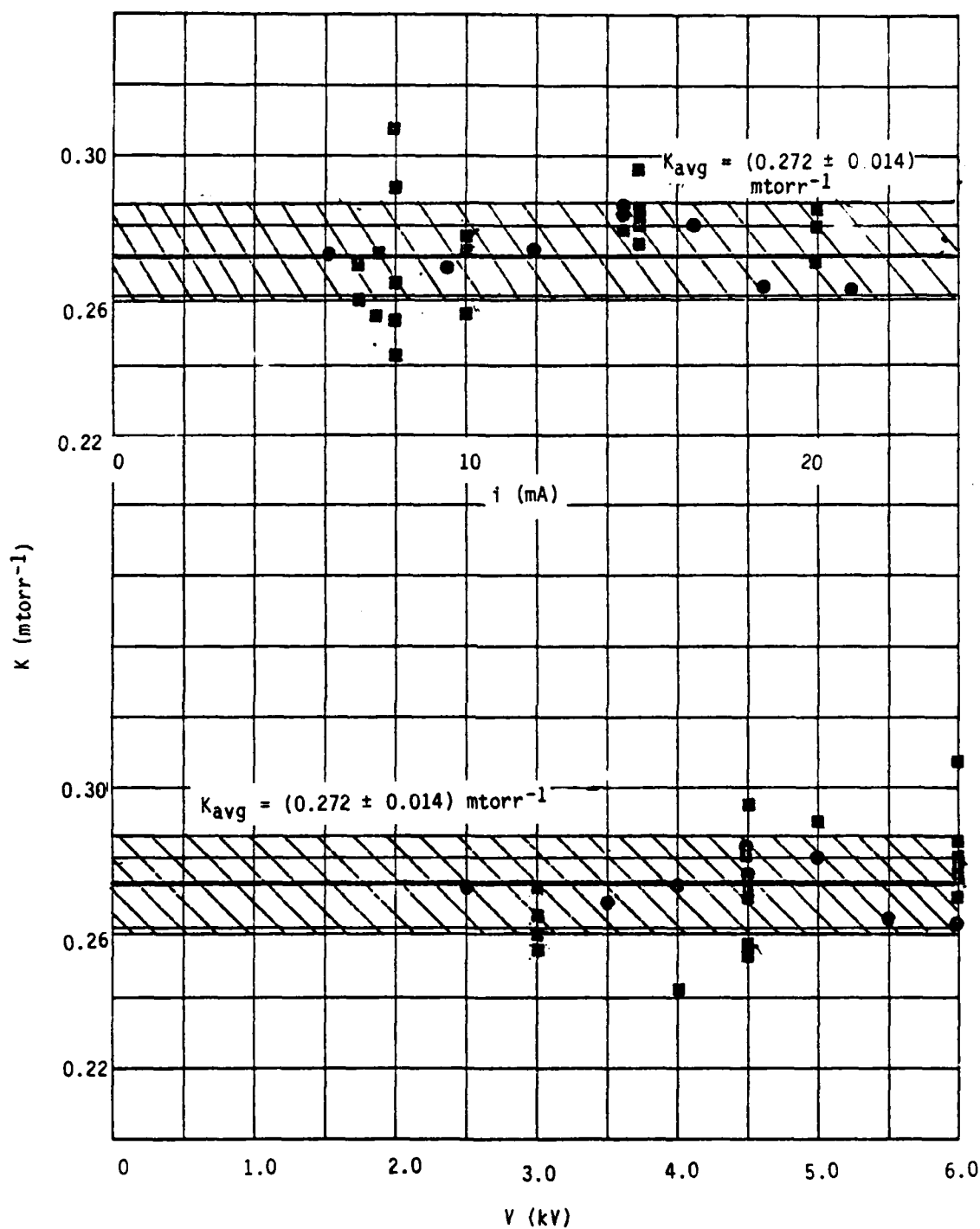


Figure 74. Variation in the ratio of the 391.4 nm intensity to that for the Meinel 2,0 band as a function of pressure of air. All data sets have been normalized to a value of 1.0 at 3 mtorr.



A-1821

Figure 75. Stern-Volmer quenching plot for the Meinel bands in air.



A-1822

Figure 76. Current and voltage dependence of quenching constant of Meinel 2,0 band in air.

The experimental quenching parameters - ratio of slope to intercept - were 0.272 ± 0.014 , 0.261 ± 0.017 , and 0.222 ± 0.017 mtorr⁻¹ for vibrational levels 2, 3, and 4, respectively, when quenched by air. These translate to rate coefficients of $(7.0 \pm 0.4) \times 10^{-10}$, $(7.5 \pm 1.0) \times 10^{-10}$, and $(7.0 \pm 1.0) \times 10^{-10}$ cm³ molecule⁻¹ s⁻¹ for vibrational levels 2-4 respectively.

Figures 77 and 78 show the quenching plots relevant to the measurements in the O₂/N₂ mixtures. In reducing the raw data from these runs, we had to make some small corrections for underlying oxygen radiation. Measurements of the ratio of the radiation intensity at 782.5 nm to that from the atomic oxygen line at 844.6 nm in pure oxygen, determined correction factors which were assumed valid for O₂/N₂ mixtures. These corrections generally were small, >10 percent, but were necessary to obtain linear quenching plots. These measurements give quenching parameters of (0.242 ± 0.013) and (0.290 ± 0.014) mtorr⁻¹ for oxygen and nitrogen, respectively, or quenching-rate coefficients of (6.2 ± 0.6) and $(7.5 \pm 0.8) \times 10^{-10}$ cm³ molecule⁻¹ s⁻¹ respectively.

We used Peterson and Moseley's⁹⁶ lifetime measurements (11.9, 10.7, and 9.7 μ s for levels 2-4, respectively) to establish absolute quenching rate coefficients. They agree well with those of Holland and Maier⁹⁵ and, in addition, give relative transition probabilities fully consistent with band intensity measurements of Wu and Shemansky¹¹⁵ and Gattinger and Vallance Jones.⁹¹ Peterson and Moseley claim an accuracy of better than 4 percent for their measurements.

The error limits we quote on our rate coefficients are two standard deviations from the average of all the data. These are probably reasonably accurate representations of the total uncertainty in the results because the major experimental uncertainties, the Meinel-band lifetimes, and the pressure-gauge calibration are both less than 5 percent.

Table 8 summarizes our results and compares them with available literature.

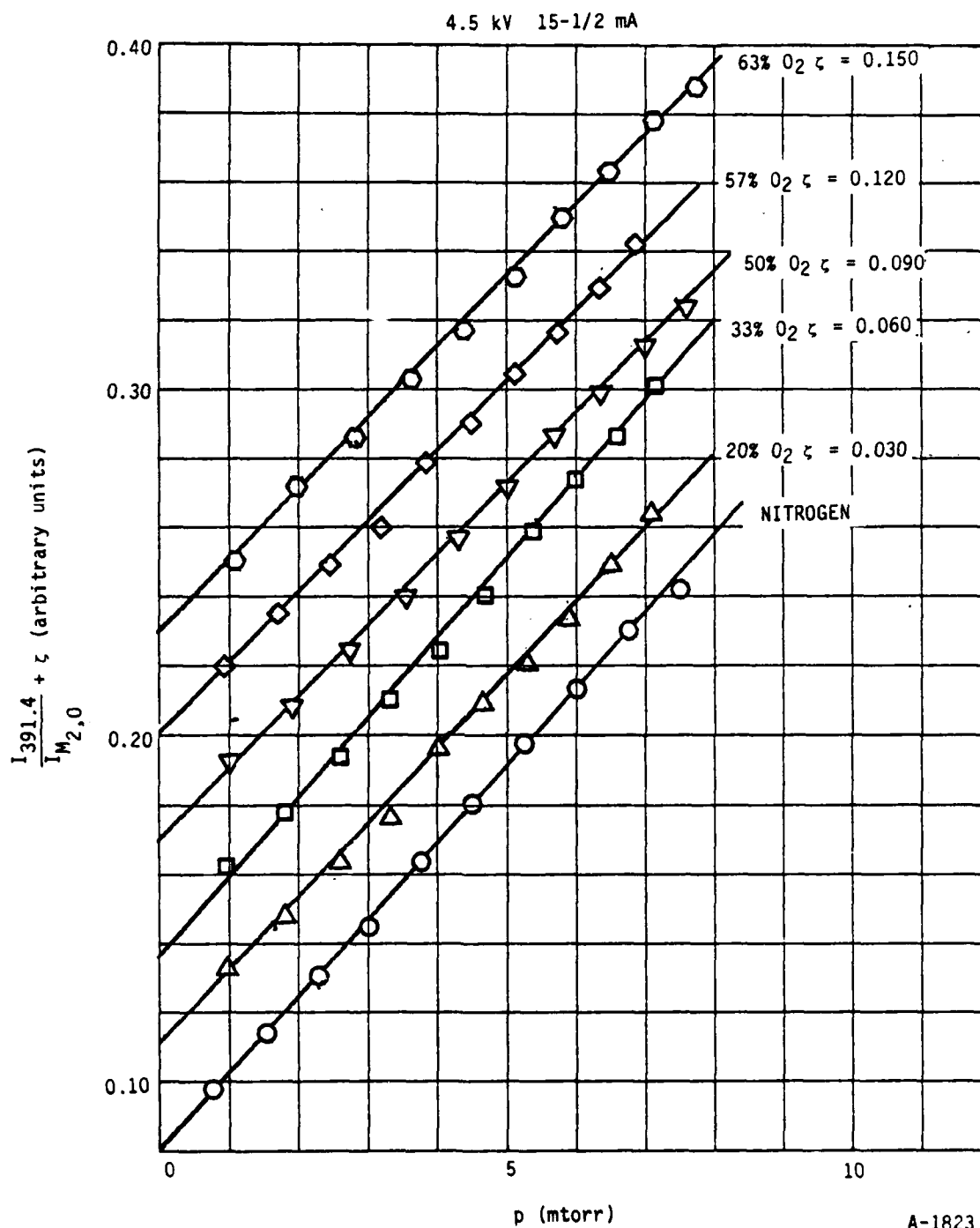
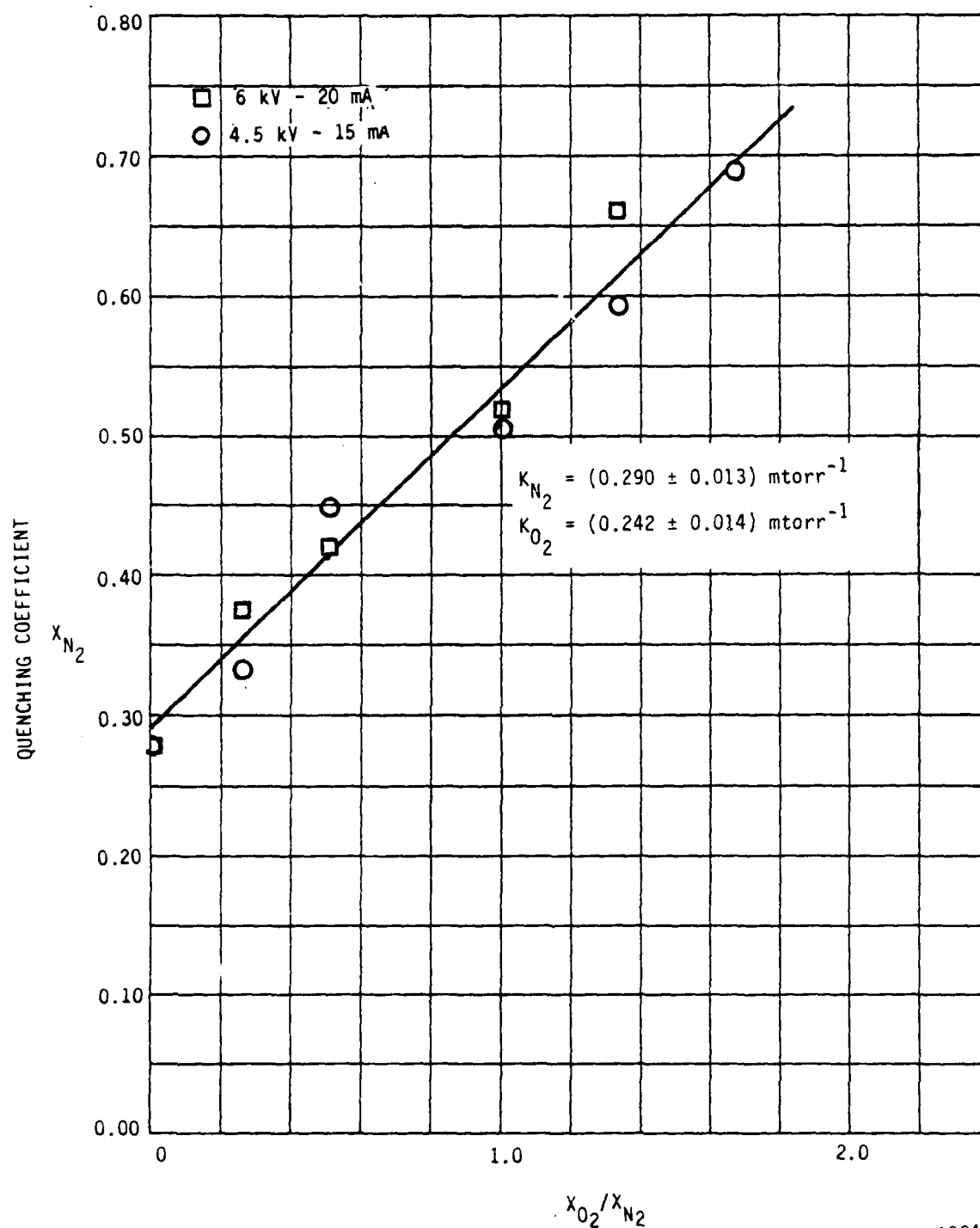


Figure 77. Meinel 2,0 quenching by N₂/O₂ mixtures.



A-1824

Figure 78. Quenching of Meinel 2,0 band in N_2/O_2 mixtures.

TABLE 8. MEINEL-BAND QUENCHING RATE COEFFICIENTS^a

Quencher	Reference	Vibrational Level		
		1	2	3
Air	Present results	7.0 ± 0.4	7.5 ± 1.0	7.0 ± 1.0
Nitrogen	Present results	7.5 ± 0.8		
	Gray, Roberts, Morack ⁹⁷	3.4 ± 1.7	5.3 ± 2.7	5.2 ± 2.6
	O'Neil, Davidson ⁹⁴	3.0	4.0	4.4
	Pendleton, Weaver ⁹⁸	8.6 ± 0.9	9.6 ± 1.3	10.5 ± 1.7
Oxygen	Present	6.2 ± 0.6		
	Pendleton, Weaver ⁹⁸	16.4^b		
	Sheridan, Merlo, Enzweiler ¹⁰⁰			13.0^c
<p>a - units are $10^{-10} \text{ cm}^3 \text{ molecule}^{-1} \text{ s}^{-1}$</p> <p>b - estimated from one measurement in 80/20 N₂/O₂ mixture</p> <p>c - at collision energies of 6 to 12 keV</p>				

7.4.2 Relative Excitation Rates - We measured the relative excitation rates of the Meinel bands by scanning the spectrum of the Meinel bands between 600 and 850 nm at very low pressures and with the spectrometer field of view restricted very severely to observe only the primary beam. The low pressures (<1 mtorr) and the restricted field of view served to eliminate the effects of quenching of the Meinel bands and excitation of interfering nitrogen first-positive emission. Under these conditions, measurements of the areas under the various emission bands when combined with the appropriate transition probabilities and corrected for changes in monochromator response give the relative populations in each of the observed emitting states. Over the spectral range covered, we were able to observe levels 2-7, and in most cases at least two different emission bands from the same upper level. Our results normalized to the population in $v'=2$ are given in Table 9. We have estimated the populations of $v'=0$ and 1 by rationating the relevant Franck-Condon factors for excitation of these levels to that of $v'=2$.

TABLE 9. RELATIVE MEINEL-BAND EXCITATION RATES

Level	Present Results	Auroral Data	Lab Data	
		Gattinger and Vallance Jones ⁹¹	Mandelbaum and Feldman ¹¹⁹	Shemansky and Broadfoot ⁹³
0		1.4	1.42	1.07
1		1.59	1.44	1.46
2	1.0	1.0	1.0	1.0
3	0.51	0.61	0.52	0.53
4	0.26	0.23	0.24	0.25
5	0.105			
6	0.047			
7	0.036			

The intercepts of the quenching plots give the ratio of the cross sections for electron-impact excitation of the nitrogen first-negative band at 391.4 nm to that of the Meinel bands observed, principally the 2,0 band. When corrected for monochromator response and the appropriate factors to convert the peak height measurements used in the quenching runs to band areas, we obtain an ionic cross section ratio, $\sigma_{B,v'=0 \rightarrow X,v''=0} / \sigma_{A,v'=2 \rightarrow X,v''=0}$ of 1.7 ± 0.2 . From the relative excitation rates, we can determine a cross section ratio for total A-state production to B-state production of 4.3 ± 0.5 . Furthermore, given that the ratio of the A-state to B-state cross sections is invariant with electron energy down to below 100 eV, we can place our A-state excitation cross section on an absolute basis using Borst and Zipf's¹¹⁶ measurement of the 391.4 nm excitation cross section at 100 eV, the peak of the excitation-function curve. This results in a N_2^+A state total excitation cross section of $(1.24 \pm 0.15) \times 10^{-16} \text{ cm}^2$ at 100 eV. Our value is compared with some values in the literature in Table 9.

7.5 Discussion

Our results indicate that the Meinel-band quenching rate in N_2 and O_2 is slightly less than that predicted by the Langevin model, 8.3 and $7.7 \times 10^{-10} \text{ cm}^3 \text{ molecule}^{-1} \text{ s}^{-1}$ respectively. Within the limits of experimental error, we saw no variation in quenching-rate coefficient with vibrational level for the runs done with room air. Because of this absence of a significant vibrational-level dependence, we focussed upon only one vibrational level for the studies in varying N_2/O_2 mixtures. Although the results of the other investigations in nitrogen which are listed in Table 8 do show an apparent increase in quenching-rate coefficient with vibrational level, none of the three studies shows an unequivocal trend given the fairly large error bars of the measurements.

Our results for the quenching of vibrational level 2 by nitrogen lie between the values reported by Gray, Roberts, and Morack⁹⁷ and O'Neil and Davidson⁹⁴ on the one hand, and by Pendleton and Weaver⁹⁸ on the other. Within the limits of uncertainty of each of the measurements, we are in accord

with them all, although more closely with the measurement of Pendleton and Weaver. Our result for the quenching of vibrational level 2 by molecular oxygen is in substantial conflict with that of Pendleton and Weaver and the measurement at 6 to 12 keV by Sheridan, Nerlo, and Enzweiler.¹⁰⁰ Pendleton and Weaver's measurement was basically an estimate based upon one measurement in an 80/20 N_2/O_2 mixture and will therefore be rather uncertain because extrapolating from small differences between two fairly large quantities. We see no reason to expect that high energy results should be congruent with those at thermal energies.

Our measurements are essentially global disappearance-rate coefficients and can provide no information on the microscopic mechanism for the removal of the observed levels. The studies of Katayama et al.¹¹⁷ suggest likely pathways for the energy flow. They performed a double-resonance experiment in which they pumped $N_2^+(A_v'=4)$ with a laser, and then probed the populations of high vibrational levels of the ground electronic state of the ion with a second laser, operating on the $B^2\Sigma^+ - X^2\Sigma^+$ transition, which was triggered after the A-state pumping laser had shut off. Nitrogen was a trace species in a bath of He for these studies. They noticed significant enhancement to the populations of vibrational levels 4-6 of the ground electronic state subsequent to pumping $A_v'=4$. In a second series of experiments they noted emission from $N_2^+(A_v'=3)$ after pumping vibrational level 4 with a laser. The rise time of the $v'=3$ fluorescence trace was equal to the decay time of the $v'=4$ fluorescence trace. The latter showed essentially prompt emission followed by a single exponential decay. The results of these two experiments inspired them to postulate that high lying levels of the X state are collisionally coupled with levels of the A states $v'=4, 3$ and 2 of the A state being coupled with $v''=8, 7$, and 6 of the X state for the collision partners. They further surmized that collisional relaxation out of $A_v'=4$, for example, proceeded into the X state manifold at $v''=8$ thence either back to lower levels at the A state, e.g. $v'=3$, or perhaps down to $X_{v''}=7$ from whence some of the energy crosses back over into the A-state manifold into $v'=3$. An alternative might be cross relaxation between $A_v'=4$ and X with a rapid coupling between $X_{v''}=7$

and $A_{v'}=3$ being responsible for the observed emission at $A_{v'}=3$. They did not make detailed measurements of all of the cross relaxation rates. They presumed that the mixing between the X and A states with energy defects less than kT happened on a per collision basis, and that the slow processes were then comprised of the larger energy-defect transitions, $X_{v''}=8$ or $A_{v'}=4$ to either $X_{v''}=7$ or $A_{v'}=3$.

A second, slightly different, alternative is suggested by the work of Dobler et al.¹¹⁸ who have determined the total removal-rate coefficients of vibrationally excited ground-state nitrogen by nitrogen and oxygen to be 5 and $1.7 \times 10^{-10} \text{ cm}^3 \text{ molecule}^{-1} \text{ s}^{-1}$ respectively. The rate coefficient for nitrogen, which is entirely a vibrational-quenching rate, is close to the A-state removal rate determined here, and suggests that perhaps the A-state crosses into the X-state manifold and is quenched from there. Dobler et al.¹¹⁸ contend that the vibrational quenching of $X_{v''}>0$ is essentially a charge transfer reaction to molecular nitrogen, producing $X_{v''}=0$. Whichever picture is correct, our results indicate that N_2^+A and N_2^+X are removed at essentially identical rates in nitrogen. This may be an indication of a similar mechanism caused by the presumably rapid cross coupling of the electronic states as proposed by Katayama et al.¹¹⁷

Our results for molecular oxygen quenching do differ quite significantly from those of Dobler et al.¹¹⁸ on the quenching of $X_{v''}>0$. This might result from actual differences in the quenching rates for the two different states, or it may be an indication that the higher levels of the X state quench or react more rapidly with oxygen than is the case for lower vibrational levels. Dobler et al.'s experiment can only distinguish between $v''=0$ and higher vibrational levels. Most of the vibrationally excited nitrogen in their reactor, however, will be in the first two or three vibrational levels, whereas our cross coupling would be into levels 6-8. Only quite detailed laser experiments like those of Katayama et al.¹¹⁷ could unravel these microscopic differences in behavior.

Our values for the relative electron-impact excitation rates of the various vibrational levels of the A state agree quite well with the auroral observations of Vallance Jones and Gattinger⁹¹, and with the laboratory measurements of Mandlebaum and Feldman¹¹⁹ and of Shemansky and Broadfoot.⁹³ As noted previously, they also agree with Franck-Condon factors for excitation from the ground state of the nitrogen molecule.

The great variety in the values reported for the electron-impact excitation cross section of the Meinel bands is somewhat disturbing. Our results agree with the measurements of Holland and Maier⁹⁵, and, more encouragingly, our ratio of total Meinel-band excitation to total nitrogen first-negative-band excitation agrees within 10 percent to the ratio of 5.0 determined by Vallance Jones and Gattinger⁹¹ from auroral observations.

If indeed the X and A states are rapidly coupled collisionally, the possibility exists that the relative electron-impact excitation rates that we have measured are actually excitation rates into high vibrational levels of the X state, with the A state being populated only by the collisional coupling. We think this possibility is unlikely because electron impact ionization/excitation at these high electron energies is generally a Franck-Condon process, producing a vibrational distribution proportional to the appropriate Franck-Condon factors. Our A-state vibrational level distribution agrees well with the relative Franck-Condon factors.¹¹⁴ The relevant Franck-Condon factors for X-state production are down some six or seven orders of magnitude from those for A-state production.

Vallance Jones and Gattinger¹²⁰ noted that the intensities of the Meinel bands relative to those of the nitrogen first-positive bands were somewhat weaker in a bright aurora than was the case in an aurora of medium intensity. Since brighter aurorae tend to penetrate deeper into the earth's atmosphere, they speculated that the reduction in Meinel-band emission resulted from quenching of the Meinel bands at the lower altitude. The magnitude of the reduction was about 20 percent. Our quenching data combined with the U.S. Standard Atmosphere¹²¹ would indicate a 20 percent reduction in Meinel-band

emission at about 95 km. This result agrees with the estimate of Vallance Jones and Gattinger which were based upon estimates of Meinel-band quenching-rate coefficients by Cartwright et al.¹²²

7.6 Summary

We have determined experimentally both the absolute quenching coefficients and excitation notes for the N_2^+A state in various vibrational levels in electronic irradiated N_2/O_2 mixtures. The ability resolve our data spectrally and spatially has permitted us to eliminate interfering species. These results are important to our understanding of the aurorally disturbed upper atmosphere where the N_2^+A state represents a major excitation pathway.

8. ON SELF-TRAPPING OF $\text{CO}_2(\nu_3)$ FLUORESCENCE

Recently, Huddleston et al.¹²³ discussed self-trapping of $\text{CO}_2(\nu_3)$ fluorescence under conditions where the radiators were at the same rotational/translational temperature as the absorbers. Predictions for the transmission of $\text{CO}_2(00^01 \rightarrow 00^00)$ fluorescence were made vs. CO_2 pressure, for given path-lengths L , assuming a Doppler line shape and the non-overlapping line approximation.¹²⁴ These predictions were compared with the results of a laser fluorescence experiment where the $\text{CO}_2(\nu_3)$ mode was optically pumped via "hot band" transitions. The predicted $\text{CO}_2(\nu_3)$ band transmission was lower than observed for all CO_2 pressures considered, markedly so at the higher values ($P_{\text{CO}_2} \cdot L \sim 0.1\text{--}4$ torr-cm). It was suggested that this discrepancy resulted from neglect of "hot band" emissions, e.g., $01^11 \rightarrow 01^10$, falling at nearly the same frequencies as the fundamental band. They deduce that in typical fluorescence experiments where $P_{\text{CO}_2} \cdot L \sim 1$ torr-cm "the major portion of emission observed at $4.3 \mu\text{m}$ is not due to the $00^01\text{--}00^00$ transition."¹²³

This effect is well known. Detailed line-by-line predictions for $\text{CO}_2(\nu_3)$ band transmission for Lorentz lineshapes have been provided by Bulos and Phelps,¹²⁵ including the effects of hot bands. Kumer¹²⁶ has addressed the importance of hot band and isotopic species emission in the upper atmospheric transport of $\text{CO}_2(\nu_3)$ emission. Kumer and James¹²⁷ have previously provided line by line predictions for transmission of $\text{CO}_2(00^01 \rightarrow 00^00)$ fluorescence (Doppler and Voigt profiles; $T = 225\text{K}$).

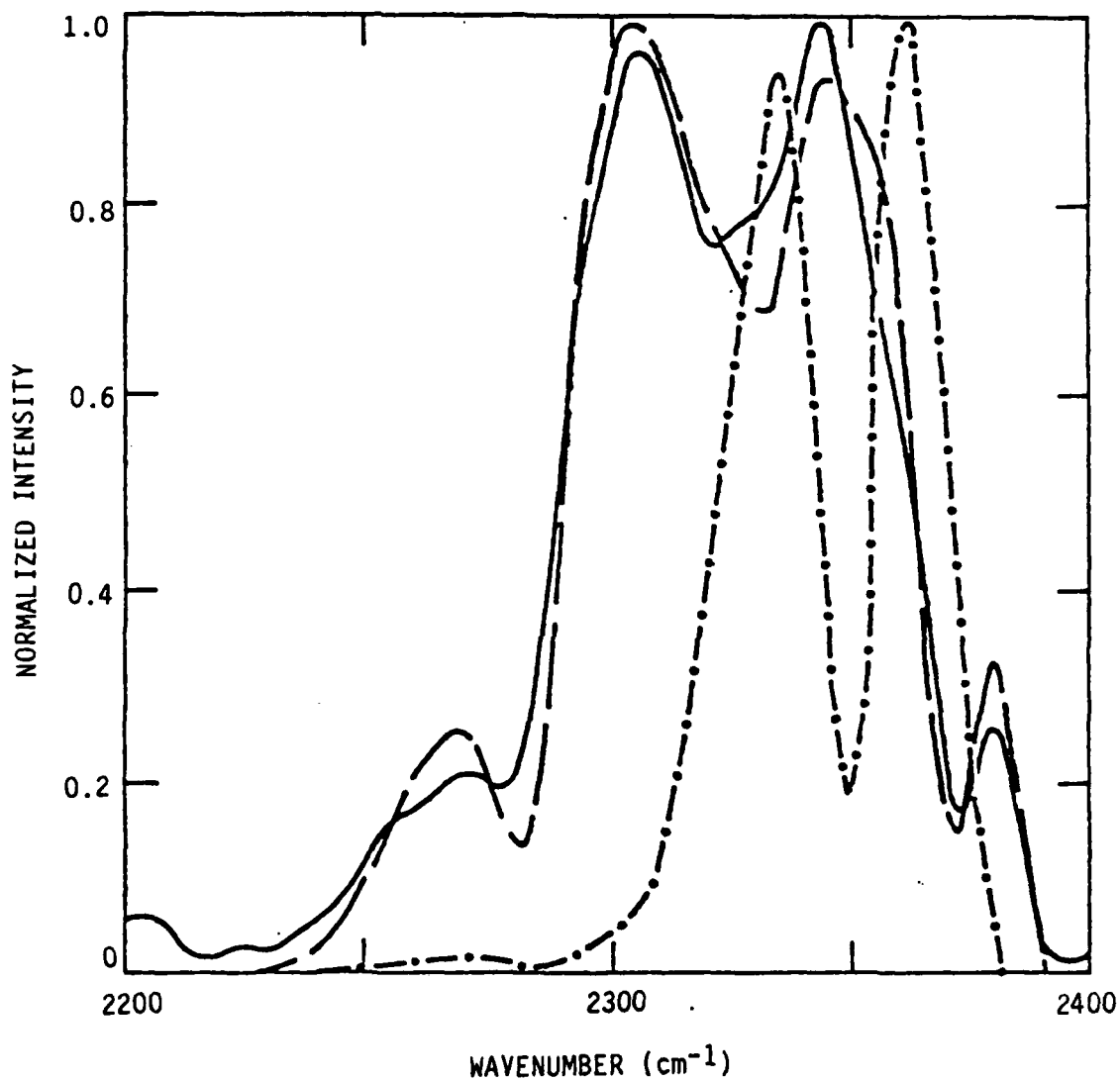
We have performed spectrally resolved measurements of ν_3 band fluorescence which graphically illustrate this effect. These measurements were performed on the higher pressure, higher voltage, room temperature LABCEDE facility¹²⁸ at the Air Force Geophysics Laboratory. In this device a pulsed, 30 keV electron beam is introduced into a low pressure chamber. As the electron beam traverses the chamber it interacts with the target gas in a narrow column losing some of its energy and providing excitation which results in fluorescence. This fluorescence is viewed at right angles to the beam by a

nitrogen-purged Michelson interferometer after passing through 11 cm of unexcited target gas. The electron beam is too weak to meaningfully perturb the gas translational temperature. The present measurements were made with gas mixes of 0.1 to 1 torr CO₂ and 9 torr argon. Spectral resolution was 10 cm⁻¹ and relative spectral response was evaluated by use of black body calibration source.

A comparison between a typical measured spectrum, $P_{\text{CO}_2} = 0.25$ torr, and a predicted unattenuated spectrum of the CO₂(ν_3) band is shown in Figure 78 (each normalized to peak value). The contrast is striking. The measured band is red-shifted, wider, and much more structured than the predicted band. These differences are typical of all our measurements taken under severe self-trapping conditions.

We have performed spectrally resolved predictions of CO₂(ν_3) band transmission using the same techniques as in Ref. 123. The strongest room temperature CO₂(ν_3) bands were included in the calculations, including the CO₂(00⁰1 + 00⁰0, 01¹1 + 01¹0, 02⁰1 + 02⁰0, 10⁰1 + 10⁰0) bands of C¹²O₂¹⁶ (626) as well as the fundamental (00⁰1 + 00⁰0) bands of the isotopic species C¹³O₂¹⁶ (636) and O¹⁶C¹²O¹⁸ (628). Bandstrengths and isotopic abundances were taken from McClatchey et al.¹²⁹; standard selection rules and partition functions were employed. The results were convoluted over the interferometer sinc scanning function.

A typical prediction is shown as the dashed line in Figure 79 (again normalized to peak value). Every feature of the data is reproduced by the theory. Calculations using a more exact Voigt line profile and accounting for limited atmospheric CO₂ absorption were performed for a slightly different set of conditions. No significant differences from the pure Doppler predictions were observed. Thus we feel that the computationally-simpler Doppler line-shapes suffice for the present comparisons and of course are appropriate for the data of Huddleston et al.¹²³ Note the fractional band transmission which could not be measured in our experiments is predicted to be ~ 6 percent.



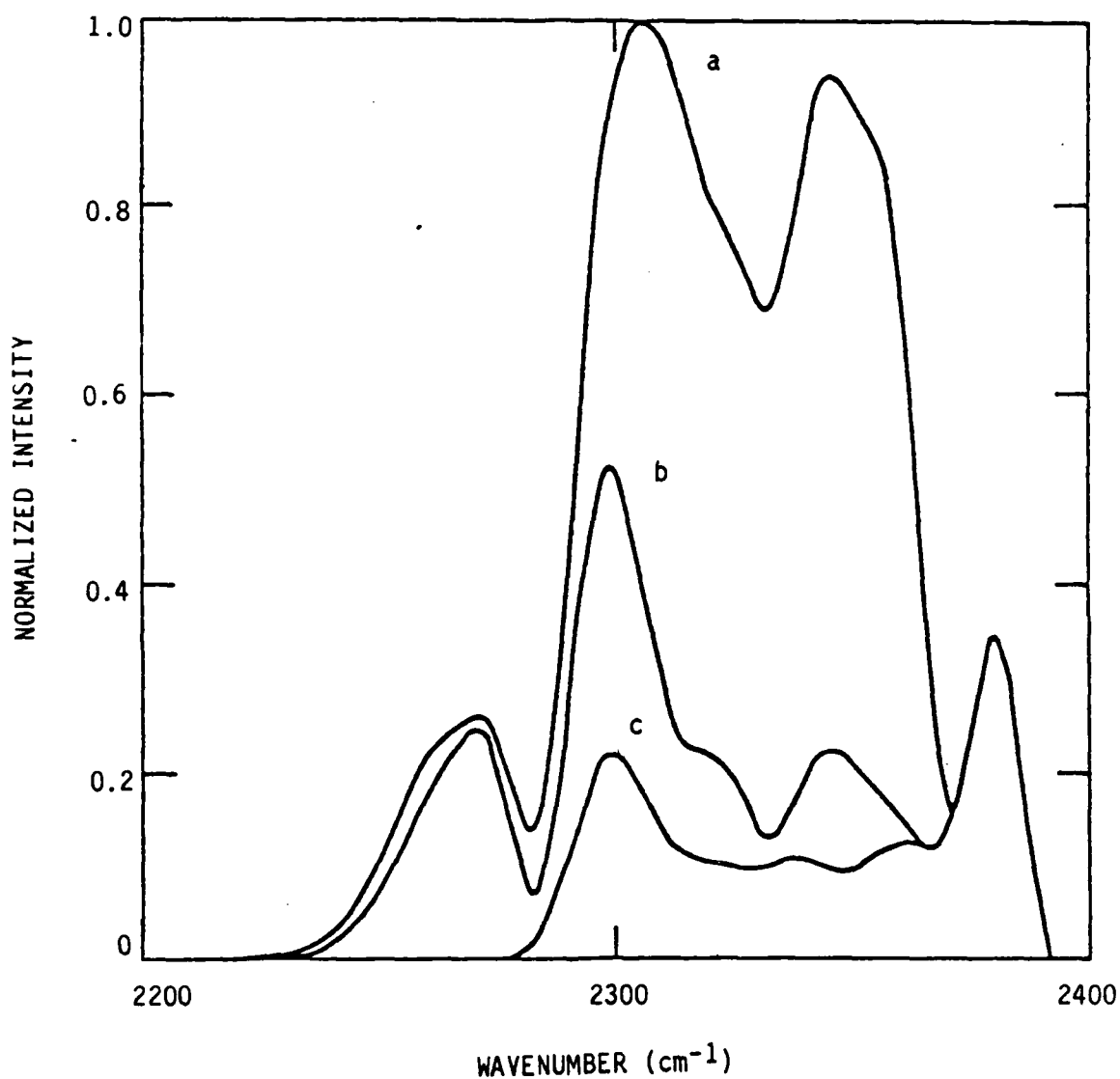
A-1825

Figure 79. Predicted and measured $\text{CO}_2(\nu_3)$ band transmitted intensity normalized to individual peak radiance. Doppler broadened lines. Resolution = 10 cm^{-1} ; $P_{\text{CO}_2} = 0.25 \text{ torr}$; $L = 11 \text{ cm}$; --- predicted, — data, -·-·- unattenuated prediction.

The transmitted intensity is made up of contributions from all the bands considered. In Figure 80, the total radiance is contrasted with that from only the fundamental band transitions of all isotopic species, and also with that of the fundamental band of the main isotopic species. As can be seen the spectral feature at $\sim 2385 \text{ cm}^{-1}$ is due primarily to the fundamental transition of $\text{C}^{12}\text{O}_2^{16}$, whereas that at $\sim 2275 \text{ cm}^{-1}$ corresponds to radiation from the fundamental transitions of the (636) isotopic species. Hot band transitions dominate the radiation between 2275 to 2375 cm^{-1} . However, we conclude that fluorescence arising primarily from fundamental band transitions can be monitored under severe self-trapping conditions with the proper choice of bandpass, 2375 to 2390 cm^{-1} .

Shown in Figure 81 is the contribution of each band to total transmitted radiation as a function of CO_2 pressure, $L = 11 \text{ cm}$. The hot band begins to dominate at $P_{\text{CO}_2} \sim 0.1 \text{ torr}$; total transmitted intensity is $\sim 9\%$. At the highest pressures considered where only $\sim 2\%$ of the fluorescence is transmitted even the isotopic CO_2 contribution dominates that of the $\text{C}^{12}\text{O}_2^{16}$ fundamental band (within the non-overlapping line approximation).

In conclusion $\text{CO}_2(\nu_3)$ band emission can undergo significant self-trapping at relatively low CO_2 pressures ($\text{CO}_2 \sim 0.1 \text{ torr}$, $L \sim 1 \text{ cm}$).^{123,124,127} When self-trapping is important $\text{C}^{12}\text{O}_2^{16}$ fundamental band emission can be overshadowed by contributions from hot bands and isotopic species. The spectral content of the resulting transmitted signal can be quite different from that of the unattenuated $\text{CO}_2(\nu_3)$ band with the various spectral regions of the emission reflecting different transitions.



A-1826

Figure 80. Comparison of three sets of Doppler predictions for CO₂(v₃) band radiation at 0.25 torr CO₂ with a) all transitions, b) no hot bands, but all isotopic fundamentals, and c) only C¹²O₂¹⁶ fundamental. All three curves are normalized to peak of curve a.

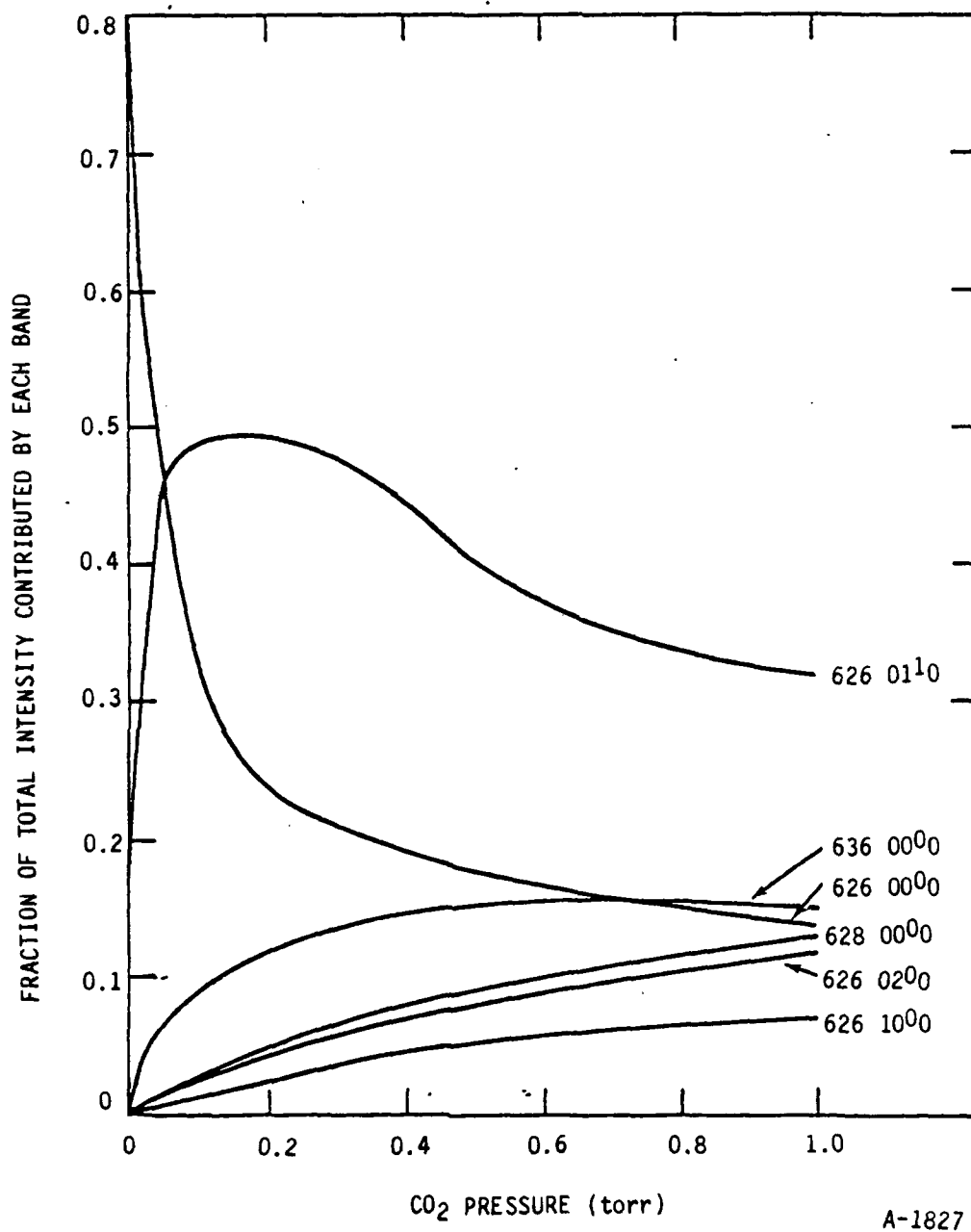


Figure 81. Relative contributions of individual bands to the total transmitted radiation as a function of CO₂ pressure. Displayed are predictions for the three most common isotopes: C¹²O₂¹⁶(626), C¹³O₂¹⁶(636), and O¹⁶C¹²O¹⁸(628), and for the lowest vibrationally excited states of C¹²O₂¹⁶.

9. PRELIMINARY OBSERVATIONS OF BEAM PLASMA DISCHARGES IN LABCEDE

9.1 Introduction

Previous observations on the old LABCEDE apparatus indicated that an intermittent instability was occurring which significantly altered the radiant intensities observed.¹³⁰ During refurbishment of the device, the large electromagnet assembly was constructed to confine the electron beam as it traverses the shroud. This was done to restrict the beam current to the observation volume so as to permit the energy deposition and radiant efficiencies of various band systems across the spectrum (UV-LWIR) to be quantified. It was immediately apparent from preliminary observations as described in Section 3, that in the refurbished LABCEDE apparatus band intensities did not vary smoothly as expected. Rather as pressure or magnetic field or current was increased, a certain threshold was exceeded and the observed intensities increased by one to two orders of magnitude. This effect was quite reproducible. The enhancement was not uniform spectrally; the molecular and atomic features were all enhanced by varying amounts. These observations have been attributed to the occurrence of a beam plasma discharge (BPD) phenomenon. Because LABCEDE was designed to simulate the auroral and nuclear disturbed upper atmosphere, the relevance of this enhancement to those situations had to be considered. Similar apparent intensity enhancements were observed during the EXCEDE mission.¹³¹ Visible and UV spectra were acquired in LABCEDE under a variety of excitation conditions. When the BPD was occurring, less energetic molecular electronic states (with excitation cross-sections peaking around 10 eV) were enhanced relative to more energetic ionic state transitions (which peak at 40 eV) as compared to laboratory spectra taken with lower levels of excitation. The laboratory spectra acquired while a BPD was occurring more closely match the spectral shapes in EXCEDE observations.¹³² A study by Archer¹³³ concluded that BPD processes probably existed during the EXCEDE flight, but did not widely occur in auroral or nuclear events. They could not be ruled out in the strong auroral arcs or in beta patches, however. The aim of our investigation of BPD processes is to quantify the role they may play in the emission spectrum of severely disturbed atmospheres.

The beam-plasma discharge (BPD) was first recognized by Getty and Smullin¹³⁴ and Kharchenko et al.¹³⁵ over 20 years ago, making it one of the earliest studied collective phenomenon. Its importance in the interpretation of experiments using electron beams in space was pointed out by Galeev et al.¹³⁶ and Bernstein et al.¹³⁷ in 1978. Although the phenomenon has been understood qualitatively for some time, it requires strong turbulence theory to make it quantitative.^{138,139} An understanding of strong turbulence has only appeared in the late 70's as large computer calculations for specific conditions have been performed to define the physical parameters. The theoretical understanding has been aided by the series of experiments conducted by Bernstein et al.¹⁴⁰ in 1979, on the large vacuum chamber facility at the NASA Johnson Space Center. This group has studied the threshold for the BPD and empirically correlated it to experimental parameters, providing some data for quantitative comparison. The LABCEDE facility should provide new and exciting data on the BPD that will significantly increase our understanding of this important phenomena. It is the purpose of this chapter to outline our quantitative understanding of BPD and its relation to the LABCEDE spectral studies; to present some preliminary LABCEDE data which begins to provide new insight into BPD phenomenology; and to suggest future experiments which will utilize LABCEDE's extremely wide range of operating conditions to define BPD further in terms of threshold parameters, intensity enhancements, and quenching of the enhanced secondary electrons.

There is an extensive literature on the beam-plasma discharge and the important related plasma physics. In our treatment of the qualitative and quantitative aspects of BPD, we will rely heavily on the recent work by Linson and Papadopoulos,¹⁴¹ who have investigated this subject because of its importance for satellite neutralization.

9.2 Qualitative Description

In the briefest terms, the beam-plasma discharge is a radio frequency (rf) discharge in which the r.f. field energy arises from the interaction of a high energy electron beam with the plasma it has created. Micro-instabilities arise that take energy out of the electron beam and convert it

to electric field energy. Once this process has occurred the beam plasma discharge is very similar to an ordinary gas discharge with a definite threshold for ignition. This occurs when there is enough radio frequency energy to overcome losses and strongly ionize the gas. In LABCEDE the process starts with the electron beam ionizing the background gas at pressures usually between 1 and 10 mtorr. The background plasma density rises until an instability between the electron beam and the background plasma can exist.

In general, whenever the total electron distribution is not at equilibrium (Maxwellian), the plasma will find a mechanism of collective interaction that will bring it to equilibrium. In LABCEDE we start with a total electron distribution comprised of high-energy, nearly monoenergetic beam electrons from the electron accelerator and a much larger number of low energy electrons that have been produced on the background gas by the beam electrons. The collective effects will take energy out of the beam electrons and deposit it into the mass of low energy electrons with the aim of making the overall electron distribution more nearly Maxwellian. This kind of instability caused by a double peaked electron energy distribution goes under the generic name of "two-stream instability." The details of the instability are required for quantitative understanding. Papadopoulos and Linson examine many candidates.

The energy from the beam electrons is transferred to the cold plasma electrons through electric fields at frequencies near the plasma frequency. These fields can transfer energy to the cold plasma electrons through collisional processes just as in any other discharge. However, in addition, when the frequency of the rf fields is near the plasma frequency, as these are, large interactions between the electric field energy and the particles can occur. This interaction involving non-linear wave-wave and wave-particle energy transfer goes by the name "strong turbulence theory." Linear plasma theory is simplified by the ability to decompose arbitrary perturbations into their eigenmodes, with each eigenmode evolving independently of the others. In weakly non-linear plasmas the eigenmodes are coupled to each other by a weak interaction such that the coefficients in the superposition of modes are slowly varying functions of time. This approach is usually referred to as

weak turbulence theory. Unfortunately it only applies when the energy in the excited spectrum of modes is small compared to the total plasma energy. When the energy in the excited modes is of the same order as the total plasma energy, the plasma is said to be strongly turbulent and the perturbation expansion fails. It is only in recent years that a reasonable theory for this regime has evolved. It is this strongly turbulent interaction that makes the BPD difficult to understand quantitatively. More importantly, it makes the BPD different from the usual rf discharge. The strong turbulence leads to cataclysmic collapses of the electric field energy, depositing all this energy into the electrons involved in the interaction. Because only a small subset of the cold plasma electrons are involved in the interaction, these electrons become very energetic ("hot"), on the order of 100 eV. These "hot" electrons ionize the background gas. This is quite different from the usual rf discharge in which the only energy transfer is collisional, and the ionization results from the few energetic electrons in the tail of the cold electron distribution. Since the ionization energy is 15 eV, the mean electron temperature must be fairly high, usually above 1 eV, in order for the small fraction of electrons with 15 eV of energy to create sufficient ionization. This is no longer the case in a BPD: the ionization can come from the "hot" electrons created by the strong turbulent collapse, the background electrons may be quite cold. It may be possible in LABCEDE to determine the temperature of these electrons assuming they are in equilibrium with the molecular vibrational distributions as deduced from infrared emissions. Preliminary interferometric measurements indicated very low electron temperatures, below 0.1 eV. Further measurements are needed to confirm this observation.

Whether or not this ionization process continues to increase depends upon a balance between the rate of loss of electrons and the degree of production by the instability. If the loss rate is low enough, the electron density will continue to rise until the whole process saturates. The radiative intensity is enhanced by nearly a factor of 100 in the LABCEDE device when this beam plasma discharge occurs.

Many kinetic and quenching measurements are planned in the LABCEDE facility. Currently, the occurrence of BPD restricts the experimental operating conditions for some of these measurements. On the other hand, its occurrence highlights the necessity for consideration of such non-linear phenomena in the scenarios LABCEDE is simulating. Its effects on kinetic measurements are at least partially a result of the altered electron distribution's "temperature" increase. For example, the 391.4 nm radiation from the N_2^+ ($B^2\Sigma_u^+$, $v'=0 \rightarrow X^2\Sigma_g^+$, $v''=0$) transformation is used to monitor the electron beam intensity in our quenching studies of the Meinel bands ($N_2^+A^2\Pi_u - X^2\Sigma_g^+$).¹⁴² However, if the "hot" electrons created by the BPD are sufficiently energetic that they are well above the excitation thresholds for the N_2^+A and N_2^+B states at 14 and 16 eV, respectively, then they should excite the N_2^+A and N_2^+B states in the same way. As a result, they can be considered along with the primary electrons as an excitation source and monitored with the 391.4 nm line. This means that the Meinel band quenching measurements can be performed at the high BPD intensities. In fact, the quenching rates observed during BPD conditions are similar to those deduced when observing just the primary beam irradiated molecules lending support to this argument.

9.3 A Quantitative Look at the Beam Plasma Discharge in the LABCEDE Device

The first step in evaluating the quantitative aspects of the beam plasma discharge is to determine the size of the electron beam in the test region. A beam of unneutralized electrons will tend to spread due to the Coulombic self-repulsion of the electrons, that is, its own space charge. This effect can be counteracted by the use of a magnetic field however; if background ions are present they can neutralize the beam and prevent this spread. The time, τ_i , required to create an electron-ion pair is given by

$$\tau_i = \frac{E_I}{v_e \frac{dW}{ds}} \quad (79)$$

where E_I is the average energy loss per ion-electron pair, v_e is the electron velocity, and $\frac{dW}{ds}$ is the electron energy loss per unit length.

Of course, it will require 10 to 100 such collisions to neutralize the beam, but τ_1 will provide us with a reference time frame.

The resultant τ_1 at 1 mtorr is 0.13 μ s, indicating that neutralization will occur on μ s time scales. Because the beam is neutralized in LABCEDE, its spatial extent will depend upon scattering.

Electron Scattering - The fractional rate of energy loss for an electron near 3 kV is given by¹⁴³

$$\frac{1}{W} \frac{dW}{ds} = - \frac{1.82 \times 10^{-12}}{W^2} N \ln \frac{W}{72.6} \quad (80)$$

with cgs units and energy (W) in eV. This corresponds to a deposition length of 3.7×10^4 cm at 1 mtorr dropping to 4.7×10^2 cm at 80 mtorr. Thus, over most of the experimental pressure range the electron beam has lost little of its energy in the 50 cm path it traverses prior to reaching the observation volume. As a result, the energy loss can be neglected in considering the beam spreading and only the multiple small angle scatterings of the electrons off the neutrals determines the beam size.

The Boltzmann equation governs the time development of a given initial electron distribution in space and direction of motion¹⁴⁴

$$\hat{u} \cdot \nabla f + \frac{1}{v} \underline{a} \cdot \nabla_u f = d\Omega' N \sigma_{(\alpha, v)} [f(\underline{r}, \hat{u}') - f(\underline{r}, \hat{u})] \quad (81)$$

where $f(\underline{r}, \hat{u})$ is the probability of finding an electron at position \underline{r} with velocity direction \hat{u} ,

\hat{u} is the direction vector of the velocity

v is the velocity

\underline{a} is the acceleration, if any

$d\Omega \equiv \sin \alpha \, d\alpha \, d\beta$

$\sigma_{(\alpha, v)}$ is the shielded Rutherford scattering cross section.

If we limit the scattering to small angles so that $\hat{u} = \eta \hat{i} + \zeta \hat{k}$ where η and ζ are small, then this equation can be rewritten for small deviations (the Fokker-Planck approximation) with the acceleration term equal to zero as¹⁶

$$\frac{\partial f}{\partial x} + \eta \frac{\partial f}{\partial y} + \zeta \frac{\partial f}{\partial z} = \frac{1}{\lambda} \left[\frac{\partial^2 f}{\partial \eta^2} + \frac{\partial^2 f}{\partial \zeta^2} \right] \quad (82)$$

where

$$\frac{1}{N\lambda} = \frac{\pi}{2} \int_0^\pi \alpha^3 \sigma(\alpha) d\alpha \quad (83)$$

For nitrogen with electron energies near 3 keV

$$\frac{1}{N\lambda} = \frac{8.55 \times 10^{-13}}{W^2} \ln \frac{W}{26.5} \quad (84)$$

with $W = 3$ keV and a pressure of 10 millitorr, this is a length $\lambda_{\text{scattering}} = 6.25 \times 10^3$ cm.

Examination of Eq. 82 indicates that the scattering in the two perpendicular directions is uncoupled, that is

$$f(y, \eta, z, \zeta | x) = f(y, \eta | x) f(z, \zeta | x)$$

where we have used probability theory notation to point out that what we are looking for is the distribution of position y and angle η at a given distance from the source x . The separated equations become

$$\left(\frac{\partial}{\partial x} + \eta \frac{\partial}{\partial y} - \frac{1}{\lambda} \frac{\partial^2}{\partial \eta^2} \right) f(y, \eta | x) = 0 \quad (85)$$

and a similar equation for the perpendicular direction, this equation can be solved by applying a Laplace transform on x and Fourier transforms on η and y . The resulting first order ordinary differential equation can be solved and then inverted to give the solution¹⁴⁵

$$f(y, \eta | x) dy d\eta = \frac{\lambda \sqrt{3}}{2\pi x^2} e^{-\frac{\lambda}{x} \left\{ y^2 - \frac{3y\eta}{x} + \frac{3\eta^2}{x^2} \right\}} dy d\eta \quad (86)$$

which is the probability that an electron, after traversing a radial distance y from the source, will have a position off the axis between y and $y + dy$ with an angle to the axis between η and $\eta + d\eta$. The energy deposition depends upon the energy (assumed constant at the initial energy for now) and the number density f and since the electron has an angle η to the axis a correction must be applied. The distance this electron goes is not Δx but $\sqrt{1 + \eta^2 + \zeta^2} dx$, which will be approximately $1 + \frac{\eta^2}{2} + \frac{\zeta^2}{2}$. The signal that will be seen by a slit of length $2L$ perpendicular to the beam (x) axis is given by

$$S = \frac{3\lambda^2}{4\pi x^3} \int_{-L}^L dy \int_{-\infty}^{\infty} dz \int_{-\infty}^{\infty} d\eta \int_{-\infty}^{\infty} d\zeta \left[1 + \frac{\eta^2}{2} + \frac{\zeta^2}{2} \right] \\ \times e^{-\frac{\lambda}{x} \left\{ \eta^2 - 3\eta \frac{y}{x} + 3 \frac{y^2}{x^2} + \zeta^2 - 3\zeta \frac{z}{x} + 3 \frac{z^2}{x^2} \right\}} \\ S = \int_{-L}^{+L} dy \left(\frac{3\lambda}{4\pi x} \right)^{1/2} \left(1 + \frac{5}{4} \frac{x}{y} + \frac{9}{8} \frac{y^2}{x^2} \right) e^{-\frac{3\lambda y^2}{4x^3}} \quad (87)$$

This integral, the distribution of the energy deposition as projected onto a plane going through the beam axis and perpendicular to the viewer, has been evaluated for $x = 45$ cm and three pressures 1 mtorr, 10 mtorr, and 80 mtorr, and is shown in Figure 82. Notice that if $L = \infty$ in Eq. (87), the signal rises as you go away from the source as

$$S = 1 + \frac{2x}{\lambda} \quad (88)$$

due to the effect of scattering in angle. Equation (88) predicts that the observed intensity will rise as you move away from the source, or rise faster than linearly as you increase pressure at a fixed distance from the source. That the signal rises is shown in Figure 83, taken from Ref. 146. However, the predicted rate of rise is considerably less than what is observed. This is because back scattering of electrons further down the beam into the first section has been neglected. The inclusion of this backscatter can be achieved by Monte Carlo methods¹⁴⁷ or by expanding in Legendre polynomials,^{148,149} but

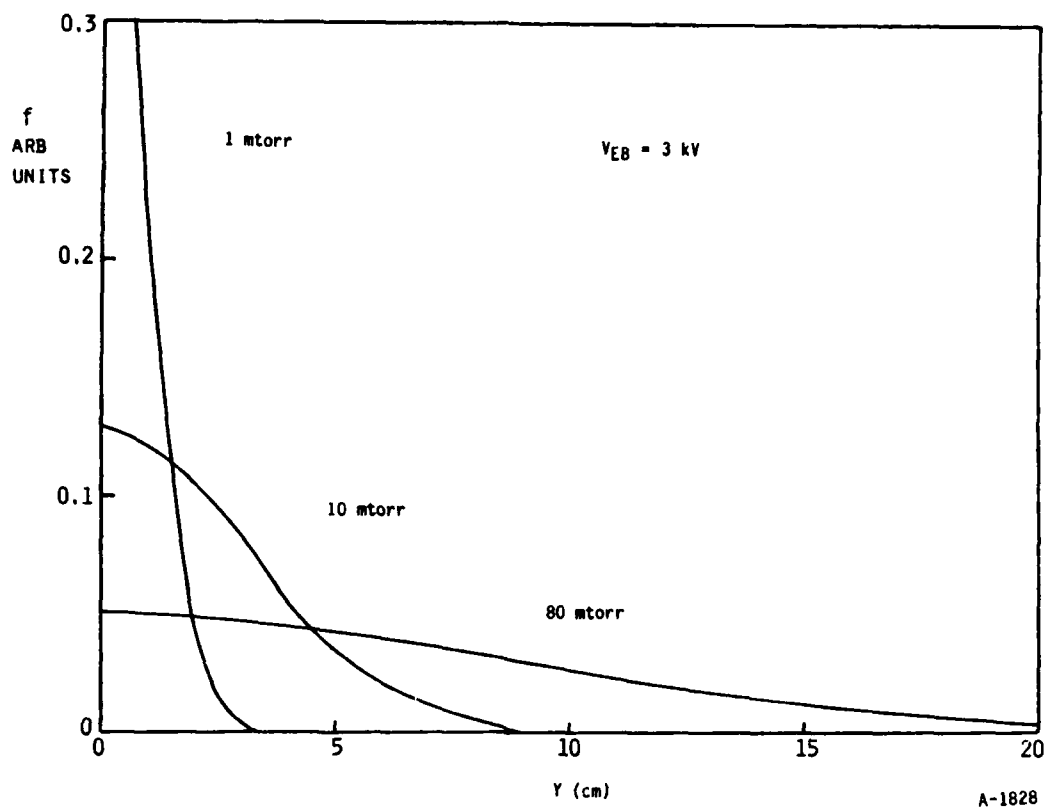


Figure 82. Energy deposition as a function of radial distance for several pressures for a 3 kV beam of electrons for scattering from a 300K gas.

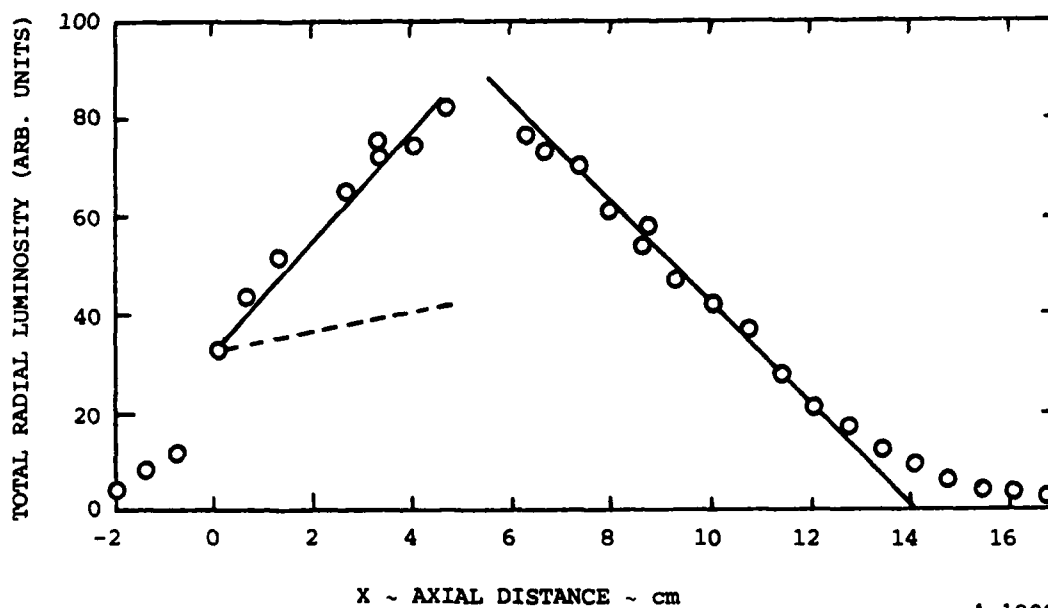


Figure 83. The total radial luminosity as a function of axial distance. The broken line illustrates the increase in signal expected due to scattering from Eq. 88. The actual increase seen in the data of Cohn and Caledonia¹⁴⁶ is three times this slope and is attributed to the backscattering of electrons from further down the beam.

does not yield to easy analysis. The effect of scattering on the observed signal as calculated by Eq. (87) as a function of pressure for different slit heights is shown in Figure 84. Notice the rise in signal with pressure for the largest slits. The effect of scattering has been compared with data in Figure 85. The signal would be expected to rise linearly proportional to pressure in the absence of scattering. The dominant effect of the scattering is to broaden the beam such that some of the excitation occurs outside the observed volume. This lowers the signal. The secondary effect of the scattering is to scatter electrons back toward the electron source. This slightly increases the signal. As just mentioned we underpredict this effect and therefore the measured signal.

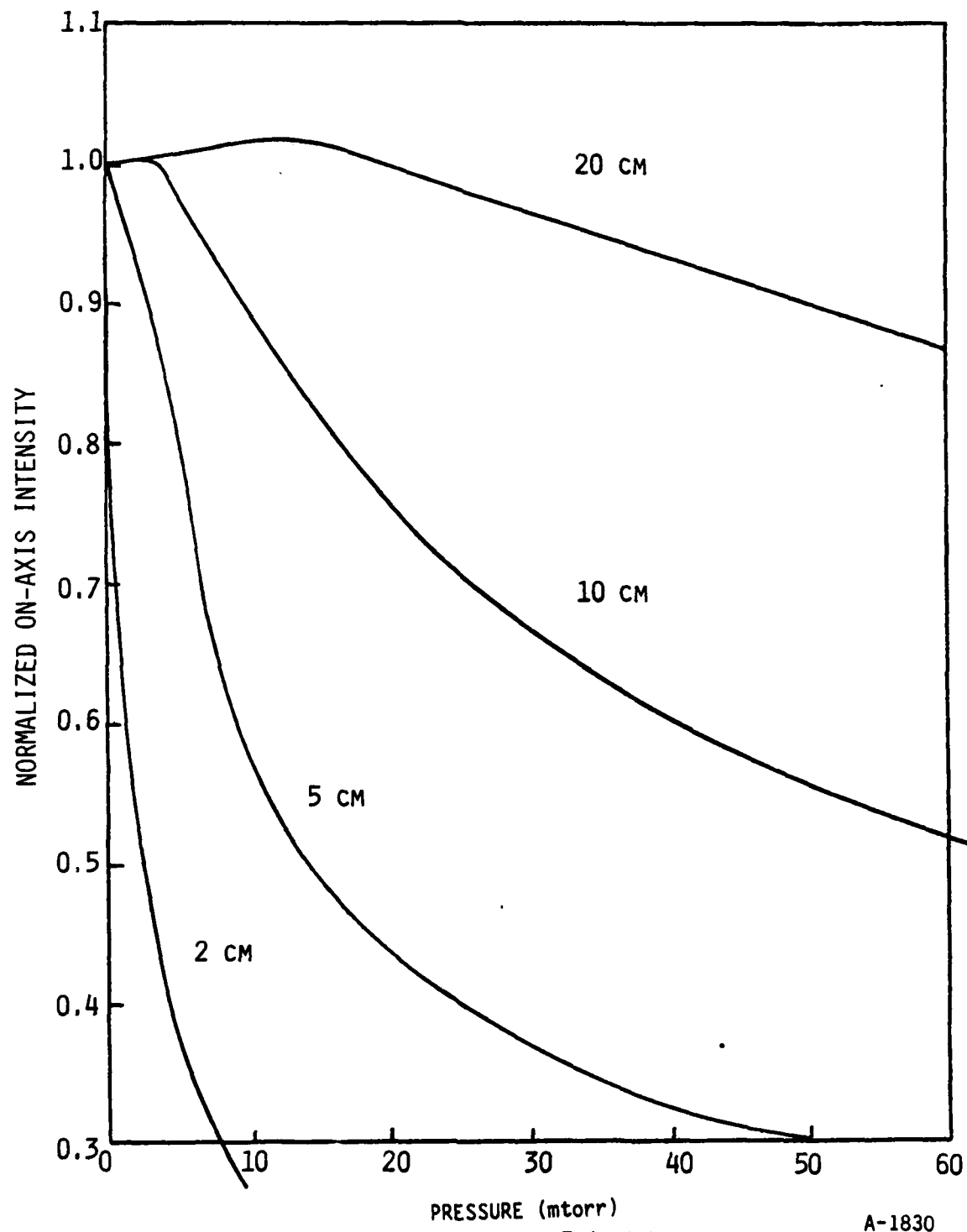
A magnetic field directed along the electron beam axis can be used to confine the beam. The scattered electrons are caused to circle the magnetic field lines and limit the beam spreading. Theoretically, the effect of the magnetic field is to provide an acceleration

$$\underline{a} = \frac{e}{m} \underline{u} \times \underline{B} , \quad (89)$$

that can be put into the Boltzmann equation (Eq. (81)). In the Fokker-Planck approximation, this leads to an equation similar to Eq. (82), but with an additional term.

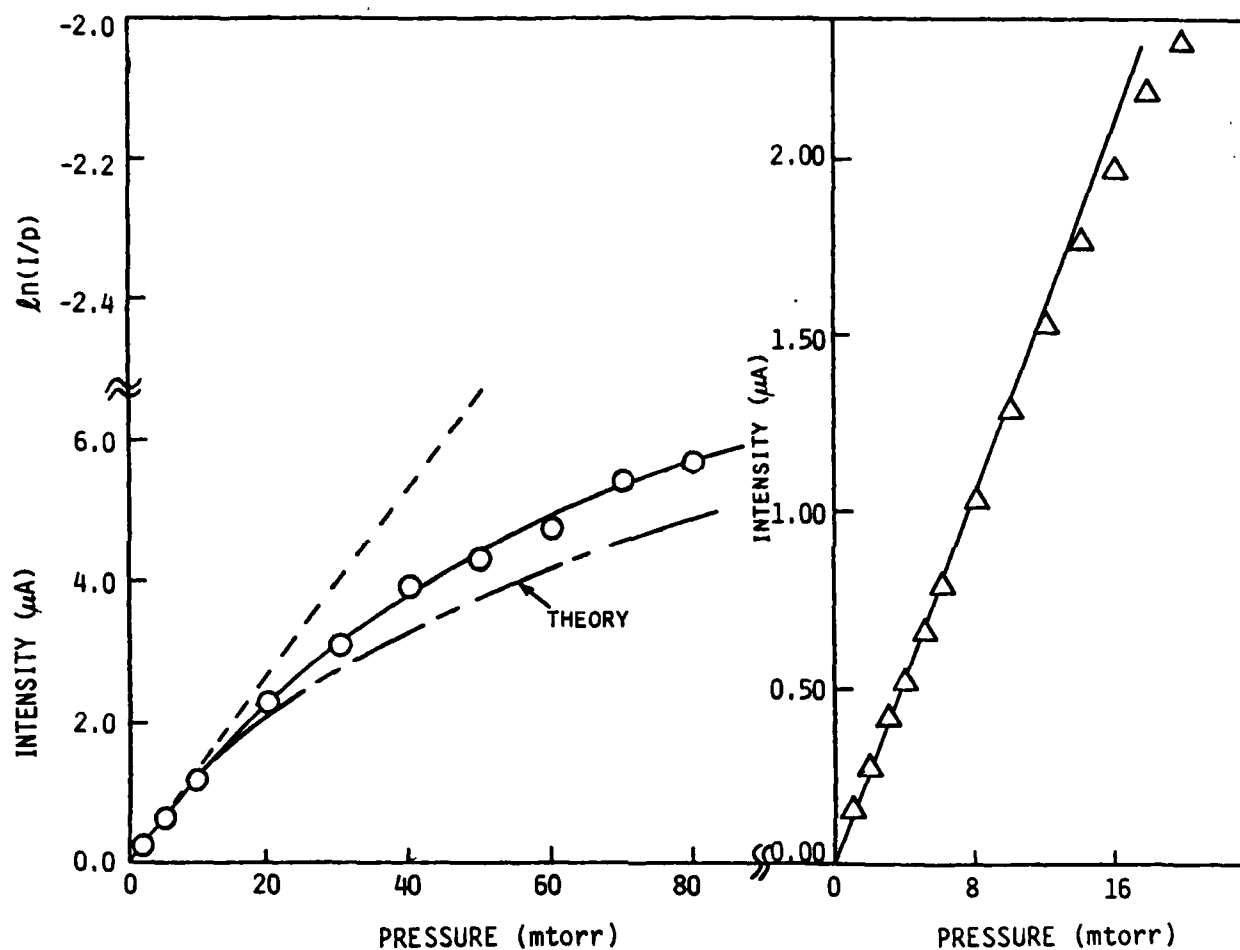
$$\frac{\partial f}{\partial x} + \eta \frac{\partial f}{\partial y} + \zeta \frac{\partial f}{\partial z} + \frac{1}{r_L} \left[\zeta \frac{\partial f}{\partial \eta} - \eta \frac{\partial f}{\partial \zeta} \right] = \frac{1}{\lambda} \left[\frac{\partial^2 f}{\partial \eta^2} + \frac{\partial^2 f}{\partial \zeta^2} \right] \quad (90)$$

Another scale length has been added, the Larmor radius, $r_L = \frac{mcu}{eB}$. More importantly, it has coupled the y and z components of velocity. The equation is no longer separable, and is very difficult to solve. For the present, it is proposed to use a very simple approximation. The angle η , with its implied perpendicular velocity ηu would lead to a gyroradius ηr_L . The approximation is to assume that the distribution for η with a magnetic field is the distribution in angle, given by Eq. (86) (integrated over η) with η replaced by $\frac{y}{r_L}$. This can be combined with the distribution for $\eta(B = 0)$ in an approximate manner to give



A-1830

Figure 84. Effect of slit height on intensity as a function of pressure.



A-1831

Figure 85. Variation in intensity of $N_2^+(B^2\Sigma_u^+, v'=0 \rightarrow X^2\Sigma_g^+, v''=0)$ at 391.4 nm as a function of pressure of air in absence of a magnetic field. Curve labeled theory is calculated from Eq. 87 in text. Electron beam current is 8 mA; beam voltage is 3 kV. Right-hand plot shows quasi-linear region with an expanded scale.

$$f(y,x) = \frac{\lambda}{4\pi x} \left(\frac{1}{r_L^2} + \frac{3}{x^2} \right)^{1/2} e^{-\frac{\lambda y^2}{4x} \left(\frac{1}{r_L^2} + \frac{3}{x^2} \right)} \quad (91)$$

This distribution is shown for $x = 45$ cm and $p = 10$ millitorr in Figure 86 for several values of magnetic field.

9.4 Experimental Results Relevant to Beam Plasma Discharges

The beam plasma discharge as discussed earlier relies upon particle micro instabilities to create the rf electric fields that ignite the discharges. The micro-instabilities, in turn, rely upon the coherent motion of groups of electrons. Collisions destroy the necessary coherence and as a result, for a set of given beam parameters (a maximum magnetic field, scale size, etc.) there will be pressure above which the instability will no longer be able to sustain the discharge. As the pressure is raised from threshold, the BPD grows in intensity and then saturates. Further increases in pressure will not increase the plasma density but only the collision frequency.

Theoretical arguments related to detailed analysis of the micro-instabilities¹⁴⁸ suggest that the frequency of the instability ω should be approximately the electron plasma frequency, ω_p , which should in turn, be approximately six times the electron gyrofrequency Ω_e (which is also known as the cyclotron frequency). If quenching occurs when the collision time is such that $\omega\tau$ falls below a certain value, then the pressure for quenching to occur should be proportional to magnetic field B . This value may be large since small collisional effects may be sufficient to disrupt the coherence required for the BPD.

Data such as shown in Figure 87 for the $N_2^+(B^2 \Sigma_u^+ v'=0)$ state and Figure 87 for the $N_2(^3\Pi_u v'=0)$ state permit estimates of the onset of quenching to be made. The data in Figure 88 was taken for another purpose and thus only coarsely bounds the onset of BPD. These bounds are shown by the

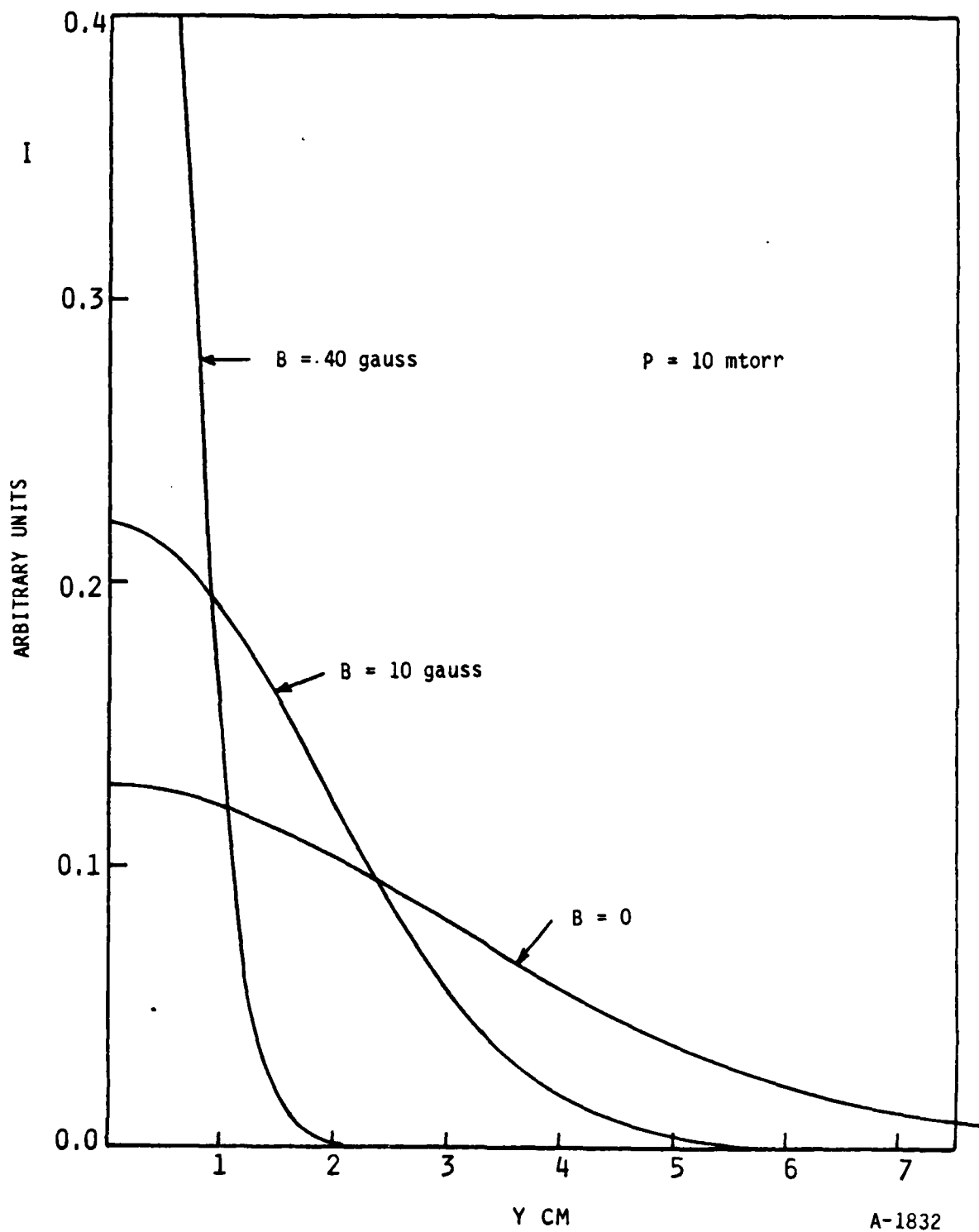
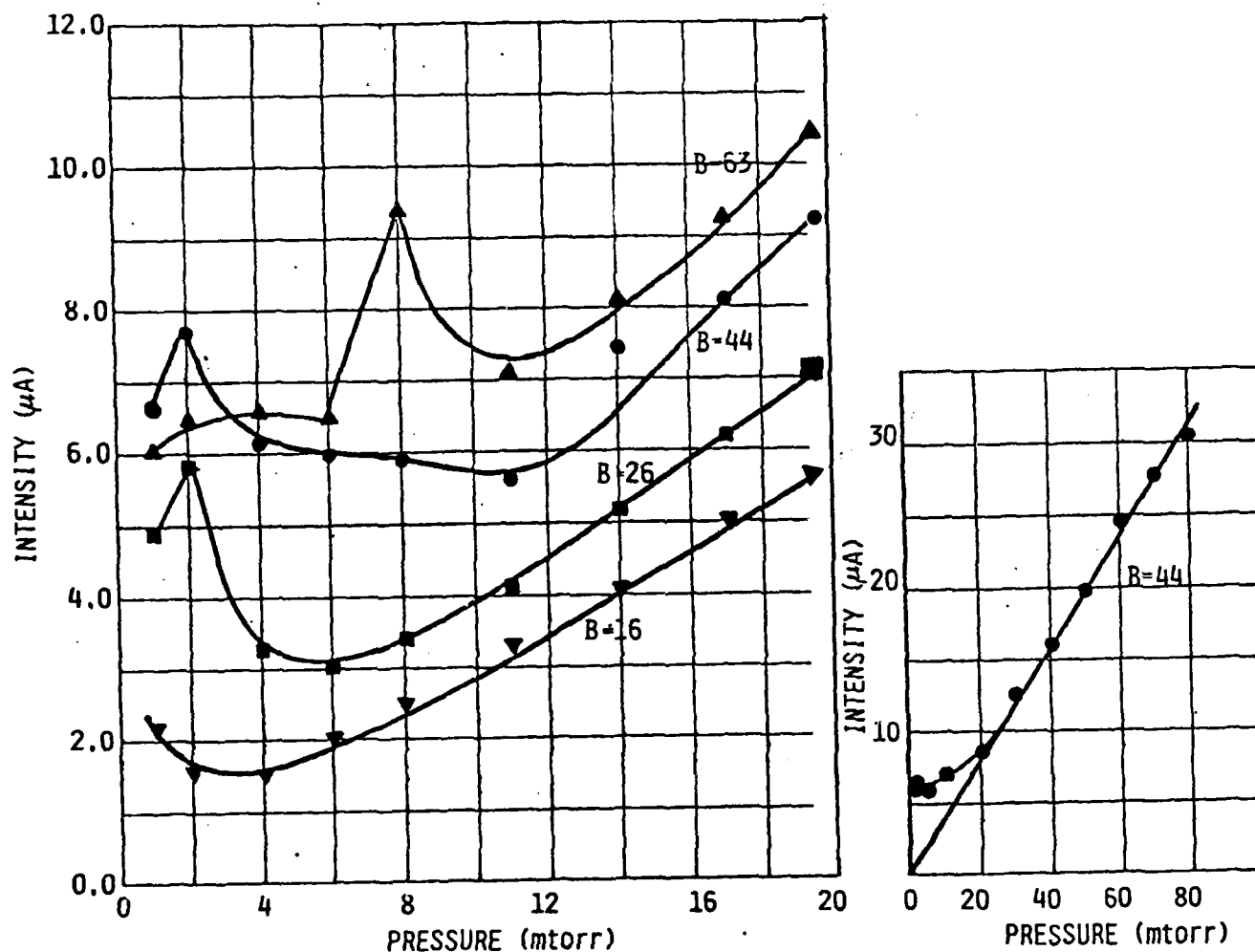
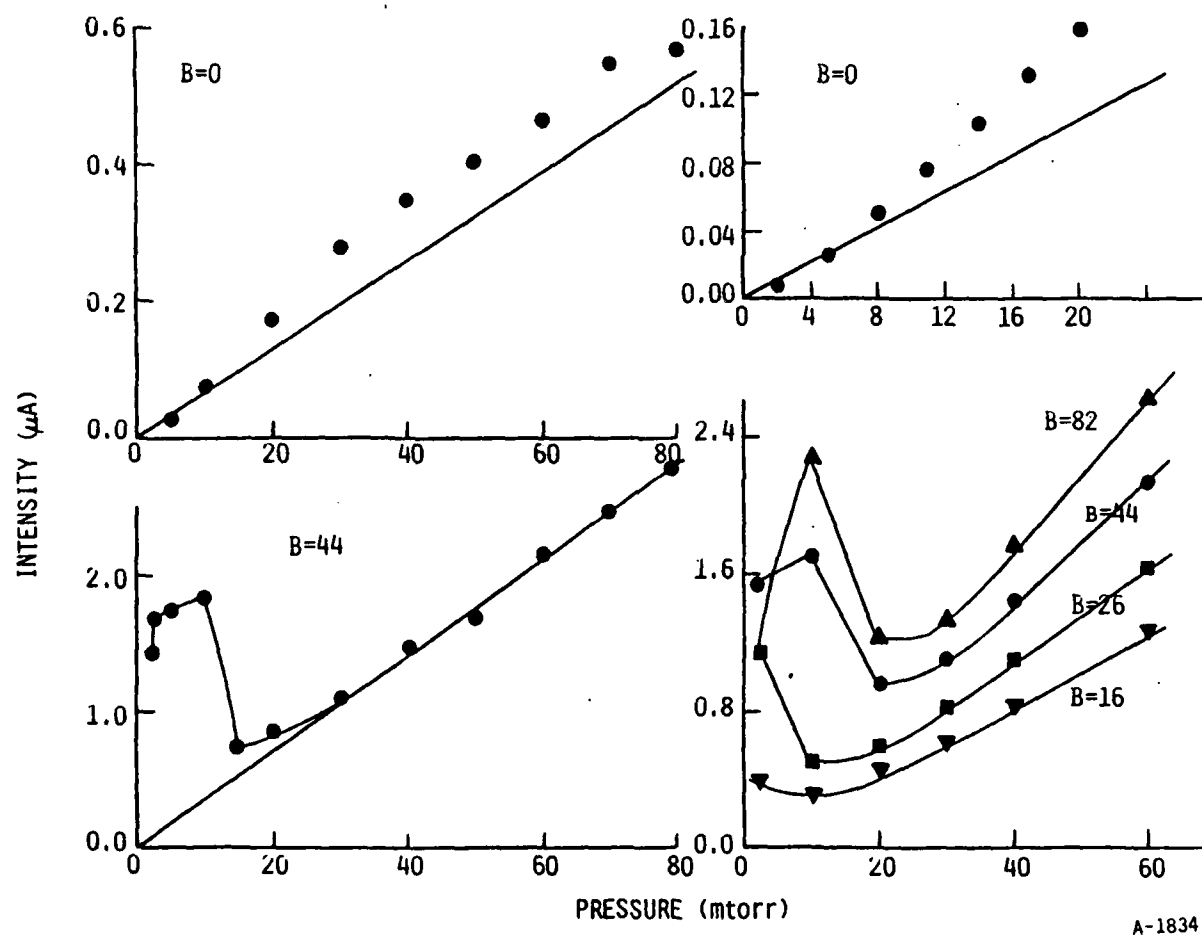


Figure 86. Effect of magnetic field on radial intensity distribution.



A-1833

Figure 87. Variation in intensity of $N_2^+(B^2\Sigma_u^+, v'=0 - X^2\Sigma_g^+, v''=0)$ band at 391.4 nm as a function of pressure of air for four different magnetic field strengths for a 3.0 kV, 8 mA beam. Magnetic field strengths are in units of gauss.



A-1834

Figure 88. Variation in intensity of $N_2(C^3\Pi_u v'=0 - B^3\Pi_g v''=2)$ band at 380.4 nm as a function of the pressure of air for several different values of magnetic field. e-beam energy = 3.0 kV, e-beam current = 8 mA.

arrows in Figure 89 which is a plot of B versus P for quenching. Data which more accurately fixes the onset of BPD places the threshold between 10 and 14 mtorr at 44 gauss. The straight line drawn satisfying the bounds from the N₂C state data has little statistical basis - a B^{1/2} line would also fit the data. Clearly, more definitive data must be obtained. If the straight line is correct, then the ω_T required to sustain the BPD can be estimated from the values $p \sim 10$ mtorr when $B = 42$ gauss.

For quenching with $B = 42$ gauss,

$$\Omega_e \equiv \frac{eB}{mc} = 7.4 \times 10^8 \frac{\text{rad}}{\text{s}} \quad (92)$$

if $\omega \sim \omega_e \sim 6\Omega_e$, then $\omega \sim 4.4 \times 10^9 \frac{\text{rad}}{\text{s}}$. This value of ω_e implies an electron density of $6 \times 10^9 \frac{\text{electrons}}{\text{cm}^3}$ from

$$\omega_e = \left(\frac{4\pi ne^2}{m} \right)^{1/2} \quad (93)$$

The condition for the onset of the beam plasma discharge can also be determined in LABCEDE. This, as mentioned earlier, would provide quantitative data to hang theoretical results on. There is some evidence for onset shown in Figure 88 where it appears that with $B = 44$ gauss the critical pressure is less than 2 mtorr. Recent data have refined this answer and a typical point for threshold in LABCEDE is given in the table below.

Previous work by Bernstein et al.¹⁴⁰ had indicated that the threshold current I_C was given by

$$I_C = A \frac{v^{3/2}}{B^{0.7}_{PL}}$$

with

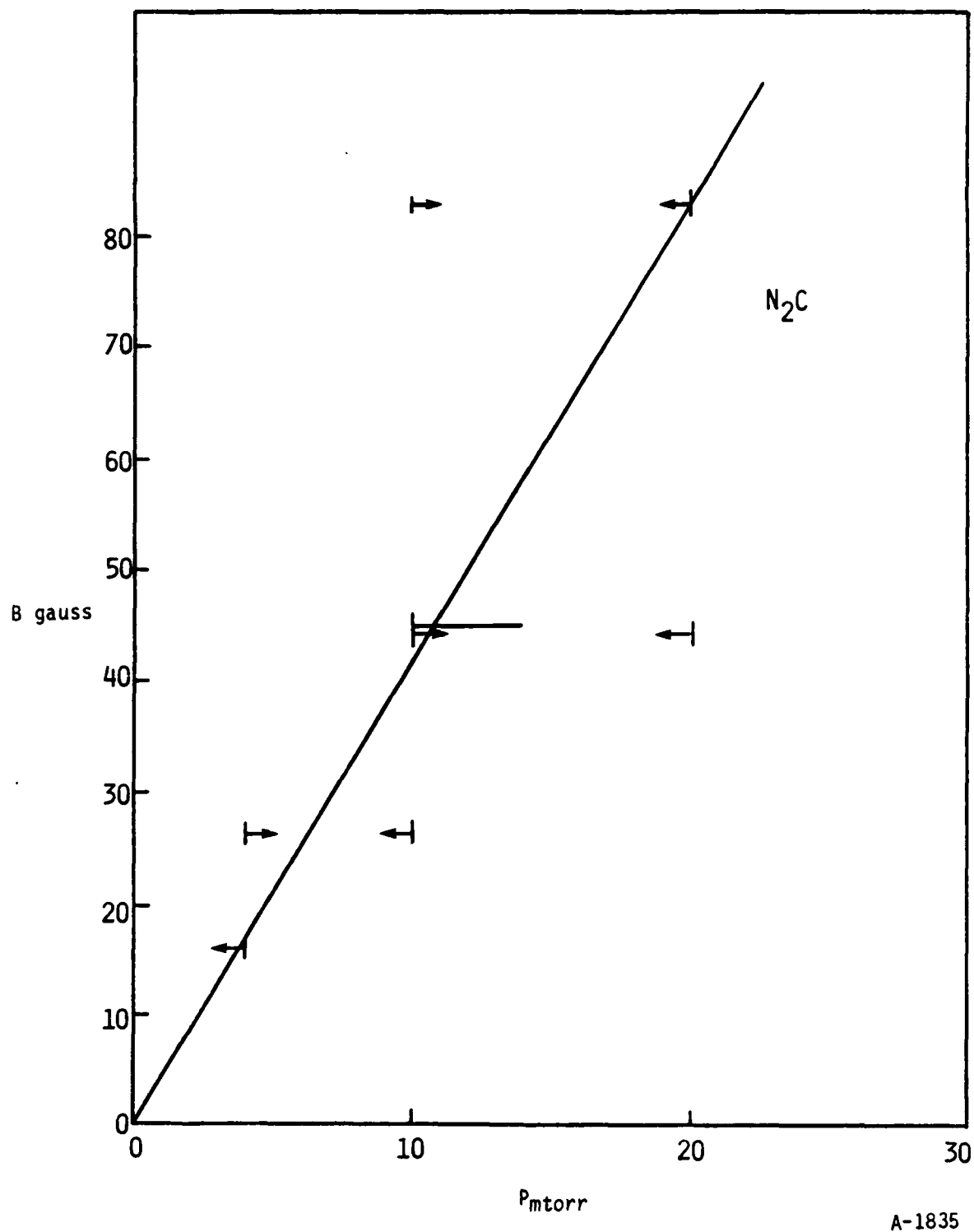


Figure 89. Bounds on quenching of BPD enhancements from the N_2C state as a function of pressure and magnetic field.

<u>Bernstein</u>	<u>LABCEDE</u>	<u>Comments</u>
$I_C = 10 \text{ ma}$	6 ma	Total current
$B = 1.14 \text{ gauss}$	20 gauss	Applied field
$V = 1 \text{ keV}$	4.5 keV	Electron voltage
$P = 1.4 \times 10^{-5} \text{ torr}$	$7 \times 10^{-4} \text{ torr}$	Background or flowing gas
$L = 2000 \text{ cm}$	90 cm	Beam path length

This implies that A should be equal to 0.31 cm^2 when units of ma, gauss, keV, torr and cm are used. The LABCEDE point gives $A = 0.32 \text{ cm}^2$. This agreement is certainly fortuitous, but the excellent agreement implies that the phenomena are closely related.

Having established this benchmark calculation, we then went on to explore the characteristic frequency regimes which we can obtain inside LABCEDE. A map displaying these frequencies is shown in Figure 90. These are the results of a zeroth-order calculation intended to guide further experiments and modeling. Angular frequency (lefthand side y axis in radians/s) is plotted against magnetic field (bottom x axis in gauss). The lowermost solid line represents the cyclotron frequency as calculated from Eq. 92

$$\Omega_e = 1.8 \times 10^7 B .$$

Over the range of magnetic fields which can be applied in LABCEDE, $\Omega_e \cong 10^7\text{-}10^9 \text{ rad s}^{-1}$. For example, when the applied field is 6 Gauss, the cyclotron frequency is $\sim 10^8 \text{ rad s}^{-1}$.

The plasma frequency, ω_p , is determined by the electron beam current, voltage and radius:150

$$\omega_p = 6 \times 10^7 \frac{I}{V^{3/2}} \frac{1}{R}^{1/2} \frac{V}{R}^{1/2} \quad (94)$$

As an example for a 10 mA beam of electrons with 3 mm radius (right-hand side y-axis and middle dashed curve), the electron density is 10^8 cm^{-3} (top x-axis) and the corresponding ω_p is $\sim 5 \times 10^8 \text{ rads}^{-1}$. The electron-neutral collision

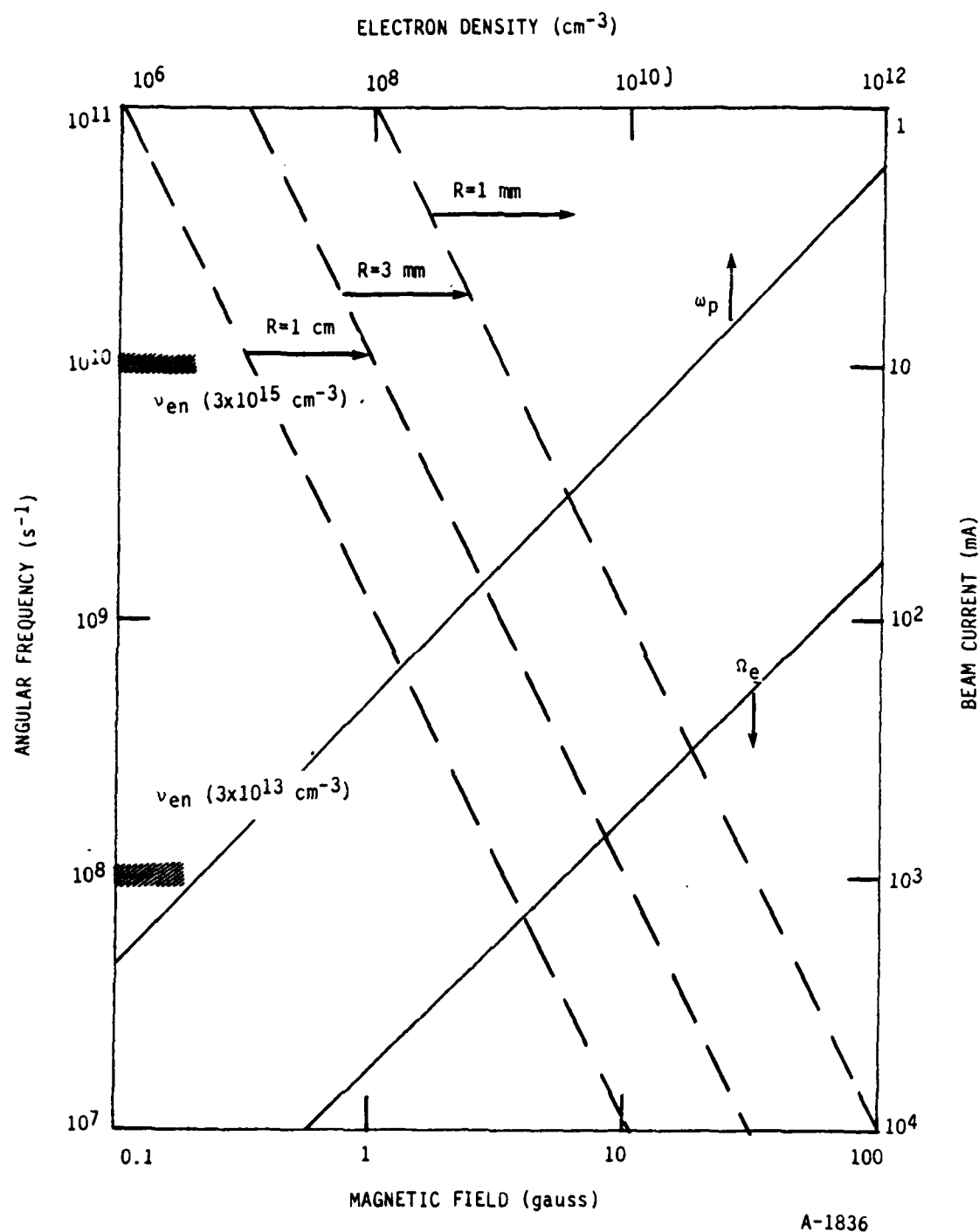


Figure 90. Characteristic beam frequencies in LABCEDE.

frequency, ν_{en} , is indicated along the left-hand y-axis. Thus the experimental parameter space which we can cover in LABCEDE allows the following characteristic frequency ranges:

$$\Omega_e = 10^7 - 10^9 \text{ s}^{-1}$$

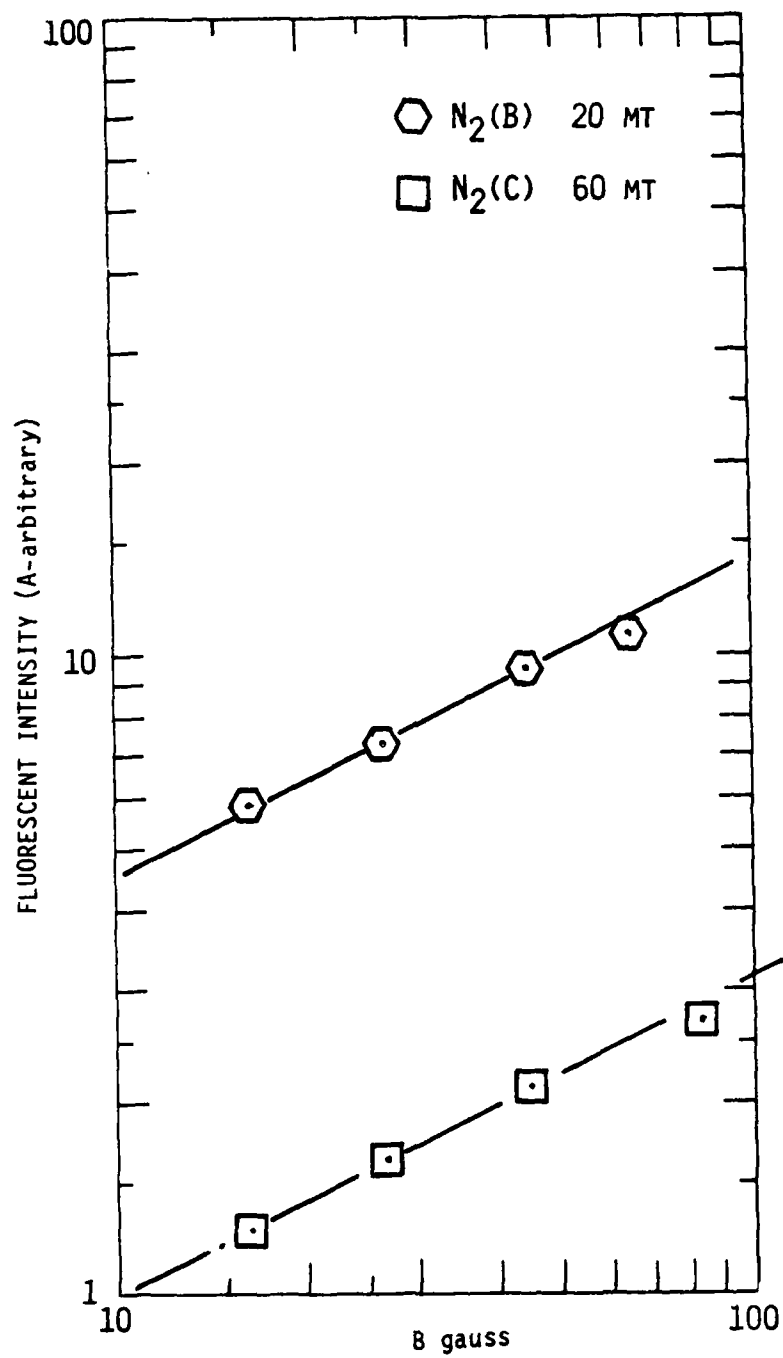
$$\omega_p = 2 \times 10^8 - 10^9 \text{ s}^{-1}$$

$$\nu_{en} \sim 10^6 - 10^9 \text{ s}^{-1}.$$

This means that we can vary Ω_e by applying an external magnetic field until $\omega_p \sim 6\Omega_e$ and the instability occurs. From Figure 90 at 15 mA and 3 mm radius, $\omega_p \sim$ several times 10^8 s^{-1} and Ω_e must be $\sim 10^8 \text{ s}^{-1}$ for instability onset. This corresponds to 6 gauss - in rough agreement with the observations of the next section. In order to damp the instability, we require $\nu_{en} > \omega_p$. This occurs for pressures $< 4 \text{ mt}$, in fair agreement with observations. Modeling at this simplistic level permits some insight into complex experimental observations and provides a useful guide for future threshold measurements. These are described in the next section.

It is expected that the magnetic field should contain the beam so that the data (as shown in Figure 85) would not fall off with increasing pressure. This is indeed the case as shown in Figure 88. The signal is linear with pressure up to pressures of 80 mtorr. However, it would be expected at first glance that once the magnetic field was sufficiently high to contain the beam and its secondaries that the signal would be independent of B. In fact, the signal increases with increasing B as seen in Figure 88 and plots of the data (shown in Figure 90) indicate it is proportional to $B^{1/2}$. Whether this is telling us about beam scattering in the presence of a magnetic field or about plasma micro-instabilities is not clear at present. This data should be examined farther and additional data must be acquired to address these effects. This increase is also seen for the N_2C state created by beam secondaries as is seen in Figure 91.

In light of these conclusions, additional laboratory data was acquired to more accurately determine BPD thresholds. This data is discussed in the next section.



A-1837

Figure 91. Effect of magnetic field on observed intensity for N_2B and N_2C state emissions.

9.5 Threshold Measurements

The fluorescence inside LABCEDE was observed using the 1/3m McPherson visible spectrometer. The primary wavelength monitored was 391.4 nm (N_2^+B , $v' = 0 \rightarrow N_2^+X$, $v''=0$). The 391.4 nm intensity was observed as a function of pressure for several beam currents at fixed values of applied magnetic field and beam voltage as shown in Figure 92 for pure N_2 . The intensity per unit beam current shows a rapid onset which is fastest at larger currents. Below this threshold the normalized intensity scales linearly with pressure and is independent of beam current as would be expected in the single particle scattering regime. The enhancement above threshold increases with current. Additionally, there is considerable, reproducible structure at pressures well above threshold. This structure is current and magnetic field dependent. As pressure increases the intensities asymptotes to the low pressure "single particle" scaling - the instability is quenched. Again as can be seen in the figure the fully quenched point is current dependent.

Under certain conditions, a temporal instability is also established - the intensity oscillates between two values with a period of a few seconds. The transition between these regimes occurs faster than the data acquisition rate (25 μ s). Finally, once the beam plasma discharge has occurred, it can be maintained at pressures well below onset thresholds. Because of the complexity of this phenomenon, we decided to concentrate on a single aspect - the current and B field scalings of the threshold.

We define threshold as the pressure at which intensity has begun to show non-linear pressure scaling. This pressure is not significantly different than the pressure at which the steep rise occurs. The threshold pressure as a function of beam current is plotted in Figure 93 for 4.5 keV electrons and a 44 gauss applied field. The thresholds fall along a straight line of slope -1.6; i.e. threshold pressure scales as $i^{-1.6}$. We performed similar observations for applied magnetic fields between 7 and 54 gauss. We then performed a visual best fit scaling of B dependence of the threshold, i.e. we forced the

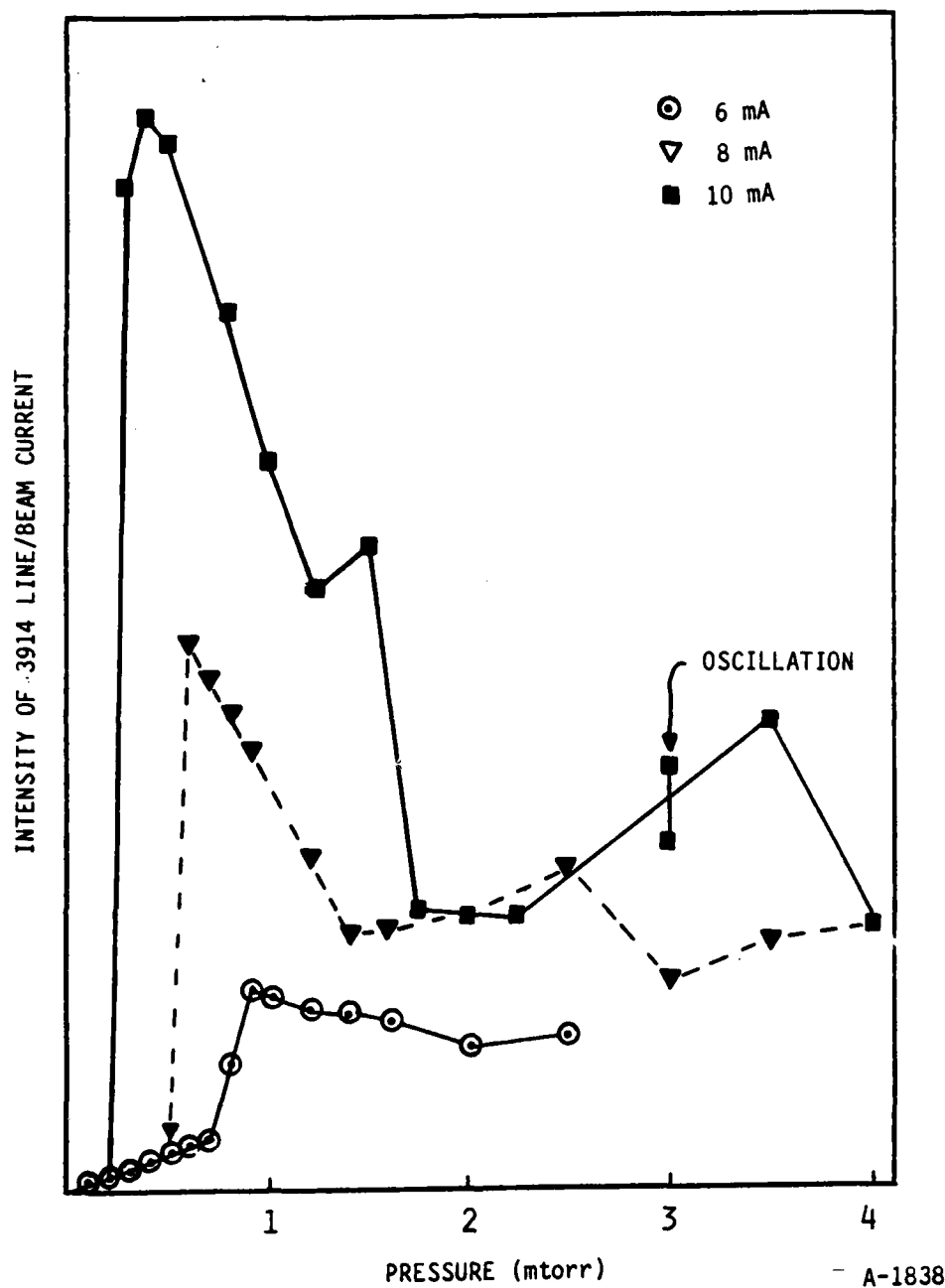


Figure 92. BPD intensity enhancements as a function of pressure for several currents. Applied field is 26G and beam voltage is 4.5 keV.

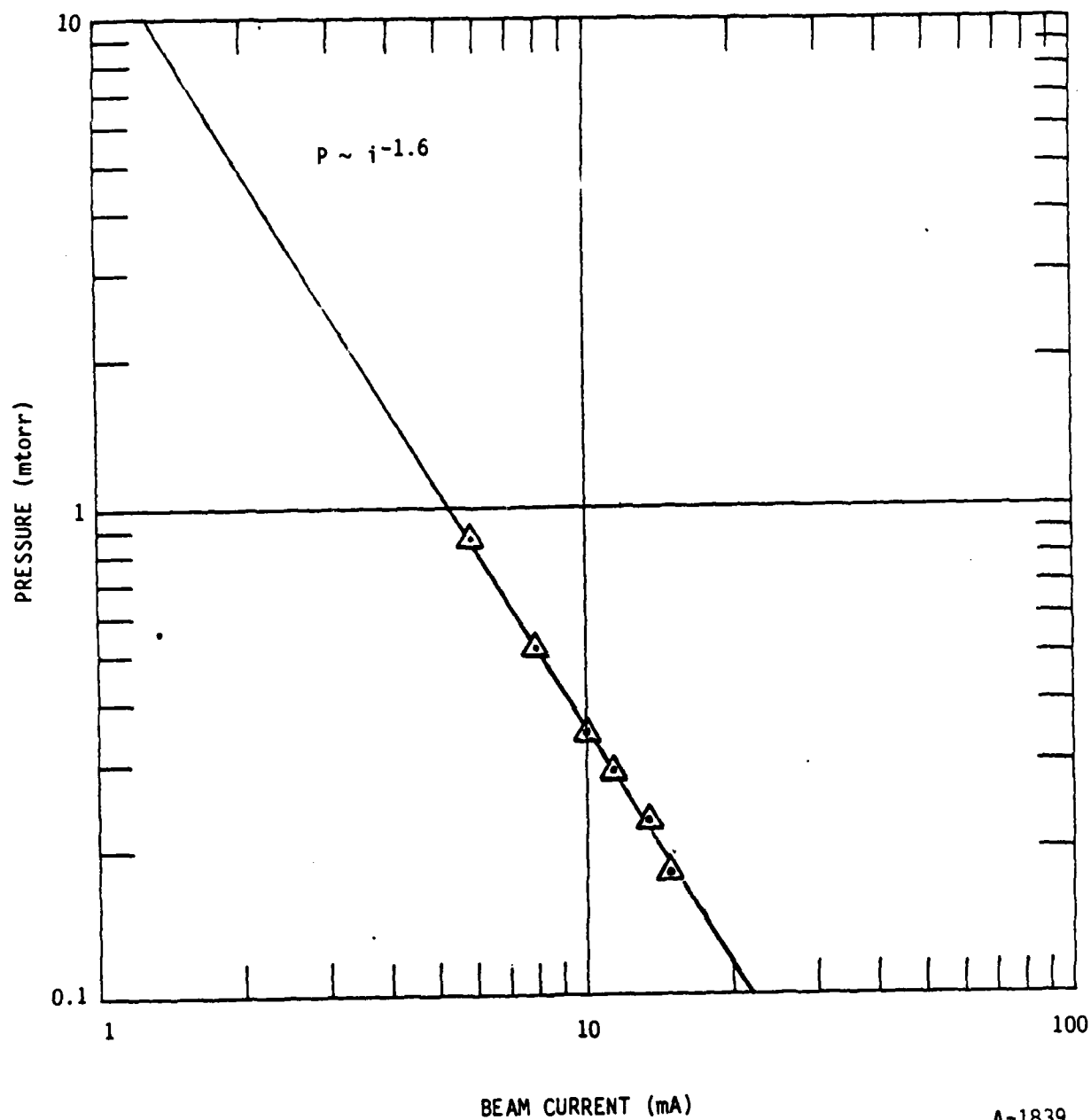


Figure 93. Pressure dependence of BPD thresholds in nitrogen as a function of beam current for 4.5 keV electrons and 44 gauss applied field.

data for different magnetic fields to overlap using a single B-field dependence. This threshold data plotted in Figure 94 versus iB^X . The data collapses nicely when a $B^{-0.16}$ scaling is applied. No data points have been removed.

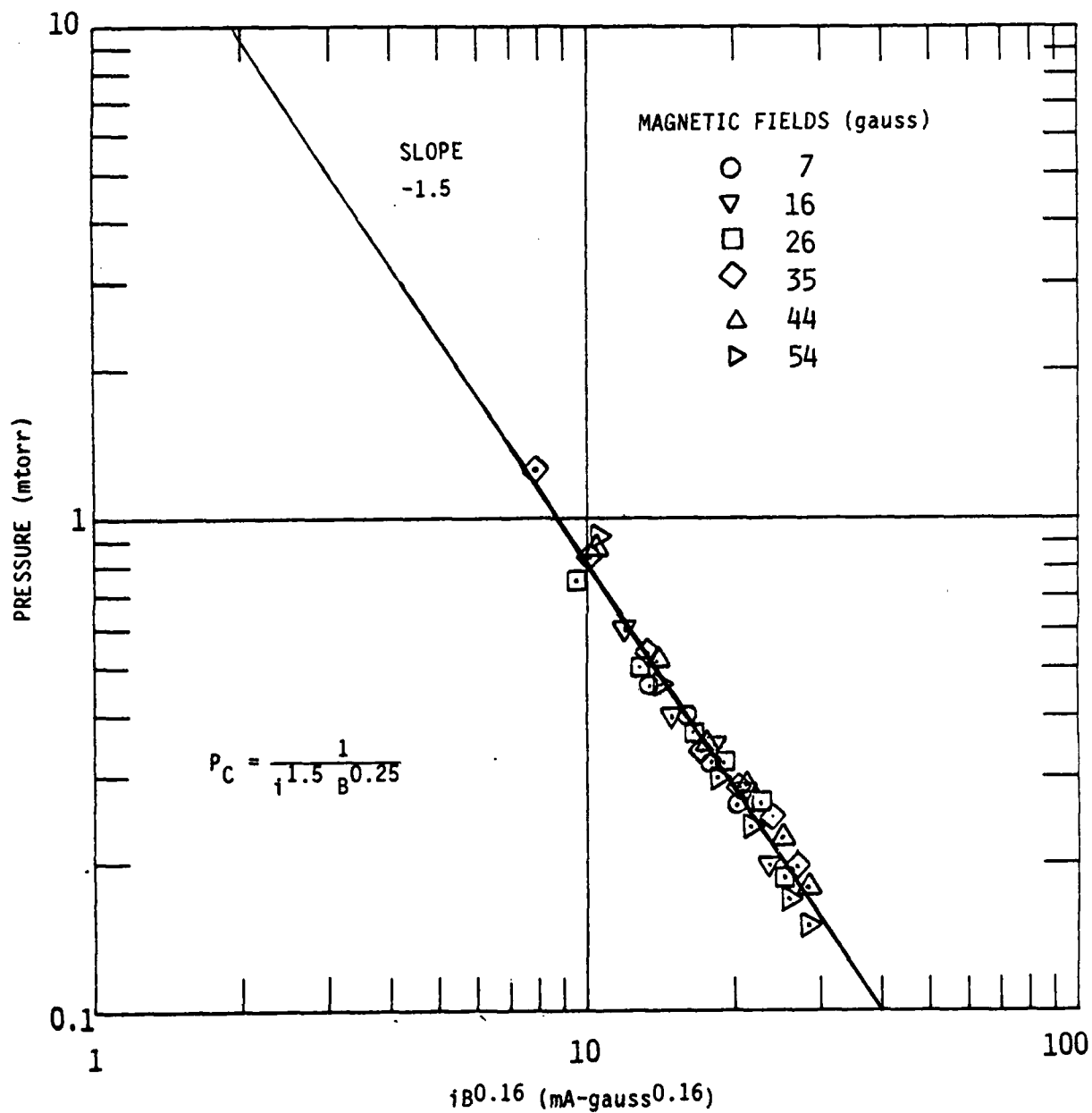
The resultant threshold pressure scaling is thus

$$P = \frac{1}{i^{1.5} B^{0.25}} \quad (95)$$

This scaling appears to apply over a factor of three variation in beam current, eight in B-field. Additionally, this study has served to define regions when BPD effects are significant (above the line) and where single particle energy deposition, band radiance, and excitation efficiency studies can be conducted.

Our threshold scalings are considerably different than Bernstein's.¹⁴⁰ Other groups¹⁵¹⁻¹⁵³ have reported scalings intermediate to our's and to the NASA/Johnson Facility scalings. These results are summarized in Table 10. As can be seen from the table all the experimental facilities cover different ranges of pressures, magnetic fields and instabilities. Additionally LABCEDE uses spectrally resolved fluorescence as a diagnostic while the others use antennas and broadband photometers. The current theoretical understanding of beam plasma instabilities is flexible enough to fit a range of scalings depending on the nature of the instability. We hope that future indepth studies will permit identification of the instability (or instabilities) present in LABCEDE.

The above measurements were made in pure N_2 . Thresholds were also determined in air and are plotted in the same manner as the pure N_2 data in Figure 95. The observed thresholds over a more limited range of B fields differ only slightly from the N_2 thresholds which are indicated as the solid line. The threshold in air is about 20 percent lower than pure N_2 but has the same scalings $P_{\text{threshold}} \sim i^{-1.5} B^{-0.25}$. Also indicated on the figure are the



A-1840

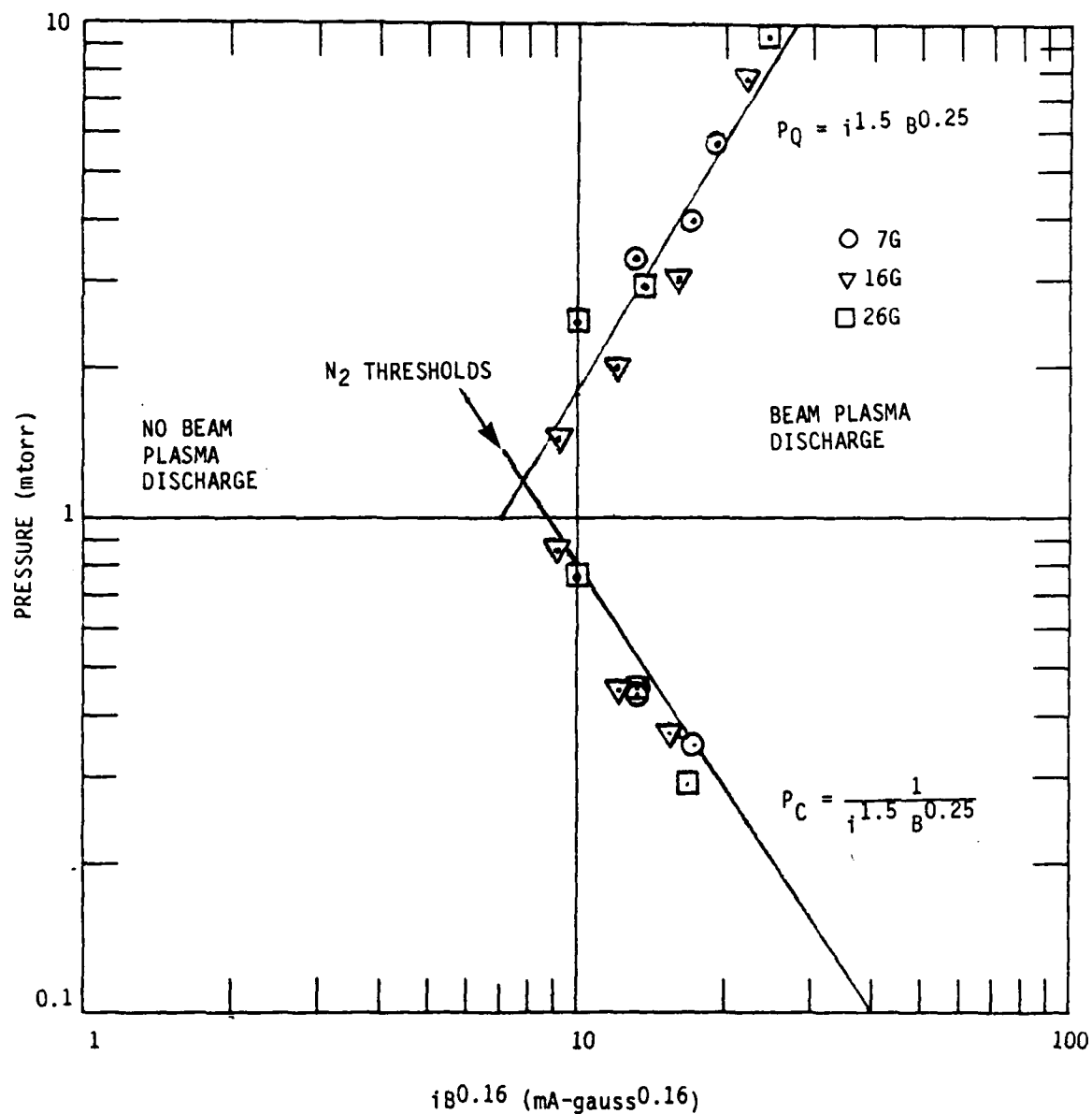
Figure 94. Discharge ignition thresholds for 4.5 keV electrons into nitrogen over a range of B field. Data collapses to a single line for $B^{0.16}$ scaling.

TABLE 10. IGNITION THRESHOLD CRITERIA FROM SEVERAL GROUPS

Scaling	Group	Operating Conditions
$I_c \propto \frac{V^{1.5}}{pB^{0.7-1.0}L}$	NASA/JSC Large (Ref. 137)	B < 2G 6(-6) to 2(-5) torr < 2 kV; < 60 mA
	Lab (Ref. 152)	B < 38G
$I_c \propto \frac{V^{1.5}}{p^{0.5}B^{0.5}L}$	NASA Between Devices	
$I_c \propto \frac{V^{1-1.5}}{pB^{0.5-1}L}$	Boswell and Kellogg (Ref. 151)	B < 200G 2(-6) to 2(-4) torr 0.1-0.3 kV; 1-15 mA
$I_c \propto \frac{1}{p^{0.6}B^{0.24}}$	LABCEDE	B < 85G 1(-7) to 1(-1) torr 1-6 kV; 2-20 mA

quenching points - the pressure at which the 391.4 nm intensity asymptotes to the extrapolation of the low pressure single particle behavior. This data has large error bars but follows a systematic trend on this same plot. An inverse scaling to thresholds are observed $P_{\text{quenching}} \sim i^{1.5} B^{0.25}$. More quenching data must be acquired, but these intriguing results indicate that the stronger the instability, the wider the pressure range that it persists.

The enhancement of other spectral features is even more dramatic. The ionic N_2 bands (First Negative and Meinel) which have electron excitation cross sections which peak at 100 eV are enhanced by the BPD by about an order of magnitude. The neutral triplet states (B,C) whose excitation cross sections peak between 10 and 15 eV are increased in concentration by about 100. This observation indicates that 10 eV electrons are enhanced even more than



A-1841

Figure 95. Ignition and quenching thresholds in air from 391.4 nm measurements for 4.5 keV electrons.

100 eV electrons in the beam plasma instability. The $N_2(W^3\Delta)$ state samples the same energy electrons at the $B^3\pi_g$ and should be enhanced accordingly. As described in Section 4, $N_2(W-B)$ emissions can be observed in the infrared between 2 and 5 μm only when BPD is occurring. In the LWIR $O_3(\nu_3)$ and $CO_2(\nu_2)$ emissions increase greatly in intensity and change spectral distribution when BPD is present. As an example, fluorescence as acquired using the Circular Variable Filter Spectrometer looking at pure O_2 irradiated by 6 mA of 5.5 keV electrons is shown in Figure 96 for two experimental conditions. The lower trace is the signal from 6.3 mtorr of O_2 with no field applied. The ozone signal decreases rapidly with pressure and is essentially in the noise below 2 mtorr. When a strong external magnetic field is applied the signal increases dramatically and is noticeably red-shifted. More highly-excited vibrational states of the molecule are produced relative to $(\nu_3, v=1)$ when BPD is occurring. At 15 μm in (Ar/ CO_2) mixtures $CO_2(\nu_2)$ emission and $(\nu_1 + \nu_2)$ emission at 13.9 μm are observed.

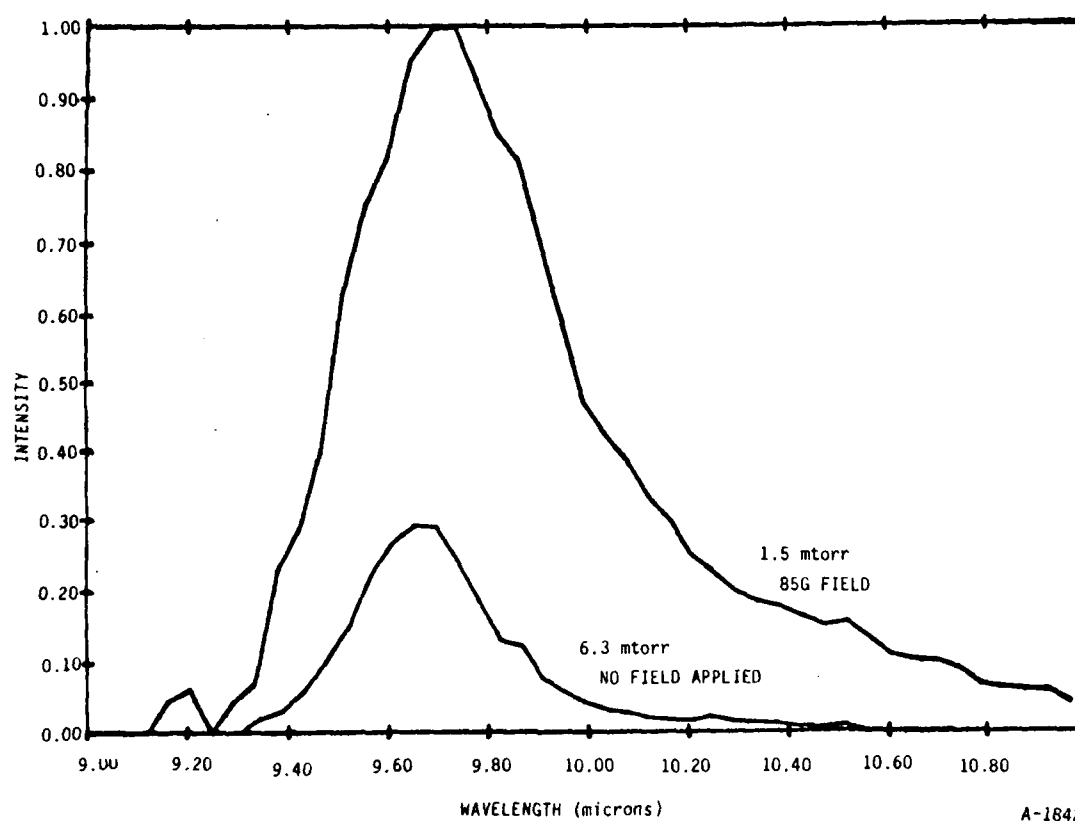


Figure 96. BPD enhancement of the $O_3(\nu_3)$ band from pure O_2 irradiated by 6 mA of 5.5 keV electrons.

9.6 Future Investigations

Obvious further studies suggested by these results are to considerably extend the range of both threshold and quenching studies in order to verify the $P = (I^3/2B^{1/4})X$ scaling where X is -1 for threshold and $X = +1$ for quenching. Voltage dependence should also be investigated. The goal being an identification of the type of the instability which operates in LABCEDE. To our knowledge, LABCEDE is the only facility capable of observing quenching effects in the laboratory. Thus it can provide significant new input to our understanding of BPD quenching. Additionally, quantitative studies on other band systems will allow us to coarsely probe the secondary electron distributions in the instability and to see if different scaling relationships apply for different systems.

Another parameter of interest is the spatial and temporal behavior of the instability. Visual observations indicate node structure along the beam and the slow oscillation has been reproducibly observed. Investigations of the onset time would prove valuable information about the nature of the instability and the characteristic frequencies operating inside LABCEDE.

The key experimental parameter is not the total current, but rather the current density. Measurements using the scanning photometer will be able to measure electron beam spatial distributions just at threshold and determine critical current densities.

The huge enhancement in O_3 emission could be the result of chemical enhancements of O_3 production during to BPD where the electrons act as the third body in $O+O_2+e \rightarrow O_3+e$ recombination. Alternative possibilities include very efficient pumping of $O_3(v)$ or an enhanced production due to a two-body process such as $O_2(A)+O_2 \rightarrow O_3+O$. Experimental measurements programs will be designed to isolate the O_3 excitation mechanism.

One of the more exciting aspects of the BPD is the presence of strong turbulence and its manifestation in ("hot") electrons. The LABCEDE data

clearly shows the presence of these hot electrons as they are presumably responsible for the large increases in the $N_2^+(B)$ state, which is excited by electrons with energies in excess of 18 eV. These enhancements are not likely to be due to the background (cold) plasma electrons. The background electrons will be heated in the usual collisional manner in the presence of the instability - created rf fields and might be expected to be at an elevated temperature relative to the background gas. Knowledge of the temperature of these cold electrons in conjunction with the increase in $N_2^+(B)$ state emission will provide important data on the tradeoff between the two important energy dissipation processes. The cold electron temperature could perhaps be deduced from the vibrational emission of an infrared active gas (such as CO) while the discharge was occurring.

The square root variation shown in Figure 90 should be pursued further in order to determine whether plasma micro-instabilities are involved. The slit height should be varied and more data at small values of magnetic field should be gathered. If it is possible to lower the beam current to avoid BPD but still show observable signals, this should also provide interesting data. Of course, implementation of the 391.4 nm diagnostic will be instrumental in answering many questions. This monitor will allow the quantitative determination of the N_2^+B creation rate in the observation volume. When BPD is not occurring, this creation rate is proportional to the electron-ion pair creation rate and is an indicator of energy deposition. Use of this diagnostic may permit determination of these quantities in the BPD regime.

Theoretical work should include both fundamental studies on the plasma physics of the BPD as well as a calculation of the expected signals from scattering in the presence of an aligned magnetic field.

The LABCEDE apparatus can thus be used to verify and extend the Johnson Space Center and other observations of the beam plasma discharge phenomenon. Quantification of threshold and quenching criteria will permit better assessment of the importance of this phenomenon in the greatly disturbed upper atmosphere, and the impact of BPD on the spectral radiances throughout the spectrum UV-LWIR.

10. REFERENCES

1. Green, B.D., Caledonia, G.E., Piper, L.G., Goela, J.S., Fairbairn, A., and Murphy, R.E., "LABCEDE Studies," AFGL-TR-82-0060, (September 1981), ADA114389.
2. Bailey, C.A., in Advanced Cryogenics (Plenum, London, 1971) Chapter 5. Other excellent cryogenics texts we found useful include: R. B. Scott, Cryogenic Engineering (van Nostrand, Toronto, 1959). and M. McClintock, Cryogenics (Reinhold, New York, 1964).
3. Dushman, S., Scientific Foundations of Vacuum Technique, (Wiley, New York, 1962), Chapter 2.
4. Green, B.D., Goela, J.S., Krech, R.H., "Calibration Facility Refurbishment," PSI TR-242, December 1980.
5. Avidor, J.M., Kemp, N.H., and Knight, C.J., "Experimental and Theoretical Investigation of Flow Generated by an Array of Porous Tubes," AIAA J., 14, 1534-40 (1976).
6. Youngquist, G.R., "Diffusion and Flow of Gases in Porous Solids," American Chemical Society, Washington, D.C., p. 68 (1970).
7. Caledonia, G.E., Green, B.D., Simons, G.A., Kennealy, J.P., Robert, F.X., Corman, A., and DelGreco, F.P., "COCHISE Studies I: Fluid Dynamical and Infrared Spectral Analyses," AFGL-TR-77-0281 Dec. 1977, ADA053218.
8. Glasstone, S., Laidler, K.J., and Eyring, H., The Theory of Rate Processes (McGraw-Hill, New York, 1941).
9. Wheeler, W.R., "Selecting Materials and Hardware," Physics Today (August 1972).
10. Carslaw, H.S. and Jaeger, J.C., Conduction of Heat in Solids, (Oxford University Press, 1947.)
11. Green, B.D., Caledonia, G.E., Piper, L.G., Goela, J.S., Fairbairn, A., and Murphy, R.E., "LABCEDE Studies," AFGL TR-82-0060 (September 1981). ADA114389.
12. Sawada, T., Sellin, D.L., and Green, A.E.S., J. Geo. Res. 77, 9819 (1972).
13. Kieffer, L.J., "A compilation of Electron Collision Cross-Section Data for Modeling Gas Discharge Lasers," JILA Information Center Report 13(1973).
14. Opal, C.B., Beaty, E.C., and Peterson, W.K., "Tables of Energy and Angular Distributions of Electrons Ejected from Simple Gases by Electron Impact," Joint Institute for Laboratory Astrophysics Report No. 108 (1971).

15. Opal, C.B., Peterson, W.K., and Beaty, E.C., "Measurements of Secondary-Electron Spectra Produced by Electron Impact Ionization of a Number of Simple Gases," J. Chem. Phys. 55, 4100 (1971).
16. Barrett, J.L. and Hays, P.B., "Spatial Distribution of Energy Deposited in Nitrogen by Electrons," J. Chem. Phys. 64, 743 (1976).
17. Cohn, A. and Caledonia, G.E., "Distribution of the Fluorescent Radiation Emission Caused by an Electron Beam," J. Appl. Phys. 41, 3767 (1970).
18. Peterson, L.R., Sawada, T., Bass, J.N., and Green, A.E.S., "Electron Energy Deposition in a Gaseous Mixture," Comp. Phys. Comm. 5, 239 (1973). Also Jackman, C.H., Garvey, R.M., and Green, A.E.S., "Electron Impact on Atmospheric Gases I. Updated Cross Sections" J. Geophys. Res. 82, 5081 (1977).
19. Space Material Handbook, Goetzl, C.G., Rittenhouse, J.B., and Singletary, J.B., eds. (Addison-Wesley, Reading, MA, 1965).
20. Green, B.D., Rawlins, W.T., and Caledonia, G.E. "High Altitude Radiation Signatures," Physical Sciences Inc., TR-296, (February 1982).
21. Hollander, Redus, F. and Maier, William, B., II, "Study of the A+X Transitions in N_2^+ and CO^{+*} ," J. Chem. Phys. 56, 5229 (1972).
22. Peterson, J.R. and Moseley, J.T., "Time-of-flight Determination of Lifetimes of $N_2^+(^2\Pi_u)$ -the Meinel Band System," J. Chem Phys. 58, 172 (1973).
23. Gattinger, R.L. and Vallance, Jones, A., "Quantitative Spectroscopy of the Aurora II. The Spectrum of a Medium Intensity Aurora Between 4500 and 8900 Å," Can. J. Phys. 52, 2343 (1974).
24. Piper, L.G., unpublished results (July 1980).
25. O'Neil, R.R., private communication (1982).
26. Loftus, A. and Krapenie, P.H., "The Spectrum of Molecular Nitrogen," J. Phys. Chem. Ref. Data 6, 113 (1977).
27. Peterson, L.R., Sawada, T., Bass, J.N., and Green, A.E.S., "Electron Energy Deposition in a Gaseous Mixture," Comp. Phys. Comm. 5, 239 (1973). Also Jackman, C.H., Garvey, R.M., and Green, A.E.S., "Electron Impact on Atmospheric Gases I. Updated Cross Sections" J. Geophys. Res. 82, 5081 (1977).
28. Mitchell, K.B., "Fluorescence Efficiencies and Collisional Deactivation Rates for N_2 and N_2^+ Bands Excited by Soft X-Rays," J. Chem. Phys. 53, 1975 (1970).
29. Cohn, A. and Caledonia, G.E., "Distribution of the Fluorescent Radiation Emission Caused by an Electron Beam," J. Appl. Phys. 41, 3767 (1970).

30. Barrett, J.L. and Hays, P.B., "Spatial Distribution of Energy Deposited in Nitrogen by Electrons," J. Chem. Phys. 64, 743 (1976).
31. Cook, F.M. and Murphy, R.E., "A Synchronous Signal Processing Technique for Repetitive Arbitrary Waveforms," AFCRL-TR-76-0035 (1976), ADA024000.
32. Murphy, R.E., Cook, F.M., and Sakai, M., "Time Resolved Fourier Spectroscopy," J. Opt. Soc. Amer. 65, 600 (1975).
33. Caledonia, G.E., Green, B.D., and Murphy, R.E., "A Study of the Vibrational Level Dependent Quenching of CO($v=1-16$) by CO₂," J. Chem. Phys. 71, 436 (1979).
34. Green, B.D., Caledonia, G.E., and Murphy, R.E., "A Determination of the Nitric Oxide Einstein Coefficient Ratios," J. Quant. Spectrosc. Radiat. Transfer 26, 215 (1981).
35. Green, B.D., Caledonia, G.E., Murphy, R.E., and Robert, F.X., "The Vibrational Relaxation of NO($v=1-7$) by O₂," J. Chem. Phys. 76, 2441 (1982).
36. Green, B.D., Caledonia, G.E., Piper, L.G., Goela, J.S., Fairbairn, A., Murphy, R.E., "LABCEDE Studies," AFGL-TR-82-006 (1981), ADA114389.
37. Cartwright, D.C., "Vibrational Populations of the Excited States of N₂ Under Auroral Conditions," J. Geophys. Res. 83, 517 (1978).
38. Caledonia, G.E. and Kennealy, J.P., "NO Infrared Radiation in the Upper Atmosphere," Planet. Space Sci. 30, 1043 (1982).
39. Kennealy, J.P., DelGreco, F.P., Caledonia, G.E., and Green, B.D., "Nitric Oxide Chemiexcitation Occurring in the Reaction Between Metastable Nitrogen Atoms and Oxygen Molecules," J. Chem. Phys. 69, 1574 (1978).
40. Rawlins, W.T., Caledonia, G.E., Gibson, J.J., and Stair, A.T., Jr., "HIRIS Rocketborne Spectra of Infrared Fluorescence in the O₃(v_3) Band Near 100 km," PSI SR-136, J. Geophysical Research, 90, 2896 (1985).
41. Horiguchi, H. and Tsuchiya, S., "Vibrational Relaxation of NO($X^2\Pi$) in the States of $V = 2-10$," Japanese J. of Appl. Phys. 18, 1207 (1979).
42. Stephenson, J.C., "Vibrational Relaxation of NO($X^2\Pi$) ($V = 1$) in the Temperature Range 100-300 K," J. Chem. Phys. 60, 4289 (1974).
43. Donovan, R.J. and Gillespie, H.M., "Reactions of Atoms in Ground and Electronically Excited States," Reaction Kinetics, Vol. I, ed. P.G. Ashmore (The Chemical Society, London, 1975).
44. Schofield, K., J. Phys. Chem. Ref. Data 8, 723 (1979).
45. Kennealy, J.P., DelGreco, F.P., Caledonia, G.E., and Green, B.D., J. Chem. Phys. 69, 1574 (1978).

46. Murphy, R.E., Cook, F.H., and Sakai, H., J. Opt. Soc. Amer. 65, 600 (1975).
47. Caledonia, G.E., Green, B.D., and Murphy, R.E., J. Chem. Phys. 71, 4369 (1979).
48. Hansen, P., Sakai, H., and Esplin, M., "Observations of NH Infrared Emission Using Fourier Spectroscopy," in Proc. Soc. Photo-Opt. Instrument. Engin. Vol. 191, ed. G.A. Vanasse, Aug. 1979, pp. 15-20.
49. Das, G., Wahl, A.C., and Stevens, W.J., J. Chem. Phys. 61, 433 (1974).
50. Varney, R.N., J. Chem. Phys. 23, 866 (1955).
51. Tanaka, J. and McNesby, J.R., J. Chem. Phys. 36, 3170 (1962).
52. Brown, R.L., Internat. J. Chem. Kinetics 5, 663 (1973).
53. Piper, L.G., J. Chem. Phys. 70, 3417 (1979).
54. Donovan, R.J. and Husain, D., Chem. Rev. 70, 489 (1970).
55. Husain, D., Mitra, S.K., and Young, A.N., J. Chem. Soc. Faraday II, 70, 1721 (1974).
56. Fehsenfeld, P.C., Schmeltekopt, A.L., and Fergusun, E.E., J. Chem. Phys. 46, 2802 (1967).
57. Smith, D., Adams, N.G., and Miller, T.M., J. Chem. Phys. 69, 308 (1978).
58. Herbst, E., Bohme, D.K., Payzant, J.D., and Schiff, H.I., Astrophys. J. 201, 603 (1975).
59. Roche, A.E., Sutton, M.M., Dohme, D., and Schiff, H.I., J. Chem. Phys. 55, 5480 (1971).
60. Caledonia, G.E., Green, B.D., and Murphy, R.E., J. Chem. Phys. 71, 4369 (1979).
61. Murphy, R.E., Cook, F.H., and Sakai, H., J. Opt. Soc. Am. 65, 600 (1975).
62. Green, B.D., Caledonia, G.E., Murphy, R.E., and Robert, F.X., J. Chem. Phys. 76, 2441 (1982).
63. Center, R.E., Phys. Fluids. 13, 79 (1970).
64. Billingsley, F.P., J. Molec. Spect. 61, 53 (1976). Theoretical predictions verified by laboratory observations: Green, B.D., Caledonia, G.E. and Murphy, R.E., "A Determination of the Nitric Oxide Einstein Coefficient Ratios," J. Quant. Spect. Rad. Transfer 26, 215 (1981). Recent calculations would place the values as 22% larger. If these values were adopted, our calculated populations and efficiency would be reduced by this fraction: J.R. Gillis and A. Goldman, Appl. Opt. 21, 1161 (1982).

65. Kennealy, J.P., DelGreco, F.P., Caledonia, G.E., and Green, B.D., J. Chem. Phys. 69, 1574 (1978).
66. Husain, D., Kirsch, L.J., and Wiesenfeld, J.R., Faraday Disc. Chem. Soc., 53, 233 (1972).
67. Husain, D., Mitra, S.K., and Young, A.N., J. Chem. Soc. Farad. II 70, 1721 (1974).
68. Iannuzzi, M.P. and Kaufman, F., J. Chem. Phys. 73, 4701 (1980).
69. Lin, C.L. and Kaufman, F., J. Chem. Phys. 55, 3760 (1971).
70. Slinger, T.G., Wood, B.J., and Black, G., J. Geophys. Res. 76, 8430 (1971).
71. Davenport, J.E., Slinger, T.G., and Black, G., J. Geophys. Res. 81, 12 (1976).
72. Berger, M.J. and Seltzer, S.M., NASA Report SP-3012 (1964).
73. Brittain, F.H., Sandia Report SC-TM-68-713 (1979).
74. ARPA-NRL Laser Program, NRL Mem. Rpt. 3084, p. 76-99 (1971).
75. Whyte, G.N., Rad. Res. 18, 265 (1963).
76. Peterson, L.R., Sawada, S., Bass, J.N., and Green, A.E.S., Comp. Phys. Comm. 5, 239 (1973).
77. Jackman, C.H., Garvey, R.H., and Green, A.E.S., J. Geophys. Res. 82, 5081 (1977).
78. Porter, H.S., Jackman, C.H., and Green, A.E.S., J. Chem. Phys. 65, 154 (1976).
79. Roble, R.G. and Rees, M.H., Planet. Space Sci. 25, 991 (1977); and Frederick, J.E. and Rusch, D.W., J. Geophys. Res. 82, 350 (1977).
80. Bardsley, J.N. and Biondi, M.A., in "Advances in Atomic and Molecular Physics," Vol. 6, ed. D. R. Bates 1-57 (1970).
81. Albritton, D.L., Atomic Data and Nuclear Data Tables 22, (1978).
82. Mahdavi, M.R., Hasted, J.B., and Nakshbandi, M.M., J. Phys. B; Atom Molec. Phys. 4, 1726 (1971).
83. Green, B.D., Caledonia, G.E., Piper, L.G., Goela, J.S., Fairbairn, A., and Murphy, R.E., Air Force Geophysics Laboratory Technical Report AFGL-TR-82-0060 (1981), ADA114389.

84. Caledonia, G.E. and Kennealy, J.P., "NO Infrared Radiation in the Upper Atmosphere," Planet. Space Sci. 30, 1043 (1982).
85. Stair, A.T., Jr., Pritchard, J., Coleman, I., Bohne, C., Williamson, W., Rogers, J., and Rawlins, W.T., "The Rocket Borne Cryogenic (10 K) High Resolution Interferometer Spectrometer Flight - HIRIS: Atmospheric and Auroral Infrared Emission Spectra," submitted to Appl. Opt. 1982.
86. Rawlins, W.T., Caledonia, G.E., Gibson, J.J., and Stair, A.T., Jr., J. Geophys. Res. 86, 1313 (1981).
87. Stair, A.T., Jr. presentation at IMAP Meeting 1981.
88. Jones, A. Vallance and Gattinger, R.L., Can. J. Phys. 50, 1833 (1972).
89. Jones, A. Vallance and Gattinger, R.L., Can. J. Phys. 52, 2343 (1974).
90. Jones, A. Vallance and Gattinger, R.L., Can. J. Phys. 54, 2128 (1976).
91. Gattinger, R.L. and Jones, A. Vallance, Can. J. Phys. 59, 480 (1981).
92. Wallace, L. and Broadfoot, A.L., Planet. Space Sci. 17, 975 (1969).
93. Shemansky, D.E. and Broadfoot, A.L., J. Quant. Spectrosc. Radiat. Transfer 11, 1401 (1971).
94. O'Neil, R. and Davidson, G., Air Force Cambridge Research Laboratories Report No. AFCRL-67-0277 (1967), ADA673995.
95. Holland, R.F. and Maier II, W.B., J. Chem. Phys. 56, 5229 (1972).
96. Peterson, J.R. and Moseley, J.T., J. Chem. Phys. 58, 172 (1973).
97. Gray, D.D., Roberts, T.D., and Morack, J.L., J. Chem. Phys. 57, 4190 (1972).
98. Pendleton, W.R., Jr. and Weaver, L.D., ARPA Report No. 1691 under Contract No. F33657-71-C-0174 (1973).
99. Simpson, F.R. and McConkey, J.W., Planet. Space Sci. 17, 1941 (1969).
100. Sheridan, J.R., Merlo, T.A., and Enzweiler, J., J. Chem. Phys. 68, 4343 (1978).
101. P.N. Stanton and R.M. St. John, J. Opt. Soc. Amer. 59, 252(1969).
102. a. B.N. Srirastara and I.M. Mizrh, Phys. Rev. 168, 86(1968).
b. B.N. Srirastara and I.M. Mazra, Chem. J. Phys. 47, 475(1969).

103. B.D. Green, G.E. Caledonia, L.G. Piper, J.S. Goela, A. Fairbairn, and R.E. Murphy, AFGL-TR-82-0060 (1981). Available from the authors upon request, ADA114389.
104. B.D. Green, G.E. Caledonia, G. Kothandaraman, and H.C. Murphy, PSI TR-287 (1981). Available from the authors upon request.
105. B.D. Green and Piper, L.G., PSI TR-339 (1982). Available from the authors upon request.
106. Stern, O. and Volmer, M., Phys. Zeits. 20, 183 (1919).
107. Jackman, C.H., Garvey, R.H., and Green, A.E.S., J. Geophys. Res. 82, 5081 (1977).
108. Peterson, L.R., Sawada, T., Bass, J.N., and Green, A.E.S., Comp. Phys. Comm. 5, 239 (1973).
109. Mitchell, K.B., J. Chem. Phys. 53, 1795 (1970).
110. Brocklehurst, B., Trans. Faraday Soc. 60, 2151 (1964).
111. Hirsh, N.M., Halpern, G.M., Slevin, J.A., and N. Wolf, U.S. Army Report. ECOM-10354-F (1967).
112. Barrett, J.L. and Hays, P.B., J. Chem. Phys. 64, 743 (1976).
113. Cohn, A. and Caledonia, G.E., J. Appl. Phys. 41, 3767 (1970).
114. Loftus, A. and Krupenie, P.H., J. Phys. Chem. Ref. Data 6, 113 (1977).
115. Wu, H.H. and Shemansky, D.E., J. Chem. Phys. 64, 1134 (1976) and private communication from D. E. Shemansky to L. G. Piper (1982).
116. Borst, W.L. and Zipf, E.C., Phys. Rev. A 1 834 (1970).
117. Katayama, D.H., Miller, T.A., and Bondybey, V.E., J. Chem. Phys. 72, 5469(1980).
118. a. Dobler, W., Howorka, F., and Lindinger, W., Plasma Chem. Plasma Process. 2, 353(1982).
b. Dobler, W., Villinger, H., Howorka, F., and Lindinger, W., Int. J. Mass Spect. Ion Phys. 47, 171(1983).
119. Mandlebaum, D. and Feldman, P.D., J. Chem Phys. 65, 672 (1976).
120. Jones, A. Vallance and Gattinger, R.L., J. Geophys. Res. 83, 3255(1978).
121. U.S. Standard Atmosphere 1976 (NOAA/NASA/USAF), U.S. Government Printing Office, Washington, D.C. October 1976.

122. Cartwright, D.C., Pendleton, W.R., Jr. and Weaver, L.D., J. Geophys. Res. 80, 651(1975).
123. Huddleston, R.K., Fujimoto, G.T., and Weltz, E., J. Chem. Phys. 76, 3839 (1982).
124. Mitchell, A.C.G. and Zemansky, M.W., "Resonance Radiation and Excited Atoms," Cambridge, London (1934), p. 101.
125. Bulos, B.R. and Phelps, A.V., Phys. Res. A 14, 615 (1976).
126. Kumer, J.B., J. Geophys. Res. 82, 2203 (1977).
127. Kumer, J.B. and James, T.C., J. Geophys. Res. 79, 638 (1974).
128. Caledonia, G.E., Green, B.D., and Murphy, R.E., J. Chem. Phys. 71, 4369 (1979).
129. McClatchey, R.A., Benedict, W.S., Clough, S.A., Burch, D.E., Calfee, R.F., Fox, K., Rothman, L.S., and Garing, J.S., "AFCRL Atmospheric Absorption Line Parameters Compilation," AFSC Report AFCRL-TR-73-0096, January 1973, ADA762904.
130. Fairbairn, A.R., Girnius, R., Wolkik, S.J., "SWIR Studies in LABCEDE Facility: Initial Findings," Air Force Geophysics Laboratory AFGL-TR-80-0054 (Feb. 1980), ADA090503.
131. O'Neil, R.R., Lee, E.T.P., Stair, A.T., Jr., and Ulwich, J.C., "EXCEDE II," Air Force Geophysics Laboratory Report AFGL-TR-76-0308 (Dec. 1976); and R.R. O'Neil private communications, 1982, ADA042491.
132. Green, B.D., Piper, L.G., Caledonia, G.E., Murphy, H.C., Krech, R.H., and Pugh, E.R., "LABCEDE Fluorescence Studies," PSI Interim Scientific Report TR-356 (Feb. 1983).
133. Archer, D.H., "Infrared Program Support - EXCEDE and Related Topics," Defense Nuclear Agency TR-81-45 (Nov. 1981).
134. Cetty, W.D. and Smullin, L.D., "Beam-Plasma Discharge. Buildup of Oscillations," J. Appl. Phys. 34, 3421 (1963).
135. Karchinko, I.F., et al., Sov. Phys. Tech. Phys. 6, 551 (1962).
136. Galeev, A.A., et al., Sov. Phys. Dokl. 21, 641 (1976).
137. Bernstein, W., Leinbach, H., Kellogg, P.J., Monson, S., Hallinan, T., Garriott, O.K., Kouradi, A., McCoy, J., Daly, P., Baker, B. Anderson, H.R., "Electron Beam Injection Experiments: The Beam Plasma Discharge at Low Pressures and Magnetic Field Strengths," Geophys. Res. Lett. 5, 127 (1978).

138. Papadopoulos, K. and Freund, H., "Scaling Laws for the Strongly Turbulent Electron-Beam-Plasma Interaction," *Comments Plasma Phys.* 15, 113 (1979).
139. Rowland, H., "Strong Turbulence Effects on the Kinetic Beam Plasma Instability," *Phys. Fl.* 23, 508 (1980).
140. Bernstein, W., Leinbach, H., Kellogg, P.J., Monson, S.J., and Hallinan, T., "Further Laboratory Measurements of the Beam Plasma Discharge," *J. Geophys. Res.* 84, 7271 (1979).
141. Linson, L.M. and Papadopoulos, K., "Theoretical Support of the Space Lab Instrument/Experiment Definition of a Theoretical and Experimental Study of Beam Plasma Physics," Final Report, LAPS 76, SAI 023-81-316-LJ, September 1981.
142. Piper, L.G. and Green, B.D., "Quenching of $N_2^+(A \ ^2\Pi_u)$, $v'=2, 3$, and 4 lines by Nitrogen and Air; Preliminary Results," PSI Technical Report TR-365 (Feb. 1983).
143. Berger, M.J., *Methods in Computational Phys.* Academic Press, Vol. 1, 135 (1963).
144. Bette, H.A., Rose, M.E., Smith, L.P., *Proc. Am. Phil. Soc.* 78, 753 (1938).
145. Scott, W.T., *Phys. Rev.* 76, 212 (1949).
146. Cohn, A. and Caledonia, G.E., "Distribution of the Fluorescent Radiation Emission Caused by an Electron Beam," *J. Appl. Phys.* 41, 3767 (1970).
147. Smith, R.C., *Appl. Phys. Lett.* 21, 352 (1972).
148. Spencer, L.V., *Phys. Rev.* 98, 1587 (1955).
149. Jacob, J.H., "Penetration and Energy Deposition of Electrons in Thick Targets," *J. Appl. Phys.* 45, 467 (1974).
150. Rowland, H.L., Chang, C.L., and Papadopoulos, K., "Scaling of the Beam-Plasma Discharge," *J. Geophys. Res.* 86, 9215 (1981).
151. Boswell, R.W. and Kellogg, P.J., "Characteristics of Two Types of Beam Plasma Discharge in a Laboratory Experiment," *Geophys. Res. Lett.* 10, 565 (1983).
152. Konradi, A., Bernstein, W., Bulgher, D.L., McGarrity, J.O., and Winkler, J.L., Jr., "Initial Experimental Results from a Laboratory Size Beam-Plasma Discharge Device," *Proc. International Conference on Active Experiments in Space*, 1983.
153. Bernstein, W., McGarrity, J.O., and Konradi, A., "Electron Beam Injection Experiments: Replication of Observations in a Laboratory Beam Plasma Discharge," *Geophys. Res. Lett.* 10, 1124 (1983).

APPENDIX A

REPORT ON THE CONCEPTUAL DESIGN OF THE LABCEDE CRYOSHOUD

REPORT ON THE CONCEPTUAL DESIGN
OF
THE LABCEDE CRYOSHOULD

Prepared For

PHYSICAL SCIENCES, INC.
30 COMMERCE WAY
WOBURN, MA 01801

By

FRANK E. RUCCIA
ARTHUR D. LITTLE, INC.
20 ACORN PARK
CAMBRIDGE, MASSACHUSETTS 02140

SEPTEMBER 19, 1980

C83546

TABLE OF CONTENTS

Page

- I. SUMMARY
 - A. Purpose
 - B. Scope
 - C. Results
- II. CRYOSHOUD
 - A. Existing Cryoshroud
 - B. Deficiencies
 - C. Aluminum Cryoshroud Modification
 - D. Copper Cryoshroud
- III. LIQUID NITROGEN FUEL SYSTEM
 - A. Present System
 - B. Feed System Concepts
 - C. Pump
 - D. Flash Tank

APPENDIX A--Preliminary Requirements for LABCEDE Cryoshroud

APPENDIX B--Flash Tank Quotation

I. SUMMARY

A. PURPOSE

The LABCEDE Experimental facility located at the Air Force Geophysical Laboratories (AFGL), Hanscom Air Force Base, was built and used in the 1970's for atmospheric physics. A number of modifications to this facility are contemplated to enhance its utility. Physical Sciences, Inc. (PSI), under contract to AFGL, has been authorized to redesign the system. In turn, Arthur D. Little, Inc. has been given the responsibility for the LABCEDE Chamber Cryoshroud and its ancillary systems. More specifically, our responsibility is to recommend a practical concept that will meet specific operating requirements of the system.

B. SCOPE

Our investigation included visits to the LABCEDE facility, interviews with Dr. B. David Green and LABCEDE facility personnel, and a review of the available documentation. We used these observations and information to identify the conditions, practices and operating problems associated with the existing Cryoshroud and its ancillary systems. A set of requirements for the revised systems were prepared by us and approved by PSI. Several concepts were evaluated and the cost, availability and delivery of specialized equipment were determined. From this, one concept was selected and is recommended for implementation.

C. RESULTS

A set of requirements were prepared for the performance of the LABCEDE cryoshroud and approved by PSI and are presented in Appendix A. These were used as a basis for evaluating the existing systems and new system concepts. Our findings, conclusion and recommendations are noted below.

1. Findings

a. Based upon the past operating experience with the LABCEDE cryoshroud, it does not meet important present operating requirements because of:

- Gas leaks,
- High internal radioactivity; and
- Poor experiment volume pressure control.

b. The cost to repair the vacuum leaks in the cryoshroud liquid nitrogen piping are uncertain because of the number of welded joints and the inaccessibility of portions of the joint welds.

c. A copper shroud about 1/16 inch thick of riveted or welded construction and coiled with copper tubing offers the best means for achieving the required leak, light and gas tightness with minimal hot spots.

d. The temperature of the cryoshroud can be maintained below 90K by any of three liquid nitrogen feed systems. These are:

- Pump recirculation systems;
- Gravity recirculation systems;
- Pressure-trickle systems.

The pump recirculation system is best suited for producing low and even temperature distributions in the shroud surfaces.

e. The existing shroud was not thermally insulated in previous service. Thermal insulation on the shroud exterior will eliminate hot spots and promote low and even temperature distribution in the shroud surfaces.

f. The pump recirculation system requires a cryogenic pump and a liquid-gas separation tank. These items are available at reasonable cost and delivery from equipment manufacturers.

2. Conclusions and Recommendations

a. A new copper cryoshroud of acceptable cost, reliability and performance can be achieved with greater confidence than by a modification of the existing aluminum shroud.

b. The pump recirculation system is the most practical liquid nitrogen feed system for the cryoshroud. It offers the greatest design and operating flexibility with good reliability.

c. It is recommended that a design based upon the pump recirculation system and a new copper cryoshroud be implemented.

II. CRYOSHROUD

A. Existing Aluminum Cryoshroud

The cryoshroud is a cylinder approximately 15-feet in length and 39-inch Dia., tongue and groove fitted plates with 13/16-inch high fins facing the shroud interior. The shroud has two chevron-baffled gas pumping ports at each end on the bottom quarter, each having a length of 3-feet. There are several apertures in the shroud, the largest being 19-1/2-inches. Two 2-3/8-inch O.D. aluminum tubes, one at 12 o'clock and one at 6 o'clock serve as headers for the 28 D-tube segments welded to the outer shroud surface. There are a minimum of 30 welded joints in the header-tube piping system.

The ends of the shrouds are separate from the shroud and separately cooled. They are flat and are also constructed from 2-3/8-inch O.D. header tubes and D-tubes mounted to outside of the finned panels. There are a minimum of 16 welded joints in the cooling piping for each end.

Because the headers and D-tubes lie against the outer surface of the shroud, the back sides of all pipe joints are inaccessible for repair except by cutting away sections of the finned panels, which form the cryoshroud enclosure.

The liquid nitrogen feed and vent piping to each of the three cryoshroud components feed through packing glands in the end-doors of the vacuum chamber. The piping and glands must be broken whenever access to the chamber is required. Further, this construction prevents close coupling of the spectrometer and experiment because of physical interferences between spectrometer and liquid nitrogen inlet headers.

B. Deficiencies

The existing cryoshroud has a number of deficiencies of which the major ones are:

- Gas leaks,
- High internal radiosity,
- Poor experiment volume pressure control.

1. Gas Leaks

Operating personnel indicate the presence of gas leaks in the liquid nitrogen cooling lines attached to the shroud. The dynamics of this leak are such that an operating pressure between 3 and 60 microns cannot be achieved in the gas-reaction space of the cryoshroud. This inhibition prevents the conduct of a large number of experiments which must be performed in the 1 to 100 micron pressure range. (See Appendix A.) Thus, the gas leaks must be eliminated from the liquid nitrogen system.

2. High Internal Radiosity

The background radiation level is reported to be excessive. Its sources are the high shroud temperature and openings in the shroud. The shroud temperature is reported to be at about 100K. This can result from poor circulation of liquid nitrogen within the cooling coils and from high heat load to the shroud which is uninsulated from the room temperature vacuum chamber. Thus, the liquid nitrogen recirculation system must be improved and thermal insulation must be applied to the cryoshroud.

A second source of the internal radiosity is from openings in the shroud which admit 300K radiation from the vacuum chamber walls. Openings exist at the ends of the chamber where the end covers mate to the shroud, in the end covers themselves and at the shroud apertures. These openings, therefore, must be minimized.

3. Poor Experiment Volume Pressure Control

The poor control of pressure within the gas-reaction space, which has been reported, is the result of at least three conditions, i.e., the:

- Gas leak,
- Shroud openings and
- Absence of a pressure control mechanism.

The interaction of the reaction gas flow, the gas leak, shroud openings and vacuum system produce dynamic conditions that mitigate against the requirement for constant predetermined pressure levels between 1 and 100 microns (see Appendix A) during tests. Thus, in addition to the elimination of gas leaks and the reduction of shroud openings, that were previously mentioned, a gas pressure control mechanism is required.

C. Aluminum Cryoshroud Modification

There are a number of reasons which may make reuse of the existing cryoshroud difficult, costly and uncertain. These include:

- Modifications are extensive and difficult.
- Many openings must be sealed and
- the liquid nitrogen cooling system must be made gas tight.

The achievement of the last item is the most difficult and the most uncertain of the three indicated. The gas leak does not appear when the system is warm but only when it is cold. If this leak cannot be located by pressurizing the shroud manifolds and D-tubes when warm, then the entire system must be cooled with liquid nitrogen and each joint must be checked in this condition in a vacuum chamber. There are three sections to the cryoshroud presently containing a total of about 60 to 70 joints; cutting a seven foot segment, required for the new system, from the cryoshroud will reduce this number by about 16 joints. When the leak or leaks are located, repair will be difficult because portions of each joint are presently inaccessible for repair. If any leaks are in accessible areas, then portions of the shroud must be cut away to provide access. The heavy and finned wall of the shroud will increase the difficulties associated with this repair.

A preliminary estimate was made of effort required to locate and repair the gas leak in the shroud. Considering all the modifications to the vacuum chamber needed for leak checking the cryoshroud components, special gadgets for cold joint isolation, shroud joint repairs and retesting, a nominal effort of 80 engineering and 250 technician hours will be required. The cost for this, using qualified personnel and equipment, could be in the \$7,500 to \$10,000 range. Further, the results of this effort are not certain to produce a leak tight system.

The modifications to the cryoshroud components to achieve gas pressure tightness, radiation tightness and the introduction of new apertures will be difficult but not impossible to make because of the thick and finned walls of the cryoshroud. However, the effort required for this is probably only a fraction of the effort required to locate and seal the gas leak.

D. Copper Cryoshroud

A new copper cryoshroud can be built instead of rehabilitating and modifying the existing aluminum cryoshroud. Many copper cryoshrouds have been built and utilized at Arthur D. Little, Inc. in cryogenic equipment,

dewars and chambers over the last three decades which have demonstrated excellent performance and reliability. A properly designed copper cryoshroud could be guaranteed to meet the leak, gas and radiation tightness required. Protected with a thermal insulation and provided with an appropriate liquid nitrogen supply and vent system (see Section III), such a shroud would operate at less than 80°F over its entire surface.

The cryoshroud would be made from copper sheet having a nominal thickness of .035-inches. Copper angles would be welded to the shroud ends for bolt attachment of the heads. A single copper coil with not more than one joint would be spiraled around the cylinder and exit radially through the chamber wall through stainless steel boots. The shroud cylinder would contain flush mounted aperture ports welded into the side for attachment of flanges, windows, etc. The internal radiation baffling, located at reaction gas exit end, would be directly cooled with liquid nitrogen cooling coil. The end covers for the shroud would be made from flat copper sheet 1/16 to 1/8 inch thick and bolted to the shroud cylinder angle flange. The two ends would be directly cooled with liquid nitrogen cooling coils. The heads would contain welded ports for the instrument apertures. The entire shroud would be insulated with a fibrous insulation to reduce the shroud load below about 50 watts. The cryoshroud would be supported on the vacuum chamber rail through low conductance supports.

In selecting a cryoshroud with a smooth surface, it is assumed that the internal radiational properties required for the experiment can be achieved without the finned surface of the existing cryoshroud. Through the use of paints, such as 3M-Black Velvet, surface emittances of about 0.95 can be achieved. It is not presently known whether this or similar paints are acceptable in the gas-reaction experiment area. If not, black anodized aluminum foam can be applied to selected areas to achieve the necessary emittance. This requirement must be ascertained prior to preparation of the cryoshroud design.

The painted cryoshroud interior can absorb moisture when it is opened for access to the instruments. This moisture may interfere with the gas-reaction experiments and produce unwanted experimental results. The moisture can be rapidly pumped from the system by heating the shroud at vacuum after exposure to the atmosphere. Electric surface heaters can be placed on the exterior of the cryoshroud to raise its temperature to the 150-200°F range to effect this bakeout. This requirement must be ascertained prior to preparation of the cryoshroud design.

This shroud could be fabricated for a cost comparable to the cost estimated for modifying and rehabilitating the existing aluminum shroud.

III. LIQUID NITROGEN FEED SYSTEM

A. Present System

The existing cryoshroud was cooled with liquid nitrogen fed directly from the ground level pressurized storage tank. The feed to the shroud cylinder, the two ends, and the other cooled elements were individually controlled by automatic on-off valves that obtained their control signals

from temperature sensors located in vertical sections of the vent liner. This system was not witnessed in operation and, in fact, was dismantled when the facility was inspected during a recent visit. Because it was not witnessed during actual operation, it is difficult to establish reasons for the high shroud temperatures reportedly observed during operation.

Little is known about the operation of control system used to operate each cooling circuit. Each controller apparently uses two thermocouples for developing liquid level signals; one for the high level and one for the low level. However, because of the small diameter of the riser in which the sensors are located and the heavy insulation thermally insulating the outside, it is doubtful that the controls operated as intended. Quite likely, the system produced large temperature cycles in the cryoshroud and wastes large quantities of liquid nitrogen.

It is recommended that the liquid nitrogen feed system be radically altered in order to achieve the required temperature performance in the cryoshroud.

B. Feed System Concepts

Three types of liquid nitrogen feed systems could be utilized in this application. They are:

- Pump recirculation
- Gravity recirculation
- Pressure feed trickle

Schematics of each method are shown in Figure 1. In the first two, the ground level pressurized liquid nitrogen storage delivers liquid to a small insulated tank and maintains a constant liquid level in it as controlled from a properly installed liquid level device (one of the exciting liquid level systems could be used for this application). The first method uses a pump to circulate the liquid nitrogen through the shroud returning it to the tank where it flashes to atmospheric pressure and is separated into 77K liquid and gas. The liquid is recirculated and the gas is vented to the atmosphere. The second method uses gravity for recirculation. However, because only a very small driving pressure is developed, the feed system and cryoshroud lines must be large and carefully designed to assure an appropriate amount of liquid feed.

The third method uses the liquid under pressure directly from the ground level storage to feed the cryoshroud. It depends upon manual control settings (could be automatic) to establish the appropriate liquid feed rate. The liquid consumption of this method could be significantly larger than either of Methods 1 and 2.

The pump recirculation system is the best system for the present application. The temperature performance of the cryoshroud will be the lowest attainable and evenly distributed with minimal liquid consumption. Also, the system design is less critical than that of either of the other two systems.

Further, the liquid lines can be smaller in diameter than the gravity system, and they are always filled with liquid, i.e., no gas present. In the event of pump failure, the pump recirculation system can also be temporarily operated as a pressure trickle system offering additional operating reliability. However, the pump is the critical element of this system and its selection must be carefully considered.

C. Pump

The principal performance requirements of the pump are:

- Capacity of 5 gallons per minute
- Discharge head of 100 feet (35 psi)
- Net positive suction head of about 2 feet

At these conditions, the pump would circulate about 2000 pounds of liquid nitrogen per hour and have the capacity to absorb 1000 Btu of heat (about 300 watts) for a temperature rise 1.0°F. Due to the flash down that takes place in the flash tank when the liquid is returned, the temperature of the liquid entering the pump is always at about 77K (depending on the atmospheric pressure). This liquid is circulated in the cryoshroud cooling lines and emerges, still as a liquid, with a temperature rise of less than 1.0°F. The pressure of the liquid is relieved through a valve before entering the flash tank where the heat pickup causes some vaporization of the liquid. The gas and liquid are then separated; the liquid is reused and the gas is vented to the atmosphere.

A pump with the requisite performance and reliability manufactured by a trustworthy manufacturer has been located. The company is the Cosmodyne Corp. of Torrence, California. Data and information concerning a pump to meet cryoshroud application are being forwarded to us. A preliminary estimate of the cost for the pump and spare seals is \$2500-3000.

D. Flash Tank

The function of the flash tank is to provide a constant pump feed by liquid nitrogen saturated at close to atmospheric pressure. It accomplishes this by separating the liquid and gas returned from the cryoshroud and, through a liquid level controller, it draws liquid from the pressurized ground storage to make up for any liquid losses.

The flash tank is a vertical cylinder about 1 ft. in diameter and 4.5 ft. high. The bottom and about 75 percent of the side is vacuum insulated; the top is uninsulated. The pump feed line exits from the bottom; all other lines and the liquid level controller sensors enter through a flat head that seals the top of the tank. The tank will stand 2-3 ft. off of the floor on legs and the pump will be located adjacent to it with its inlet directly connected to the tank outlet.

A cost estimate based on preliminary tank requirements was received from Janis Research Company, Inc. A copy of the quotation is attached as Appendix B.

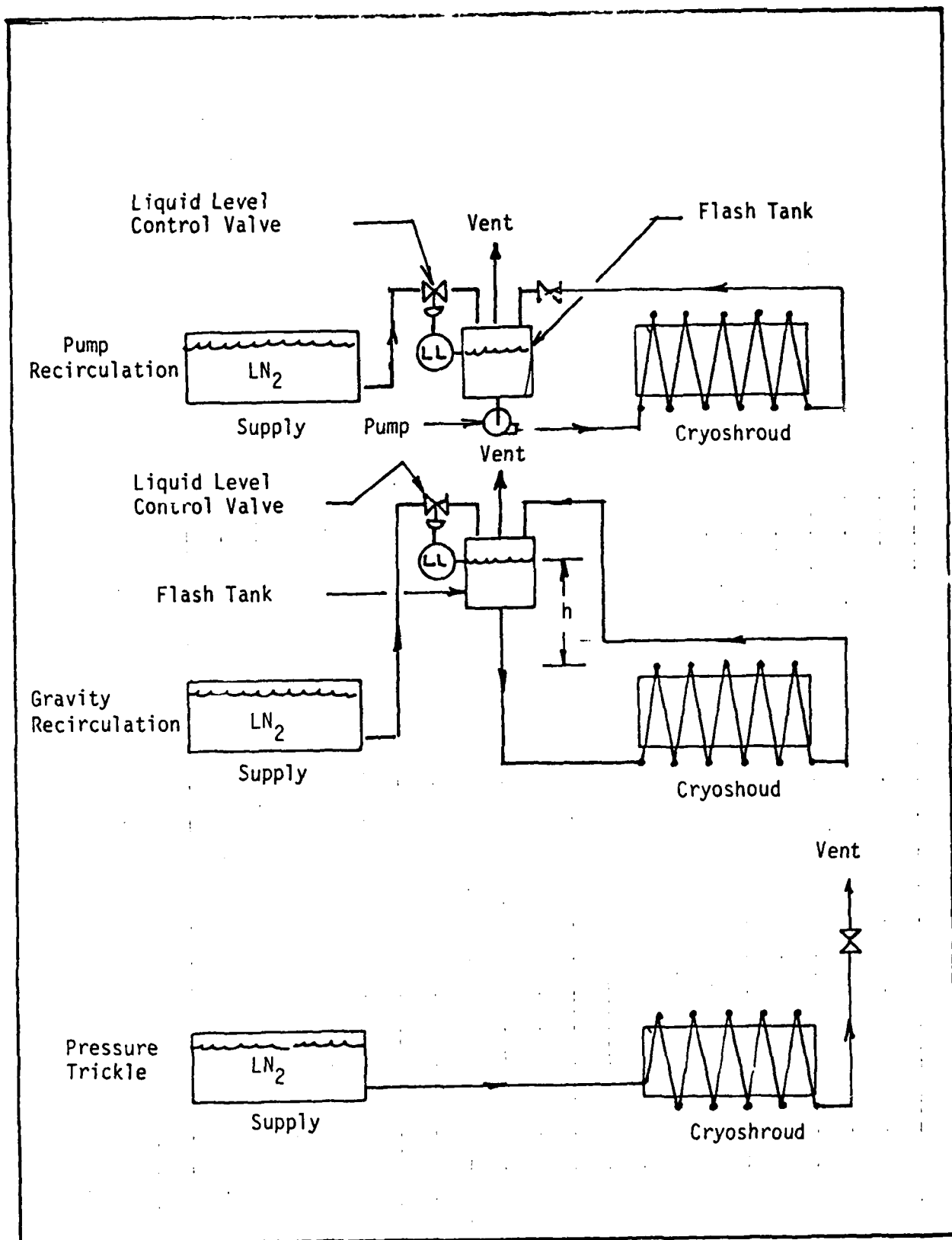


FIGURE 1

CONCEPTS FOR CRYOSHROUD LIQUID

NITROGEN FEED SYSTEM

APPENDIX B

REPORT ON THE DESIGN OF THE LABCEDE CRYOSHROUD

TABLE OF CONTENTS

- I. SUMMARY
 - A. PURPOSE
 - B. SCOPE
 - C. RESULTS
- II. DESIGN INFORMATION
 - A. DESCRIPTION
 - B. SPECIFICATION
 - C. CRYOSHROUD WARM-UP HEATERS
- III. ATTACHMENTS
 - 1. Design Requirements, LABCEDE Cryoshroud
 - 2. Flowsheet for the LABCEDE Rehabilitated Cooling System
 - 3. Equipment, Instrument and Valve List
 - 4. Operating Procedure
 - 5. Specification 85722-01, Liquid Nitrogen Pump, Item 103
 - 6. Specification 85722-02, Liquid Nitrogen Flash Tank, Item 102
 - 7. Valve Specifications
 - 8. LABCEDE Cryoshroud Drawing No. 4187, Sheets 1 through 19
 - 9. LABCEDE, Cryoshroud Cooling System Layout, Drawing No. 4187-1, Sheet 1 of 1

I. SUMMARY

A. PURPOSE

This effort was undertaken to prepare a detail design for a new cryoshroud system to be fabricated for the rehabilitated LABCEDE experimental facility located at the Air Force Geophysical Laboratories, Hanscom Air Force Base, Massachusetts.

B. SCOPE

The design of the cryoshroud was based on the requirements established in a previous study⁽¹⁾ and includes the preparation of detail design drawings, specification for system components, and an operating procedure for the cryoshroud and its cooling system. The work was performed in close cooperation with Physical Sciences, Inc. to insure the compatibility of the cryoshroud with the vacuum chamber and the scientific instruments at the interfaces.

C. RESULTS

The principal results of the design program are the documents and drawings contained in the attachments to this report.

(1) Ruccia, F.E., "Report on the Conceptual Design of the LABCEDE Cryoshroud", Prepared for Physical Sciences, Inc., on September 19, 1980.

II. DESIGN INFORMATION

A. DESCRIPTION

The cryoshroud cooling system consists of an existing liquid nitrogen storage system and a new cryoshroud and liquid nitrogen recirculation system. The system requirements, process flowsheet, equipment list, and operating procedures are contained in Attachments 1, 2, 3 and 4, respectively.

The cooling system recirculates liquid nitrogen from the Flash Tank (Item 102) through the Cryoshroud (Item 104) by means of a centrifugal Pump (Item 103) and back to the flash tank. The fluid in the cryoshroud is liquid at all times during steady state operation and is able to absorb all the heat to the cryoshroud with a temperature rise less than 1°F. The liquid is flashed down through Valve 111MCV and the liquid and gas are separated in the flash tank. The gas is vented from the system to the atmosphere and the liquid is recirculated through the shroud. The liquid losses from the recirculation system, represented by the vented gas, are automatically made up from the Storage Tank (Item 101) by the Flow Control Valve, 108 FCV, operated from the Flash Tank, Liquid Level Controller, 116LLC.

Procedures for startup and shutdown of the system are contained in Attachment 4.

B. SPECIFICATIONS

Specifications for the pump (Item 103), Flash Tank (Item 102) and valves used in the recirculation system are contained in Attachments 5, 6 and 7, respectively. Line sizes are shown in the Flowsheet, Attachment 2, and can be constructed either of copper tubing or 300 Series stainless steel.

C. CRYOSHROUD WARMUP HEATERS

The cryoshroud will contain heaters to warm it from room temperature for vacuum bakeout at 200°F and to warm it from -320°F to room temperature after shutdown of the liquid nitrogen recirculation system. The energy required for the former is about 3500 watt-hours and for the latter about 9500 watt-hours. To accomplish these functions, about 6000 watts of heater power is provided.

The heaters have been sized for parallel operation with 110 volt AC electric power source. Each heater has a nominal resistance of 50 ohms and will operate at a nominal power level of 100 watts. The parallel operation of the heaters allows each heater to operate independently of the other heaters, in the event that one or more may become inoperative.

The heaters specified for the cryoshroud are those manufactured by Minco Products, Inc. The heaters are flexible for fitting to curved surfaces and made up of Kapton film laminar assemblies and encapsulated resistance elements. The elements are to be adhesive bonded to the cryoshroud to establish intimate thermal contact to the shroud.

The adhesive specified for bonding the heaters to the shroud is Eccobond 285 plus catalyst No. 21 manufactured by Emerson & Cuming, Inc. The manufacture suggests surface preparation prior to bonding including roughening of the Kapton surface with abrasives or by etching.

Because of the heater-to-shroud bond is critical to the operation of the heaters, it is suggested that the surface preparation and bonding procedures be confirmed in the laboratory. Sample heaters should be bonded to copper and cycled between -320 and 200°F to assure that reliable heater attachments can be made. Alternate adhesives also suggested for bonding tests are Eccobond 285 plus Catalyst II and Armstrong C7 adhesive manufactured by Armstrong Products of Warsaw, Indiana.

ATTACHMENT #1

For PSI
C-85722

Revised 1/14/81
9/10/80

DESIGN REQUIREMENTS

LABCEDE CRYOSHROUD

By F. E. Ruccia

The LABCEDE cryoshroud is to provide controlled temperature, thermal radiation and gas pressure environments for the electron beam, gas-reaction experiments. The principal requirements for the operation and performance of the cryoshroud are identified below.

1. Operation

The operational goal of the LABCEDE system is the performance of ten gas-reaction experiments per working day each lasting about 1/2 hours.

2. Cryoshroud Location

The cryoshroud is to be placed inside of the existing LABCEDE vacuum chamber modified to the new shortened (11 foot length) configuration.

3. Dimensions

Horizontal cylinder with external cooling tubes about 9 feet in length and an outer diameter greater than 36 inches but less than 39 inches, closed at both ends except as noted below.

4. Operation Temperatures

The maximum temperature of any interior cryoshroud surface is to be less than 90 K.

5. Pressure Rating

The maximum differential pressure between the interior and exterior of the shroud is less than 0.001 atmospheres in either direction. The cryoshroud will contain a safety system to prevent internal or external overpressurization. The closed position of the gas impedance valve is to be limited to gas flow area of 15 cm².

6. Operating Pressure

The internal pressure of the cryoshroud during gas reaction tests will be constant at between 1 and 100 microns. At the same time, the external pressure of the cryoshroud will be nominally held at 1 micron.

AD-A161 674

FLUORESCENCE FROM ELECTRON IRRADIATED GASES IN
REFURBISHED LABCEDE(U) PHYSICAL SCIENCES INC ANDOVER MA
B D GREEN ET AL SEP 85 PST-TR-433 AFGL-TR-84-0218
F19628-80-C-0168

4/4

UNCLASSIFIED

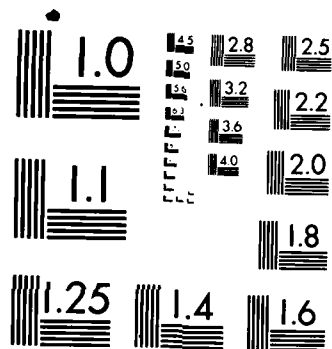
F/G 4/1

NL

END

FILED

DTIC



MICROCOPY RESOLUTION TEST CHART
NATIONAL BUREAU OF STANDARDS-1963-A

When there is no reaction gas flow, the internal and external pressure of the cryoshroud will be nominally at 0.01 microns.

7. Refrigeration

The cryoshroud is to be cooled with liquid nitrogen circulating through cooling coils attached to the outer surfaces. The heat leak to the shroud through its supports and insulation is to be limited to about 150 watts.

8. Thermal Insulation

The external surfaces of the cryoshroud are to be thermally insulated.

9. Supports

The cryoshroud is to be supported on rollers inside of the vacuum chamber to permit easy removal when required. The lateral movement during normal operation and use is to be appropriately restrained. In addition to its own weight, the cryoshroud must support internal instruments and the weight of a person crawling its entire length.

The radiation baffle, valve collar, and collar ring are to be supported from the interior walls of the cryoshroud and are to be thermally connected to it. The valve collar and the collar ring are to be directly cooled with liquid nitrogen.

10. End Plates

The interior of the cryoshroud is to be accessible from either end. The end plates are bolted in place with radiation tight flanges. The end plates are to be directly cooled with liquid nitrogen.

11. Liquid Nitrogen Piping

The feed and vent lines are to be permanently installed through the shell of the chamber to permit access to the chamber interior without disturbing the liquid nitrogen system.

The connecting piping and cryoshroud cooling coils are to have a pressure rating of 100 psi minimum. Appropriate pressure reliefs are to be provided to prevent pressures within these lines from exceeding 100 psi.

The pressure loss in the liquid nitrogen piping system (internal to the chamber) is to be limited to a maximum of 30 psi when the shroud is being maintained in the cold condition.

12. Cryoshroud Interior Surfaces

The interior cylindrical surfaces of the cryoshroud in the gas reaction space (between reaction gas inlet and radiation baffle) are to be smooth and free of gas flow disturbers.

The aperture nozzles are permitted to extend up to 1/2 inch into the reaction chamber space and the shroud flange legs downstream of the reaction space are permitted to extend up to 1/4 inch into the reaction chamber.

The interior surfaces of the cryoshroud at the reaction end for a distance of 76 inches are to have an emittance of less than 0.1. All surfaces within the shroud downstream of this section are to have an emittance greater than 0.85.

13. Apertures

The cryoshroud is to have a number of instrument and other apertures as identified below:

13.1 Reaction Gas Feed End Plate	Location ⁽¹⁾	Nominal Dia. (in) ⁽²⁾
13.1.1 Monochrometer Port, #12	Axis	4
13.1.2 Laser Port, #13	3	4
13.1.3 Laser Port, #14	9	4
13.2 Shroud Cylinder		
13.2.1 Electron Beam Source, #1	3	4
13.2.2 Electron Beam Exit, #2	9	6
13.2.3 Laser Source, #3	3	4
13.2.4 Laser Detector, #4	9	4
13.2.5 Detector, #5	12	4
13.2.6 Detector, #6	6	4
13.2.7 Detector/Inst. Feed Thrus, #7	12	4
13.2.8 Detector/Inst. Feed Thrus, #8	3	4
13.2.9 Pressure Tap, #9	12	4
13.2.10 Port, #10	3	4
13.2.11 Pumping Port, #11	360°	2500 cm ²
13.3 Gas Evacuation End		

A covered opening is to be provided in the end plate at the evacuation end of the cryoshroud. It is to provide access to the blow out discs in the gas impedance valve. The cover is to contain a clearance opening for feed through of impedance valve shaft.

The cryoshroud nozzles to be used for mounting instruments, windows, etc. are to be machined from copper and brazed into the cryoshroud wall. They are to be designed for mounting flanges both from the interior and the exterior of the cryoshroud.

14. Gas Leakage

The leakage area of gas from the chamber annular spaces into the cryoshroud, up stream of the manual pressure control valve, is to be limited to a total of 15 cm². This applies to instrument apertures as well as other openings. This applies mainly to attachments to the cryoshroud apertures, which represents work done by others.

15. Radiation Leakage

The leakage of thermal radiation from vacuum chamber walls into the cryoshroud must be limited by proper design of the joints and closures.

16. Cooldown Time

The cryoshroud is to have a cooldown time of about one hour (80°F to -320°F).

17. Vacuum Bake Out

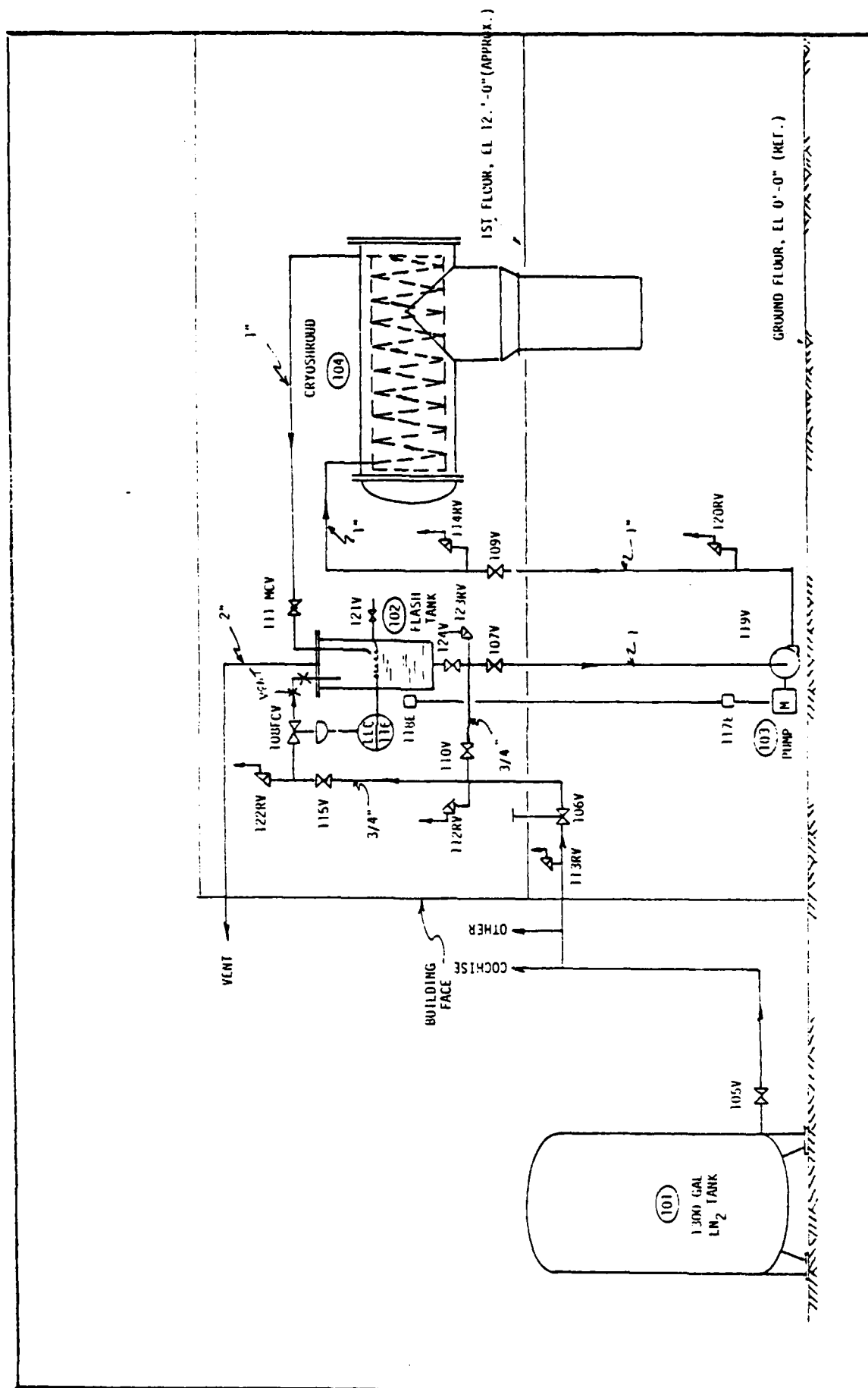
Heaters are to be provided on the cryoshroud to heat the cryoshroud to room temperature from -320°F and to heat the cryoshroud to about 200°F from room temperature for vacuum bake-out.

Warm-up of the cryoshroud to the bake-out temperature is to be accomplished in about one hour.

The softening point of all solders and brazes used in the fabrication of the cryoshroud are to have a minimum softening point of about 350°F.

Heaters are to remain bonded to cryoshroud in the temperatures regime of -320°F to 200°F and an air pressure regime from one atmosphere to 10⁻⁶ mm Hg. under repeated cycling.

ATTACHMENT #2



FLUWSHEET FOR THE LABEIDE FACILITY REHABILITATED CRYOSHROUD COOLING SYSTEM

Revised 1/14/81

Arthur D Little Inc.

ATTACHMENT #3
EQUIPMENT, INSTRUMENT AND VALVE LIST
LABCEDE FACILITY

Revised 1-14-81
11-13-80

REHABILITATED CRYOSHOULD COOLING SYSTEM

Item No.	Description	Req'd.	Extg.	New or Salvage (1)
101	1300 Gallon Liquid Nitrogen Storage Tank, Linde Serial 150 VST-474, Rated for 85 psi operation.	1	1	0
102	Liquid Nitrogen Flash Tank, Rated for Atmospheric Pressure	1	0	1
103	Recirculation Pump and Motor, Rated for 5-10 gpm at 100 ft. head	1	0	1
104	Cryoshroud for LABCEDE Chamber	1	0	1
105V	Storage Tank Shut-Off Valve	1	1	0
106V	Transfer Line Shut-Off Valve	1	1	0
107V	Pump Inlet, Shut-Off Valve, 1-1/2 Inch	1	0	1
108FCV	Automatic On-Off Fill Valve for Flash Tank, 1/2 Inch Approximately	1	1	0
109V	Pump Discharge, Shut-Off Valve, 1 Inch	1	0	1
110V	Shut-Off Valve, 1 Inch	1	0	1
111MCV	Manual Flow Control Valve, 1 Inch Globe	1	0	1
112RV	Fill Line Relief Valve	1	0	1
113RV	Transfer Line Relief Valve	1	0	1
114RV	Cryoshroud Line Relief Valve	1	0	1
115V	Fill Line Shut-Off Valve	1	0	1
116LLC	Liquid Level Controller, Flash Tank	1	1	0
117E	Circuit Breaker for Recirculation Pump	1	0	1
118E	Remote On-Off Switch for Recirculation Pump	1	0	1
119V	Drain Valve, 1/2 Inch	1	0	1
120RV	Pump Line Relief Valve	1	0	1
121V	Liquid Pet Cock	1	0	1
122RV	Fill Line Relief Valve	1	0	1
123RV	Flash Tank Drain, Relief Valve	1	0	1
124V	Flash Tank Drain Valve	1	0	1

(1) Salvage from existing facility where possible

OPERATING PROCEDURELABCEDE FACILITYREHABILITATED CRYOSHROUD COOLING SYSTEM

At start-up, the facility is at room temperature and all valves, except 105V, are assumed closed. Storage tank (Item 101) is assumed to contain a sufficient quantity of liquid nitrogen and be pressurized to 30-40 psig for the liquid transfer operation. Further, the LABCEDE chamber is assumed to be at a vacuum of less than 1 mm Hg.

Start-Up

The following steps are then taken, in the order given, to cool the Cryoshroud (Item 104) and make it operational at 77K.

1. Open 110V, 107V, 109V, 111MCV and 106V in the order given.
2. Allow the system to cool. Observe when liquid nitrogen flows from pet cock 121V.
3. Shut 121V and 110V.
4. Energize liquid level controller, 116LLC.
5. Open 124V and 115V in the order given.
6. Start pump (Item 103) to complete cooldown and initiate operation at 77K.

Shut Down

To shut down the cryoshroud cooling system, proceed as follows:

1. Stop pump, Item 103.
2. Shut valve, 106V.
3. Deenergize liquid level controller, 116LLC.
4. Allow system to warm up overnight. To expedite warm up, drain the system through Valve 119V.
5. When system is at or near room temperature, shut all cooling system valves, except 105V.

ATTACHMENT #5

By F. E. Ruccia

11-25-80
85722

SPECIFICATION 85722-01

LIQUID NITROGEN PUMP, ITEM 103

1. Function: Recirculate liquid nitrogen from flash tank to cryoshroud.
2. Description: Cryogenic centrifugal pump, Type TC21, 3/4 x 1 x 4, for the conditions and requirements specified herein.
3. No. Required: One (1) complete pump, motor, belt drive and spare parts.
4. Fluid Pumped: Liquid nitrogen at approximately atmospheric pressure and at a temperature of -320°F.
5. Flow Rate and Head: Operating point, 10 gpm at 100 ft head.
Efficiency: Greater than 50 percent at operating point.
6. NPSH Available: 8 feet.
7. Seals: Mechanical type.
8. Materials of Construction: Aluminum, stainless steel and bronze are all acceptable. Determine by best availability and lowest cost.
9. Motor
Enclosure: Totally enclosed
Power: 110 volt, single phase, or vendors standard
Horsepower: The motor h.p. is to be equal to or greater than the h.p. required by the pump over its head and flow range.
Speed: By vendor
Coupling: Belt drive
10. Operation: Pump must operate continuously 24 hrs./day 7 days per week for several weeks at a time.
11. Cooldown: Pump is cooled from pressurized LN2 storage tank operating at a pressure of about 40 psig.

SPECIFICATION 85722-01 (CONT'D.)

LIQUID NITROGEN PUMP, ITEM 103

12. Spare Parts:

The vendor is to identify those components, which, based upon his experience, are required as replacement spares.

A single set of spares is to be included in the original order.

The vendor bid is to specify the nominal delivery time required for additional spares.

13. Documentation:

Within three (3) weeks after receipt of order, the vendor is to provide the purchaser with 6 copies of:

1. Certified construction drawings;
2. Operating conditions and precautions;
3. Maintenance instructions;
4. Spare parts lists;
5. Brochures describing the equipment, special features and operation.

14. References

With his bid, the vendor is to provide the purchaser with at least three user references who are utilizing the same or similar equipment for pumping liquid nitrogen at or near the conditions specified.

15. Vendor Information:

Cosmodyne
2920 Columbia Street
Torrance, CA 90509
Attention: V. A. Scopack
(213) 320-5650

By F. E. Ruccia

11-25-80
85722

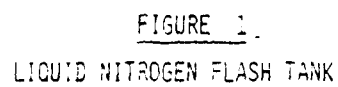
SPECIFICATION 85722-02

LIQUID NITROGEN FLASH TANK, ITEM 102

1. Function: A component of the cryoshroud recirculation system required to separate the liquid and gas from the two phase nitrogen mixture.
2. Description: A vertical cylindrical dewar with flat ends, an internal volume of about 5 ft³, an evacuated thermal insulation, bottom outlet and top connections.
3. No. Required: One
4. Fluid Handled: Liquid nitrogen at -320°F and gaseous nitrogen in the range of -320 to 100°F.
5. General Configuration: See attached Figure 1 for configuration and dimensions.
6. Materials of Construction: 300 Series Stainless Steel.
7. Inner Vessel:
 - 7.1 Internal Pressure: 20 psia (max.)
 - 7.2 External Pressure: 0 psia (min.), 18 psia (max.)
 - 7.3 Wall Thickness: Minimum thickness consistent with shell pressure requirements and fabrication methods.
 - 7.4 Ends: Flat plate, top common with outer vessel
 - 7.5 LN₂ Despin Baffles:
 - No. Required: 4
 - Locations: Spaced 90° apart at positions indicated in Figure 1.
 - Material: 304 S/S Plate, 1/8" thick
 - Attachment: Stitch weld to inner vessel.
 - 7.6 Anti-Vortex Cruciform
 - Material: 304 S/S plate, 1/8" thick
 - Attachment: Stitch weld to bottom head
 - 7.7 Supports: Inner vessel is to be supported from the top head common to both inner and outer vessels

SPECIFICATION 85722-02 (CONT'D.)
LIQUID NITROGEN FLASH TANK, ITEM 102

- 7.8 Stilling Tube:
Diameter: 4" S/S Tube
Connection: 4" flange, outside of vessel
Bottom: Plate with one-1/2" dia. opening welded to bottom opening
Vent: 2-1/2 inch diameter openings located as indicated in Figure 1.
- 7.9 Vent: 2 inch diameter with pipe threaded end
- 7.10 Refill Line: 3/4 inch diameter with threaded end outside and horizontally directed outlet inside
- 7.11 Recycle Line: 1 inch diameter with threaded end outside and horizontally directed outlet inside
- 7.12 Pet Cock: 1/4 inch tube, welded into inner and outer vessel with expansion loop in vacuum space.
- 7.13 Outlet: 1-1/2" tube, with threaded end outlet
8. Outer Vessel:
- 8.1 Internal Pressure: 0 psia (min.), 18 psia (max.)
8.2 External Pressure: 15 psia at all times
8.3 Wall Thickness: Thickness consistent with the shell pressure requirements
8.4 Evacuation Valve: Connection and valve required
8.5 Relief Valve: One required, crack at 17 psia
8.6 Ends: Flat plate, top common with inner vessel
8.7 Supports: 4 angle type supports or equal for bolting to floor. Provide 1-1/2 inch diameter hole in each of four floor plates
9. Vacuum Space:
9.1 Leakage Rate: Less than 10^{-8} std. cc/sec.
9.2 Insulation: On sides and bottom only. The effective thermal conductance of the insulation material is to be less than $\frac{0.005 \text{ Btu}}{\text{hr. ft}^2 \text{ } ^\circ\text{F}}$
10. Remarks: The successful vendor is to furnish with the deliverable item six (6) sets of drawings to the purchaser showing the locations and dimensions of the dewar and its connections for installation purposes.



296

ATTACHMENT 7

VALVE SPECIFICATIONS

LARGE CRYOSPHROUD RECIRCULATION SYSTEM

85722
1-15-81

Item No. (1)	107V	109V	110V	111 MCV	112RV, 113RV 114RV, 120RV 122RV, 123RV	115V	119V	121	124
Function	Pump Inlet	Pump Discharge	Shut-Off	Manual Control	Pressure Relief	Shut-Off	Drain	Pet Cock	Tank
Description	Gate Valve	Gate Valve	Ball Valve	Globe Valve	Relief Valve	Gate Valve	Ball Valve	Ball Valve	Gate Valve
Process Fluid	LN ₂	LN ₂	LN ₂	LN ₂	GN ₂ , LN ₂	LN ₂	LN ₂	LN ₂	LN ₂
Temp. Range (°F)	-320 to 100	-320 to 100	-320 to 100	-320 to 100	-320 to 100	-320 to 100	-320 to 100	-320 to 100	-320 to 100
Max. Pressure (PSI)	150	150	150	150	150	150	150	150	150
Cracking Pressure (PSIA) (2)	N/A	N/A	N/A	N/A	100	N/A	N/A	N/A	N/A
Nominal Size (in.)	1	1	1/2	1	1/4	3/4	1/2	1/4	1"
Materials	Cryogenic	Cryogenic	Cryogenic	Cryogenic	Cryogenic	Cryogenic	Cryogenic	Cryogenic	Cryogenic
Connections	Screwed	Screwed	Screwed	Screwed	Screwed	Screwed	Screwed	Screwed	Screwed
Valve Stem	Extended, 14"	Extended, 14"	Standard	Extended, 13"	Standard	Extended, 14"	Standard	Standard	Extended, 14"
Source (4)	Braman Dow	Braman Dow	Jamesbury	Braman Dow	Circle Seal	Braman Dow	Jamesbury	HOKE	Braman Dow
Source Cat. No. (4)	Powell #7035	Powell #7035	1/2" D-33 TT	Powell #70102	5180 B-2MP-100	Powell #7035	1/2" D33 TT	7115G4S	Powell #7035

(1) Refer to the flowsheet and to equipment and instrument list for location in the system.

(2) Applies to relief valves only.

(3) Acceptable cryogenic materials include bronze, brass, stainless steel (300 series), teflon (for seats and seals), 17-7 PH steel (for springs only)

(4) Conperable hardware produced by other manufacturers is acceptable.

APPENDIX C

LABCEDE SPECTROMETER ANALYSIS

LABCEDE SPECTROMETER ANALYSIS

March, 1981

Prepared by

Michael Hercher and Geert Wyntjes

OPTRA, Inc.
1727 Revere Beach Parkway
Everett, MA 02149
(617) 389-7711

for

PHYSICAL SCIENCES, Inc.
30 Commerce Way
Woburn, MA 01801
(617) 933-8500

[Ref. P.O.#3693]

TABLE OF CONTENTS

Section	Title
1	Introduction
2	Summary of the Problem
3	Parametric Analyses
4	Radiometric Analysis of Available Instruments
5	Recommendations
Appendix I ...	N.E.S.R. Calculations for Different Types of Spectroradiometer

1.0 INTRODUCTION

This report covers the first phase of a study to determine the best choice of spectroradiometric instrumentation for use with Labcede in two different situations:

(1) A measurement, to be completed by the end of the summer of 1981, whose objective is to demonstrate the effectiveness of the modified Cryogenic Labcede in obtaining IR spectra from E-beam-excited gases at low pressure; and

(2) A series of measurements, to be carried out over the next 12 to 18 months, in which high-quality spectroradiometric data can be obtained from a variety of gases in Labcede, under a variety of experimental conditions.

In the first instance [(1) above] the most important considerations are (a) selection of a specific measurement which represents a judicious compromise between (i) certainty of success, (ii) relevance to the customer's interests, and (iii) a level of difficulty which adequately demonstrates the capability of the overall system; and (b) selection of instrumentation which is either on-hand or readily obtainable, capable of the required measurement, and which can be made operable within the next few months.

In the second instance, the major objective is to define spectroradiometric instrumentation which will be optimum for obtaining the desired data at a reasonable cost.

Section 2 of this report summarizes the spectroradiometric problem; Section 3 contains parametric analyses of a number of different spectroscopic approaches; Section 4 is a survey of the characteristics and operational status of a number of available instruments; and Section 5 contains our recommendation for the experimental configuration to be used for the demonstration measurement to be completed this summer. The definition of the optimum instrumentation for an extended measurement program will be addressed in a subsequent report.

2.0 SUMMARY OF THE PROBLEM

2.1 General

The Cryogenic Labcede currently being modified by PSI is shown in fig.2.1-1. Flowing gas at a velocity on the order of 20 meters/sec is carried through a collimated electron-beam, whose diameter is approximately 4 cm. The immediate objective is to observe the emission spectra of gases within an 8 cm long excitation region, and at various positions downstream. The downstream measurements are intended to provide data on emission which takes place at different time intervals following excitation by the E-beam.

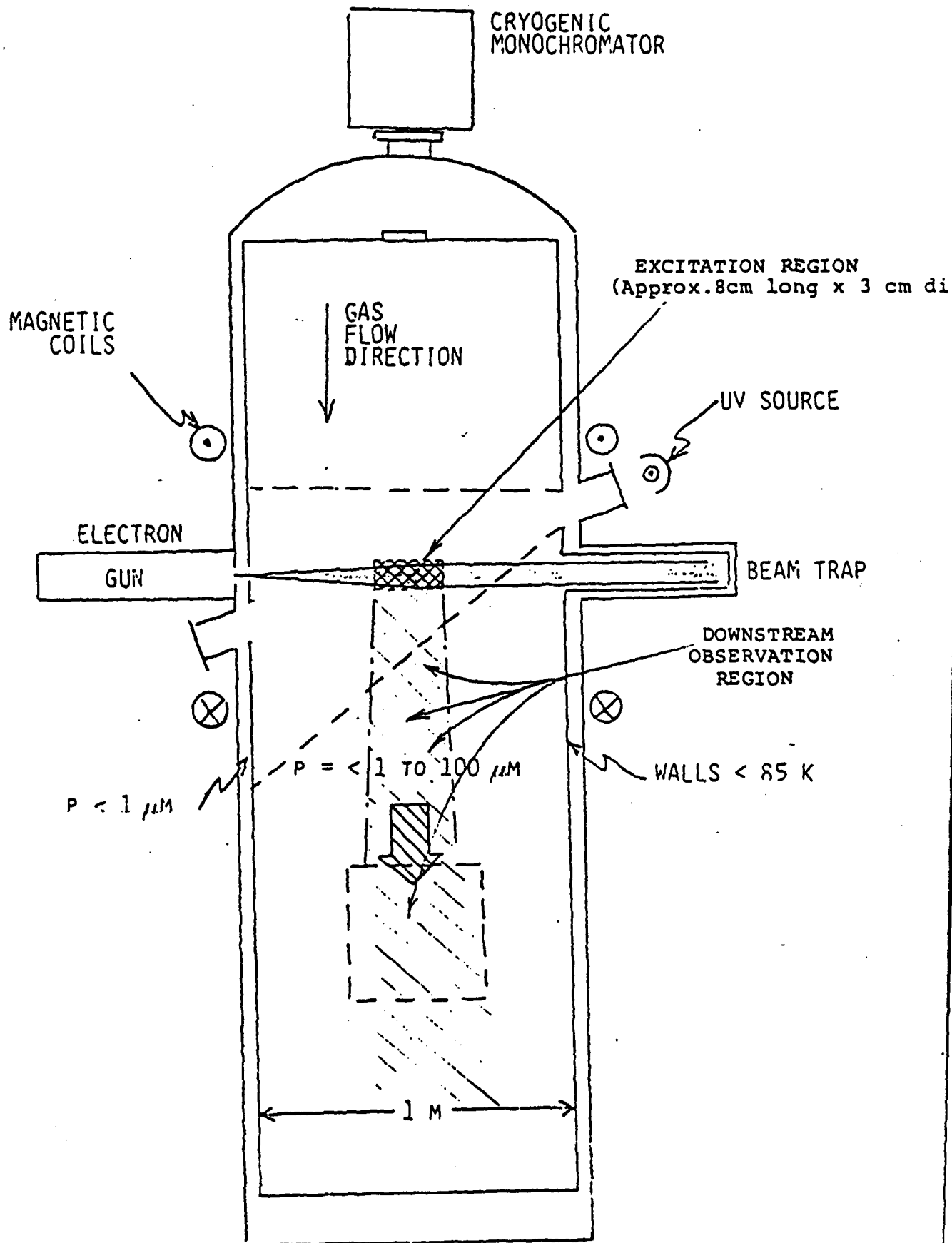
The desired spectral resolution has been defined as follows:

- 10 inverse cm resolution: only marginally acceptable;
- 2 inverse cm resolution: desirable; and
- <0.5 inverse cm resolution: may be advantageous in some circumstances.

With this in mind, our nominal target resolution will be 2 inverse cm, but we will not rule out instruments whose resolved bandwidth is as large as 10 inverse cm.

2.2 Predicted Radiant Intensities

Three upper atmosphere species have been identified as being of particular interest: nitrogen oxide (NO); ozone (O₃); and carbon dioxide (CO₂). Table 2.2-1 lists the spectral regions to be monitored for each of these gases, and gives estimates of both the spectrally integrated in-band radiant intensity, and the radiant intensity of single spectral components for each of these species at different pressures in the range 1 to 300 microns (Hg). These values (which are unpublished estimates provided by PSI) are based on the assumption of a 100 cubic cm excited volume (a cylinder approximately 8 cm long and 4 cm in diameter).



MODIFIED CRYOGENIC LABCEDE (TOP VIEW)

Figure 2.1-1



TABLE 2.2-1

ESTIMATED RADIANT INTENSITIES
(100 CC ASSUMED SOURCE VOLUME)

GAS	NITROGEN OXIDE				OZONE		CARBON DIOXIDE	
WAVELENGTH, MICRONS (APPROXIMATE)	5 - 7				9.3 - 11		13 - 17	
ESTIMATED BANDWIDTH (WAVENUMBERS)	350				150		100	
PRESSURE, MICRONS OF MERCURY	1	10	100	300	1	10	100	
RADIANT INTENSITY (WATTS/STERAD) (INTEGRATED OVER BAND)	1.2E-9	1.2E-7	3E-10	1.2E-8	3.8E-11	3.7E-9	>2E-8	
RADIANT INTENSITY (WATT/STERAD) (2 WAVENUMBER BANDWIDTH)	6.9E-12	6.9E-10	4E-12	1.6E-10	7.6E-13	7.4E-11	>4E-10	

NOTE: THE SOURCE WAS ASSUMED TO BE A CYLINDER, 8CM LONG AND
4 CM IN DIAMETER. THUS, TO CONVERT RADIANT INTENSITIES
(FROM THE LAST TWO LINES OF THE TABLE ABOVE) TO RADIANCES,
THE VALUES ABOVE SHOULD BE DIVIDED BY 30 CM².

3.0 PARAMETRIC ANALYSES

3.1 Radiometric Considerations

Fig.3.1-1 illustrates a generalized spectroradiometric measurement. The source is characterized by a spectral radiance N_s (watt/sq cm-sterad-cm⁻¹), a projected area in the direction of the instrument A_s (sq cm), and a solid angle Ω_s into which it emits. (The spectral radiant intensity J_s is related to the spectral radiance by: $N_s = J_s/h_s$.)

The spectrometer is characterized by a spectral bandwidth $\Delta\sigma_i$ (cm⁻¹), a transmission (which generally includes the transmission of the auxiliary optics) t_i , an entrance aperture area A_i (sq cm), and an acceptance solid angle Ω_i (sterad). The product of the latter two parameters is the throughput, or etendue of the instrument; and the product of the instrument's transmission (or efficiency) and its throughput is termed the Net Throughput.

The detector has an area A_d (sq cm), an acceptance solid angle Ω_d (sterad) (which is usually close to pi steradians), a spectral bandwidth $\Delta\sigma_d$ (cm⁻¹) within which it has significant sensitivity, and an intrinsic sensitivity which is characterized by its D^* (cm Hz^{1/2}watt⁻¹). In addition, the detector may be provided with a cold filter at a temperature T_f and with a transmission t_f , and a spectral bandpass $\Delta\sigma_f$ (cm⁻¹) centered on a wavenumber σ_f (cm⁻¹) ($\Delta\sigma_f < \Delta\sigma_d$).

In addition to the components mentioned above, the system will have various optical components which serve to get the radiation from one place to another, and which are used to match the throughputs of the source, instrument, and detector.

In terms of the parameters defined above, the radiant power from the source incident on the detector is given by:

$$(3.1-1a) \quad P_s = N_s [t_i A_i \Omega_i \Delta\sigma_i] \text{ watts (no cold filter), or}$$

$$(3.1-1b) \quad P_s = N_s [t_i A_i \Omega_i \Delta\sigma_i] t_f \text{ watts (with cold filter),}$$

where it is assumed that the source throughput exceeds that

of the instrument (clearly the case in these measurements), and that the detector is chosen so that its throughput matches or exceeds that of the instrument.

The effective (in terms of eliciting a significant detector response) amount of background radiation P_b incident on the detector is given by:

$$(3.1-2a) \quad P_b = A_d \Omega_d \int_{\Delta\sigma_i} \epsilon N_{bb}(\sigma, T_b) d\sigma \quad \text{watts (no cold filter), or}$$

$$(3.1-2b) \quad P_b = A_d \Omega_d [\epsilon t_f N_{bb}(\sigma, T_b) \Delta\sigma_f + \int_{\Delta\sigma_f} \epsilon_f N_{bb}(\sigma, T_f) d\sigma] \\ \text{watts (with cold filter),}$$

where $N_{bb}(\sigma, T)$ denotes the spectral radiance of a blackbody at temperature T , T_b is the background temperature, ϵ is the effective emissivity of the background (typically ranging from 0.1 to 0.4) and ϵ_f is the in-band emissivity of the cold filter.

The key parameters over which we have control are:

Instrument: $A_d \Omega_d$ (generally a function of $\Delta\sigma_i$), t_f , and $\Delta\sigma_f$;

Detector + Cold Filter: A_d , D^* , T_f , $\Delta\sigma_f$, and t_f ; and

Environment: T_b and ϵ .

3.2 Parametric Analyses of Various Spectrometers

Without much loss in generality we can consider just five types of instrument:

- (a) Dispersive (e.g. grating or prism);
- (b) Fourier Transform Spectrometer (FTS);
- (c) Scanning Fabry-Perot Interferometer (+ blocking filter(s));
- (d) A Set of Bandpass Filters, or Circular Variable Filter (CVF); and
- (e) An Optical Heterodyne Spectrometer.

Brief analyses of these classes of instruments are given in the following paragraphs.

3.2.1 Grating Spectrometer:

The standard grating equation is: $d(\sin\theta_1 + \sin\theta_2) = m\lambda$, where d is the ruling spacing, λ is the wavelength, θ_1 and θ_2 are the angles of incidence and diffraction respectively, and m is the order number. We will assume a Littrow mount, for which θ_1 and θ_2 are approximately equal. The basic parameters which describe a grating instrument are:

$$N = 1/d = \text{rulings/cm};$$

$$A = \text{area of grating (cm}^2\text{)} \\ (\text{projected area} = A \cos\theta_2);$$

$$h = \text{slit height (cm)};$$

$$\Delta\sigma = \text{wavenumber resolution (cm}^{-1}\text{)};$$

$$f = \text{focal length (cm)}; \text{ and}$$

$$t_g = \text{transmission (or efficiency)}.$$

In terms of these parameters, we can further define:

$$\Delta x = \text{slit width (cm)} \\ = Nm f \Delta\sigma / (\sigma^2 \cos\theta_2);$$

$$A_g = \text{entrance aperture area (cm}^2\text{)} \\ = h \Delta x; \text{ and}$$

$$\Omega_g = \text{acceptance solid angle (sterad)} \\ = A \cos\theta_2 / f^2.$$

Finally, the throughput, U_g , and net throughput, $U_g(\text{net})$ are given by:

$$(3.2.1-1) \quad U_g = hA(\Delta\sigma/\sigma)/f \text{ (cm}^2\text{-sterad)}, \text{ and}$$

$$U_g(\text{net}) = U_g t_g,$$

where we have assumed that the angle of incidence at the grating is approximately 30 degrees, so that $N = \sigma/m$.

It should be pointed out that, due to aberrations of the

optical system, f and h are not independent: a reduction in the focal length, f , is generally accompanied by a reduction in the slit height, h , in order to form a satisfactory image of the slit. It should also be mentioned that there is a practical difficulty in matching the throughput of a grating spectrometer to that of a detector: this is because the spectrometer slit is generally imaged onto the detector, but detectors are usually either round or square, so that the detector area needed to accomodate the image of the slit is usually much greater than the area of the slit image. The net result is excess noise due to background radiation incident on the excess detector area.

Example: for the following realistic parameter values;

$$A = 25 \text{ sq cm (2" x 2" grating);}$$

$$h = 2 \text{ cm;}$$

$$f = 50 \text{ cm;}$$

$$\sigma = 667 \text{ cm}^{-1} \text{ (15 micron wavelength);}$$

$$\Delta\sigma = 2 \text{ cm}^{-1}; \text{ and}$$

$$t_s = 0.1,$$

we calculate a net throughput of:

$$U_s(\text{net}) = 3 \times 10^{-4} \text{ sq cm-sterad.}$$

3.2.2 Fourier Transform Spectrometer:

In a Michelson-type Fourier Transform Spectrometer, the relevant system parameters are:

A_i = mirror area (cm^2);

$\Delta\sigma$ = wavenumber resolution (cm^{-1});

σ = center of wavenumber range of interest (cm^{-1}); and

t_i = efficiency (or effective transmission).

The maximum physical displacement of the moving mirror is defined by the required resolution [$d=1/(2\sigma_r L)$], and this in turn defines the angular field of view and acceptance solid angle:

$\Delta\theta$ = angular radius of the field of view (rad)
= $(2\Delta\sigma/\sigma)^{1/2}$; and

Ω_i = acceptance solid angle
= $2\pi\Delta\sigma/\sigma$ sterad. (Rayleigh Criterion)

Thus, the throughput and net throughput for a Fourier Transform Spectrometer are given by:

$$(3.2.2-1) \quad U_i = 2\pi A_i (\Delta\sigma/\sigma), \text{ and}$$

$$U_i(\text{net}) = U_i t_i.$$

For comparable spectral resolutions, a Fourier Transform Spectrometer generally has a much greater net throughput than that of a grating instrument. The multiplex advantage of an FTS, when applicable, gives it a further edge over a grating instrument..

Example: for the following realistic parameter values,

$A = 20 \text{ sq cm}$ (2" diameter mirrors);

$\Delta\sigma = 2 \text{ cm}^{-1}$;

$\sigma = 667 \text{ cm}^{-1}$ (15 micron wavelength); and

$$t_i = 0.1,$$

we calculate a net throughput of:

$$U_i(\text{net}) = 0.038 \text{ sq cm-sterad.}$$

We should point out that since the largest sensitive IR detectors generally available are on the order of 4 mm square (or 4 mm in diameter), and since the fastest detector optics are in the range $f/0.7$ to $f/1$, the detector throughput of an IR system is limited in practice to a value on the order of 0.1 to 0.2 sq cm-sterad. Thus, using very large mirrors on an F.T.S. would not improve the throughput beyond this limiting value--although this approach could be used to improve the spectral resolution at the maximum throughput.

For a given spectral region and resolution, the ratio of the net throughput of a Fourier Transform Spectrometer to that of a grating instrument is given by:

$$(3.2.2-2) \quad U(\text{FTS,net})/U(\text{grating,net}) = 2\pi (t_i/t_g) (f/h) (A_i/A).$$

3.2.3 Scanning Fabry-Perot Interferometer

The Fabry-Perot Interferometer turns out to be very similar to the Fourier Transform Spectrometer--except, of course, that it requires an auxiliary bandpass filter(s) to block unwanted orders, has no multiplex advantage, and does not require data processing in order to obtain a spectrum. The relevant instrument parameters are:

A_{fp} = area of F.P. mirror (sq cm);

F = Finesse $\leq \pi\sqrt{R}/(1-R)$, where R = mirror reflectance;

$\Delta\sigma$ = spectral bandpass (cm^{-1})
 $= 1/(2dF)$, where d is the mirror spacing; and

t_{fp} = peak transmission (typically 0.2 to 0.7).

In terms of these parameters, the half-field angle is $(F\sigma d)^{-1/2}$, and the throughput is given by:

$$(3.2.3-1) \quad U_{fp} = 2\pi A_{fp} (\Delta\sigma/\sigma), \text{ or}$$

$$U_{fp}(\text{net}) = t_{fp} U_{fp}.$$

Example: for a realizable Fabry-Perot interferometer designed to operate at 15 microns, the following parameters are reasonable:

$A = 5 \text{ sq cm (1" diam.)};$

$\sigma = 667 \text{ cm}^{-1} \text{ (15 micron wavelength);}$

$\Delta\sigma = 2 \text{ cm}^{-1};$

$R = 85\% (F = 20); \text{ and}$

$t_{fp} = 0.4.$

In which case, the net throughput of the interferometer is:

$$U_{fp}(\text{net}) = 0.38 \text{ sq cm-sterad.}$$

3.2.4 Circular Variable Filter (Interference Filter)

An interference filter is, of course, essentially the same as a Fabry-Perot etalon. The principal difference is that because of the practical limitation on the physical thickness of the spacing layer, the spectral bandpass of the filter is limited to larger values than can be readily attained with an air-spaced Fabry-Perot etalon. The expression for the throughput of an ideal interference filter is the same as that for a Fabry-Perot interferometer.

Example: an available Circular Variable Filter (CVF) has a 3% bandpass, a peak transmission of 60%, and a usable area (maintaining the 3% bandpass) of approximately 0.1 sq cm. The net throughput of this CVF is approximately:

$$(3.2.4-1) \quad U_{\text{CVF}}(\text{net}) = 0.011 \text{ sq cm-sterad},$$

while having a spectral bandwidth (at 15 microns) of approximately 18 cm^{-1} .

3.2.5 Heterodyne Spectrometer

In a heterodyne spectrometer, radiation from the source to be measured is coherently added to quasi-monochromatic radiation from a tunable laser (acting as a local oscillator), and the signal is detected at an IF frequency which is the difference between the laser frequency and that of the source. Ideally (but usually not in practice in the IR), the local oscillator power is made large enough to insure that its shot noise dominates all other noise sources, in which case the Noise Equivalent Power incident on the detector is given by:

$$(3.2.5-1) \quad NEP = 2hc\sigma(c\Delta\sigma\Delta f)^{1/2}/Q,$$

where Δf is the post-detection measurement bandwidth, $c\Delta\sigma$ is the IF bandwidth (which defines the spectral bandwidth of the measurement), and Q is the detector quantum efficiency. The factor of 2 in this expression arises because only half of the unpolarized radiation from the source can interfere with the polarized radiation from the local oscillator. Eq(3.2.5-1) predicts an admirably low Noise Equivalent Power but, unfortunately (because of the low throughput associated with heterodyne detection) corresponds to a relatively high Noise Equivalent Spectral Radiance (NESR).

Because, in a heterodyne measurement, the radiation from the source under measurement must be coherently added to radiation from the local oscillator, the irradiated region of the detector must correspond to the diffraction limit of the optical system used to collect the radiation. This, in turn, means that the maximum attainable throughput for a heterodyne system is equal to the square of the wavelength:

$$(3.2.5-2) \quad U_k = \lambda^2 = 1/\sigma^2 \text{ sq cm-sterad.}$$

Using this value for the throughput, the Noise Equivalent Spectral Radiance for heterodyne detection is given by:

$$(3.2.5-3) \quad NESR = 2hc^{1/2}\sigma^3(\Delta f/\Delta\sigma)^{1/2}/Q.$$

Example:

Consider a collection lens with a diameter D and a focal length f . The coherence area in the focal plane of the lens has a diameter of approximately $1.22 f\lambda/D$, so that the usable detector area is:

$$A = 1.22(\pi/4)(f\lambda/D)^2.$$

The collection solid angle is approximately:

$$\Omega = (\pi/4)(D/f)^2,$$

so that the throughput, U , is approximately λ^2 . For a wavelength of 15 microns this gives:

$$U_{\lambda} = 2.3 \times 10^{-6} \text{ (sq cm-sterad).}$$

3.3 Radiometric Sensitivity

In practice, the sensitivities of most IR quantum detectors are limited by background noise. That is, by fluctuations in the number of current carriers due to irradiation of the detector by thermal radiation from both the environment of the detector, and from the background within the target scene. Following equations (3.1-1) and (3.1-2), we can write the following expressions for the number of current carriers produced per unit time by signal (n_s) and background (n_b) radiation:

(3.3-1) NO COLD FILTER:

$$n_s = N_A [t_i A_i \Omega_i \Delta\sigma_i] (Q/hc\sigma), \text{ \&}$$

$$n_b = (A_d \Omega_d) \int_{\Delta\sigma_d} (Q \epsilon / hc\sigma) N_{BB}(\sigma, T_b) d\sigma \text{ carriers/sec,}$$

and,

(3.3-2) WITH COLD FILTER (t_f , T_f , σ_f , $\Delta\sigma_f$)

$$n_s = N_A [t_i A_i \Omega_i \Delta\sigma_i] (t_f Q/hc\sigma), \text{ \&}$$

$$n_b = (A_d \Omega_d) [\epsilon t_f N_{BB}(\sigma, T_b) \Delta\sigma_f Q/hc\sigma + \int_{\Delta\sigma_d} (Q \epsilon_f N_{BB}(\sigma, t_f) / hc\sigma) d\sigma],$$

where Q is the quantum efficiency of the detector and $hc\sigma$ is the energy of a photon at wavenumber σ . (The other parameters are defined in section 3.1.)

The Noise Equivalent Spectral Radiance (NESR) for background-limited detection is given by:

$$(3.3-3) \text{ NESR} = \Delta f^{1/2} n_b^{1/2} / [n_s / N_{\sigma}],$$

where Δf is the measurement bandwidth and $[n_s / N_{\sigma}]$ is the detector responsivity (carriers/sec per unit source spectral radiance) as defined by eq(3.3-1) and (3.3-2). Table 3.3-I gives the specific form of this equation for a number of different limiting situations of interest.

The background noise is often described in terms of the spectral D^* of the detector:

TABLE 3.3-I

NOISE EQUIVALENT SPECTRAL RADIANCE

I. GENERAL EXPRESSIONS

No Cold Filter:

$$(a) \quad NESR = [hc\sigma_i / (t_i U_i \Delta\sigma_i Q)] \\ \times [A_d \Omega_d \Delta f \int (Q\epsilon / hc\sigma) N_{bb}(\sigma, T_b) d\sigma]^{1/2}.$$

With Cold Filter:

$$(b) \quad NESR = [hc\sigma_i / (t_i U_i t_f Q)] \\ \times [A_d \Omega_d \Delta f \{ \epsilon t_f N_{bb}(\sigma_f, T_b) \Delta\sigma_f Q / (hc\sigma) \\ + \int Q\epsilon_f N_{bb}(\sigma, T_f) d\sigma / (hc\sigma) \}]^{1/2}.$$

Heterodyne Detection:

$$(c) \quad NESR = 2hc^{3/2} \sigma^3 (\Delta f / \Delta\sigma)^{1/2} / Q.$$

II. SPECIAL CASE

With Cold Filter: $T_f < 20 \text{ deg.K}$; $T_b > 77 \text{ deg.K}$; $\Delta\sigma_f / \sigma_f > 2\%$

$$(d) \quad NESR = [A_d \Omega_d \epsilon \Delta\sigma_f hc\sigma_f \Delta f N_{bb}(\sigma_f, T_b) / (t_f Q)]^{1/2} / [t_i U_i \Delta\sigma_i].$$

In all of the above expressions, integrations are over the spectral bandwidth of the detector response. Subscripts "i" refer to the instrument, subscripts "d" refer to the detector, and subscripts "f" refer to the cold filter.

$$(3.3-4) \quad D_{\sigma}^* = (A_{\Delta} \Delta f)^{1/2} / (NEP)_{\sigma},$$

where $(NEP)_{\sigma}$ is the spectral Noise Equivalent Power, or the incident r.m.s. monochromatic signal power required to produce a signal-to-noise ratio of unity, with a measurement bandwidth of Δf . In terms of D^* , the NESR is given by:

$$(3.3-5) \quad NESR = (A_{\Delta} \Delta f)^{1/2} / (D^* t_i t_f A_i \Omega_i \Delta \sigma_i),$$

where, as before, we have assumed that throughputs are matched, and that the source and detector throughputs equal or exceed that of the instrument. Note that this equation is also valid when the limiting noise is intrinsic detector noise, rather than background noise.

3.4 Multiplex Advantage of Fourier Transform Spectrometers

In deriving the expressions for Noise Equivalent Spectral Radiance (Section 3.3) it was assumed (except in the case of the Fourier Transform Spectrometer) that the spectrometer was set at the precise wavelength of interest, and that it detected signal radiation only within the resolution element centered on that wavelength. In order to make measurements for N spectral resolution elements, either N separate detectors, or N separate measurements would be required. In the latter instance, the overall measurement duration would have to be increased by a factor of N . Thus, if a Fourier Transform Spectrometer and a non-FTS instrument have equal NESR's, then the non-FTS instrument will require a measurement duration which is N times longer than that required by the FTS in order to make a measurement of N spectral resolution elements at a given Signal-to-Noise ratio.

Another way of expressing this Multiplex Advantage of an FTS (sometimes referred to as Fellgett's Advantage) is to note that [in a background noise-limited situation] if an FTS and non-FTS instrument have equal throughputs, equal transmissions, equal measurement durations, and identical detectors, then in a measurement encompassing N spectral resolution elements, the FTS measurement will be characterized by a Signal-to-Noise ratio which exceeds that of the non-FTS instrument by a factor equal to the square root of N .

4.0 RADIOMETRIC ANALYSIS OF AVAILABLE INSTRUMENTS

4.1 Sensitivity of Various Spectroradiometric Systems

For the purposes of this report, we have considered three different spectral regions: 5 microns (NO); 10 microns (O3); and 15 microns (CO2). Of these three, it appears that the 15 micron measurement would be the most attractive initial effort. We have also considered 4 different experimental configurations: 300 degree K background, with and without a cold filter; and 85 degree K background, with and without a cold filter. In all cases we assume that the detector is at a temperature of 20 degrees K, and that the cold filter is at the detector temperature. At 15, 10 and 5 microns the cold filter bandwidths are, respectively, 50, 100 and 200 cm^{-1} .

In order to provide a vehicle for representative sensitivity calculations, we have considered 6 different realistic spectroradiometric systems. Table 4.1-I summarizes the sensitivities of these different spectroradiometers for each of the various experimental configurations, and Table 4.1-II summarizes the specifications of the different spectroradiometers. [Appendix I contains a more detailed account of the sensitivity calculations summarized in Table 4.1-I.]

As mentioned in Section 3.4, NESR determinations, such as those given in Table 4.1-I, are primarily relevant to the detection of radiation at the single spectral resolution element to which the spectrometer is set. In a spectroradiometric measurement involving a number of spectral resolution elements, we can define a parameter $\text{NESR}^*(N)$, which is the Noise Equivalent Spectral Radiance for a measurement of N spectral resolution elements. In other words, it is the spectral radiance of the source which yields a S/N of 1 in each of N channels, each of which corresponds to a single spectral resolution element. The NESR^* of a spectroradiometer is a function of the net throughput of the spectrometer, the post-detection measurement bandwidth [equal to the reciprocal of the measurement duration], the number of resolution elements observed, the area of the detector, and its D^* :

(4.1-1) Non-FTS Measurement:

$$\text{NESR}^* = (A_d N \Delta f)^{1/2} / (D^* t_d U_i \Delta \sigma_i); \text{ and}$$

TABLE 4.1-1

SUMMARY OF NESR CALCULATIONS FOR DIFFERENT SPECTROMETERS,
SPECTRAL REGIONS, AND MEASUREMENT CONFIGURATIONS.

1 SEC MEASUREMENT TIME (1 KHZ POST-DETECTION BANDWIDTH)

N.E.S.R. (IN UNITS OF $1E-10$ WATTS/SQ CM-STERAD-CM⁻¹)

WAVELENGTH, BACKGROUND TEMP. & COLD FILTER STATUS	GRATING (2CM ⁻¹)	FTS(1*MIRRORS) (2CM ⁻¹)	FTS(2*MIRRORS) (1CM ⁻¹)	FABRY-PEROT(1") (2CM ⁻¹)	CIRC.VAR.FILTER (3% BANDWIDTH)	HETERODYNE (2CM ⁻¹)
15 MICRONS 300 DEG K NO COLD FILTER	890	4.8	5.6	2.4	1.6	29
15 MICRONS 300 DEG K COLD FILTER	220	1.2	1.4	.61	.41	29
15 MICRONS 85 DEG K NO COLD FILTER	16	.09	.1	.05	.03	29
15 MICRONS 85 DEG K COLD FILTER	3.8	.02	.02	.01	.007	29
10 MICRONS 300 DEG K NO COLD FILTER	1400	6	7.6	3	1.6	98
10 MICRONS 300 DEG K COLD FILTER	470	2	2.5	.98	.52	98
10 MICRONS 85 DEG K NO COLD FILTER	5.9	.02	.03	.01	.007	98
10 MICRONS 85 DEG K COLD FILTER	1.1	.005	.006	.002	.001	98
5 MICRONS 300 DEG K NO COLD FILTER	850	2.3	1.3	1.2	.46	780
5 MICRONS 300 DEG K COLD FILTER	480	1.3	.74	.67	.27	780
5 MICRONS 85 DEG K NO COLD FILTER	.006	.0018	.0018	.0018	.0018	780
5 MICRONS 85 DEG K COLD FILTER	.003	.0018	.0018	.0018	.0018	780

(THESE CALCULATIONS DO NOT INCLUDE THE MULTIPLEX ADVANTAGE OF F.T.S. SPECTROMETERS; SEE TEXT & TABLE 4.1-III)

1 N.E.S.R. LIMITED TO 0.001 WATT/(SQ CM-STERAD-CM⁻¹) BY PREAMP GAIN:BANDWIDTH CONSIDERATIONS.

optica

TABLE 4.1-II

REPRESENTATIVE INSTRUMENT SPECIFICATIONS

1. GRATING SPECTROMETER:

GRATING SPACING1 WAVELENGTH (5, 10 OR 15 MICRONS)
 GRATING CONFIGURATION....LITTON MOUNT (30 DEG)
 FOCAL LENGTH.....50 CM
 FOCAL RATIO.....F/10
 GRATING SIZE.....5 CM X 5 CM
 SLIT HEIGHT.....2 CM
 SPECTRAL RESOLUTION.....2 CM⁻¹
 TRANSMISSION.....10%
 THROUGHPUT.....0.003 CM²-STERAD
 DETECTOR AREA.....2MM X 2MM = 0.04 CM²

2. & 3. FOURIER TRANSFORM SPECTROMETER

1" MIRRORS APERTURE AREA.....5.1 CM²
 SPECTRAL RESOLUTION.....2 CM⁻¹
 TRANSMISSION.....10%
 THROUGHPUT.....0.095 CM²-STERAD (AT 15 MICRONS)
 DETECTOR AREA.....0.12 CM² (AT 15 MICRONS)

2" MIRRORS APERTURE AREA.....20.3 CM²
 SPECTRAL RESOLUTION.....1 CM⁻¹
 TRANSMISSION.....10%
 THROUGHPUT.....0.19 CM²-STERAD (AT 15 MICRONS)
 DETECTOR AREA.....0.16 CM² (AT 15 MICRONS)

4. SCANNING FABRY-PEROT INTERFEROMETER

APERTURE AREA.....5.1 CM² (1" DIAM)
 SPECTRAL RESOLUTION.....2 CM⁻¹
 TRANSMISSION.....20%
 THROUGHPUT.....0.095 CM²-STERAD (AT 15 MICRONS)
 DETECTOR AREA.....0.12 CM²

5. CIRCULAR VARIABLE FILTER

APERTURE AREA.....0.1 CM² (APPROX 1 CM X 0.1 CM)
 SPECTRAL RESOLUTION.....3% (18 CM⁻¹ AT 15 MICRONS)
 TRANSMISSION.....20%
 THROUGHPUT.....0.018 CM²-STERAD (AT 15 MICRONS)
 DETECTOR AREA.....0.16 CM²

6. HETERODYNE SPECTROMETER

APERTURE AREA.....N.A.
 SPECTRAL RESOLUTION.....2 CM⁻¹
 TRANSMISSION.....25%
 THROUGHPUT.....WAVELENGTH SQUARED (CM²-STERAD)
 DETECTOR AREA.....N.A.
 LOCAL OSCILLATOR POWER...SUFFICIENT FOR SHOT NOISE
 TO DOMINATE OTHER NOISE
 SOURCES (FOR AN MESR OF
 1E-11 AT 15 MICRONS, THE
 REQUIRED LOCAL OSCILLATOR
 POWER IS 8 MILLIWATTS)

(4.1-1) FTS Measurement:

$$\text{NESR}^* = (A_d \Delta f)^{1/2} / (D \cdot t_f \cdot U_i \Delta \sigma_i);$$

where A_d is the detector area, Δf is the post-detection bandwidth, N is the number of spectral resolution elements--each having a spectral bandwidth $\Delta \sigma_i$ --covered by the measurement, t_f is the transmission of the cold filter, and U_i is the net throughput of the spectrometer.

Table 4.1-III summarizes the NESR* values for the same instruments and experimental configurations that were covered by Table 4.1-I, assuming a measurement encompassing 20 resolution elements, and a measurement time of 100 seconds (corresponding to a post-detection bandwidth of 0.01 hertz). (The number of spectral resolution elements is somewhat arbitrary, but is approximately equal to the number of resolution elements contained within the bandpass of the cold filter at 15 microns.)

The implications of the results shown in Table 4.1-III are straightforward and have been well-understood for some time:

The high spectral resolution and throughput of a Fourier Transform Spectrometer, in combination with the multiplex advantage which obtains when the dominant noise source is shot noise in the background radiation, makes it a clearly superior instrument for obtaining IR spectra of weak sources.

If the number of spectral resolution elements to be observed is small, then a Fabry-Perot interferometer or etalon offers high spectral resolution and high throughput.

If high spectral resolution is not required, then a Circular Variable Filter offers moderately high throughput--although the aspect ratio of its useful aperture makes it difficult to obtain a good throughput match to a small detector.

We might also note that where very high spectral resolution and throughput are required--without a requirement for covering a large number of spectral resolution elements--a Spherical Fabry-Perot interferometer is ideal, since its

TABLE 4.1-111

SUMMARY OF NESR: CALCULATIONS FOR DIFFERENT SPECTROMETERS,
SPECTRAL REGIONS, AND MEASUREMENT CONFIGURATIONS

MEASUREMENT COVERS 20 SPECTRAL RESOLUTION ELEMENTS

MEASUREMENT TIME IS 100 SEC (POST-DETECTION BANDWIDTH OF 0.01 HZ)

N.E.S.R.: IN UNITS OF $1\text{E-10 WATT/SQ CM-STERAD-CM}^{-1}$

WAVELENGTH, BACKGROUND TEMP. & COLD FILTER STATUS	GRATING (2CM^{-1})	FTS(1*MIRRORS) (2CM^{-1})	FTS(2*MIRRORS) (1CM^{-1})	FABRY-PEROT(1*) (2CM^{-1})	CIRC.VAR.FILTER (3% BANDWIDTH)	HETERODYNE (2CM^{-1})
15 MICRONS 300 DEG K NO COLD FILTER	401	.48	.56	1.1	.72	29
15 MICRONS 300 DEG K COLD FILTER	99	.12	.14	.27	.18	29
15 MICRONS 85 DEG K NO COLD FILTER	7.1	.009	.01	.022	.013	29
15 MICRONS 85 DEG K COLD FILTER	1.7	.002	.002	.0045	.0031	29
10 MICRONS 300 DEG K NO COLD FILTER	626	.6	.76	1.3	.72	98
10 MICRONS 300 DEG K COLD FILTER	210	.2	.25	.44	.23	98
10 MICRONS 85 DEG K NO COLD FILTER	2.6	.002	.003	.0045	.0031	98
10 MICRONS 85 DEG K COLD FILTER	.49	.0005	.0006	.0009	.0005	98
5 MICRONS 300 DEG K NO COLD FILTER	380	.23	.13	.54	.21	780
5 MICRONS 300 DEG K COLD FILTER	210	.13	.074	.3	.12	780
5 MICRONS 85 DEG K NO COLD FILTER	.0027	.00018	.00018	.00018	.00018	780
5 MICRONS 85 DEG K COLD FILTER	.0013	.00018	.00018	.00018	.00018	780

* NESR: LIMITED TO 0.0001 WATT/(SQ CM-STERAD-CM⁻¹) BY PREAMP GAIN*BANDWIDTH CONSIDERATIONS.

throughput increases with its spectral resolving power.

4.2 Available Instruments

4.2.1 Cryogenic Grating Spectrometer

There is an f/10 cryogenic grating spectrometer, with a helium-cooled Si:As detector, available at AFGL. The specifications for this instrument closely match those given for the grating spectrometer in Tables 4.1-I, 4.1-II and 4.1-III. The detector is not equipped with a cold filter, although it would not be difficult to add a cold filter. At present it is difficult, if not impossible, to cool this instrument to 100 degrees K or less. The problems include leaking seals, and a large thermal mass.

4.2.2 Fourier Transform Spectrometers

There is one FTS instrument immediately available to P.S.I. at AFGL: this FTS has 1" diameter mirrors, and requires a different beamsplitter for use at 15 microns. It is not designed for use at cryogenic temperatures, although it can of course be used with a cooled detector. Its specifications (assuming replacement of the beamsplitter) closely match those of the 1" FTS described in Table 4.1-II. As far as we know, this instrument is operational--although it has not been used recently, and would require a thorough checkout. The Si:As detector described above is available and suitable for use with this FTS.

In addition to this instrument, there are a number of other FTS instruments, both cryogenic and non-cryogenic, in other laboratories at AFGL. We do not know to what extent these instruments are available to P.S.I. for the proposed experiment.

There are a number of data systems for FTS spectrometers in various laboratories at AFGL, and it is not anticipated that there would be any difficulty in obtaining a suitable data system for use in an experimental program this summer (1981).

4.2.3 Circular Variable Filter Spectrometers

There are two cryogenic Circular Variable Filters + detectors which may be available to this program by the

summer. These instruments were built by Utah State, and are currently in Utah being modified: their specifications closely match those given for the CVF in Table 4.1-II. One of these instruments is described in further detail in Section 5. It should be noted that these instruments are not suited, in their present configuration, for use with a 300 degree K background.

4.2.4 Other Available Spectrometers

There are no other spectrometers, to our knowledge, which are both available and suited for the P.S.I./AFGL measurement program envisioned for this summer.

5. RECOMMENDATIONS

5.1 Selection of Molecular Species and Wavelength

The three molecular species (and wavelength regions) under consideration are (1) nitric oxide [5 microns], (2) ozone [10 microns], and (3) carbon dioxide [15 microns]. It has generally been agreed that ozone should be ruled out for consideration as a demonstration measurement because of the high degree of uncertainty associated with the theoretical predictions for its emission under E-beam excitation. Emission from nitric oxide, on the other hand, is predicted with reasonable certainty to be easily measurable--so much so that such a measurement would hardly constitute a significant test of the spectroradiometric measurement system. By the process of elimination we are therefore left with the measurement of carbon dioxide emission in the vicinity of 15 microns. There is a reasonable level of confidence in the theoretical predictions for carbon dioxide, and the predicted emission levels are sufficiently low to define a challenging measurement.

Our recommendation is to measure the emission spectrum of E-beam excited carbon dioxide in the vicinity of 15 microns.

5.2 Predicted Emission by E-beam-Excited Carbon Dioxide

Based on the data in Table 2.2-I, which have been provided by P.S.I., the predicted radiance of F-beam-excited carbon dioxide in the vicinity of 15 microns is as shown in Table 5.2-I. Figure 5.2-1 illustrates the shape of the predicted spectrum: the dominant feature in the spectrum is the central Q-branch, which contains approximately 30% of the total emission, and whose spectral width is expected to be on the order of 2 wavenumbers or less. With a spectral resolution of 2 wavenumbers it should also be possible to resolve spectral structure within the P and R-branches. At the maximum experimentally attainable pressure of 100 microns (Hg), the predicted integrated spectral radiance, within the 2 cm^{-1} instrumental bandwidth, at the peak of the Q-branch, is approximately $\geq 1.3\text{E-}10\text{ watt/(sq cm-sterad)}$.

TABLE 5.2-I

ESTIMATED RADIANCES FOR E-BEAM-EXCITED
CARBON DIOXIDE

(BASED ON CALCULATIONS MADE BY PSI INC.)

ASSUMED E-BEAM DIAMETER.....4 CM
 OVERALL BANDWIDTH AT 15 MICRONS....100 CM⁻¹

	GAS PRESSURE IN MICRONS HG		
	1	10	100
RADIANCE FOR ENTIRE BAND (WATT/SQCM-STERAD)	1.3E-12	1.2E-10	>6.7E-10
AVERAGE RADIANCE FOR 2CM ⁻¹ BANDWIDTH (WATT/SQCM-STERAD)	2.5E-14	2.4E-12	>1.3E-11
SPECTRAL RADIANCE AT Q-BRANCH PEAK (WATT/SQCM-STRD-CM ⁻¹)	2.2E-13	2.0E-11	>1.1E-10

NOTE: Q-BRANCH HAS A BANDWIDTH OF APPROXIMATELY 2 CM⁻¹

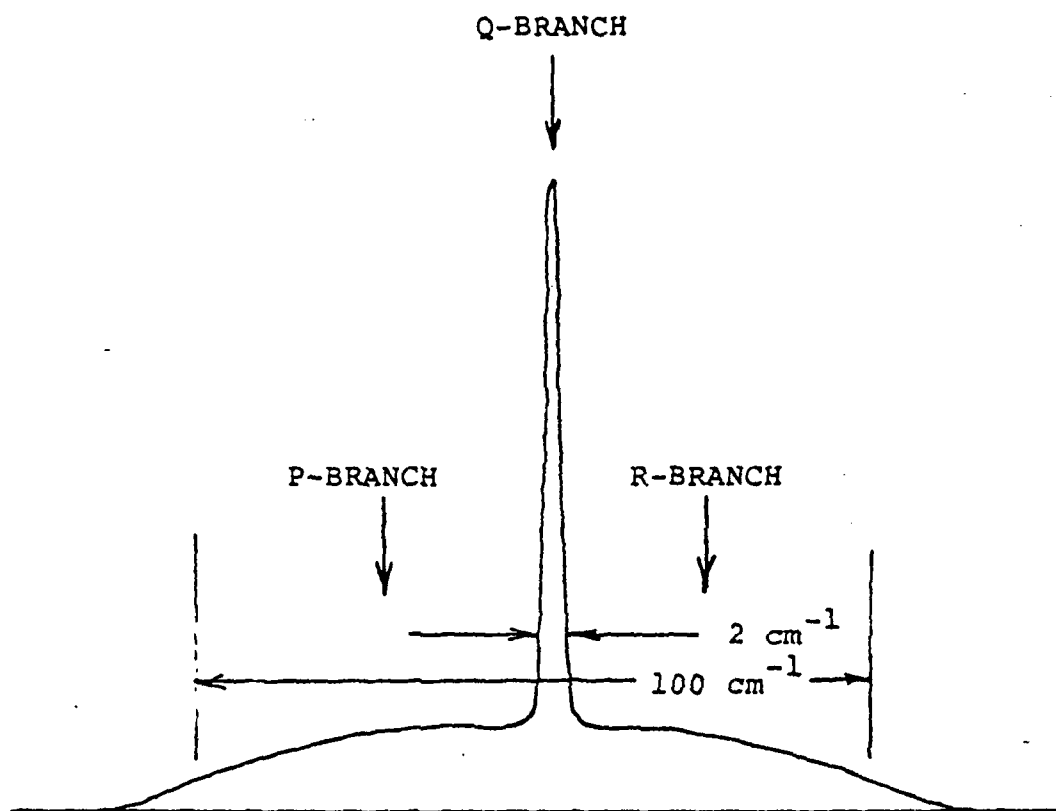


Fig.5.2-1

Predicted Spectral Profile for
E-beam-excited Emission from
CO₂ in vicinity of 15 microns.

5.3 Recommended Spectrometers

Comparing Table 4.1-III (NESR* values for a 100 second measurement encompassing 20 spectral resolution elements) with the predicted peak Q-branch spectral radiance of $1.3\text{E}-10$ watt/(sq cm-sterad-cm⁻¹) [for carbon dioxide at 100 microns pressure], it appears that either of the Fourier Transform Spectrometers would give a satisfactory measurement with a 300 degree K background, providing a cold filter is used in front of the detector.

Another candidate spectrometer which is satisfactory in terms of sensitivity, although only marginally tolerable in terms of spectral resolution, is the Utah State-built cryogenic scanning wedge filter radiometer (CVF). This is an all cryogenic system which, based on experiemntal measurements, has an NESR of approximately $4.5\text{E}-11$ watt/(sq cm-sterad-cm⁻¹). This instrument scans over approximately 30 spectral resolution elements at a rate of 2 scans/sec; its spectral resolution is on the order of 30 cm⁻¹, and its Field of View is 5 degrees. Normalized for the conditions cited in Table 4.1-III, the measured NESR* for this instrument would be $6.0\text{E}-13$ watt/(sq cm-sterad-cm⁻¹). [This number is within a factor of two of that predicted for a cold CVF at 15 microns (see Tab.4.1-III); this relatively good agreement is undoubtedly fortuitous to some extent, but does suggest that the results shown in Table 4.1-III are not too far from reality.] Unfortunately, the available CVF spectrometers are only capable of operating cold (<20 deg K), and with a cold background (<100 deg K). [Operating with a warm background would probably require major changes in the detector, preamp, and biasing system--and would require use of a cold filter. The low resolution of the CVF makes background discrimination considerably more difficult than is the case with higher resolution instruments.] According to A. Fairbanks (AFGL) the CVF sensor is being modified, and improved drives are being added which should allow both coherent addition of scans and measurements at a single fixed wavelength. To the extent that this instrument is available, it may be considered for future low resolution work, when the chamber is cold (85 deg K).

For the near term (3 to 6 months) our recommendation for the spectrometer is a room-temperature FTS with a cooled detector and cold filter (20 deg K), special auxiliary optics (see Sect.5.4), and with a room-temperature background. Canditade instruments are the Idealab interferometric spectrometer presently in the Labcede facility at AFGL, and the similar instrument now at P.S.I. Both of these instruments would require some work and/or

minor modifications (in addition to suitable foreoptics and detector optics) before being operational. The available 3 mm x 3 mm Si:As detector (with dewar) should be entirely adequate. A suitable cold filter may be available at AFGL. Primarily for reasons of mechanical stability and immunity from low frequency vibrations, but also for reasons of improved dynamic range, the FTS interferometer should be operated at the maximum practical scan rate; this will be in the vicinity of 5 cm/sec (retardation rate).

5.4 Dynamic Range Considerations & Auxiliary Optics

We have already assessed the recommended FTS system in terms of sensitivity: we now consider other factors such as dynamic range and optimization of the measurement configuration.

In practice, the dynamic range is limited by the number of bits available in the output of the A/D converter--which in turn is related to the A/D bandwidth.

A typical FTS is illustrated in fig.5.4-1. In the absence of a source, the interferogram recorded by the detector is characteristic of the background radiation. More precisely, the interferogram resulting from the motion of the interferometer mirror can be understood as follows: as the mirror moves, the interferometer alternately serves to transmit radiation from the source region to the detector, and to reflect the detector back upon itself (the frequency and phase of this alternation depends on the wavelength). Thus the background interferogram--upon which the signal interferogram is superposed--has an amplitude given by:

$$(5.4-1) \quad I_b = A(N_b - N_d),$$

where I_b is the background interferogram amplitude, A is a constant (characteristic of the interferometer), and N_b and N_d are the background and detector radiances respectively--both filtered by the cold filter. Assuming that the low end of the dynamic range is set by the Noise Equivalent Radiance (in interferogram space), the required post-detection dynamic range is given by:

$$(5.4-2) \quad \text{Dynamic Range} = (N_b - N_d)/\text{NER}.$$

With a 300 degree K background and a cooled detector with a

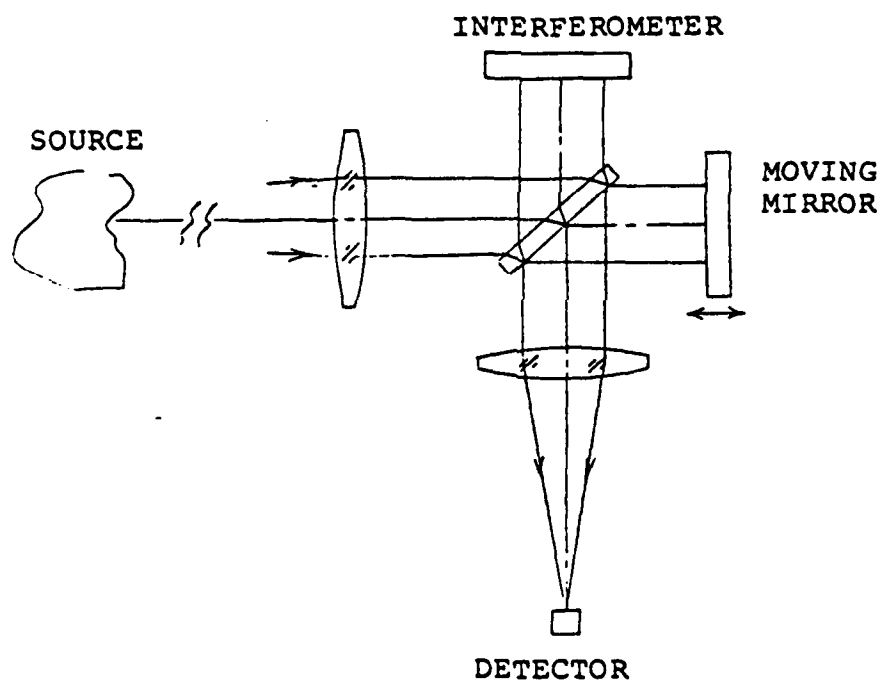


Fig.5.4-1

Fourier Transform Spectrometer

reasonable D^* , this dynamic range can easily be very large--in excess of 10,000. From the expression above it is clear that the required dynamic range can be reduced either by (1) increasing the NER , or (2) reducing the quantity $(N_b - N_d)$. We will consider each of these approaches--and ultimately recommend using both. [A third technique, modulation of the signal and subsequent detection of the interferogram in the vicinity of the modulation carrier frequency, is effective but inefficient in that it requires discarding half of the signal power.]

The first approach, increasing the NER , is accomplished by increasing the scan rate and thereby increasing the measurement bandwidth associated with a single scan. At first, this appears self-defeating in that the required dynamic range is reduced at the expense of a reduced sensitivity (measured in terms of the NER): but the sensitivity can be recovered by co-adding interferograms from successive scans. This reduces the measurement bandwidth, and introduces no noise since the co-adding is done following digitization.

The second method for reducing the dynamic range requirement is to minimize the numerator $(N_b - N_d)$ in eq.(5.4-2). The ultimate solution to this problem would be to make both terms go to zero--cool everything! A less drastic and more subtle approach is to make both terms in the numerator approximately equal. One way to accomplish this is to make sure that the detector sees a reflection of itself regardless of whether the interferometer is in a transmissive or reflective mode. This is illustrated in fig.5.4-2: a spherical mirror, located behind the signal source so as to image the source back upon itself, also serves to return an image of the detector back upon itself. This arrangement has the bonus of doubling the amount of signal received at the detector (as long as the source region is essentially transparent at the wavelengths of interest). Ideally, the auxiliary mirror would either have a very high reflectivity (and thus a correspondingly low emissivity), or would be cooled so that its thermal emission would be negligible. If the mirror temperature were controllable, the background interferogram could be nulled out--which would improve both the dynamic range, and the background-limited sensitivity.

We recommend using a relatively high scan frequency in conjunction with digital co-adding of interferograms, and use of an auxiliary mirror both to increase the signal level, and reduce the amplitude of the background interferogram.

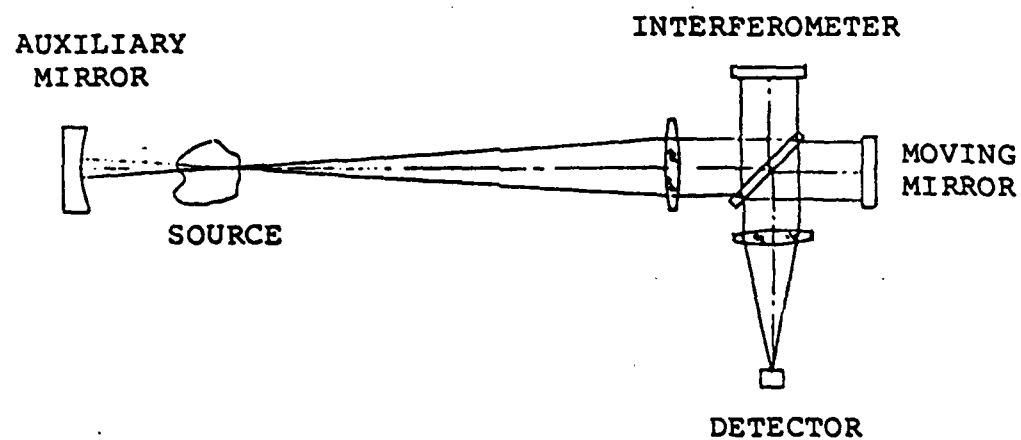


Fig.5.4-2

FTS Instrument and Source + Auxiliary Mirror

5.5 Cost Impact

The cost of making an available FTS system operational and suitable for the planned measurement has not been determined. The major cost items are:

- (a) New beamsplitter for use at 15 microns;
- (b) 60 wavenumber bandpass cold filter;
- (c) Auxiliary mirror + foreoptics & detector optics (if required)
- (d) Mechanical & electronic checkout of existing FTS instrument; repairs as required; and
- (e) Integration of FTS instrument with an available data system + checkout.

With the funds remaining in the current contract, Optra will provide cost estimates for these items, and a work statement for completing the recommended measurement by the end of the summer (1981). In addition, Optra will supplement this report with a section defining an optimized spectroradiometer for an extended series of Labcede measurements during the next 12 to 18 months.

5.6 Summary

(a) The Labcede demonstration experiment to be completed this summer should be a measurement of the emission spectrum from E-beam-excited carbon dioxide at a pressure of 100 microns. This measurement may be made either at 300 deg.K, or at cryogenic temperatures (or both).

(b) The recommended spectrometer is a room-temperature FTS equipped with a cooled detector and cold filter, and designed to operate in the vicinity of 15 microns with a 2 wavenumber resolution. The available grating spectrometer is not capable of making the required measurement.

(c) The recommended experimental configuration is to locate the FTS spectrometer outside the Labcede chamber, and to view the chamber through a clean window. An auxiliary mirror should be located inside the chamber to increase the signal to the spectrometer, and to image the detector back on itself.



APPENDIX D

N.E.S.R. CALCULATIONS FOR DIFFERENT TYPES
OF SPECTRORADIOMETER

(All calculations were made using the relevant expressions
from Table 3.3-I.)

NOISE EQUIVALENT SPECTRAL RADIANCE CALCULATIONS

1. GRATING SPECTROMETER

BACKGROUND TEMPERATURE (DEG K)	300	300	85	85
COLD FILTER (Y/N)	NO	YES	NO	YES
WAVENUMBER (CM-1)	667	667	667	667
SPECTRAL RESOLUTION (CM-1)	2	2	2	2
EFFICIENCY (OPTICAL & ELECTRICAL)	.1	.1	.1	.1
THROUGHPUT (SQ CM-STERAD)	.0003	.0003	.0003	.0003
DETECTOR AREA (SQ CM)	.04	.04	.04	.04
MEASUREMENT DURATION (SEC)	1	1	1	1
DETECTOR QUANTUM EFFICIENCY	.5	.5	.5	.5
BACKGROUND EMISSIVITY	.5	.5	.5	.5
COLD FILTER BANDPASS (CM-1)	NA	50	NA	50
COLD FILTER TRANSMISSION	NA	.7	NA	.7
N.E.S.R. (WATT/SQ CM-STERAD-CM-1)	8.9E-8	2.2E-8	1.6E-9	3.8E-10

NOISE EQUIVALENT SPECTRAL RADIANCE CALCULATIONS

1A. GRATING SPECTROMETER

BACKGROUND TEMPERATURE (DEG K)	300	300	85	85
COLD FILTER (Y/N)	NO	YES	NO	YES
WAVENUMBER (CM-1)	1000	1000	1000	1000
SPECTRAL RESOLUTION (CM-1)	2	2	2	2
EFFICIENCY (OPTICAL & ELECTRICAL)	.1	.1	.1	.1
THROUGHPUT (SQ CM-STERAD)	.0002	.0002	.0002	.0002
DETECTOR AREA (SQ CM)	.04	.04	.04	.04
MEASUREMENT DURATION (SEC)	1	1	1	1
DETECTOR QUANTUM EFFICIENCY	.5	.5	.5	.5
BACKGROUND EMISSIVITY	.5	.5	.5	.5
COLD FILTER BANDPASS (CM-1)	NA	100	NA	100
COLD FILTER TRANSMISSION	NA	.7	NA	.7
N.E.S.R. (WATT/SQ CM-STERAD-CM-1)	1.4E-7	4.7E-8	5.9E-10	1.1E-10

1B. GRATING SPECTROMETER

BACKGROUND TEMPERATURE (DEG K)	300	300	85	85
COLD FILTER (Y/N)	NO	YES	NO	YES
WAVENUMBER (CM-1)	2000	2000	2000	2000
SPECTRAL RESOLUTION (CM-1)	2	2	2	2
EFFICIENCY (OPTICAL & ELECTRICAL)	.1	.1	.1	.1
THROUGHPUT (SQ CM-STERAD)	.0001	.0001	.0001	.0001
DETECTOR AREA (SQ CM)	.04	.04	.04	.04
MEASUREMENT DURATION (SEC)	1	1	1	1
DETECTOR QUANTUM EFFICIENCY	.5	.5	.5	.5
BACKGROUND EMISSIVITY	.5	.5	.5	.5
COLD FILTER BANDPASS (CM-1)	NA	200	NA	200
COLD FILTER TRANSMISSION	NA	.7	NA	.7
N.E.S.R. (WATT/SQ CM-STERAD-CM-1)	8.5E-8	4.8E-8	6.3E-13	3.1E-13

NOISE EQUIVALENT SPECTRAL RADIANCE CALCULATIONS

2. FOURIER TRANSFORM SPECTROMETER (2.54 CM DIAMETER MIRRORS)

BACKGROUND TEMPERATURE (DEG K)	300	300	85	85
COLD FILTER (Y/N)	NO	YES	NO	YES
WAVENUMBER (CM-1)	667	667	667	667
SPECTRAL RESOLUTION (CM-1)	2	2	2	2
EFFICIENCY (OPTICAL & ELECTRICAL)	.1	.1	.1	.1
THROUGHPUT (SQ CM-STERAD)	.095	.095	.095	.095
DETECTOR AREA (SQ CM)	.12	.12	.12	.12
MEASUREMENT DURATION (SEC)	1	1	1	1
DETECTOR QUANTUM EFFICIENCY	.5	.5	.5	.5
BACKGROUND EMISSIVITY	.5	.5	.5	.5
COLD FILTER BANDPASS (CM-1)	NA	50	NA	50
COLD FILTER TRANSMISSION	NA	.7	NA	.7
N.E.S.R. (WATT/SQ CM-STERAD-CM-1)	4.8E-10	1.2E-10	8.9E-12	2.1E-12

NOISE EQUIVALENT SPECTRAL RADIANCE CALCULATIONS

2A. FOURIER TRANSFORM SPECTROMETER (2.54 CM DIAMETER MIRRORS)

BACKGROUND TEMPERATURE (DEG K)	300	300	85	85
COLD FILTER (Y/N)	NO	YES	NO	YES
WAVENUMBER (CM-1)	1000	1000	1000	1000
SPECTRAL RESOLUTION (CM-1)	2	2	2	2
EFFICIENCY (OPTICAL & ELECTRICAL)	.1	.1	.1	.1
THROUGHPUT (SQ CM-STERAD)	.063	.063	.063	.063
DETECTOR AREA (SQ CM)	.07	.07	.07	.07
MEASUREMENT DURATION (SEC)	1	1	1	1
DETECTOR QUANTUM EFFICIENCY	.5	.5	.5	.5
BACKGROUND EMISSIVITY	.5	.5	.5	.5
COLD FILTER BANDPASS (CM-1)	NA	100	NA	100
COLD FILTER TRANSMISSION	NA	.7	NA	.7
N.E.S.R. (WATT/SQ CM-STERAD-CM-1)	6.0E-10	2.0E-10	2.5E-12	4.7E-13

2B. FOURIER TRANSFORM SPECTROMETER (2.54 CM DIAMETER MIRRORS)

BACKGROUND TEMPERATURE (DEG K)	300	300	85	85
COLD FILTER (Y/N)	NO	YES	NO	YES
WAVENUMBER (CM-1)	2000	2000	2000	2000
SPECTRAL RESOLUTION (CM-1)	2	2	2	2
EFFICIENCY (OPTICAL & ELECTRICAL)	.1	.1	.1	.1
THROUGHPUT (SQ CM-STERAD)	.032	.032	.032	.032
DETECTOR AREA (SQ CM)	.032	.032	.032	.032
MEASUREMENT DURATION (SEC)	1	1	1	1
DETECTOR QUANTUM EFFICIENCY	.5	.5	.5	.5
BACKGROUND EMISSIVITY	.5	.5	.5	.5
COLD FILTER BANDPASS (CM-1)	NA	200	NA	200
COLD FILTER TRANSMISSION	NA	.7	NA	.7
N.E.S.R. (WATT/SQ CM-STERAD-CM-1)	2.3E-10	1.3E-10	1.8E-15	8.7E-16

NOISE EQUIVALENT SPECTRAL RADIANCE CALCULATIONS

3. FOURIER TRANSFORM SPECTROMETER (5 CM DIAMETER MIRRORS)

BACKGROUND TEMPERATURE (DEG K)	300	300	85	85
COLD FILTER (Y/N)	NO	YES	NO	YES
WAVENUMBER (CM-1)	667	667	667	667
SPECTRAL RESOLUTION (CM-1)	1	1	1	1
EFFICIENCY (OPTICAL & ELECTRICAL)	.1	.1	.1	.1
THROUGHPUT (SQ CM-STERAD)	.19	.19	.19	.19
DETECTOR AREA (SQ CM)	.16	.16	.16	.16
MEASUREMENT DURATION (SEC)	1	1	1	1
DETECTOR QUANTUM EFFICIENCY	.5	.5	.5	.5
BACKGROUND EMISSIVITY	.5	.5	.5	.5
COLD FILTER BANDPASS (CM-1)	NA	50	NA	50
COLD FILTER TRANSMISSION	NA	.7	NA	.7
N.E.S.R. (WATT/SQ CM-STERAD-CM-1)	5.6E-10	1.4E-10	1.0E-11	2.4E-12

NOISE EQUIVALENT SPECTRAL RADIANCE CALCULATIONS

3A. FOURIER TRANSFORM SPECTROMETER (5 CM DIAMETER MIRRORS)

BACKGROUND TEMPERATURE (DEG K)	300	300	85	85
COLD FILTER (Y/N)	NO	YES	NO	YES
WAVENUMBER (CM-1)	1000	1000	1000	1000
SPECTRAL RESOLUTION (CM-1)	1	1	1	1
EFFICIENCY (OPTICAL & ELECTRICAL)	.1	.1	.1	.1
THROUGHPUT (SQ CM-STERAD)	.13	.13	.13	.13
DETECTOR AREA (SQ CM)	.12	.12	.12	.12
MEASUREMENT DURATION (SEC)	1	1	1	1
DETECTOR QUANTUM EFFICIENCY	.5	.5	.5	.5
BACKGROUND EMISSIVITY	.5	.5	.5	.5
COLD FILTER BANDPASS (CM-1)	NA	100	NA	100
COLD FILTER TRANSMISSION	NA	.7	NA	.7
N.E.S.R. (WATT/SQ CM-STERAD-CM-1)	7.6E-10	2.5E-10	3.1E-12	6.0E-13

3B. FOURIER TRANSFORM SPECTROMETER (5 CM DIAMETER MIRRORS)

BACKGROUND TEMPERATURE (DEG K)	300	300	85	85
COLD FILTER (Y/N)	NO	YES	NO	YES
WAVENUMBER (CM-1)	2000	2000	2000	2000
SPECTRAL RESOLUTION (CM-1)	2	2	2	2
EFFICIENCY (OPTICAL & ELECTRICAL)	.1	.1	.1	.1
THROUGHPUT (SQ CM-STERAD)	.13	.13	.13	.13
DETECTOR AREA (SQ CM)	.16	.16	.16	.16
MEASUREMENT DURATION (SEC)	1	1	1	1
DETECTOR QUANTUM EFFICIENCY	.5	.5	.5	.5
BACKGROUND EMISSIVITY	.5	.5	.5	.5
COLD FILTER BANDPASS (CM-1)	NA	200	NA	200
COLD FILTER TRANSMISSION	NA	.7	NA	.7
N.E.S.R. (WATT/SQ CM-STERAD-CM-1)	1.3E-10	7.4E-11	9.7E-16	4.8E-16

NOISE EQUIVALENT SPECTRAL RADIANCE CALCULATIONS

4. FABRY-PEROT INTERFEROMETER (2.54 CM DIAMETER MIRRORS)

BACKGROUND TEMPERATURE (DEG K)	300	300	85	85
COLD FILTER (Y/N)	NO	YES	NO	YES
WAVENUMBER (CM-1)	667	667	667	667
SPECTRAL RESOLUTION (CM-1)	2	2	2	2
EFFICIENCY (OPTICAL & ELECTRICAL)	.2	.2	.2	.2
THROUGHPUT (SQ CM-STERAD)	.095	.095	.095	.095
DETECTOR AREA (SQ CM)	.12	.12	.12	.12
MEASUREMENT DURATION (SEC)	1	1	1	1
DETECTOR QUANTUM EFFICIENCY	.5	.5	.5	.5
BACKGROUND EMISSIVITY	.5	.5	.5	.5
COLD FILTER BANDPASS (CM-1)	NA	50	NA	50
COLD FILTER TRANSMISSION	NA	.7	NA	.7
N.E.S.R. (WATT SQ CM-STERAD-CM-1)	2.4E-10	6.1E-11	4.6E-12	1.0E-12

NOISE EQUIVALENT SPECTRAL RADIANCE CALCULATIONS

4A. FABRY-PEROT INTERFEROMETER (2.54 CM DIAMETER MIRRORS)

BACKGROUND TEMPERATURE (DEG K)	300	300	85	85
COLD FILTER (Y/N)	NO	YES	NO	YES
WAVENUMBER (CM-1)	1000	1000	1000	1000
SPECTRAL RESOLUTION (CM-1)	2	2	2	2
EFFICIENCY (OPTICAL & ELECTRICAL)	.2	.2	.2	.2
THROUGHPUT (SQ CM-STERAD)	.063	.063	.063	.063
DETECTOR AREA (SQ CM)	.07	.07	.07	.07
MEASUREMENT DURATION (SEC)	1	1	1	1
DETECTOR QUANTUM EFFICIENCY	.5	.5	.5	.5
BACKGROUND EMISSIVITY	.5	.5	.5	.5
COLD FILTER BANDPASS (CM-1)	NA	100	NA	100
COLD FILTER TRANSMISSION	NA	.7	NA	.7
N.E.S.R. (WATT/SQ CM-STERAD-CM-1)	3.0E-10	9.8E-11	1.2E-12	2.4E-13

4B. FABRY-PEROT INTERFEROMETER (2.54 CM DIAMETER MIRRORS)

BACKGROUND TEMPERATURE (DEG K)	300	300	85	85
COLD FILTER (Y/N)	NO	YES	NO	YES
WAVENUMBER (CM-1)	2000	2000	2000	2000
SPECTRAL RESOLUTION (CM-1)	2	2	2	2
EFFICIENCY (OPTICAL & ELECTRICAL)	.2	.2	.2	.2
THROUGHPUT (SQ CM-STERAD)	.032	.032	.032	.032
DETECTOR AREA (SQ CM)	.032	.032	.032	.032
MEASUREMENT DURATION (SEC)	1	1	1	1
DETECTOR QUANTUM EFFICIENCY	.5	.5	.5	.5
BACKGROUND EMISSIVITY	.5	.5	.5	.5
COLD FILTER BANDPASS (CM-1)	NA	200	NA	200
COLD FILTER TRANSMISSION	NA	.7	NA	.7
N.E.S.R. (WATT/SQ CM-STERAD-CM-1)	1.2E-10	6.7E-11	8.8E-16	4.4E-16

NOISE EQUIVALENT SPECTRAL RADIANCE CALCULATIONS

5.CIRCULAR VARIABLE FILTER (0.1 SQ CM APERTURE)

BACKGROUND TEMPERATURE (DEG K)	300	300	85	85
COLD FILTER (Y/N)	NO	YES	NO	YES
WAVENUMBER (CM-1)	667	667	667	667
SPECTRAL RESOLUTION (CM-1)	18	18	18	18
EFFICIENCY (OPTICAL & ELECTRICAL)	.2	.2	.2	.2
THROUGHPUT (SQ CM-STERAD)	.018	.018	.018	.018
DETECTOR AREA (SQ CM)	.16	.16	.16	.16
MEASUREMENT DURATION (SEC)	1	1	1	1
DETECTOR QUANTUM EFFICIENCY	.5	.5	.5	.5
BACKGROUND EMISSIVITY	.5	.5	.5	.5
COLD FILTER BANDPASS (CM-1)	NA	50	NA	50
COLD FILTER TRANSMISSION	NA	.7	NA	.7
N.E.S.R. (WATT/SQ CM-STERAD-CM-1)	1.6E-10	4.1E-11	3.0E-12	7.1E-13

NOISE EQUIVALENT SPECTRAL RADIANCE CALCULATIONS

5A. CIRCULAR VARIABLE FILTER (0.1 SQ CM APERTURE)

BACKGROUND TEMPERATURE (DEG K)	300	300	85	85
COLD FILTER (Y/N)	NO	YES	NO	YES
WAVENUMBER (CM-1)	1000	1000	1000	1000
SPECTRAL RESOLUTION (CM-1)	30	30	30	30
EFFICIENCY (OPTICAL & ELECTRICAL)	.2	.2	.2	.2
THROUGHPUT (SQ CM-STERAD)	.012	.012	.012	.012
DETECTOR AREA (SQ CM)	.16	.16	.16	.16
MEASUREMENT DURATION (SEC)	1	1	1	1
DETECTOR QUANTUM EFFICIENCY	.5	.5	.5	.5
BACKGROUND EMISSIVITY	.5	.5	.5	.5
COLD FILTER BANDPASS (CM-1)	NA	100	NA	100
COLD FILTER TRANSMISSION	NA	.7	NA	.7
N.E.S.R. (WATT/SQ CM-STERAD-CM-1)	1.6E-10	5.2E-11	6.6E-13	1.25E-13

5B. CIRCULAR VARIABLE FILTER (0.1 SQ CM APERTURE)

BACKGROUND TEMPERATURE (DEG K)	300	300	85	85
COLD FILTER (Y/N)	NO	YES	NO	YES
WAVENUMBER (CM-1)	2000	2000	2000	2000
SPECTRAL RESOLUTION (CM-1)	60	60	60	60
EFFICIENCY (OPTICAL & ELECTRICAL)	.2	.2	.2	.2
THROUGHPUT (SQ CM-STERAD)	.006	.006	.006	.006
DETECTOR AREA (SQ CM)	.16	.16	.16	.16
MEASUREMENT DURATION (SEC)	1	1	1	1
DETECTOR QUANTUM EFFICIENCY	.5	.5	.5	.5
BACKGROUND EMISSIVITY	.5	.5	.5	.5
COLD FILTER BANDPASS (CM-1)	NA	200	NA	200
COLD FILTER TRANSMISSION	NA	.7	NA	.7
N.E.S.R. (WATT/SQ CM-STERAD-CM-1)	4.6E-11	2.7E-11	3.5E-16	3.2E-15

NOISE EQUIVALENT SPECTRAL RADIANCE CALCULATIONS

6. HETERODYNE SPECTROMETER

IDEALLY, A HETERODYNE SPECTROMETER IS LIMITED BY SHOT NOISE IN THE LOCAL OSCILLATOR (NORMALLY A TUNABLE LASER). IN THIS CASE THE N.E.S.R. IS GIVEN BY EQ(3.2.5-3). WORKING AT 667 WAVENO. (15 MICRONS) WITH A 2 WAVENO. SPECTRAL RESOLUTION, AND ASSUMING VALUES OF 1 HZ AND 50% FOR THE POST DETECTION BANDWIDTH AND DETECTOR QUANTUM EFFICIENCY, RESPECTIVELY, WE OBTAIN THE FOLLOWING VALUE FOR THE N.E.S.R:

$$\text{N.E.S.R.} = 2.9\text{E-9 WATT/(SQ CM-STERAD-CM}^{-1}\text{)}$$

6A. HETERODYNE SPECTROMETER

AT A WAVELENGTH OF 10 MICRONS:

$$\text{N.E.S.R.} = 9.8\text{E-9 WATT/(SQ CM-STERAD-CM}^{-1}\text{)}$$

6B. HETERODYNE SPECTROMETER

AT A WAVELENGTH OF 5 MICRONS:

$$\text{N.E.S.R.} = 7.8\text{E-8 WATT/(SQ CM-STERAD-CM}^{-1}\text{)}$$

END

FILMED

1-86

DTIC